Ollscoil na Gaillimhe
University of Galway

Provided by the author(s) and University of Galway in accordance with publisher policies. Please cite the published version when available.

Title	An experimental and modelling study of selected oxygenated biofuels
Author(s)	Burke, Ultan
Publication Date	2014-10-13
Item record	http://hdl.handle.net/10379/4832

Downloaded 2024-04-24T23:58:37Z

Some rights reserved. For more information, please see the item record link above.

An Experimental and Modelling Study of Selected Oxygenated Biofuels

Ultan A. Burke, B. Sc.

NUI Galway
OÉ Gaillimh

School of Chemistry

Presented for the degree of Ph. D. of the National University of Ireland, Galway

Submitted December, 2014

Supervisor: **Prof. Henry J. Curran**
Head of Department: **Prof. P. Murphy**

Abstract

Detailed chemical kinetic models are useful tools for the development of more efficient combustion systems. These models require validation of the elementary kinetics used in order for them to be accurate and reliable. The range of pressures, temperatures, and mixture compositions related to practical combustors means that these models need to be validated over a wide range of conditions. Shock tubes and rapid compression machines, such as the ones used during *this study*, are well suited to provide these validation data due to the well characterised conditions of temperature and pressure during these experiments. *This study* aims to provide both the fundamental experimental data for model validation, and accurate and robustly validated chemical kinetic models, in particular for oxygenated biofuels.

Methane (CH_4), dimethyl ether (DME), 80/20 CH_4/DME and 60/40 CH_4/DME in 'air' ignition delay times were recorded for $p = 7 - 44$ atm, $T = 600 - 1600$ K, and equivalence ratios of $0.3 - 2.0$. These ignition delay times show that as the concentration of DME increases the ignition delay time decreases. The ignition delay times measured provide new validation targets at engine relevant conditions to validate a new chemical kinetic model. This model incorporates updated thermochemical group values based on the calculations of Yamada *et al.* used for the calculation of the thermochemical data for DME combustion species presented in this model (Mech_56.54). Pressure-dependent rate constants have been applied for the first time to the main low-temperature reactions pertaining to the oxidation of DME. High-level calculations and measurements have been applied to the other major reactions of the DME mechanism where available. This model has been validated not only against the new data collected but also against existing literature data in order to constrain the reaction rate constants and reduce the uncertainty in the assignment of the rate constants in the model. The result is a robustly validated mechanism, that can accurately predict the validation targets.

Methanol (CH_3OH) is the simplest alcohol, and its reaction mechanism is well known. However there is a lack of experimental data available for model validation at engine relevant conditions. In *this study* ignition delay times have been recorded for CH_3OH concentrations ranging from $1.5 - 21.9\%$, at $p = 2 - 50$ atm, $T = 850 - 1600$ K, and equivalence ratios of $0.5 - 2.0$. The wide range of conditions studied allowed for the re-validation of a CH_3OH chemical kinetic mechanism. At the high pressure conditions of the data measured, sensitivity was observed to the rate constant $CH_3OH + H\dot{O}_2 \rightleftarrows \dot{C}H_2OH + H_2O_2$. This rate constant is still disputed, with differences in the available quantum chemical calculations ranging from a factor of 3 to an order of magnitude. The wide range of validation data collected during *this study* helped to assign an optimum rate constant for this reaction. The updated model was also validated against existing literature data.

Previous studies have shown tri-propylene glycol monomethyl ether (TPGME) to be an effective soot reducing additive when used in research diesel engines. There is no fundamental experimental data available for the validation of chemical kinetic mechanisms

describing its oxidation. *This study* presents the first experimental data for TPGME at 0.25% TPGME, $p = 10$ and 20 atm, $T = 980 - 1545$ K, and for equivalence ratios of $0.5 - 2.0$. These data are being used in the validation of a chemical kinetic mechanism currently in development. The model agrees well with the ignition delay times measured. Flux analyses showed that the fuel was being consumed mainly by molecular elimination and H-atom abstraction reactions under the conditions studied.

2-Methylfuran (2-MF) and propene (C_3H_6) ignition delay times have also been measured. 2-MF measurements were taken at 1% 2-MF, $p = 1$ atm, $T = 1200 - 1800$ K and over equivalence ratios of $0.5 - 2.0$. C_3H_6 ignition delay times were measured for 0.89% C_3H_6, 4.00% O_2, $p = 40$ atm, $T = 1175 - 1500$ K. The 2-MF data was the first ever measurements of its ignition delay times. This data provided valuable validation targets for the development of a chemical kinetic model which was subsequently published. The C_3H_6 data provided a cross-facility check with equivalent data from Stanford University and was also used in the validation of a chemical kinetic mechanism which has also been published.

This study provides a large quantity of high-pressure ignition delay times for a wide range of oxygenated compounds. It also provides chemical kinetic mechanisms for CH_3OH and DME, the simplest alcohol and ether respectively, and can act as the basis for the further development of chemical kinetic mechanisms for alcoholic and ether compounds.

Publications

Peer-Reviewed Papers in Print

1. S.M. Burke, U. Burke, R. McDonagh, O. Mathieu, I. Osorio, C. Keesee, A. Morones, E.L. Petersen, W. Wang, M.A. Oehlschlaeger, B. Rhodes, R.K. Hanson, D. Davidson, B.W. Weber, C.J. Sung, J. Santner, Y. Ju, E.N. Volkov, A.A. Konnov, M. Alrefae, F. Khaled, A. Farooq, H.J. Curran, "An experimental and modeling study of propene oxidation. Part 2: Ignition delay times and flame speeds", *accepted for publication in* Combust. Flame, September 2014.

2. U. Burke, K.P. Somers, P. O'Toole, C.M. Zinner, N. Marquet, G. Bourque, E.L. Petersen, W.K. Metcalfe, Z. Serinyel, H.J. Curran, "An ignition delay and kinetic modeling study of methane, dimethyl ether and their mixtures at high pressures", *accepted for publication in* Combust. Flame, August 2014.

3. M. Pelucchi, K.P. Somers, K. Yasunaga, U. Burke, A. Frassoldati, E. Ranzi, H.J. Curran, T. Faravelli, "An experimental and kinetic modeling study of the pyrolysis and oxidation of n-C_3–C_5 aldehydes in shock tubes", *accepted for publication in* Combust. Flame, July 2014.

4. M. Pelucchi, K.P. Somers, U. Burke, C. Saggese, A. Frassoldati, E. Ranzi, H.J. Curran, T. Faravelli, "Kinetic modelling of biofuels: Pyrolysis and auto-ignition of aldehydes", Chem. Eng. Trans., 2014, 37, 871–876.

5. K.P. Somers, J.M. Simmie, F. Gillespie, U. Burke, J. Connolly, W.K. Metcalfe, F. Battin-Leclerc, P. Dirrenberger, O. Herbinet, P.A. Glaude, H.J. Curran, "A high temperature and atmospheric pressure experimental and detailed chemical kinetic modelling study of 2-Methylfuran oxidation", Proc. Combust. Inst., 34, 2013, 225–232.

Peer-Reviewed Papers in Review

1. U. Burke, W.K. Metcalfe, S.M. Burke, K.A. Heufer, H.J. Curran, "A kinetic modeling and ignition delay study of methanol oxidation at high pressures", *submitted for publication in* Combust. Flame, August 2014.

Posters and Invited Presenatations

1. U. Burke, W.J. Pitz, H.J. Curran, "Experiments and modeling of a large oxygenated molecule: Tri-propylene glycol mono-methyl ether (TPGME)", *Presented poster at the 35th international symposium on combustion, San Francisco, August 2014.*

2. U. Burke, "Experiments and detailed kinetic model development of selected biofuels", *Invited presentation to Tailor-Made Fuels from Biomass (TMFB) cluster, RWTH Aachen, June 2014.*

3. U. Burke, W.K. Metcalfe, S.M. Burke, K.A. Heufer, H.J. Curran, "A shock tube and rapid compression machine study of methanol oxidation at high pressures", *Presented poster at the European Combustion Meeting (ECM), Lund 2013.*

4. U. Burke, "Second generation biofuels, their place in a sustainable future", Ryan Institute, NUIG, *Official opening, May 2012.*

To Dad

Acknowledgements

I'd like to begin by thanking my supervisor Prof. Henry Curran for giving me this oppurtunity and his continued guidance and help throughout the course of my Ph.D and beyond.

To everyone I have had the privilege of working with in the combustion chemistry centre, I would like to sincerely thank you all. In particular Wayne, Alex, Sinead, Prof. Simmie, Colin and Dan. Wayne for his endless patience and teaching me many of the intricacies of modelling and perhaps even more importantly, that Steven Gerrard's best position is right back. Sinead, thanks for keeping me company in the back of the room, and the many discussions varying from kinetic modelling to politics, never a dull moment. Prof. Simmie for his patience and his help when everything was going wrong on the experimental apparatus, always had another idea in order to guide me in the right direction. Colin and Dan for their help with the experiments, I will always remember that if all else fails give the shock tube a bit of a shake and ya never know... Alexander, where to start, thanks for teaching me everything from A-Z about shock tubes and rapid compression machines. Thanks for teaching me the ways of the engineer! More importantly still, thanks for trusting and me and giving me my next opportunity to work alongside you again in Aachen.

To all the good folks of the chemistry dept. I have met along the way. It is because of the people I met that my experience was so good during Ph.D. thanks to you all!

Three people I would like to specifically mention are Kieran, John and Matteo. You guys made it so that not one day was work, there was always a joke, an arguement, a chicken fillet roll and a pint of guinness at the end of it all. Matteo your time in Galway was filled with craic from your great quotes of "how old are your horses", to your amazing hospitality during our visit to Italy thanks for all your help and continued frienship. Bugler, always a good man for a fact about migratory birds, thanks for putting up with my grumpiness and the ridiculous amount of abuse thrown at ya. I don't think I have ever met a man with so many ridiculous stories, and probably the most higly functional alcoholic in Ireland!! Somers thanks for everything, always the man I went to for advice and help. More importantly though you were the man I could always count on for a good discussion/argument whether it was work, football, well to be honest I think there was very little we couldn't find opposing arguments for, I think one of my favourites was the difference between a great club or a great team!! Thanks for everything guys!

To my family and friends at home, thanks for all yer love and support especially when things were at there darkest, especially my mother and siblings Paul and Ann-Marie. To the lads Cill, Roar, Stevie, Paul, Shane, Murf, Eoin and Mícheál thanks for always reminding me I was terrible at keeping in touch!

To my loving girlfriend Claire. How you put up with me I will never know but thanks for listening to me, for your endless love and support, you are the single greatest influence in my life. Your strength, positivity and resilience never cease to amaze me.

Finally to my father, the loss felt after your untimely passing cannot be decribed, but I know that without your love and guidance throughout my life I would never have come anywhere close to achieving anything like this. I am proud to be your son.

It always seems impossible until it's done.

Nelson Mandela

Contents

1 Introduction **1**
- 1.1 Environmental Impacts of Combustion . . . 1
- 1.2 Irelands's Energy . . . 3
- 1.3 Dimethyl Ether . . . 5
- 1.4 Methanol . . . 5
- 1.5 2-Methylfuran . . . 5
- 1.6 TPGME . . . 5
- 1.7 Overall Goals . . . 5

2 Experimental **7**
- 2.1 Shock Tubes . . . 7
  - 2.1.1 Background . . . 7
  - 2.1.2 Shock Dynamics . . . 8
  - 2.1.3 NUIG High Pressure Shock Tube . . . 11
  - 2.1.4 NUIG Low Pressure Shock Tube . . . 17
- 2.2 Rapid Compression Machine . . . 22
  - 2.2.1 Background . . . 22
  - 2.2.2 NUIG RCM . . . 22
- 2.3 Procedures . . . 25
  - 2.3.1 NUIG High Pressure ST . . . 25
  - 2.3.2 NUIG Low Pressure ST . . . 29
  - 2.3.3 NUIG RCM . . . 32

3 Methane and Dimethyl ether **37**
- 3.1 Abstract . . . 37
- 3.2 Introduction . . . 37
- 3.3 Experimental . . . 39
- 3.4 Computational Modeling . . . 40
  - 3.4.1 RCM Simulation . . . 40
  - 3.4.2 Shock Tube Simulation . . . 41
- 3.5 Chemical Kinetic Model . . . 41
  - 3.5.1 Thermodynamic Data . . . 41
  - 3.5.2 Rate Constants . . . 42
- 3.6 Results and Discussion . . . 46
  - 3.6.1 Methane Oxidation . . . 46
  - 3.6.2 80% CH_4 / 20% DME . . . 50
  - 3.6.3 60% CH_4 / 40% DME . . . 55
  - 3.6.4 Dimethyl Ether Oxidation . . . 58
  - 3.6.5 Influence of Mixture Composition . . . 65

3.7 Conclusions . . . 67

4 Methanol **69**
4.1 Abstract . . . 69
4.2 Introduction . . . 69
4.3 Experimental . . . 72
4.4 Results and Discussion . . . 73
4.4.1 New Ignition Delay Time Measurements . . . 73
4.4.2 H-Atom Abstraction by Hydroperoxyl Radical . . . 80
4.5 Conclusions . . . 88

5 Tri-Propylene Gylcol Mono-Methyl Ether **91**
5.1 Abstract . . . 91
5.2 Introduction . . . 91
5.3 Experimental . . . 92
5.4 Results and Discussion . . . 94
5.5 Conclusion . . . 96

6 Other Compounds **99**
6.1 Propene . . . 99
6.2 2-Methylfuran . . . 102
6.3 Conclusions of these studies . . . 102

7 Conclusions and Outlook **105**
7.1 CH_4/DME . . . 105
7.2 Methanol . . . 105
7.3 TPGME . . . 106
7.4 Other Compounds . . . 106
7.5 Outlook . . . 106

A Dimethyl Ether Mechanism Validation **117**
A.1 Updated Group Values . . . 117
A.2 CH_4 Experimental Data . . . 117
A.3 Validation of the DME Model . . . 146

B Methanol **157**
B.1 Methanol Experimental Data . . . 157
B.2 Methanol Validation . . . 162

C TPGME **169**

D Other Compounds **173**

List of Figures

1.1 Energy production compared to global population from 1980 to 2012 [3]. – Global population, – global energy production. 2
1.2 Energy flow in Ireland in 2012. Sustainable Energy Authority of Ireland (SEAI), *Energy in Ireland: Key Statistics 2013*. 3
1.3 Energy consumption in Ireland per sector. 4
1.4 Transport energy consumption breakdown. Energy flow in Ireland in 2012. Sustainable Energy Authority of Ireland (SEAI), *Energy in Ireland: Key Statistics 2013*. 4

2.1 Schematic x-t diagram of the shock dynamics during a typical shock tube experiment. IS - incident shock, CS - contact surface, RT - rarefaction tail, RH - rarefaction head, p - pressure, T - temperature and t - time [17]. . . . 8
2.2 Laboratory fixed and shock fixed relations [18]. 10
2.3 NUIG high pressure ST. 11
2.4 Fully opened post-experiment aluminum diaphragm. 12
2.5 The mixing manifold of the NUIG high pressure shock tube. 12
2.6 Shock velocity calculation example. (a) PCB traces outlining time interval measurements and magnitude of distances between each transducer. (b) Shock velocities calculated for a typical experiment and linear fit used to determine shock velocity at the point of reflection at the endwall through the intercept. 13
2.7 High pressure ST pressure trace. 14
2.8 High pressure ST pressure trace exhibiting first stage ignition. 14
2.9 Ignition delay times for $\phi = 1.0$ n-Heptane in 'air' $p_5 = 13$ bar mixtures.■ – NUIG HPST, ● – Previous NUIG ST Facility, ▲ – Gauthier *et al.* [24], ▼ – Heufer and Olivier [25]. 15
2.10 Schematic diagram of the LPST. 17
2.11 The mixing manifold of the NUIG low pressure shock tube. 18
2.12 The cutter bursting mechanism of the NUIG low pressure shock tube. . . . 19
2.13 Example of the ignition delay time definition used to measure the methanol data using the NUIG low pressure ST. 20
2.14 Example of the ignition delay time definition used to measure the 2-MF and n-heptane data in the NUIG low pressure ST. 21
2.15 Ignition delay times for $\phi = 1.0$, 0.4% n-heptane, 0.4% O_2, 95.2% Argon, $p_5 = 2$ atm.■ – Smith [17], ● – Davidson *et al.* [26], ▲ – *This Study*. 21
2.16 NUIG RCM. 22
2.17 Schematic diagram of one side of the NUIG RCM. 23
2.18 Creviced piston heads versus non-creviced piston heads. 23
2.19 Typical pressure profile captured using the NUIG RCM. The method of measuring the ignition delay time is outlined. 24

2.20 Schematic diagram of the HPST mixing manifold. 27
2.21 Schematic diagram of the HPST. 28
2.22 Schematic diagram of the LPST manifold. 30
2.23 Schematic diagram of the LPST. 32
2.24 NUIG RCM combustion chamber parts to be cleaned. 33
2.25 Schematic of the NUIG RCM mixing manifold. 34
2.26 NUIG RCM control box for automated use of the RCM. 35

3.1 Rate constants for $CH_3O\dot{C}H_2 \rightleftharpoons \dot{C}H_3 + CH_2O$. 44
3.2 Comparison of ignition delay times over a range of pressures for DME in 'air' $\phi = 1.0$ from this study ($p_5 = 11.9$ and 25.0 atm) and Pfahl *et al.* [64] ($p_5 = 12.8$ and 39.5 atm). Symbols are experimental results; ■ – $p_5 = 11.9$ atm, ● – $p_5 = 12.8$ atm, ▲ – $p_5 = 25.0$ atm, ▼ – $p_5 = 39.5$ atm. Solid lines are predictions using the current mechanism using pressure-dependent rate constants, dashed lines represent the predictions of the current mechanism using high-pressure limiting rate constants, dotted lines represent the predictions using pressure-dependent rate constants for all reactions except methoxymethyl radical β-scission and dash -dot lines represent the predictions of the Curran/Fischer *et al.* mechanism [49,50]. 45
3.3 Influence of pressure on pure methane in air mixtures at ■ – ∼ 10 atm, ● – 25 atm (15 atm for Fig. 3.3(d) ST data), ▲ – 44 atm. Open symbols are RCM data, filled symbols ST data, half-filled symbols are ST data measured during *this study*. Lines are Mech_56.54 predictions, dashed lines are simulations accounting for RCM facility effects. 47
3.4 Sensitivity analyses at 1177 K and at $\phi = 0.30$, ■ – 9.9 atm, ■ – 19.7 atm, ■ – 41.6 atm. 48
3.5 Influence of equivalence ratio on CH_4 mixtures at ■ – $\phi = 0.3$, ● – $\phi = 0.5$, ▲ – $\phi = 1.0$, ▼ – $\phi = 2.0$. Open symbols are RCM data, filled symbols ST data, half-filled symbols are ST data measured during *this study*. Lines are Mech_56.54 predictions, dashed lines are simulations accounting for RCM facility effects. 49
3.6 Sensitivity analyses CH_4/'air' mixtures, ■ – $\phi = 2.0$, ■ – $\phi = 1.0$, ■ – $\phi = 0.5$. 50
3.7 Influence of pressure on 80/20 CH_4/DME mixtures. ■ – ∼ 10 atm, ● – ∼ 20 atm, ▲ – ∼ 30 atm. Open symbols are RCM data, filled symbols ST data. Lines are Mech_56.54 predictions, dashed lines are simulations accounting for RCM facility effects. 51
3.8 Sensitivity to ignition delay time at 706 K, $\phi = 2.0$ at ■ – 5.9 atm, ■ – 25.3 atm. 52
3.9 Influence of equivalence ratio for 80/20 CH_4/DME mixtures. ■ – $\phi = 0.3$, ● – $\phi = 0.5$, ▲ – $\phi = 1.0$, ▼ – $\phi = 2.0$. Open symbols are RCM data, filled symbols ST data. Lines are Mech_56.54 predictions, dashed lines are simulations accounting for RCM facility effects. 53
3.10 Sensitivity analyses for ignition delay times at $p = 10$ atm and at ■ – $\phi = 2.0$, ■ – $\phi = 1.0$, ■ – $\phi = 0.5$. 54
3.11 Flux analyses at 1250 K and $p = 17.0$ atm in 'air', $\phi = 2.0$ – **bold font**, $\phi = 0.5$ – *italic font*. 55

3.12 Model predictions for n-C_3H_8, DME, and 80/20 CH_4/(DME or n-C_3H_8) in 'air' mixtures at p = 30 atm. Black lines are n-C_3H_8, red lines are DME. Solid line are 80/20 mixtures, dashed lines are pure fuels. 56

3.13 Influence of pressure on 60/40 CH_4/DME mixtures. ■ – ∼ 8 atm, ● – ∼ 20 atm, ▲ – ∼ 30 atm. Open symbols are RCM data, filled symbols ST data. Lines are Mech_56.54 predictions, dashed lines are simulations accounting for RCM facility effects. 57

3.14 Sensitivity to ignition delay time at 1135 K, ϕ = 1.0 at ■ – 34.1 atm, ■ – 23.2 atm, ■ – 8.2 atm. 58

3.15 Flux analyses at 1135 K and ϕ = 1.0 in 'air', p = 23.2 atm – **bold font**, p = 8.2 atm – *italic font*. 59

3.16 Influence of pressure on DME mixtures, ■ – ∼ 11 atm, ● – ∼ 25 atm, ▲ – ∼ 30 atm. Open symbols are RCM data, filled symbols ST data, half-filled symbols are ST data measured during *this study*. Solid lines – Mech_56.54, dashed lines – Zhao *et al.* [51], dotted lines – Fischer/Curran *et al.* [49, 50]. 60

3.17 Sensitivity analysis at 827 K and ϕ = 0.50 at ■ – 12.4 atm, ■ – 24.7 atm. . 61

3.18 Flux analyses at 827 K and ϕ = 0.50, 12.4 atm – bold font, 24.7 atm – italic font. 61

3.19 Influence of equivalence ratio for DME mixtures. ■ – ϕ = 0.3, ● – ϕ = 0.5, ▲ – ϕ = 1.0, ▼ – ϕ = 2.0. Open symbols are RCM data, filled symbols ST data, half-filled symbols are ST data measured during *this study*. Lines are Mech_56.54 predictions, dashed lines are simulations accounting for RCM facility effects. 61

3.20 Sensitivity analyses at p = 10 atm and at ■ – ϕ = 0.3, ■ – ϕ = 0.5, ■ – ϕ = 1.0, ■ – ϕ = 2.0. 62

3.21 First stage ignition delay times for a range of compressed pressures and equivalence ratios. ■ – ϕ = 0.43, ● – ϕ = 0.75, ▲ – ϕ = 1.50, filled symbols - 10bar, open symbols - 15 bar, half-filled symbols - 20bar. Lines are Mech_56.54 predictions, all simulations account for RCM facility effects. . . 63

3.22 Influence of mixture composition at p = 7 – 10 atm, ■ – CH_4, ● – 80/20 CH_4/DME, ▲ – 60/40 CH_4/DME, ▼ – DME. Open symbols are RCM data, filled symbols ST data, half-filled symbols are ST data measured during *this study*. Lines are Mech_56.54 predictions, dashed lines are simulations accounting for RCM facility effects. 65

3.23 Sensitivity analyses at 1237 K and ∼ 10 atm. Comparing mixture composition. ■ – CH_4 (9.4 atm), ■ – 80/20 CH_4/DME (7.7 atm), ■ – 60/40 CH_4/DME (7.3 atm), ■ – DME (11.4 atm). 66

4.1 3.10% CH_3OH, 4.65% O_2 (Mixture 13), ϕ = 1.0 at p = 10 atm. ■ – Noorani *et al.* [102], ● – *This study*. Lines are Mech_56.55 predictions. . . . 74

4.2 5.70% CH_3OH, 8.55% O_2, ϕ = 1.0. (a) p = 10 atm. Open symbols correspond to RCM data (Mixture 10), filled symbols correspond to ST data (Mixture 8). Lines represent Mech_56.55 predictions. (b) ■ – p = 10 atm (Mixture 8), ● – p = 50 atm (Mixture 9). Lines represent Mech_56.55 predictions. 75

4.3 (a) CH_3OH with 8.55% O_2, open symbols – $p = 30$ atm (Mixes 3, 11 and 16), solid symbols – $p = 40$ atm (Mixes 4, 12 and 17). ■ – $\phi = 0.5$, ● – $\phi = 1.0$, ▲ – $\phi = 2.0$. Lines represent Mech_56.55 predictions, dashed lines – $p = 30$ atm, solid lines – $p = 40$ atm. (b) CH_3OH with 8.55% O_2 $p = 40$ atm, solid lines – Mech_56.55, dashed lines – Li *et al.*'s [122] mechanism. ■ – $\phi = 0.5$ (Mixture 4), ● – $\phi = 1.0$ (Mixture 12), ▲ – $\phi = 2.0$ (Mixture 17). 76

4.4 Flux analyses at 5.70% CH_3OH, 8.55% O_2, $\phi = 1.0$, $p = 38.4$ atm (Mixture 12), $T = 906$ K. Mech_56.55 – **Bold font**, Li *et al.*'s mechanism – *Italic font.* 77

4.5 Influence of dilution. (a) ■ – 3.1% CH_3OH (Mixture 13), ● – 5.7% CH_3OH (Mixture 8). (b) ■ – 5.7% CH_3OH (Mixture 9), ● – 12.28% CH_3OH (Mixture 7). Lines are Mech_56.55 predictions. 78

4.6 Influence of Pressure. (a) ■ – $p = 30$ atm (Mixture 6), ● – $p = 50$ atm (Mixture 7). Lines represent Mech_56.55 predictions. (b) ■ – $p = 2$ atm (Mixture 14), ● – $p = 50$ atm (Mixture 15). Lines represent Mech_56.55 predictions. 79

4.7 Measured RCM ignition delay times. (a) Influence of pressures. ■ – $p = 10$ atm (Mixture 10), ● – $p = 30$ atm (Mixture 11), ▲ – $p = 40$ atm (Mixture 12). Lines represent Mech_56.55 predictions. (b) Influence of equivalence ratios. ■ – $\phi = 0.5$ (Mixture 3), ● – $\phi = 1.0$ (Mixture 11), ▲ – $\phi = 2.0$ (Mixture 16). Lines represent Mech_56.55 predictions. 80

4.8 Influence of equivalence ratios, CH_3OH in "air", $p = 50$ atm. Lines represent Mech_56.55 predictions, ■ – $\phi = 0.5$ (Mixture 2), ● – $\phi = 1.0$ (Mixture 7), ▲ – $\phi = 2.0$ (Mixture 15). 81

4.9 (a) Sensitivity analyses for 8.55% O_2, $p = 40$ atm and $T = 885$ K (Mixes 4, 12 and 17). (b) Temperature dependent rate constants for the reaction $CH_3OH + H\dot{O}_2 \rightleftarrows \dot{C}H_2OH + H_2O_2$. 82

4.10 Constant O_2 concentration of 8.55% O_2, $p = 40$ atm. ■ – $\phi = 0.5$ (Mixture 4), ● – $\phi = 1.0$ (Mixture 12), ▲ – $\phi = 2.0$ (Mixture 17). 83

4.11 Flux analyses at CH_3OH = 5.70%, O_2 = 8.55% and N_2 = 85.75%, T = 880 K, p = 38.90 atm. Using the rate constants of Cathonnet *et al.* [105] (**Bold figures**) and Klippenstein *et al.* [119] (*Italic figures*). 84

4.12 Sensitivity analyses for 5.70% CH_3OH, 8.55% O_2, $p = 10$ atm and T = 956 K. 85

4.13 Fuel in "air" mixtures showing the influence of equivalence ratio, p = 50 atm. ■ – $\phi = 0.5$, ● – $\phi = 1.0$, ▲ – $\phi = 2.0$. 86

4.14 Sensitivity analyses for Methanol in "air", $p = 50$ atm, $T = 1060$ K. (a) – Klippenstein *et al.*'s [119] rate constant, (b) – Cathonnet *et al.*'s [105] rate constant. 87

4.15 Effect of varying the rate constant for $H\dot{O}_2 + H\dot{O}_2 \rightleftarrows H_2O_2 + O_2$ using Klippenstein *et al.*'s [119] rate constant for H-atom abstraction by hydroperoxyl radical. 8.55% O_2, $p = 40$ atm. ■ – $\phi = 0.5$, ● – $\phi = 1.0$, ▲ – ϕ = 2.0. Solid lines are predictions using [130]'s rate constant for $H\dot{O}_2 + H\dot{O}_2 \rightleftarrows H_2O_2 + O_2$, dashed lines represent predictions applying a factor of 2 decrease to this rate constant. 88

5.1 All possible TPGME structural isomers in the isomeric mixture experimentally studied. 92

5.2 Laser absorption measurements. ■ – Test cell, ● – In-situ. Line is a linear correlation to the test measurements. Absorption measured at a wavelength of 3.39 μm, using a He-Ne laser. 93
5.3 Experimental pressure trace. Reflected shock conditions: p = 10.4 atm, T = 1154 K, ϕ = 1.0 94
5.4 Effect of equivalence ratio, 0.25% TPGME. ■ – ϕ = 2.0, ● – ϕ = 1.0, ▲ – ϕ = 0.5. Lines represent LLNL_Mech simulation results. 95
5.5 Effect of pressure and ϕ, 0.25% TPGME. Filled symbols are p_5 = 10 atm and open symbols are p_5 = 20 atm. ■ – ϕ = 2.0, ● – ϕ = 1.0, ▲ – ϕ = 0.5. Lines represent LLNL_Mech simulation results. Solid lines = 10 atm data, dashed lines = 20 atm data. 96
5.6 Flux analysis for 0.25% TPGME, 1.69% O_2, 98.06% Ar for p_5 = 18.41 atm, T_5 = 1187 K, ϕ = 2.00 and at 20% fuel consumed. Percentages represent net flux of reaction from indicated species. 97

6.1 Ignition delay time data sets measured previously and in [139]. 100
6.2 Comparison of ignition delay times measured for 0.89% C_3H_6, 4% O_2 and p = 40 atm in the STs at SU and NUIG. 100
6.3 Effect of equivalence ratio, 1.00% 2-MF, p_5 = 1 atm. ■ – ϕ = 2.0, ● – ϕ = 1.0, ▲ – ϕ = 0.5. Solid lines = updated mechanism [140], dashed lines = original mechanism [138]. 102

A.1 Atmospheric Flow Reactor Data: H. Guo, W. Sun, F. M. Haas, T. Farouk, F. L. Dryer, Y. Ju, Proceedings of the Combustion Institute, 34, (2013), 573–581. 146
A.2 Atmospheric Flow Reactor Data: H. Guo, W. Sun, F. M. Haas, T. Farouk, F. L. Dryer, Y. Ju, Proceedings of the Combustion Institute, 34, (2013), 573–581. 147
A.3 Jet Stirred Reactor: P. Dagaut, C. Daly, J. M. Simmie, M. Cathonnet, Symposium (International) on Combustion, 27, (1998) 361–369. 148
A.4 Flame Speed: J. de Vries, W. B. Lowry, Z. Serinyel, H. J. Curran, E. L. Petersen, Fuel, 90 (2011) 331–338. 149
A.5 Ignition Delay Times: An Experimental and Modelling Study of the Combustion of Oxygenated Hydrocarbons, Ph.D. Thesis, Fiona R. Gillespie, Department of Chemistry, National University of Ireland Galway, Ireland, 2014. 149
A.6 Ignition Delay Times: R. D. Cook, D. F. Davidson, R. K. Hanson, Proceedings of the Combustion Institute, 32, (2009), 189–196. 150
A.7 Ignition Delay Times: G. Mittal. M. Chaos, C. -J. Sung, F. L. Dryer, Fuel Processing Technology, 89, (2008), 1244–1254. 150
A.8 ST Speciation: S. H. Pyun, W. Ren, K. -Y. Lam, D. F. Davidson, R. K. Hanson, Combustion and Flame, 160, (2013), 747-754. 151
A.9 Variable Pressure Flow Reactor Data: H. J. Curran, S. L. Fischer, F. L. Dryer, International Journal of Chemical Kinetics, 32, (2000), 741–759. S. L. Fischer, F. L. Dryer, H. J. Curran, International Journal of Chemical Kinetics, 32, (2000), 713–740. 152
A.10 Variable Pressure Flow Reactor Data: H. J. Curran, S. L. Fischer, F. L. Dryer, International Journal of Chemical Kinetics, 32, (2000), 741–759. S. L. Fischer, F. L. Dryer, H. J. Curran, International Journal of Chemical Kinetics, 32, (2000), 713–740. 153

A.11 Atmospheric Flow Reactor Data: F. Herrmann, B. Jochim, P. Oβwald, L. Cai, H. Pitsch, K. Kohse-Höinghaus, Combustion and Flame, 161, (2014), 384-397. 154
A.12 Flame Speciation Data: D. Liu, J. Santner, C. Togbé, D. Felsmann, J. Koppmann, A. Lackner, X. Yang, X. Shen, Y. Ju, K. Kohse-Höinghaus, Combustion and Flame, 160, (2013), 2654-2668. 155
A.13 Flame Speed Data: D. Liu, J. Santner, C. Togbé, D. Felsmann, J. Koppmann, A. Lackner, X. Yang, X. Shen, Y. Ju, K. Kohse-Höinghaus, Combustion and Flame, 160, (2013), 2654-2668. 155
A.14 Ignition Delay Time Data: Z. Li, W. Wang, Z. Huang, M. A. Oehlschlaeger, Energy & Fuels, 27, (2013), 2811–2817. 156

B.1 Flow Reactor Data: V. Aranda, J. M. Christensen, M. U. Alzueta, P. Glarborg, S. Gersen, Y. Gao, P. Marshall, International Journal of Chemical Kinetics, 45, (2013), 283–294. 163
B.2 Flow Reactor Data: T. J. Held, F. L. Dryer, International Journal of Chemical Kinetics, 30, (1998), 805–830. 164
B.3 Flow Reactor Data: T. J. Held, F. L. Dryer, International Journal of Chemical Kinetics, 30, (1998), 805–830. 165
B.4 Ignition Delay Time Data: C. T. Bowman, Combustion and Flame, 25, (1975), 343–354. 166
B.5 Ignition Delay Time Data: K. Fieweger, R. Blumenthal, G. Adomeit, Combustion and Flame, 109, (1997), 599–619. 167
B.6 Ignition Delay Time Data: K. Natarajan, K. A. Bhaskaran, Combustion and Flame, 43, (1981), 35–49. 167
B.7 Ignition Delay Time Data: J. Herzler, C. Naumann, Work in Progress Presentation (P3-8), In: *European Combustion Meeting 2013*, Lund, Sweden. . 167
B.8 Ignition Delay Time Data: K. E. Noorani, B. Akih-Kumgeh, J. M. Bergthorsen, Energy & Fuels, 24, (2010), 5834–5843. 168

List of Tables

3.1 CH_4 ignition delay time studies from the literature. 39
3.2 Summary of DME ignition delay time studies from the literature. 39
3.3 CH_4/DME mixtures tested in the present study. Compositions reported in percentage volume. 40
3.4 Modified H-atom abstraction reactions. A, n and E_a (cal mol^{-1}) in ChemkinPRO [71] format. 42
3.5 Low-temperature DME reactions treated as pressure dependent. 43

4.1 Experimental data for the pyrolysis and oxidation of methanol. 71
4.2 Experimental data sets studied. % Molar volumes of each constituent. . . . 73

5.1 Experimental data sets studied showing species concentrations on % molar volume. 93

6.1 C_3H_6 ignition delay time data sets measured by each of the collaborating institutes. Species concentrations presented as % molar volume. Dataset taken by *this author* is highlighted in bold. 103

A.1 Optimised Group Values Pertaining to Ether Thermochemistry. 117

Chapter 1

Introduction

The interpretation of complex chemical kinetic models involves understanding of kinetic rate parameters, thermodynamic data, physics of a wide range of environments, and knowledge of computer hardware and software. In addition, the theoretical inferences made by these models require experimental validation in order to provide realistic grounding and to extract realistic physical data and conclusions from these theoretical models. *This study* aims to generate fundamental experimental data, available for the validation of theoretical models, and develop accurate chemical kinetic models capable of providing information on the complex mechanisms of oxidation and pyrolysis of selected oxygenated biofuels under conditions relevant to combustion environments (high pressures and a wide range of temperatures).

The motivation for the development of these models under the conditions mentioned above, is derived from the continued wide use of combustion in order to provide modern society with energy. The increased attention to environmental impacts of combustion, such as increased emissions and global warming, has catalysed society's interest into the chemical processes involved during combustion. These chemical kinetic models offer a relatively affordable and expeditious source of information, enabling the development of more efficient and safer combustion, and may act as guides to potential alternative fuels in order to move away from non-renewable hydrocarbon fuels commonly used.

1.1 Environmental Impacts of Combustion

The main environmental concern with respect to combustion is focused around global warming. However, considering the increasing demand for energy in developing countries, the increased emissions of possibly toxic and/or carcinogenic combustion products are also a growing concern.

The global warming phenomenon, which is inextricably linked to climate change, causes global temperature increase due to degradation of the earth's ozone and increased emissions of greenhouse gases such as CO_2, CH_4, NO_2, etc. [1]. These compounds are all well known products of combustion. As the global population continues to increase, so does the demand for energy as shown in Fig. 1.1. Global energy currently relies on fossil fuels to provide 81.6% of its total energy supply based on 2011 figures [2]. This points to a link between global warming and global energy production from combustion. Due to economic and technological constraints, the current available renewable energy options are not yet in a position to satisfy the ever growing global energy demands. An alternative for the short- to mid-term is to improve the efficiency, and attempt to reduce emissions of the

combustion processes currently providing the majority of global energy. To achieve this, the chemistry controlling the combustion of compounds being burned must be explored in order to inform further developments.

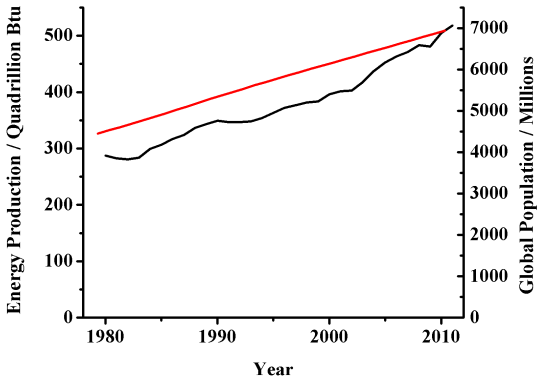

Figure 1.1: Energy production compared to global population from 1980 to 2012 [3]. – Global population, – global energy production.

The use of biofuels has long been considered as a potential alternative to traditional fossil fuels. The most common biofuel currently used is ethanol. It has been shown to reduce the emissions of greenhouse gases when blended with petrol [4]. However, one of the major intermediate species produced from alcohol combustion are aldehydes. These compounds are considered carcinogens [5]. Chemical kinetic models can predict the possible results of burning new compounds. Using the knowledge derived from these predictions large and unnecessary investments into potential biofuels before fully considering the myriad of possible environmental impacts can be prevented.

1.2 Irelands's Energy

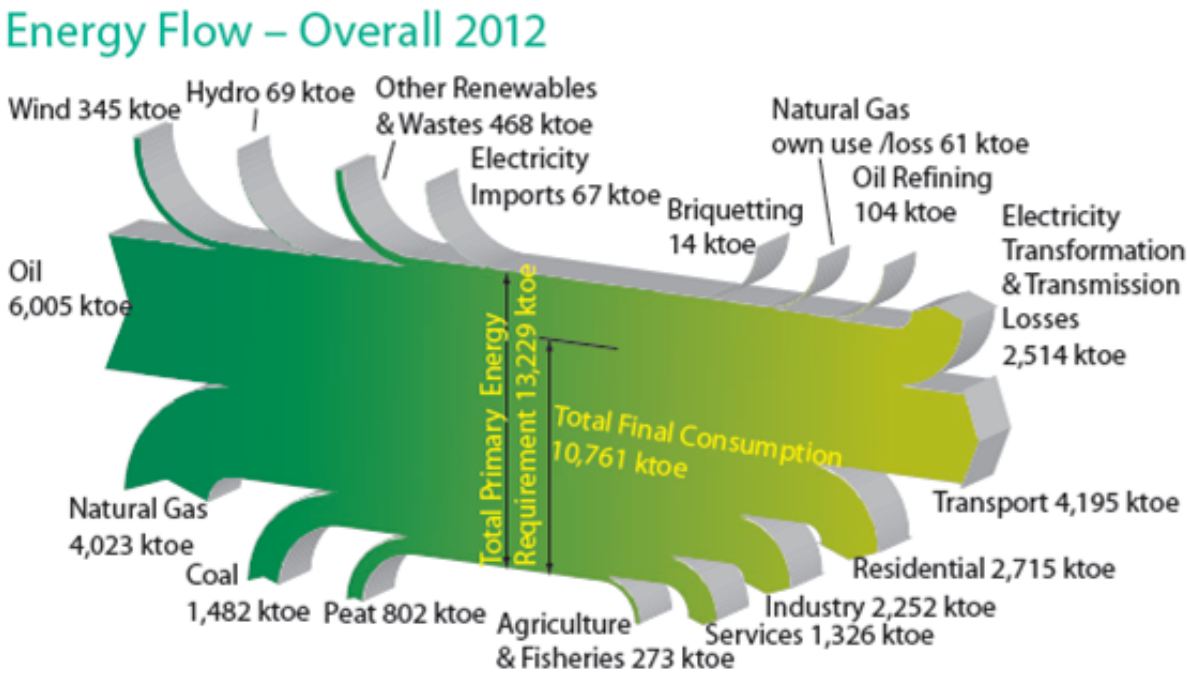

Figure 1.2: Energy flow in Ireland in 2012. Sustainable Energy Authority of Ireland (SEAI), *Energy in Ireland: Key Statistics 2013*.

Figure 1.2 illustrates how Ireland currently satisfies its energy needs. Oil, natural gas, coal, and peat provide the majority of Ireland's raw energy. These fuels are all burned, and are almost completely produced from non-renewable fossil fuels. The main renewable energy resources being utilised are wind and hydro-electric. The transportation sector is the main one consuming energy in Ireland, Fig. 1.3, and considering the existing transport infrastructure these renewable sources are unlikely to provide alternatives to the burning of fossil fuels.

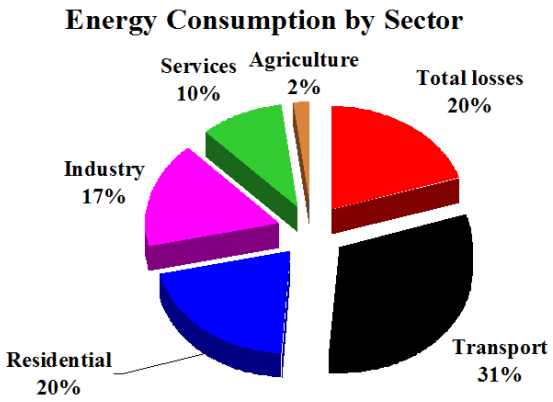

Figure 1.3: Energy consumption in Ireland per sector.

For this reason oxygenated biofuels are being considered as supplements, or potential replacements, to the fossil fuels currently in use. Figure 1.4 shows that currently 2% of Ireland's transport energy is provided from biofuels. Due to new European Union (EU) guidelines, all EU member states must rely on renewable energy sources to produce at least 20% of their energy for transport by 2020 [6]. Therefore, considerable work is needed to meet this target. These guidelines also outline that biofuels have a role to play in reaching these targets, particularly, in the transportation sector.

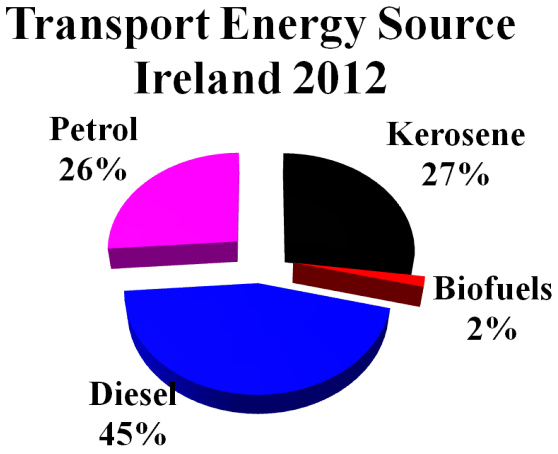

Figure 1.4: Transport energy consumption breakdown. Energy flow in Ireland in 2012. Sustainable Energy Authority of Ireland (SEAI), *Energy in Ireland: Key Statistics 2013*.

As discussed previously, in order to meet these targets, decisions informed by combustion modelling, are required. *This study* is motivated by this to consider the development of chemical kinetic models for oxygenated biofuels.

1.3 Dimethyl Ether

Dimethyl ether (DME) is considered to be a promising diesel additive or substitute. Its high cetane number (≈ 55) makes it a good candidate. This idea is supported by the fact that Volvo, in the U.S.A, has launched its VNL 300 DME trucks. These run on pure DME. Currently, DME is mainly produced from syngas through a dehydration reaction of methanol. However, it can also be produced from gasification of biomass. The main advantage of DME is the significant reduction in emissions of greenhouse gases when compared to diesel.

1.4 Methanol

Methanol is the simplest alcohol and was used in the mid-80s to the late-90s as a gasoline additive in petrol engines in the U.S.A. Its low energy density, corrosivity, and the emergence of ethanol as a more favourable alternative, means that methanol is not being considered as an answer to our liquid fuel needs. However, it is being used in fuel cells, in the production of plastics, and from a combustion modelling point of view is the foundation for further development of mechanisms for larger alcohols.

1.5 2-Methylfuran

2-Methylfuran (2-MF) is produced from waste biomass through recent novel synthetic pathways from the platform chemical 5-hydroxymethylfurfural [7, 8]. Numerous studies testing the use of 2-MF in spark-ignition engines [9–11] have been carried out since the synthetic pathway was established. No fundamental data for model validation was available at the beginning of *this thesis*. 2-MF has a similar energy density (27.6 MJ/L) and research octane number (≈ 100.7) as gasoline. 2-MF is currently one of a number of cyclic ether compounds being considered as possible alternative oxygenated biofuels.

1.6 TPGME

Tri-propylene glycol mono-methyl ether (TPGME) is highly branched large oxygenated compound. It has low toxicity and vapour pressure and is commonly used as an industrial solvent, chemical intermediate and/or for ink in ballpoint or felt-tipped pens [12]. Recent studies [13, 14] have found TPGME to be an effective soot reducing additive in diesel research engines. To date, there is no fundamental experimental data available at combustion relevant conditions for the validation of a chemical kinetic model in order to elucidate TPGME's mechanism of oxidation under engine relevant conditions.

1.7 Overall Goals

The overall goal of *this study* is to measure fundamental ignition delay time data for the aforementioned oxygenated biofuels, which can then be used to validate chemical kinetic models. Additionally, *this study* aims to develop robustly validated chemical kinetic models in an effort to provide well founded information on the combustion of the oxygenated compounds. This information is needed, as the variety and number of oxygenated compounds continue to emerge as potential fuels.

First, the experimental methods used will be described. The experiments and modelling of methane, DME and their mixtures completed during *this study* will be presented. Next, the data and modelling of methanol will be discussed. Works completed on TPGME, propene and 2-MF will be presented after this. Finally, conclusions from *this study* and an outlook for future work related to the research discussed in *this thesis* will be discussed.

Chapter 2

Experimental

This study utilised shock tubes (ST) and a rapid compression machine (RCM) to record the ignition delay times presented. A high-pressure ST, a low-pressure ST and a twin opposed-piston RCM were used.

2.1 Shock Tubes

2.1.1 Background

A ST is a device used to monitor shock wave dynamics in a controlled environment. *This study* concentrates on the use of the reflected shock technique to measure ignition delay times of reactive (fuel/oxidiser/diluent) gaseous mixtures.

The reflected shock technique for measuring ignition delay times has been widely used for many years. An early review by Belford and Strehlow [15] outlined the era when the shock tube had begun to be widely used to study chemical kinetics. Since the early studies the shock tube has been used to study a variety of chemical kinetic effects, from ignition delay times to elementary rate constants.

The popularity of the ST apparatus to study, in particular, high-temperature chemical kinetics ($>$ 1000 K) lies with the near ideal conditions within the reaction zone post arrival of the reflected shock. The conventional design of an ST for studying chemical kinetics is a cylindrical tube (usually metal) of uniform internal diameter. This tube is separated into two sections; the driver (high pressure) and the driven (low pressure) sections. These sections must be separated from one another using a divider. The most common design for this uses a diaphragm (the material for this differs from polycarbonate to aluminium, essentially a suitably labile compound which can be breached) which must burst "instantaneously" in order to form the incident shock front. Once the diaphragm has been burst an incident shock front is formed which propagates through the test mixture, a rarefaction fan propagates in the opposite direction through the driver gas while the slower physical gas flow forms a contact surface moving in the same direction as the incident shock front (Fig. 2.1).

The incident shock front moves through the test gas causing a nearly instantaneous increase in temperature, pressure and density. It is reflected at the endwall and as it moves back through the already heated test gas it causes a further increase in temperature, pressure and density. The test gas post reflected shock is considered to have negligible flow under ideal conditions and will remain at these reflected shock conditions until the arrival of the contact surface. The available test time for reflected shock experiments is

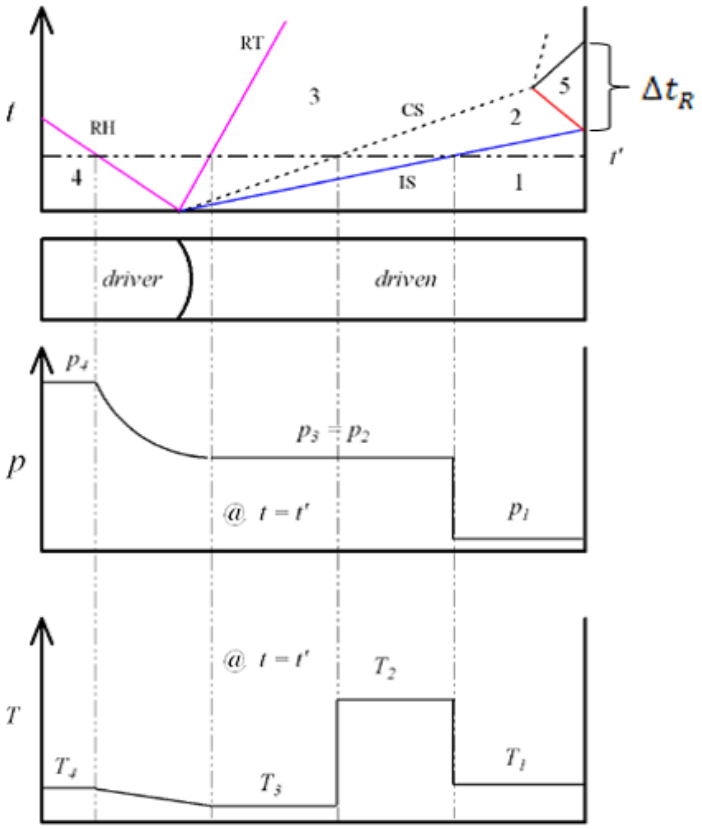

Figure 2.1: Schematic x-t diagram of the shock dynamics during a typical shock tube experiment. IS - incident shock, CS - contact surface, RT - rarefaction tail, RH - rarefaction head, p - pressure, T - temperature and t - time [17].

considered as the time between heating of the test gas by the reflected shock wave and the arrival of the contact surface (Δt_R in Fig. 2.1).

As mentioned above, the reflected shock ideally heats the test gas instantaneously and the test gas then remains under constant reflected shock conditions. However, one must consider non-ideal shock effects to interpret results correctly. These effects are mainly dependent upon the tube geometry, diaphragm bursting mechanism and gas mixture composition. A detailed description of the non-ideal effects encountered in reflected shock wave experiments was presented by Petersen [16].

2.1.2 Shock Dynamics

The general description of a typical reflected shock wave experiment has been outlined in the previous section. Most pertinent to *this study* is the calculation of the pressure and temperature conditions post reflected shock front.

To examine the gaseous conditions present during a ST experiment, the regions are defined (Fig. 2.1). "Region 1" denotes the initial test gas conditions. "Region 2" refers to the conditions of the gas particles between the contact surface and the incident shock front. The conditions of the gas between the contact surface and the rarefaction fan is denoted "region 3". The initial driver gas conditions are in "region 4" while the post reflected shock conditions are in "region 5".

Figure 2.1 presents the trends of pressure, temperature and the development of the shock waves with time across the length of the shock tube throughout a typical experiment. This diagram shows the pressure in the driver section (p_4) dropping and the increase in pressure as the incident shock front moves through the gas (p_1 to p_2). Also shown is the increase in temperature across the shock front (T_1 to T_2). What is clear is that there is an increase in temperature and pressure moving from "region 1" to "region 2". The change in conditions in these two regions is caused by the passage of the incident shock front.

Shock Mach Number and the Isentropic ratio

Underpinning the calculation of the post-shock conditions is knowledge of the shock Mach number (M_i, equation 2.1). Mach number is defined as the ratio of the speed of a body (u_i, equation 2.1) to the speed of sound in the surrounding medium(a_i, equation 2.1).

$$M_i = \frac{u_i}{a_i} \tag{2.1}$$

Also required for the post-shock conditions calculation is the ratio of specific heats (C_p the heat capacity at constant pressure and C_v the heat capacity at constant volume), equation 2.2) of the test gas, more commonly known as the isentropic ratio (γ, equation 2.2).

$$\gamma = \frac{C_p}{C_v} \tag{2.2}$$

Assuming an ideal gas under non-viscous flow conditions, the post-shock conditions can be calculated as will be shown in the following sections.

Laboratory Time and Gas-Particle Time

Two frames of reference should be considered when understanding the gas dynamics during an experiment.

- Laboratory-fixed time (t_l)
- Shock-fixed time (t_p)

Laboratory-fixed time considers the movement of the shock through the gas while shock-fixed time refers to the movement of the gas through a static shock front. These definitions are illustrated in Fig. 2.2.

Shock-fixed time (t_p) concerns the time with respect to the flowing gas particles. Laboratory time (t_l) records the time on an external device, therefore the gas particles have been at the post-shock conditions for some time longer (t_p), than the t_l recorded.

To determine the variables across the shock front it is common to consider the gas motion relative to the shock front to be moving with a velocity u_1 into the shock front and leaving the shock front with a velocity u_2 (in t_p). The incident shock velocity in t_l is U_s, while the gas velocity after passage of the shock front is denoted U_2. These variables are related by the following relationships and again are illustrated in Fig. 2.2.

$$u_1 = U_s \tag{2.3}$$

$$u_2 = U_s - U_2 \tag{2.4}$$

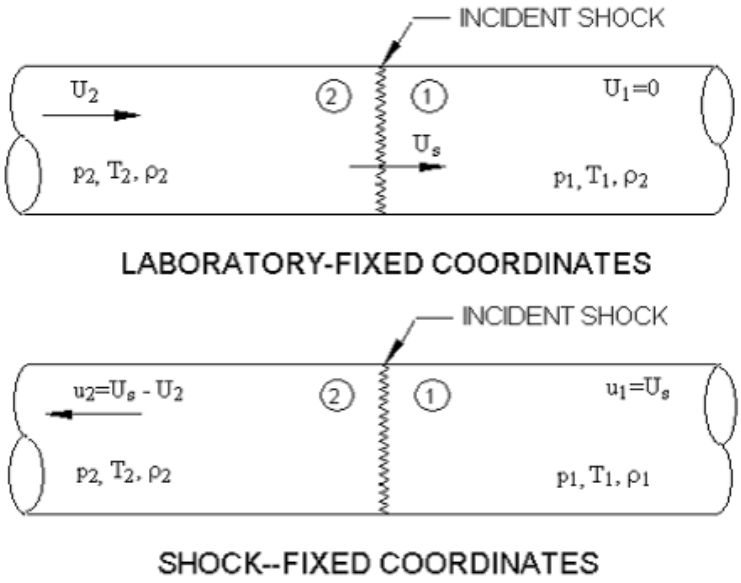

Figure 2.2: Laboratory fixed and shock fixed relations [18].

Post-Shock Conditions Calculation

The theory behind the conditions across the shock front are governed by the equations of conservation of mass, momentum and energy (shown by Rankine-Hugoniot [19, 20]) and the ideal gas equation.

$$\rho_1 u_1 = \rho_2 u_2 \tag{2.5}$$

$$p_1 + \rho_1 u_1^2 = p_2 + \rho_2 u_2^2 \tag{2.6}$$

$$h_1 + \frac{u_1^2}{2} = h_2 + \frac{u_1^2}{2} \tag{2.7}$$

$$pV = nRT \tag{2.8}$$

Subscript 1 is assigned to initial conditions downstream of the incident shock front and subscript 2 represents the post-shock conditions. Above, ρ denotes density, u is gas velocity, p is pressure, h is enthalpy, V is volume, R is the universal gas constant and T is temperature.

The four equations above contain four unknowns ρ_2, p_2, u_2 and h_2. Using the four equations above it is possible to calculate the four unknowns using the simultaneous equations technique. Evaluating these four unknowns provides the values of density, pressure, velocity and enthalpy of the gas after passage of the incident shock front. The knowledge of the gaseous conditions behind the incident shock front is then applied a second time using the same method and equations to calculate the gaseous conditions after passage of the reflected shock front.

2.1.3 NUIG High Pressure Shock Tube

This facility is a stainless steel cylindrical tube. It consists of a 3.0 m driver section, a 3.0 cm double diaphragm mid-section and a 5.73 m driven section. It has an internal diameter of 63.5 mm and wall thickness of 15.3 mm. The tube has a maximum static pressure and temperature of 450 bar and 473 K, respectively. Tubes are secured together using six 20 mm bolts through mounted buttress threaded flanges. Each connection is sealed using viton o-rings. This facility was designed and constructed during the course of *this study*. The tube was designed by Dr. Alexander Heufer according to TRD AD2000 regulations. This tube is shown in Fig. 2.3.

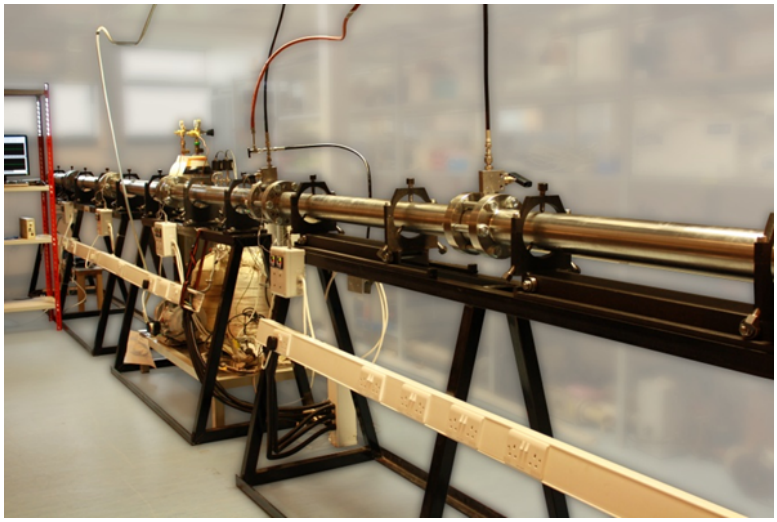

Figure 2.3: NUIG high pressure ST.

Driver Section/Double Diaphragm Mid-Section

The driver section is connected through a Maximator 21V9M071 valve to the high pressure manifold where driver gas (usually helium) can be added. It is mounted on movable rolling clamps to allow the diaphragms to be changed between experiments. The mid-section is situated between the driver and driven sections. It houses two aluminum diaphragms bordering it on both the driver and driven section sides. This mid-section acts as the triggering mechanism for the user. Approximately half the total drive pressure is filled into the mid-section, acting as a buffer between the much lower initial test gas pressure, (p_1) and the much higher driver gas pressure (p_4). The aluminium diaphragms are scored with a cross-shape, using a diamond tipped blade and a mechanical press. This facilitates the bursting of the diaphragms and ensures that they open as completely as possible, as shown in Fig. 2.4.

Driven Section/Mixing Manifold

The driven section houses six PCB 113B24 high frequency pressure transducers spaced axially from the endplate up to a distance of 2.59 m. A Kistler 603B pressure transducer is also located within the plug-style endplate. These transducers are coated with silicone thermal paste in order to protect the sensors from the thermal heat shock effect which causes a lower than reality reading from the sensor. The driven section is connected to the mixing manifold *via* a Maximator 21V9M071 valve (high pressure valve, Fig. 2.5).

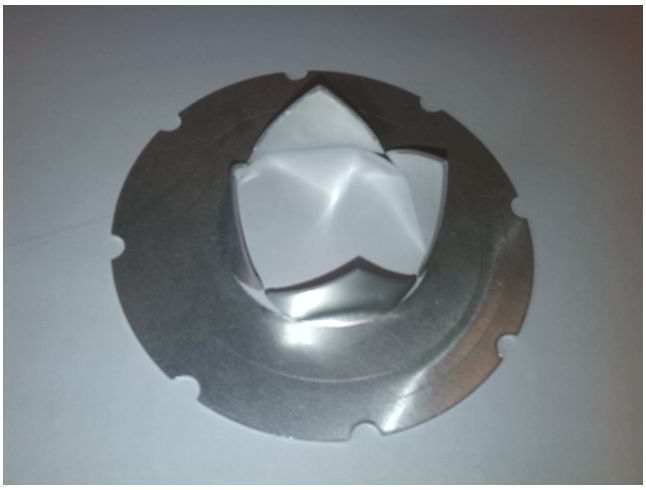

Figure 2.4: Fully opened post-experiment aluminum diaphragm.

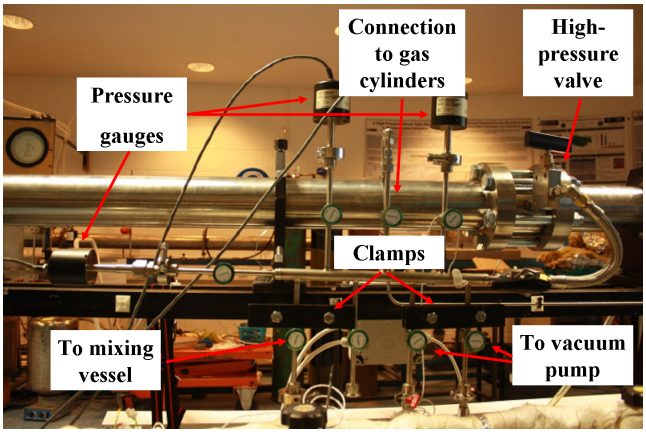

Figure 2.5: The mixing manifold of the NUIG high pressure shock tube.

The manifold is connected to three MKS pressure transducers (Model 121AA) rated to 100, 1000 and 5000 Torr, and an Edwards vacuum gauge. A 60 L stainless steel mixing vessel which has been rated to a maximum static working pressure of 20 bar, is used to prepare the pre-mixed mixtures. This vessel is equipped with a magnetically driven stirring fan used to ensure homogeneous mixtures. A compression sealed SGE Analytical grade Science 10mm Septa is used to allow direct injection of liquid fuels into the evacuated mixing vessel. The manifold is also connected to an Edwards XDS10 scroll pump used for evacuating the mixing vessel and tube between experiments, and the nitrogen and oxygen bath gases used for mixture preparation. Swagelok valves are used to control all connections to the mixing manifold. A picture of the mixing manifold can be seen in Fig. 2.5.

Heating System

The heating system on the NUIG high-pressure shock tube (HPST) was installed to allow users to work with low vapour pressure compounds without condensation occurring. This setup has been described in detail by Darcy *et al.* [21] The heating system was installed on the mixing manifold, driven section, the mid-section, and a 0.5 m length of the driver

section closest to the mid-section. Flexelec RV1 1250W heating tapes were used to heat the tube sections and the mixing vessel. Flexelec single strand heating tape was used to heat the mixing manifold. A Horst heated transfer line was used to connect the mixing manifold to the ST. Hennlich temperature controllers were used to control the heating tapes and type-T thermocouples were connected to the outer surfaces to measure the temperature. This heating system was capable of maintaining a homogeneous temperature within ±2 K of the set temperature. This heating system was insulated by first wrapping it with fibreglass cloth followed by rock wool of similar thickness to the tube and finally secured in place with fibreglass insulating blankets.

Data Collection

During an experiment the pressure is monitored by a series of high frequency piezoelectric pressure transducers (described in section 2.1.3, above). The signal produced by the six PCB's are relayed to a PCB Piezotronics 482 signal conditioner. This signal is then passed to a TiePie Handyscope HS4 oscilloscope which provides the user with the output pressure traces as a function of time. The signal produced from the Kistler 603B in the endwall of the ST is passed through a Kistler 5018 signal conditioner before being recorded digitally by a TiePie Handyscope HS4 oscilloscope.

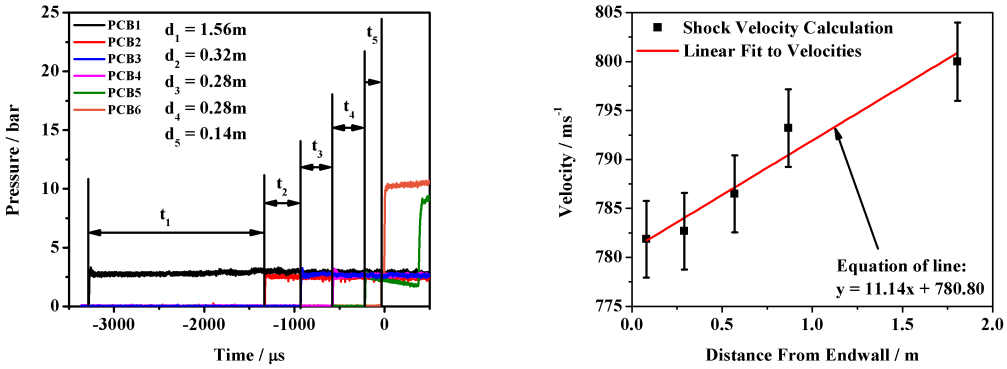

(a) PCB Pressure Traces

(b) Shock Velocity Curve

Figure 2.6: Shock velocity calculation example. (a) PCB traces outlining time interval measurements and magnitude of distances between each transducer. (b) Shock velocities calculated for a typical experiment and linear fit used to determine shock velocity at the point of reflection at the endwall through the intercept.

Figure 2.6 illustrates the method of calculating the shock velocity from the time intervals measured between the six PCB transducers and using a linear fit to extrapolate the velocity to the endwall, this accounts for shock attenuation in the shock velocity calculation.

The definition used for ignition delay time for all the data measured using this facility is shown in Fig. 2.7. The ignition delay time is measured at the observation point and defined as the time from the arrival of the reflected shock wave to highly exothermic release of energy, which is observed *via* pressure here, caused due to ignition. This phenomenon is all but instantaneous for fuel in "air" mixtures. For dilute cases however the increase in pressure can be more gradual and due to this the ignition time is taken by extrapolating a tangent to the maximum rate of pressure increase until intersection with the original reflected shock pressure, this method is used and explained in detail by Davidson and

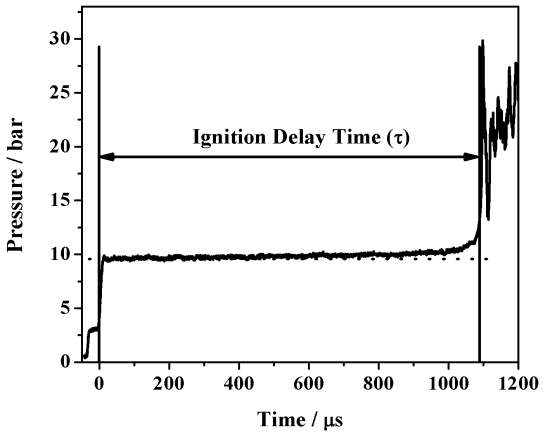

Figure 2.7: High pressure ST pressure trace.

Hanson [22]. These definitions are also used to define the ignition delay time for any simulations of data from this facility throughout *this thesis*. First stage ignition times were also observed during the DME and *n*-heptane measurements, an example of this is shown in Fig. 2.8. The uncertainty in the ignition delay times measured in the NUIG high-pressure ST is 20%. This is assigned by determining the level of uncertainty in all the relevant parameters i.e. mixture composition, initial temperature, initial pressure and shock velocity calculation. When all these parameters are assigned uncertainty values the total uncertainty in the ignition delay time measurement is assigned cumulatively. The absolute figures vary between 15-20% so for simplicity the worst case scenario of 20% is assigned to the ignition delay time measurements presented.

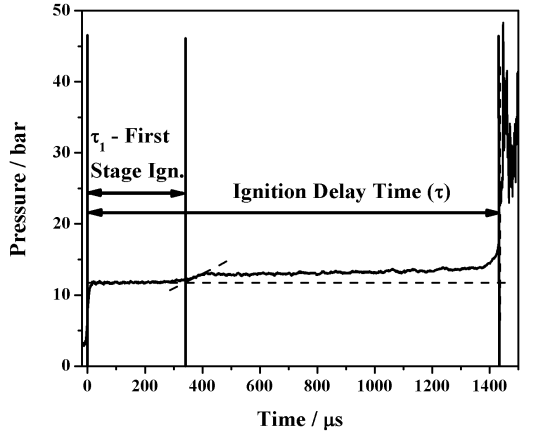

Figure 2.8: High pressure ST pressure trace exhibiting first stage ignition.

Validation

The NUIG high pressure ST was validated by comparing ignition delay times measured in this facility with previously published ignition delay times measured in different ST

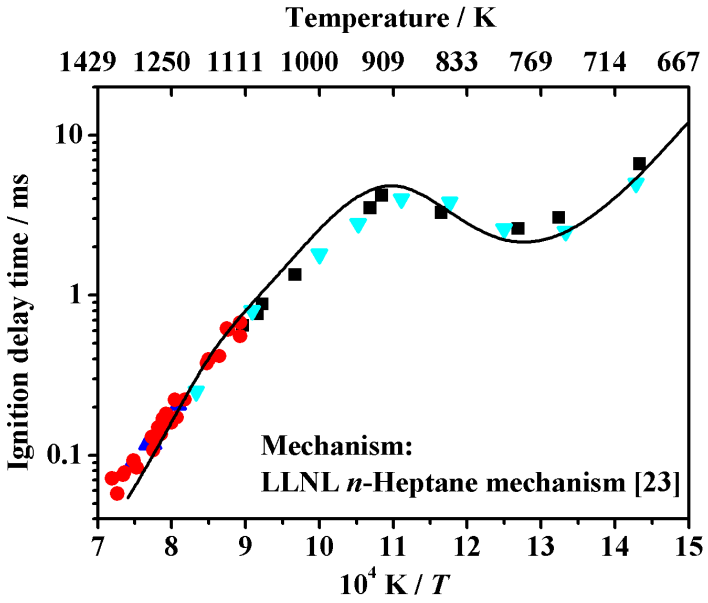

Figure 2.9: Ignition delay times for $\phi = 1.0$ n-Heptane in 'air' $p_5 = 13$ bar mixtures.■ – NUIG HPST, ● – Previous NUIG ST Facility, ▲ – Gauthier *et al.* [24], ▼ – Heufer and Olivier [25].

facilities for a mixture of $\phi = 1.0$ in 'air', n-heptane, $p_5 = 13$ bar. The results of the comparison are shown in Fig. 2.9, where good agreement is seen across a wide temperature range ($T_5 = 697 - 1359$ K).

Other Notes

This author contributed to the assembly and documentation of this facility by aiding in the assembly, validation and writing the 'Instructions for assembly of temperature controller boxes - HPST' section in the documentation.

2.1.4 NUIG Low Pressure Shock Tube

This facility, made entirely of stainless steel, has an overall length of 6.22 m (5.42 m driven section), with an inner diameter of 10.24 cm and a wall thickness of 5.8 mm. The driver section is somewhat unique, as it is barrel shaped, with a 52 cm outer diameter and is 53 cm in length. This is welded to a cylindrical translational piece 8.0 cm in length. This driver section is mounted upon a movable wheeled stand which can be moved in order to exchange diaphragms in between each experiment. This tube can be used for reflected shock experiments of pressures up to 3 atm. This facility has been described in detail in the Ph. D. thesis of Smith [17]. A schematic diagram of this facility is shown in Fig. 2.10. This diagram outlines the major features of this ST which a relevant to *this thesis*.

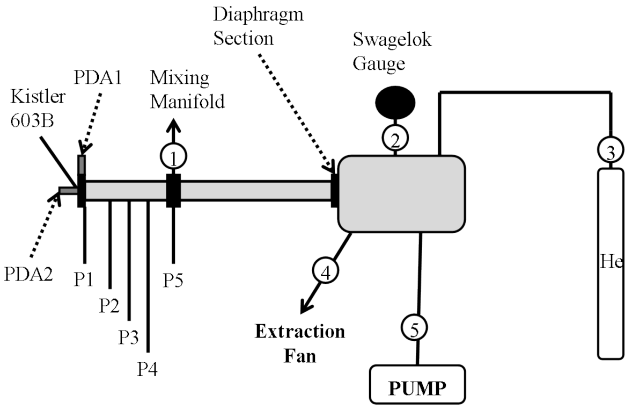

Figure 2.10: Schematic diagram of the LPST.

Driver section

The barrel-shaped driver section can be evacuated *via* an Edwards E2M5 two-stage rotary oil pump to a pressure of $\approx 10^{-2}$ Torr. Helium (99.99% purity; BOC) driver gas is added through a Swagelok thermoplastic hose through the top of the driver section. The pressure can be monitored within this section using a Swagelok pressure gauge and exhaust gases may be vented through a Whitey air admittance valve positioned atop this section adjacent to the pressure gauge.

This section is welded to an 8.0 cm translational piece with an attached flange where four 8.0 mm holes house four bolts which align directly with the driven section allowing polycarbonate diaphragms (thicknesses of either 125 or 200 μm) to be placed between the driver and driven sections. A seal is made between the diaphragm and the driver section by an embedded viton o-ring which is 4 mm thick and has an outer diameter of 117 mm.

Driven Section

This section is cylindrically shaped and as mentioned above is 5.42 m in length. From a distance of up to 189 cm away from the endplate there are five PCB Piezotronics 113A21 pressure transducers embedded into the sidewall of the tube used for measuring the shock velocity in the same fashion as described in Section 2.1.3 'Data Collection'. This facility utilises 4 electronic timers (One Philips and three Fluke PM 6666) to measure the time intervals between the five PCB pressure transducers. These transducers are situated at distances of 2.99, 23.69, 36.59, 49.49 and 188.72 cm from the endplate. The 20 mm thick endplate is also equipped with a Kistler 603B (due to the fact that this sensor is only

used to measure the time coating to prevent thermal heat shock was unnecessary), and a 4 mm diameter hole houses a fused silica window to allow optical access. This endplate has six 10.3 mm holes to allow bolts to be used to secure the endplate to the tube during experiments.

A 60 mm long cylindrical optics section is located between the endplate and the tube which houses four fused silica optical windows spaced at equidistant 90 degree increments around this section. These windows are a distance of 30 mm from the endplate, and are 9 mm thick with a width of 19 mm and allow sidewall optics to be used to measure ignition delay times.

Mixing Manifold

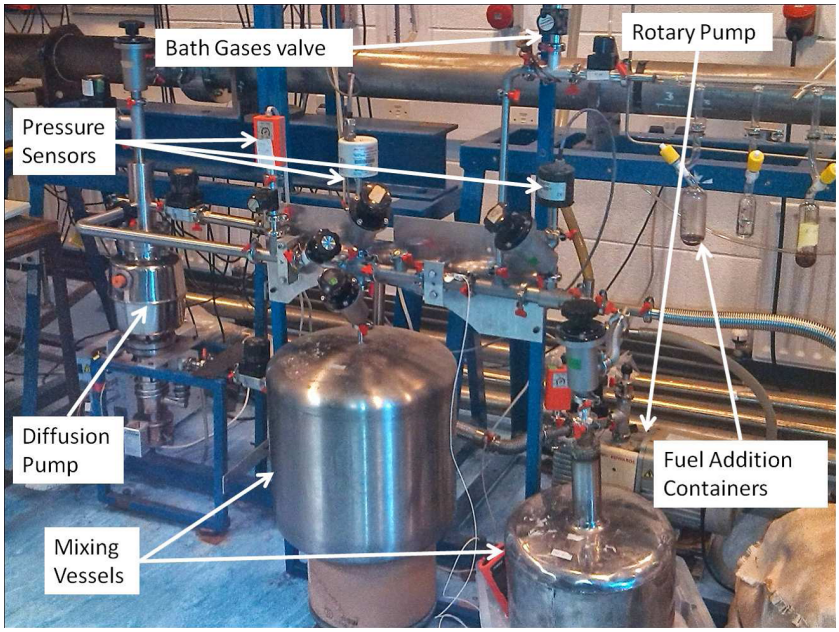

Figure 2.11: The mixing manifold of the NUIG low pressure shock tube.

The mixing manifold (outlined in Fig. 2.11) is equipped with two pressure sensors, one an MKS model 121AA (valid for measuring pressures from $0 - 100$ Torr) and the other a BOC Edwards Barocel sensor (valid for measuring pressures from $0 - 1000$ Torr). An Edwards Active Pirani vacuum gauge is attached to monitor pressures below 1 Torr more accurately. Two stainless steel mixing tanks are attached and sealed using MKS single-stage valves. Two separate Speedivalves are used to control the flow of oxygen ($\geq$ 99.5% purity; BOC), argon ($\geq$ 99.998% purity; BOC) and the fuels. Liquid fuels are introduced into the tanks through the mixing manifold *via* a glass manifold with three separate connections clamped to three sealed glass containers. The fuel is first degassed using the freeze-pump-thaw method. This uses liquid N_2 to freeze the fuel in the glass bulb any unfrozen gas is then evacuated and the fuel is then left to thaw. This procedure is repeated 3 times before preparation of the test mixtures. The amount of fuel is measured using the aforementioned pressure gauges and the fuel vapour is introduced from the glass manifold into the mixing manifold *via* a Swagelok Speedivalve. The mixing manifold can be isolated from the tube and the pumping section via a Nor-Cal angle-in-line valve. The pump section is connected to an Edwards E2M5 two-stage rotary oil pump. This pump is capable of achieving pressures of $\approx 10^{-2}$ Torr within the closed test system. The initial

pressures for the low-pressure ($1 - 3$ atm) experiments are ≤ 200 Torr. For this reason high vacuum is required ($\leq 10^{-2}$ Torr). To obtain these pressures an Edwards EO2K water-cooled oil diffusion pump is used. This pump is capable of reaching pressures of $\approx 10^{-4}$ Torr, however the "rough" vacuum of $\approx 10^{-2}$ Torr must be obtained before the diffusion pump is utilised.

Diaphragm Bursting Mechanism

Unlike the double diaphragm bursting mechanism used in the NUIG HPST (described in Section 2.1.3) the low-pressure shock tube uses a single diaphragm which is burst using a cross-shaped cutter, Fig. 2.12. This cutter consists of two laser-cut Olfa TCB-1 blades which are assembled in a cross-shape. This is then held in a threaded bar using Loctite 638 glue. The threaded bar is held in the middle of the tube by a circular bracket which itself is held in the driven section using 4 grub screws. The threading on the bar allows the distance of the cutter from the diaphragm to be varied.

During experiments, the driver section is filled with Helium. The increasing pressure exerts force on the polycarbonate diaphragm causing it to stretch into the driven section. When the diaphragm comes into contact with the cutter it ruptures causing the formation of the incident shock front.

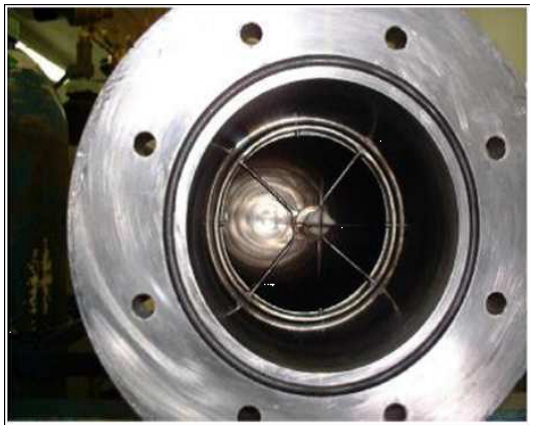

Figure 2.12: The cutter bursting mechanism of the NUIG low pressure shock tube.

Validation of the Low-pressure ST

Thes ignition delay times measured using this facility were defined in one of two ways. For the methanol measurements the ignition delay time was taken as $\mathrm{d}P/\mathrm{dt} = \mathrm{MAX}$, as shown in Fig. 2.13. This definition refers to the time between the arrival of the reflected shock wave at the observation point to the time where there is an almost instantaneous increase in pressure due to ignition.

The second way ignition delay time was defined when measured in this facility was using the emission of light due to the presence of CH*, at a wavelength of 431nm. This wavelength was isolated using a narrow bandpass filter from Knight Optics. This method was used when measuring the ignition delay times for 2-MF and n-heptane, an example of this is shown in Fig. 2.14. Time zero is defined as the arrival of the reflected shock wave visualised using the pressure trace and the ignition delay time is then the difference between this time zero and the tangent to the maximum rate of CH* increase which is extrapolated to the zero signal as shown in Fig. 2.14.

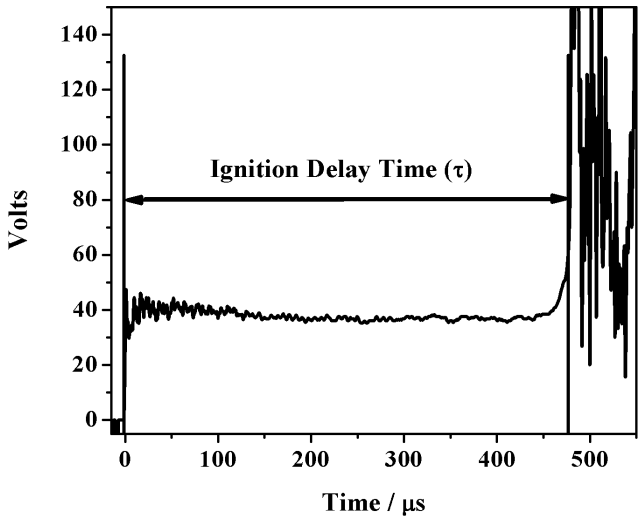

Figure 2.13: Example of the ignition delay time definition used to measure the methanol data using the NUIG low pressure ST.

Smith [17] originally validated and fully characterised this facility. The facility was validated using the available published ignition delay times of Davidson *et al.* [26]. Figure 2.15 presents the comparison of the published data versus the original validation performed by Smith [17] and the results measured during the course of *this study*. As outlined above the second method was used to define the ignition delay times for this validation. The validation serves to provide confidence in the results measured using this facility in *this study*.

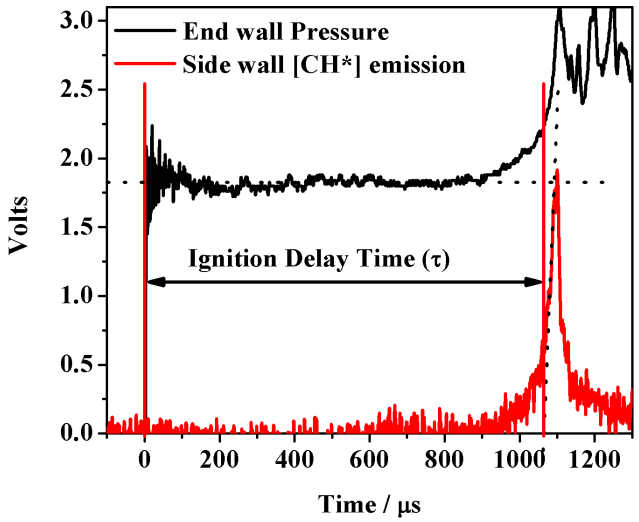

Figure 2.14: Example of the ignition delay time definition used to measure the 2-MF and *n*-heptane data in the NUIG low pressure ST.

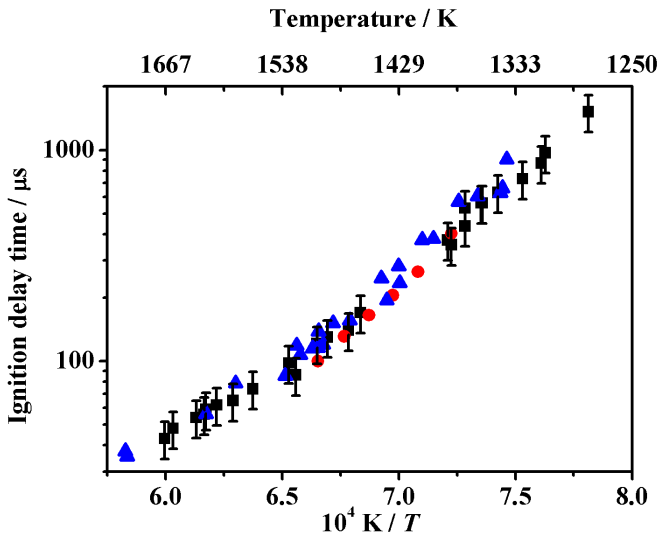

Figure 2.15: Ignition delay times for $\phi = 1.0$, 0.4% *n*-heptane, 0.4% O_2, 95.2% Argon, p_5 = 2 atm.■ – Smith [17], ● – Davidson *et al.* [26], ▲ – *This Study.*

Error bars of 20% uncertainty in ignition delay time are included. This uncertainty is determined from the cumulative uncertainty of the experiment in this facility. This value includes uncertainties in the mixture preparation (measuring the partial pressures), measuring the initial pressure and temperature and in the calculation of the shock velocity. When all these are taken into account the uncertainty value ranges from $15 - 20\%$ depending on the mixture composition and reflected shock conditions of interest, the final value reported is the worst case scenario of 20%.

2.2 Rapid Compression Machine

2.2.1 Background

The RCM is a device which mechanically compresses a gaseous sample by pneumatically moving pistons over a short time (millisecond timescales) in order to mirror a single compression within a compression ignition engine. The advantage of using an RCM is that it can be kept chemically clean (no-lubricants) and the gas temperature and pressure in the reaction core are homogeneous when a suitably-designed creviced piston head/s are used and can be measured and/or calculated. This allows data to be collected and used to validate chemical kinetic models.

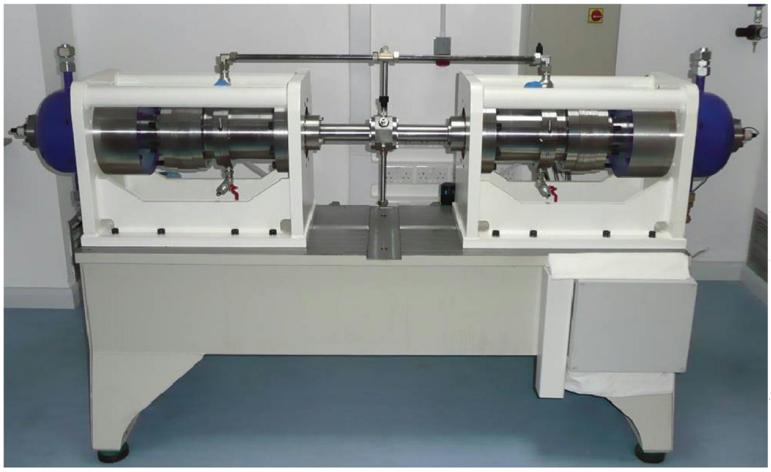

Figure 2.16: NUIG RCM.

STs (described in Section 2.1), in general, have a limited measuring time of typically up to 10 ms due to the cooling rarefaction wave. This is advantageous as the short residence time means heat loss to the walls is negligible, and the ST can be considered an almost adiabatic reactor with no exchange of mass, energy or heat to the external environment during the measuring time. RCMs differ, as there is no rarefaction wave, so after the compression, cooling of the gaseous mixture is caused by contact with the cooler walls and pistons in the combustion chamber. This trait allows the RCM to be used to measure much longer ignition delay times compared to STs ($\approx$ 200 ms for the NUIG RCM).

The typical geometry of an RCM consists of a combustion chamber usually cylindrical in shape, which contains the test gas. The test gas is compressed using a piston or pistons depending on the machine's configuration. The driving mechanism for RCMs can vary, but in general a high pressure air section drives a piston shaft whose velocity can be controlled as it moves through hydraulic oil.

2.2.2 NUIG RCM

Figure 2.16 shows the NUIG RCM used in *this study*. This RCM has a twin opposed-piston configuration. This allows the machine to reach higher compression ratios more easily when compared to a single piston setup.

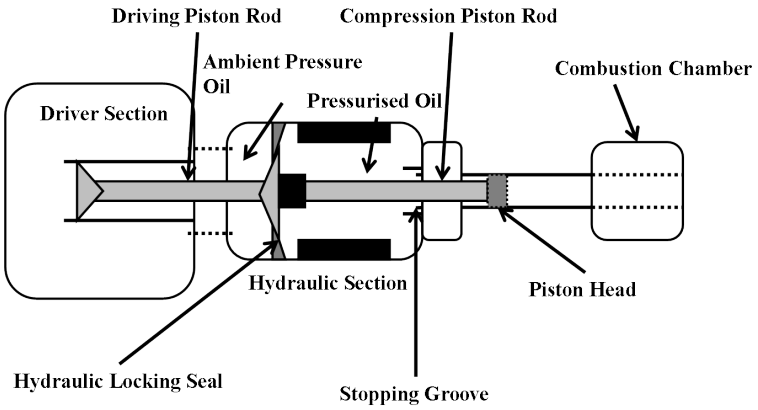

Figure 2.17: Schematic diagram of one side of the NUIG RCM.

A schematic representation of the NUIG RCM is shown in Fig. 2.17. The driver section houses the high pressure drive gas used to drive the piston and compress the test gas. Once the piston is fully retracted (Fig. 2.17) the hydraulic locking seal is made. At this point the pressure of all of the oil is ambient. In order to hold the piston in this position while the drive pressure is added, the oil nearest the combustion chamber is pressurised, as shown in Fig. 2.17. The test gas and drive pressure can now be loaded into the combustion chamber and driver section, respectively. To fire the pistons and compress the test gas the pressure in the hydraulic oil is released using a solenoid valve allowing the driver gas to push the piston forward.

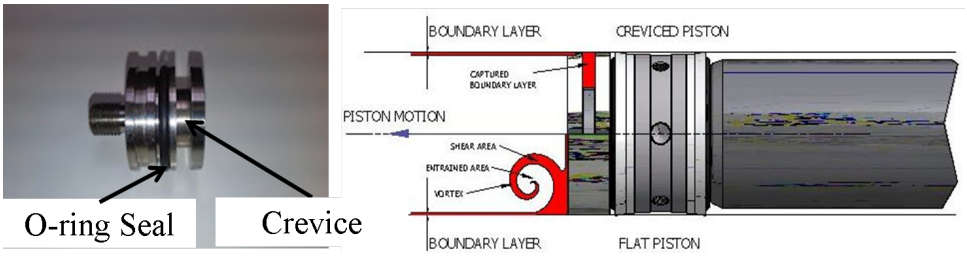

Figure 2.18: Creviced piston heads versus non-creviced piston heads.

The NUIG RCM is automated, using a vacuum pump to retract the pistons, a gear pump to apply the hydraulic locking pressure and an air compressor to add the driving pressure and a series of automated valves to control each process. This facility uses creviced piston heads in order to prevent temperature inhomogeneities due to the formation of roll-up vortices within the reaction chamber [27, 28]. Figure 2.18 illustrates the difference between the use of creviced piston heads and flat piston heads. Sung and Curran [29] showed that the use of flat piston heads results in the formation of roll-up vortices which cause temperature inhomogeneities. In order to model accurately and simply the facility effects within the combustion chamber we assume that the core of the combustion chamber is at a homogeneous temperature. This is achieved by employing creviced piston heads which suppress the roll-up vortices by capturing the cool boundary layer as the pistons compress the test gas. Figure 2.18 also shows the piston head used during *this study*. An o-ring seal (Viton, shore90, internal diameter 29.75 mm, cross-section 3.53 mm) is used to isolate the test gas from the outside atmosphere. The full details of this facility are described in detail by Darcy *et al.* [30].

A Kistler 6045A piezoelectronic pressure transducer is used to monitor the pressure in the combustion chamber during an experiment. This is also used to measure the compressed pressure from the first local maximum on the pressure trace. The movement of the pistons are tracked using two Positek LIPS100 linear position sensors. Two flow control needle valves are used to tailor the piston timings ensuring synchronicity between the movement of the two pistons. The combustion chamber is evacuated between experiments through the mixing manifold using an Edwards XDS10 scroll pump, using a liquid nitrogen trap to prevent back diffusion of oil and to trap any low vapour pressure liquid fuels. The static pressure of the initial test gas is measured by an MKS model 121AA pressure transducer located on the mixing manifold.

Figure 2.19 presents a typical pressure trace measured in the RCM. The method of measuring the ignition delay time from the pressure is outlined in this example. The ignition delay is measured from time zero which refers to the end of compression (the first local maximum on the pressure trace) to the almost instantaneous pressure increase due to ignition (i.e. t_0 = first $(dP/dt)_{max}$, and t_{ign} = second $(dP/dt)_{max}$). At the end of compression there is a sharp drop in pressure as boundary layer gases flow into the crevices. This is followed by a progressively decreasing rate of pressure drop mainly due to heat loss of the test gas to the relatively cold reactor walls. Ignition is then visualised through the highly exothermic release of energy seen through the sharp increase in the pressure signal. In order to successfully compare ignition delay times measured in the RCM to a kinetic model non-reactive pressure profiles are collected in tandem with the reactive traces. Non-reactive pressure profiles are measured by replacing the O_2 in the reactive mixture with N_2. The pressure profiles are converted into effective volume profiles which are included in the simulation. The simulated ignition delay times can then be measured from the simulated pressure profiles in the same fashion as they are measured from the experimental pressure profiles.

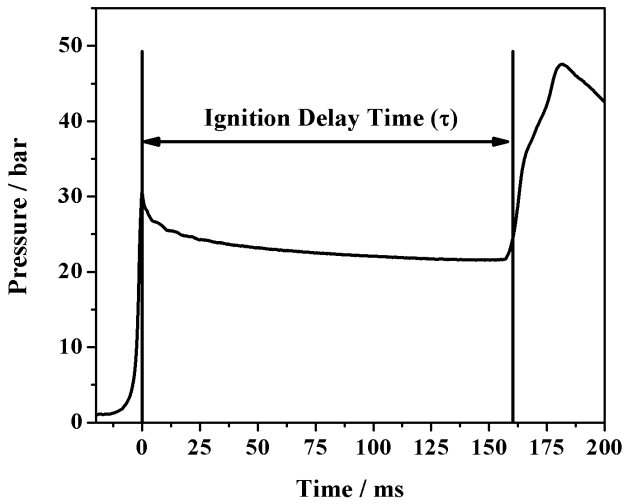

Figure 2.19: Typical pressure profile captured using the NUIG RCM. The method of measuring the ignition delay time is outlined.

This facility is equipped with a heating system allowing a variety of initial temperatures to be used, so that compressed gas temperatures can be varied. Cartridge heaters are located within the collars of the two RCM combustion chamber sleeves. These help to

heat the piston heads when the pistons are fully retracted. Three Flexelec 1250 W 1 m long heating tapes are used to heat the two sleeves and the combustion chamber.

The mixing manifold and mixing vessels are heated using 8 Flexelec 1250 W 1 m long heating tapes. Both heating systems use type T and type J thermocouples to monitor and control the temperature. On the manifold there are 16 thermocouples; 8 are used to control the heating tapes and 8 are used to check the temperature at different points along the manifold and mixing vessels ensuring a temperature homogeneity of ± 2 K. Another 10 thermocouples are used to control and check the temperature along the combustion chamber. Here, 5 are used to control the 3 heating tapes and 2 cartridge heaters, and the other 5 are used to check the temperature again ensuring a homogeneous temperature within ± 2 K.

CAL9900 temperature controllers are used throughout the heating systems to set and control, the temperature of the heating tapes and cartridge heaters. To see the temperatures two PICO TC-08 USB thermocouple data loggers are used to read the temperatures measured by the thermocouples.

2.3 Procedures

This section outlines the procedures that were followed when operating each of the facilities discussed in the previous sections ($2.1 - 2.2$). This section aims to provide first time users with step-by-step instructions, allowing one to operate the experimental facilities.

2.3.1 NUIG High Pressure ST

When using the high pressure ST the first step is to clean the facility, then prepare the mixture and perform the experiments. Each of these steps will be explained and step-by-step procedures provided.

Cleaning the Tube

The tube is cleaned using ethanol. Other solvents such as acetone can be used but before using other solvents the user should consider aspects such as the effect other solvents may have on the seals (acetone can damage viton o-rings) of the tube or indeed other apparatus used within the tube. A flexible, extendible pipe is used to push a clothed head throughout the length of the tube. It is important to clean both the driver and driven sections. Of particular importance is the last meter of the driven section (measuring section) and the endwall, as these are the sections where the most important measurements are made (ignition delay time and shock velocity).

1. Ensure both the driver and driven sections are at atmospheric pressure, opening the venting valve attached to the mid-section. Check the pressure using the gauges located in the mixing manifold and the driver manifold. The user must ensure that the tube is open to the respective manifolds before doing this.

2. Open diaphragm section removing any used diaphragms. Remove also the two side sections to allow increased access to the tube for the cleaning pipe.

3. Open the endwall by removing the securing flange first, followed by the plug-shaped endwall from the tube. If the endwall gets stuck there are two threaded holes available to the user for pusher screws to aid in its removal (THIS SHOULD ONLY BE USED AS A LAST RESORT).

4. Using the pusher pipes, with a clean dry cloth on the head, push out any remaining diaphragm debris from the previous experiments. Push the pipes from the diaphragm section down through the driven section until the head emerges from the endwall hole of the tube.

5. Dampen a new clean cloth with ethanol, and attach this to the head pipe and push this through the tube using an over and back motion to scrub along the tube. Repeat this step (changing cloths and re-applying ethanol as necessary) until the tube is clean (no visible soot on the cloth), and use the same instructions to clean the driver section.

6. Dampen a clean cloth with ethanol and use this to gently wipe the face of the endwall. At this point ensure there are no scratches or damage to the endwall. WARNING: do not scrub the Kistler sensor mounted in the endwall. Gently brush if necessary and ensure that there is a layer of silicone coating before replacing the endwall into the tube.

7. Before replacing the endwall, using a flashlight look through the driven section from the endwall to make sure there are no visible obstructions, and that the PCB sensors along the length of the tube are coated with a layer of silicone and are flush with the wall of the tube.

8. Finally, replace the endwall ensuring homogeneous tightening of the bolts in the securing flange.

9. Replace the side piece at the mid-section, push together the driver and driven sections, securing them by tightening the bolts. DO NOT leave the tube open for extended periods to the air so as to prevent unwanted contaminants entering the tube after cleaning.

Mixture Preparation

Once the tube has been cleaned the test mixture should be prepared. The mixture is prepared using the mixing manifold. The fuel is added, followed by oxygen and finally the diluent. It is important to purge the lines before and after each addition of gas. The gas flows should be kept steady when adding gases, and time should be given to allow gases to equilibrate before reading the pressure (this is dependent on the volume and the gas flow rate). All instructions below refer to Fig. 2.20.

1. Turn on the manifold heating system, setting it to the required temperature (Only necessary, usually, for low vapour pressure fuels). Allow at least 2 hours for the manifold to reach a homogeneous temperature.

2. Before beginning making the mixture the following checks should be done:

   If using liquid fuel, check the injection port at valve 6. This houses a SGE Analytical Science 10 mm CS Septa. If this is damaged in any way replace before vacuuming mixing vessel.

   The mixing vessel should be left to evacuate for at least 4 hours (All valves closed except 7 and 8).

   With the vacuum pump on, liquid N_2 trap clean and full of liquid N_2.

   Close valve 8, slowly open valve 6 and 11, allowing time for the system to equilibrate, and check the vacuum in the tank is acceptable (at least $\approx 10^{-2}$ Torr).

3. Close valves 7 and 11. Open valves 2 and 4 for injection of fuel. Add fuel until the desired pressure is reached. Allow time for equilibration of the gas pressure.

   For liquid fuels inject *via* the port at valve 6.

   For gaseous fuels connect cylinder to valve 11 by first temporarily disconnecting the vacuum gauge as this is not required when adding the fuel pressure.

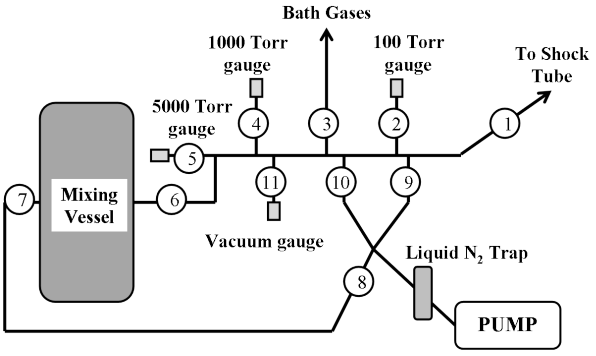

Figure 2.20: Schematic diagram of the HPST mixing manifold.

4. Close valve 6. Open valve 9 and 10 to vacuum out remaining fuel pressure in the manifold.

5. Open the oxygen cylinder. Purge the gas lines three times by opening and closing valve 3. Allow time after purging for the manifold to reach an acceptable vacuum.

6. Close valve 9 and 10. Using the appropriate gauges to monitor the pressure (valves 2, 4 and 5 depending on the fuel and oxygen total pressure) add the oxygen to the mix. In order to do this, slowly open valve 3 until the pressure in the manifold is above that of the pressure in the tank. Once this is achieved, open valve 6 and, using a steady flow rate, add oxygen until the desired pressure is reached.

7. When the pressure has been reached close valve 3 and 6 almost simultaneously. Waiting 5 – 10 minutes allow the pressure within the mixing vessel to equilibrate. Now slowly open valve 3 until the approximate pressure within the mixing vessel has been reached. Then open valve 6, adding oxygen until the total pressure of oxygen + fuel has been reached. Finally, once again close valves 3 and 6 almost simultaneously.

8. Open valves 9 and 10 to evacuate the excess oxygen pressure in the manifold.

9. Close the oxygen cylinder. Now open the diluent (nitrogen or argon etc.) cylinder.

10. Purge the manifold at least five times with diluent gas, by opening and closing valve 3 as before.

11. Following the same procedure outlined in steps 6 and 7 add the diluent up to the mixture total pressure.

12. Finally close the nitrogen cylinder and vacuum the manifold through valves 9 and 10.

13. Turn on the magnetic stirring fan at the bottom of the mixing vessel to facilitate mixing of the test mixture. The mixture should be left to mix for at least 20 minutes before beginning experiments.

Performing Experiments

After preparing the mixture and cleaning the tube, experiments can commence. Great care should be taken when performing experiments due to the high pressures being used. In particular, premature bursting of the diaphragms can occur and in these cases it is important to have the valve to the mixing manifold closed. Also, when adding the driver gas, this must be done using a steady flow rate, and as before time should be allowed for the equilibration of the gas pressure, otherwise unwanted reflected shock pressures and temperatures will be achieved. All instructions below refer to Fig. 2.21.

1. Insert the scored diaphragms into the mid-section and secure the bolts, ensuring that the scoring on the diaphragms face toward the driver section.

2. Open valves 2 and 3. Vacuum the driver section through valve 6.

3. Open valve 1 and valves 9 and 10 from Fig. 2.20 to vacuum the driven section.

4. Allow both sections to reach vacuum pressures of $\approx 10^{-2}$ and $\approx 10^{-4}$ Torr for the driver and driven sections, respectively.

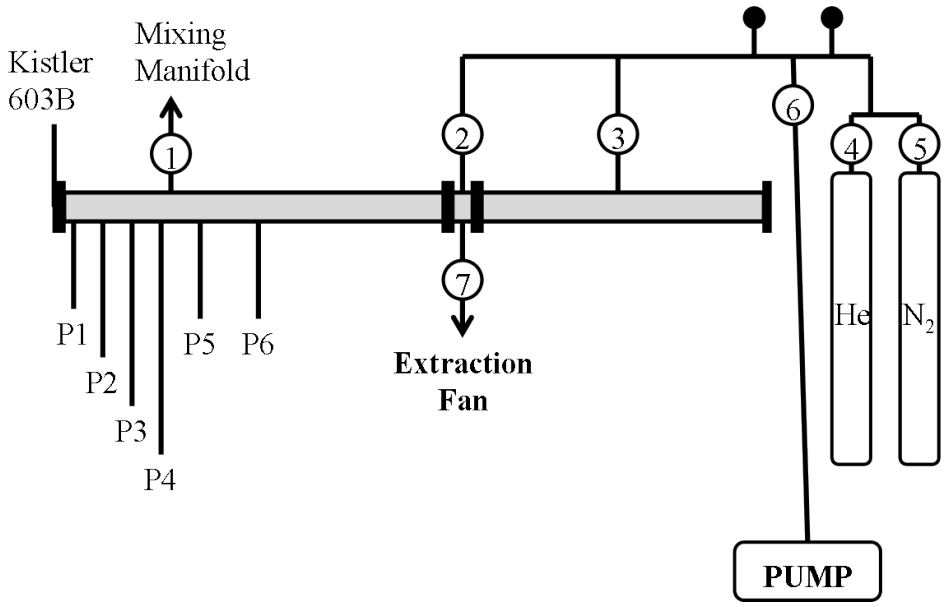

Figure 2.21: Schematic diagram of the HPST.

5. Close valves 9 and 10 from Fig. 2.20 and add the initial text mixture pressure by slowly opening valve 6, Fig. 2.20. Allow the pressure to equilibrate and once the desired pressure has been added **close valve 1, Fig. 2.21**.

6. Close valve 6 and add the driver pressure. When using the double diaphragm configuration add half the total driver pressure, then close valve 2. Fill the total driver pressure through valve 3. Once the total pressure has been reached close valve 3.

7. Ensure diagnostics (oscilloscope and pressure sensors) are ready to capture data on the computer and re-check that valve 1 is closed. Press the initiation button. This triggers a solenoid operated valve that expands the volume of the mid-section, using a dump tank, and the pressure differential between the driver and mid-section should burst the diaphragms and form the shock fronts.

8. Once the shock has been triggered save the output traces on the computer, and open valve 7 and allow the tube to reach atmospheric pressure.

9. Once atmospheric pressure is reached, close valve 7 and open valves 2, 3 and 6 and evacuate the exhaust gases.

10. Close valve 6 and add N_2 *via* valve 5 to just above atmospheric pressure. Open valve 7 again and allow the tube to reach atmospheric pressure.

11. Open the bolts at the mid-section and change the diaphragms. Repeat all steps for next experiment.

Post Experiment Procedures

Once all experiments have been completed the tube must be shut down. The tube should be left sealed overnight.

1. Ensure that the tube has been vented to atmospheric pressure through valve 7 (Fig. 2.21). The mid-section should be closed and sealed, and valves 1 and 7 (Fig. 2.21) should be closed.

2. The mixing vessel should be evacuated by opening valves 7 and 8 (Fig. 2.20). Valves 9 and 10 (Fig. 2.20) should be closed when doing this. Before evacuating the mixing vessel, the pressure within the mixing vessel should be measured by opening valves 5 and 6 (Fig. 2.20).

3. If the tube is being shut down for a weekend or an extended period of time the heating system on both the tube and mixing manifold should turned off.

4. The pumps for the mixing manifold and driver section should be turned off.

5. The pressure in the system should be atmospheric and all valves should be closed.

2.3.2 NUIG Low Pressure ST

Similar steps are taken as those described in Section 2.3.1 to operate the NUIG low pressure ST. The first step is cleaning the facility, followed by mixture preparation and finally operation.

Cleaning the Tube

1. Check that the tube is at atmospheric pressure using the pressure gauges available.

2. Open the diaphragm section removing any remaining used diaphragms.

3. Open the endplate, removing any pieces of diaphragm within reach.

4. Using the extendible piping, use a clean dry cloth to give the tube an initial wipe to remove any large debris such as diaphragm pieces.

5. Using a new cloth dampened with ethanol, use the extendible pipes to push the dampened cloth through the length of the tube. Repeat this until the tube is clean, i.e. that there is no visible soot on the cloth used for cleaning.

6. Replace the endplate and place a new diaphragm in the diaphragm section in preparation for the experiments.

Mixture Preparation

1. The pump, water cooler and oil heater should be turned on. The diffusion pump (Diff. pump in Fig. 2.22) should be filled with liquid N_2. Initially all valves should be closed except valve 5.

2. The heater should be left like this for at least 30 minutes to heat up.

3. The tanks (MV1 and MV2) should be vacuumed before making a mixture. Rough vacuum achieved using the rotary pump by opening valves 7, 10 and 2 (Fig. 2.22) with all other valves closed. This is followed by at least 4 hours of vacuuming using the diffusion pump. Valve 2 closed, valves 3 and 5 opened. The pressure should be $\approx 10^{-4}$ Torr before preparing a mixture.

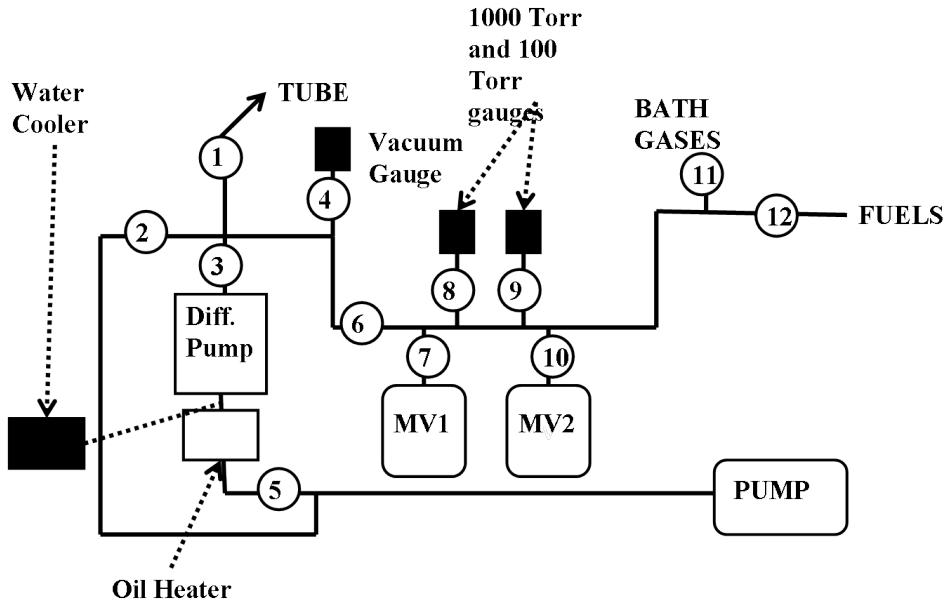

Figure 2.22: Schematic diagram of the LPST manifold.

4. Once the tanks have been evacuated the mixture can be prepared. Start with all valves closed.

5. Open valves 7, 8, 9 and 10 and add the required fuel pressure through valve 12, closing when the pressure is reached, and allowing time for the pressure to equilibrate.

6. Close valve 7 and 10 when the fuel pressure has been reached. Now open valves 2, 4 and 6 to vacuum the manifold.

7. Open O_2 cylinder. Purge the manifold at least three times by opening and closing valve 11.

8. Close valve 6. Slowly allow O_2 through valve 11 until pressure in the manifold is above the fuel pressure within MV1, then open valve 7. Continue adding oxygen at a slow steady flow rate until the desired oxygen and fuel pressure is reached, then slowly close valve 11 and valve 7.
9. Allow the gas in the tank to equilibrate for at least 10 minutes. Then repeat step 8 to top up the oxygen partial pressure.
10. Repeat steps 8 and 9 to fill MV2, replacing valve 7 with valve 10.
11. Opening valve 6, evacuate the manifold again.
12. Close oxygen cylinder and open the diluent cylinder.
13. Purge the manifold at least 5 times with diluent gas by opening and closing valve 11.
14. Using the same method as outlined in steps 8 and 9, fill the diluent gas into MV1 and MV2 until the desired total pressure is reached.
15. Once the mixtures have been prepared leave the mixtures for at least 4 hours to allowing diffusive mixing.

Performing Experiments

1. A new diaphragm should be inserted between the driver and driven sections and the cutter should be positioned at an appropriate position from the diaphragm based on the desired reflected shock conditions ($\approx$ 11 mm, 125 μm diaphragm for $p_5 \approx$ 1 atm).
2. Open valve 5 to vacuum the driver section.
3. Evacuate the tube through valve 1 (Fig. 2.23) in the same fashion that you evacuate the mixing tanks, roughly evacuating the tube using just the rotary pump to a pressure of $\approx 10^{-2}$ Torr, then use the diffusion pump to evacuate the tube to a pressure of $\approx 10^{-4}$ Torr.
4. Once the tube has been evacuated to $\approx 10^{-4}$ Torr, the initial pressure should be added from either MV1 or MV2 (Fig. 2.22) through valve 1 (Fig. 2.23). Once p_1 is reached and time allowed for equilibration, **valve 1 should be closed**.
5. Ensure that all the diagnostics have been set and are ready to begin recording data.
6. Close valve 5, and open valves 2 and 3 and begin filling the driver pressure.
7. Once the diaphragm bursts close valve 3, and open valve 4 to allow the tube to return to atmospheric pressure.
8. All collected data is saved and recorded.
9. Valve 4 is closed and valve 5 is opened to roughly evacuate any exhaust gases.
10. Valve 5 is closed and valve 4 is once again opened to allow the tube return to atmospheric pressure.
11. Once the tube is at atmospheric pressure (read off the Swagelok pressure gauge on top of the driver section) the diaphragm section can be opened and the diaphragm changed. This procedure returns to step 1 once again.

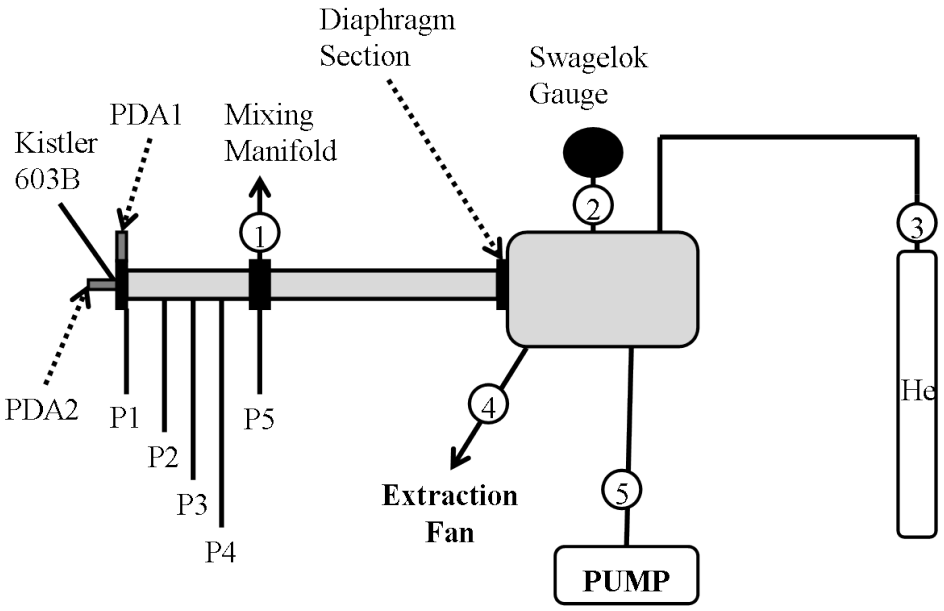

Figure 2.23: Schematic diagram of the LPST.

Post Experiment Procedures

After the experiments are finished the tube must be closed down.

1. Turn off the oil heater for the diffusion pump (Fig. 2.22). Close all valves shown on Fig. 2.22 except valve 5. After the diffusion pump oil heater has been turned off it requires approximately 3 hours pumping until is is safe to turn off the water cooler and the rotary pump. This is to prevent oil particles diffusing into the diffusion pump.

2. Using valve 4 (Fig. 2.23) allow the tube to vent to atmospheric pressure.

3. Close all valves shown in Fig. 2.23 ensuring that the helium cylinder is closed also.

4. Turn off the rotary pump for the driver section.

5. Turn off all diagnostic equipment.

2.3.3 NUIG RCM

Similar to the ST facilities, the first step is cleaning of the combustion chamber, followed by mixture preparation and operation.

Cleaning of the Combustion Chamber

Five parts of the RCM are cleaned before experiments on a new mixture. These are shown in Fig. 2.24. Ethanol is used as the solvent for cleaning and it is imperative that gloves are worn in order to ensure maximum cleanliness of the parts. Both sleeves and combustion chamber shown, Fig. 2.24, have a cylindrical hole through the middle where the piston heads move during experiments, and it is these walls that should be cleaned thoroughly.

It is important to note here that great care should be taken when taking the parts apart for cleaning and re-assembly before experiments as even small scratches and divets can cause problems with experiments, in particular leaks in the combustion chamber.

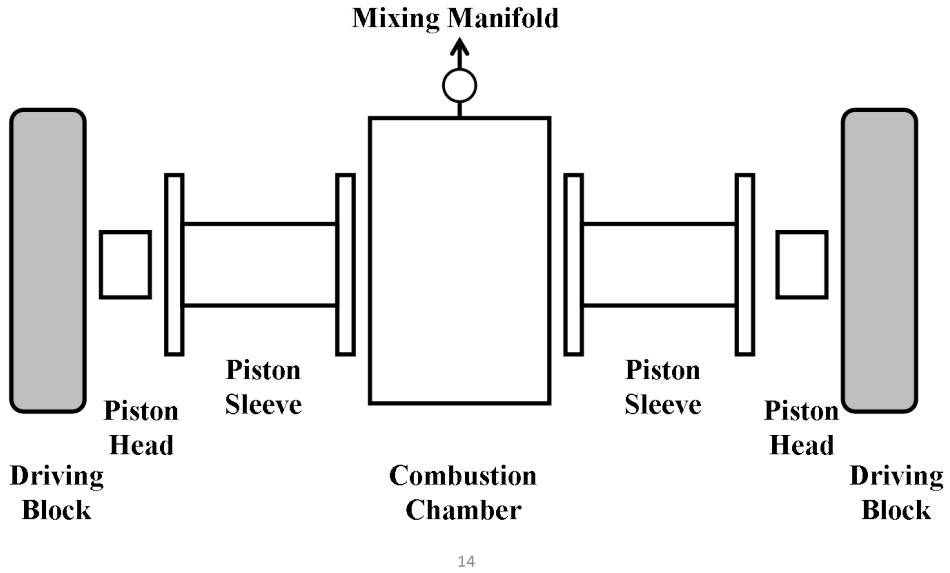

Figure 2.24: NUIG RCM combustion chamber parts to be cleaned.

Mixture Preparation

Initially, the user should consider that all valves shown in Fig. 2.25 are closed. MV1 will be used for reactive mixture, while MV2 will be used for non-reactive mixture, Fig. 2.25.

1. Turn on manifold heating system and set temperatures to desired value. Allow approximately an hour for the manifold to heat to the desired temperature.
2. Clean the liquid N_2 trap. Fill with liquid N_2 and turn on pump. Allow 5 minutes for pump to warm up.
3. Slowly open valve 6, 9, 10 and 11 in order and check the pressure in MV1 and MV2.
4. Gradually open valve 8 allowing the pump to evacuate any pressure remaining from previous experiments from MV1 and MV2. Once the bulk of the pressure is vacuumed ($p < 5$ mbar). Close valve 8 and open the N_2 cylinder, valve 2. Open valve 5 and purge mixing vessels with N_2, adding approximately 2 bar. Close valves 5 and 2 and once again vacuum the system slowly through valve 8.
5. Leave the mixing vessels to evacuate for at least 3 hours.
6. Once vacuumed, check pressure by closing valve 8 and waiting 5 minutes for pressure equilibration. The vacuum pressure can be read from the vacuum gauge and the pressure should be constant.
7. Close valves 10 and 11.
8. Open valve 8 and evacuate the manifold once more. Attach fuel vessel as shown in Fig. 2.25. For liquid fuels use the injection port as described previously.

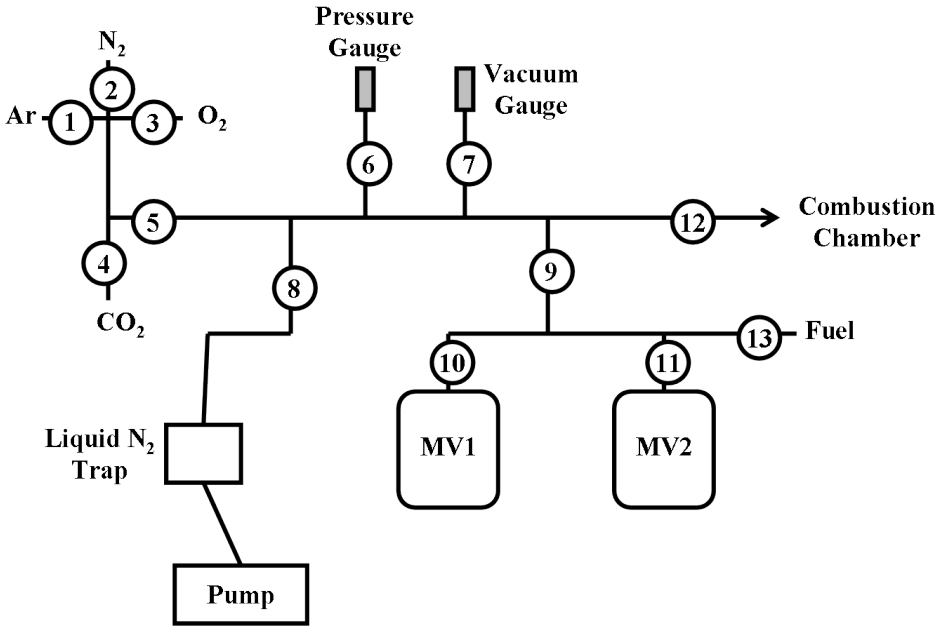

Figure 2.25: Schematic of the NUIG RCM mixing manifold.

9. Close valves 8 and 7. Open valves 10 and 11 and add the fuel partial pressure through valve 13, reading the pressure from the pressure gauge display. Always add slightly over the partial pressure required, then allow the pressure to equilibrate, and slowly use valve 8 to reach the desired partial fuel pressure in the mixing vessels.

10. Close valve 10 and 11. Open valve 8 to vacuum the manifold once more. Disconnect the fuel vessel and store safely.

11. Open valve 5 to vacuum any residual diluent gas. Close valve 5. Open O_2 cylinder (valve 3). Purge the manifold with O_2 by opening and closing valve 5 at least 3 times.

12. Close valve 8. Slowly open valve 5 until the pressure of O_2 in the manifold is at least twice the partial pressure of fuel in MV1, then open valve 10 adding O_2 to the mixture slowly and at a steady flow rate until the desired fuel and O_2 pressure is reached, then close valve 10 and 5.

13. Allow the pressure in MV1 to equilibrate for at least 10 minutes, now repeat step 12 until desired fuel and O_2 pressure is reached.

14. Close the O_2 cylinder, valve 3. Open valve 8 to vacuum the manifold and slowly open valve 5 to vacuum any residual O_2 pressure.

15. Repeating steps $11 - 13$, add N_2 in place of O_2 in MV2. Valve 3 should be replaced with valve 2 and valve 10 with valve 11.

16. Diluent gas may now be added to MV1 and MV2 in sequence using the same procedure outlined for adding the O_2 partial pressure in steps $11 - 13$, replacing valve 3 with either valves 1, 2 or 4 depending on the diluent composition.

17. Allow at least 3 hours for the mixtures to become homogeneous.

NOTE! for diluent gases with a mixture of components, step 16 should be repeated for each individual component i.e. DO NOT attempt to add the gases at the same time.

Performing Experiments

The NUIG RCM is automated and controlled mainly *via* a control box, Fig. 2.26, during experiments. Each step is linked to the last, therefore the automated control will not allow the user to move onto the next step until the previous one is completed for safety reasons.

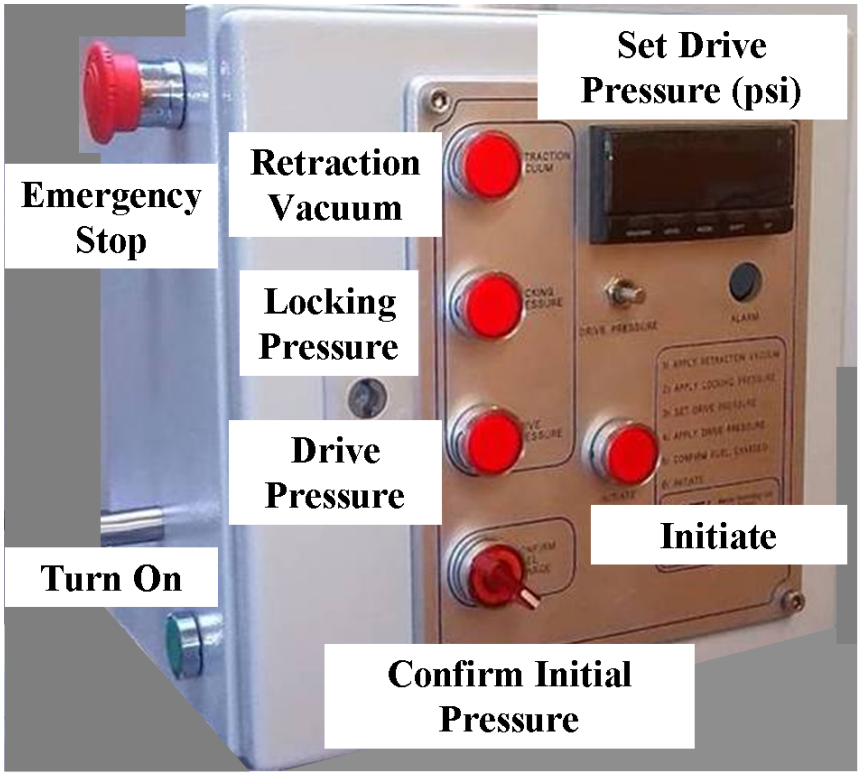

Figure 2.26: NUIG RCM control box for automated use of the RCM.

1. Turn on heating system for the combustion chamber and allow at least 40 minutes for the initial temperature to be reached and the temperature across the system to equilibrate.

2. Turn on and set all diagnostic equipment needed, including automation system, Fig. 2.26.

3. Press "Retraction Vacuum" button.

4. Vacuum the chamber through the chamber tap and valves 8 and 12, Fig. 2.25. The pressure can be monitored by the pressure gauge and vacuum gauge, Fig. 2.25.

5. Allow the chamber to evacuated for approximately $10 - 15$ mins. Close valve 8 and ensure a steady pressure in the chamber (no leaks).

6. Add the test gas initial pressure and close the chamber tap. It is important to do this at this point in order to allow as much time as might be necessary for settling of residual turbulence from the filling process in the test gas within the chamber.

7. Once the required mixing time is reached press “Locking Pressure” button, Fig. 2.26.

8. Once the button “Drive Pressure” is illuminated press it to add the driving pressure for the pistons. This pressure is set using the knob shown in Fig. 2.26. *This study* used a drive pressure of 160 psi unless otherwise stated.

9. Once the drive pressure is added the “Confirm Initial Pressure” switch will light-up. Switch this to confirm fuel charge in the chamber and that the tap is closed. Now press “Initiate” button to perform experiment.

10. After the experiment is performed the pressure in the driver section is automatically vented. Save and record all diagnostic information needed for post processing the data.

11. Experiments are then performed in the same way as described from step 3 on for the remainder of the time.

Post Experiment Procedures

Once all experiments are finished the heating systems should be turned off. All valves should be closed and the pumps shut down. The automation system can be turned off *via* the “Emergency Stop” button. Shut down the diagnostic equipment.

Chapter 3

Methane and Dimethyl ether

3.1 Abstract

The development of accurate chemical kinetic models capable of predicting the combustion of methane and DME in common combustion environments such as compression ignition engines and gas turbines is important as it provides valuable data and understanding of these fuels under conditions that are difficult and expensive to study in the real combustors. In *this work*, both experimental and chemical kinetic model-predicted ignition delay time data are provided covering a range of conditions relevant to gas turbine environments ($T = 600-1600$ K, $p = 7-41$ atm, $\phi = 0.3$, 0.5, 1.0, and 2.0 in 'air' mixtures). The detailed chemical kinetic model (Mech_56.54) is capable of accurately predicting this wide range of data, and it is the first mechanism to incorporate high-level rate constant measurements and calculations where available for the reactions of DME. This mechanism is also the first to apply a pressure-dependent treatment to the low-temperature reactions of DME. It has been validated using available literature data including flow reactor, jet-stirred reactor, shock-tube ignition delay times, shock-tube speciation, flame speed, and flame speciation data. New ignition delay time measurements are presented for methane, dimethyl ether, and their mixtures; these data were obtained using three different shock tubes and a rapid compression machine. In addition to the DME/CH_4 blends, high-pressure data for pure DME and pure methane were also obtained. Where possible, the new data were compared with existing data from the literature, with good agreement.

3.2 Introduction

The depletion of crude oil resources has motivated the search for alternative energy sources. Currently, the combustion of hydrocarbons remains the biggest producer of energy throughout the world, and in the short- to medium-term will remain so. However, the combustion of fossil fuels has contributed to global warming and increased levels of pollution. Biofuels can be produced from renewable sources and can reduce undesirable emissions associated with conventional fossil fuels. Methane (CH_4), which is the predominant component of natural gas, is a relatively clean-burning fossil fuel and can be considered a renewable energy source when produced as biomethane via anaerobic digestion of biomass [31]. Dimethyl ether (DME) is also considered a second generation biofuel as it can be produced from biomass. It is more commonly produced in a two-step process, where syngas is converted to methanol which can then be used to generate DME through a dehydration reaction [32]. Semelsburger *et al.* [33] found that DME ranks highly as an

alternative fuel for the future.

It is for these reasons that a large number of studies have been performed on the combustion of these fuels. Due to its high cetane number (> 55), DME is considered a good alternative to diesel. DME has been studied experimentally in diesel engines [34–37] showing its advantages in terms of emissions and engine efficiency. Particulate matter (PM) emissions were found to be greatly reduced, as were NO_x and SO_x, while there was a slight increase in carbon monoxide (CO) and hydrocarbon (HC) emissions.

Methane is the main component of natural gas and is commonly burned in gas turbines. Due to DME's excellent autoignition characteristics, it has been used as an additive or alternative to natural gas in gas turbines [38, 39], leading to interest in the combustion kinetics of mixtures of these two fuels. Mixtures of methane and DME have also been studied within homogeneous charge compression ignition (HCCI) engines [40, 41], where DME was found to be an excellent ignition improver. Several flame speed studies have been conducted on DME [42–47] using a variety of different methods such as constant-volume bomb using optical observation of the flame and counterflow flames; in some devices, particle image velocimetry has been utilised to determine the laminar flame speed from the observed gas velocities.

Species profiles were first measured by Dagaut *et al.* [48] in a jet-stirred reactor (JSR) using fuel mixtures highly diluted in argon, for equivalence ratios from 0.2 to 1.0, at a pressure of 10 atm, and in the temperature range $550-1100$ K. Subsequently, flow-reactor data were taken by Fischer *et al.* [49] (1118 K, 3.5 atm, and 1085 K, 1 atm, $\phi = 0.32-3.40$) and Curran *et al.* [50] ($550-850$ K, $12-18$ atm, $\phi = 0.7-4.2$). These studies [49, 50] also developed a detailed chemical kinetic mechanism to simulate their experimental data, using it to identify the important reaction pathways controlling DME fuel oxidation. This mechanism was also used to simulate JSR data [48] and shock-tube ignition delay times.

Zhao *et al.* [51] used Rice-Ramsperger-Kassel-Marcus (RRKM)/master equation calculations to calculate rate constants for the unimolecular decomposition of DME as a function of temperature and pressure. Their study also reported flow reactor data at 980 K and 10 atm as a function of residence time. A chemical kinetic model was validated using experimental data which included flow reactor, JSR, shock tube ignition delays, laminar flame speciation and flame speed measurements. Wang *et al.* [52] and Cool *et al.* [53] used electron-ionization molecular-beam mass spectrometry and photoionization molecular-beam mass spectrometry performed using synchrotron radiation for the analysis of a stabilized flat flame to provide species profiles within DME flames.

Cook *et al.* [54] used laser absorption of $\dot{O}H$ behind reflected shock waves to isolate and measure the rate constants of the decomposition of DME and the rate constant for H-atom abstraction from DME by $\dot{O}H$ radicals at high temperatures. These measurements were coupled with RRKM/master equation calculations which agreed well with the measurements. Recently, Pyun *et al.* [55] measured species profiles for CO, CH_4, and C_2H_4, during the pyrolysis of DME within a shock tube using tunable laser absorption with a quantum cascade laser. This laser absorption study was done at a range of reflected-shock temperatures ($1300-1600$ K) and at a reflected-shock pressure of 1.5 atm.

Previous ignition delay time studies of these fuels and their mixtures are summarised in Tables 3.1 and 3.2. These studies cover a wide range of conditions including low-to-high temperatures and pressures. Of these previous ignition delay time studies [56–67], only the work of Tang *et al.* [67] included mixtures of CH_4 and DME. It covered dilute mixtures within a pressure range of $1-10$ atm. The current study covers a wider range of temperatures and pressures and includes fuel in 'air' mixtures.

Recent experimental studies of DME combustion also include a flame speed and flame

Table 3.1: CH_4 ignition delay time studies from the literature.

Instrument	Mixture	p / atm	T / K	Year	Reference
Review				1994	[56]
Shock Tube	Dilute in Ar	$3-300$	1800	1974	[57]
Shock Tube	Dilute in Ar	$9-480$	$1410-2040$	1996	[58]
Shock Tube	Fuel-rich	$35-260$	$1040-1600$	1999	[59, 60]
RCM	'air'	$13-16$	$980-1060$	2001	[61]
Shock Tube	Fuel-lean	$3-450$	$1200-1700$	2003	[62]
Shock Tube	'air'	$16-40$	$1000-1350$	2004	[63]

Table 3.2: Summary of DME ignition delay time studies from the literature.

Instrument	Mixture	p / atm	T / K	Year	Reference
RCM	'air'	$9.87-19.74$	$615-735$	2008	[65]
Shock Tube	'air'	$12.83-39.48$	$662-1266$	1996	[64]
Shock Tube	Dilute in Ar	$1.58-6.51$	$1175-1900$	2009	[66]
Shock Tube	Dilute in Ar	$1.00-9.87$	$1134-2105$	2012	[67]

speciation study by Liu *et al.* [68]. The effect of diluting DME flames with 20% CO_2 was studied, and flame speeds over a range of pressures were reported. Flame speciation using electron-ionization molecular-beam mass spectrometry was measured. Guo *et al.* [69] measured low temperature species profiles in an atmospheric flow reactor with electron-ionization molecular-beam mass spectrometry used as the detection system. Herrmann *et al.* [70] used an atmospheric flow reactor to measure mole fractions of species related to DME oxidation at low temperatures ($400-1200$ K) by time-of-flight mass spectrometry. Both of these studies compared their measured data to models available in the literature.

In *this study*, we provide new ignition delay time data for these two important fuels over wide regimes of temperature and pressure at engine- and turbine-relevant conditions. A new, detailed chemical kinetic mechanism (Mech_56.54) has been developed, which is capable of predicting these new ignition delay data and available literature data. Presented first is an overview of the experiments, including details on the mixtures studied, the facilities, the measurement techniques, and modeling approaches. The experimental section is followed by a summary of the chemical kinetic mechanism and the reaction rates that were modified for the present study. A results and discussion section presents all of the ignition delay time data as well as comparisons to the kinetic mechanism. Sensitivity analyses and relevant discussions on the observed trends are also provided.

3.3 Experimental

A common set of mixtures was selected for study in both the rapid compression machine (RCM) and in the shock tubes as listed in Table 3.3. All the experimental ignition delay times are provided in Appendix A. The diluent for all the ST experiments was N_2, for the RCM experiments the diluent used were mixtures of N_2, Ar and CO_2. The details of these compositions are contained in the chemkinPRO format input files provided online at <http://c3.nuigalway.ie/ch4_dme.html>.

For the experiments at National University of Ireland Galway (NUIG), methane and DME gases were obtained from Sigma-Aldrich at $\geq 99.0\%$ and $\geq 99.9\%$ purity respectively, while all other gases were supplied by BOC Ireland; nitrogen (CP Grade) $\geq 99.95\%$,

Table 3.3: CH_4/DME mixtures tested in the present study. Compositions reported in percentage volume.

	Mix No.	% CH_4	% CH_3OCH_3	% O_2	% Diluent	ϕ
100% CH_4	1	3.055	0.000	20.367	76.578	0.3
	2	4.990	0.000	19.960	75.050	0.5
	3	9.506	0.000	19.011	71.483	1.0
	4	17.361	0.000	17.361	65.278	2.0
80%/20% CH_4/DME	5	2.228	0.557	20.423	76.792	0.3
	6	3.646	0.911	20.051	75.392	0.5
	7	6.974	1.743	19.177	72.106	1.0
	8	12.829	3.207	17.640	66.324	2.0
60%/40% CH_4/DME	9	1.535	1.024	20.471	76.970	0.3
	10	2.516	1.677	20.127	75.680	0.5
	11	4.829	3.220	19.317	72.634	1.0
	12	8.939	5.959	17.878	67.224	2.0
100% DME	13	0.000	2.058	20.576	77.366	0.3
	14	0.000	3.383	20.298	76.319	0.5
	15	0.000	6.545	19.634	73.821	1.0
	16	0.000	12.285	18.428	69.287	2.0

argon (Research Grade) $\geq$ 99.9995%, oxygen (Medical Grade) $\geq$ 99.5% and all were used without further purification. At Texas A & M University (TAMU), the DME was Grade 2.6 purity (99.6%), the methane was Grade 3.7 (99.97%), and both the O_2 and N_2 were ultra high purity grade (99.999%). All test mixtures were made in stainless steel mixing vessels using partial pressures to determine the volumetric percentage of each constituent to within 1% of their reported value. The N_2 and O_2 were mixed in the ratio of 3.76 to 1. Test mixtures were allowed to mix for at least 4 hours before use. For the Texas A&M University (TAMU) shock-tube mixing tanks, the gases were introduced into the mixing tanks through a perforated tube that extended the length of the mixing chamber, inducing turbulent mixing.

3.4 Computational Modeling

ChemkinPRO [71] was used for all simulations.

3.4.1 RCM Simulation

Roll-up vortices can cause temperature gradients within the combustion chamber due to the entrainment of the cold boundary layer from the walls into the chamber. This effect was minimised by using piston heads which have crevices to capture the boundary layer and whose dimensions were optimised for the conditions of the NUIG RCM leading to a good spatial temperature homogeneity in the combustion chamber as predicted by Würmel *et al.* [72] using computational fluid dynamics (CFD) simulations.

Due to the long residence times in the RCM, it is necessary to account for heat losses during experiments, which occur mainly via diffusion of the core test gas to the relatively cold walls of the combustion chamber. This effect was accounted for by performing non-reactive experiments concurrently with reactive experiments. These un-reactive

experiments were performed by replacing molecular oxygen with nitrogen as they have similar heat capacities and thermal diffusivities. The pressure-time profiles from these non-reactive experiments are converted to volume-time profiles. These profiles were included in the simulations to account for the pressure and temperature change in the test mixture during experiment. Once these facility effects have been accounted for, the RCM was simulated as a homogeneous batch reactor with varying volume. This method is also decribed in Chapter 2.16.

The simulated ignition delay time was determined from the simulated pressure history. The method for determining the ignition delay time from these pressure histories was the same as the method used to determine the ignition delay time from the experimental pressure histories which has been outlined in Chapter 2.2.2. Briefly, the ignition delay was measured from the first local maximum on the simulated pressure trace (End of the compression phase), to the maximum rate of pressure increase due to ignition.

3.4.2 Shock Tube Simulation

Shock-tube experiments are commonly simulated assuming either constant-volume or constant-pressure conditions. The short residence times associated with conventional shock tubes means that they can generally be assumed to be adiabatic reactors. For ignition delay times greater than 1000 μs and in particular for high pressures as discussed by Petersen [16], it may be necessary to account for non-ideal effects to accurately simulate the data. This scenario depends on the extent of the pressure/temperature change during experiments. In *this study*, the shock tubes were simulated as constant-volume, homogeneous batch reactors. The simulated ignition delay times were again determined in the same fashion as the experimental ignition delay times, described in Section 2.1.3. The maximum rate of pressure increase was used to define simulated ignition delay times for the shock tube simulations.

3.5 Chemical Kinetic Model

The data measured in this study and available literature data (JSR, flow reactor, RCM, shock tube, shock-tube speciation, flame speed, and flame speciation) have been used to validate the DME kinetic mechanism, Mech_56.54, developed here. The experimental data, ChemkinPRO [71] format input files for simulation of the RCM data and the kinetics, thermodynamics, and transport properties files are available online, these can be found at <http://c3.nuigalway.ie/ch4_dme.html>. Provided in the following subsections are details on the thermodynamic data used and the rate constants that were used in the presented mechanism.

3.5.1 Thermodynamic Data

The mechanism includes a re-evaluation of the thermodynamic properties for DME and the intermediate species relevant to its low-temperature combustion. The thermodynamic data were calculated using THERM [73] software which employed optimized group values [74] from comparison of available literature values. The study of Yamada *et al.* [75] provided thermodynamic calculations for key DME low-temperature radical intermediates ($CH_3OCH_2\dot{O}_2$ and $\dot{C}H_2OCH_2O_2H$). These calculations were used to optimize the group $C/H_2/O/OO$ and the bond dissociation group CJOC. These groups were used in the cal-

culation of the thermodynamic properties presented here and are provided in Appendix A.

3.5.2 Rate Constants

Chemical kinetic rate constants were considered after finalising the thermodynamic parameters. The rate constants altered relative to AramcoMech1.3 [76] relate exclusively to the DME sub-mechanism. These are presented and discussed in the following sections.

H-atom Abstraction Reactions

Rate constants for H-atom abstraction reactions were taken from the original work of Curran/Fischer *et al.* [49] [50], with the exception of abstraction by $H\dot{O}_2$, $CH_3\dot{O}_2$ and $\dot{C}H_3$ radicals which have been altered in this study.

Table 3.4: Modified H-atom abstraction reactions. A, n and E_a (cal mol^{-1}) in Chemkin-PRO [71] format.

Reaction	Kinetic Model	A	n	E_a
R1	*This Study*	3.17×10^{-03}	4.64	10556.0
	AramcoMech 1.3 [76]	$8.67\times10^{+02}$	3.01	12090.0
	Curran/Fischer *et al.* [49,50]	$1.68\times10^{+13}$	0.00	17690.0
	Zhao *et al.* [51]	$2.00\times10^{+13}$	0.00	16500.0
R2	*This Study*	1.27×10^{-03}	4.64	10556.0
	AramcoMech 1.3 [76]	$3.12\times10^{+02}$	3.12	13190.0
	Curran/Fischer *et al.* [49,50]	$1.68\times10^{+13}$	0.00	17690.0
R3	*This Study*	$7.02\times10^{+00}$	3.78	9687.0
	AramcoMech 1.3 [76]	1.45×10^{-06}	5.73	5700.0
	Curran/Fischer *et al.* [49,50]	1.45×10^{-06}	5.73	5700.0
	Zhao *et al.* [51]	$2.68\times10^{+01}$	3.78	9631.0

R1 – $CH_3OCH_3 + H\dot{O}_2 \rightleftarrows CH_3O\dot{C}H_2 + H_2O_2$
R2 – $CH_3OCH_3 + CH_3\dot{O}_2 \rightleftarrows CH_3O\dot{C}H_2 + CH_3O_2H$
R3 – $CH_3OCH_3 + \dot{C}H_3 \rightleftarrows CH_3O\dot{C}H_2 + CH_4$

In previous mechanisms [49–51, 76], the rate constant for H-atom abstraction by the hydroperoxyl radical was estimated using analogies to similar chemical systems. In *this study* a rate constant from the recent quantum chemical calculations by Mendes *et al.* [**?**] was used. Table 3.4 lists comparisons of the rate constants used here with those from previously published models [49–51,76]. The rate constant used is approximately 50% slower than that used in the study of Curran/Fischer *et al.* [49,50] and AramcoMech1.3 [76], at temperatures between $700 - 1100$ K. There is a factor of 3.8 difference at 1000 K in the rate constants used by Zhao *et al.* [51] and those calculated by Mendes *et al.*, which has been employed here. It should be noted that the study of Zhao *et al.* [51] did not include the H-atom abstraction from the fuel by methylperoxyl radical which may explain why it was necessary for them to increase the rate of abstraction by hydroperoxyl radical.

The rate constant for H-atom abstraction by methylperoxyl radical used here is a factor of 2.5 lower than abstraction by hydroperoxyl radical which is a ratio based on the calculations of Carstensen and Dean [77]. Curran/Fischer *et al.* [49,50] used the same rate constant for abstraction by hydroperoxyl and methylperoxyl radicals.

The rate constant for H-atom abstraction by methyl radical is based on the measurements by Tranter *et al.* [78]. We have reduced their value by 45% which is within the uncertainty reported by the authors [78] as this improved agreement with the methane speciation profiles taken by Pyun *et al.* [55].

Low Temperature Oxidation Mechanism

The low-temperature DME oxidation mechanism has been shown to proceed through a similar general reaction scheme as that for alkanes [49–51]. H-atom abstraction, mainly by hydroxyl radicals, leads to the formation of methoxymethyl ($CH_3O\dot{C}H_2$) radicals. These can either undergo β-scission to form methyl radicals and formaldehyde or add to molecular oxygen to form alkyl-peroxyl ($CH_3OCH_2\dot{O}_2$) radicals. These can isomerise via a 6-membered transition state ring to form hydroperoxyl alkyl ($\dot{C}H_2OCH_2O_2H$) radicals. $\dot{C}H_2OCH_2O_2H$ radicals can either undergo β-scission, each forming two molecules of formaldehyde and a hydroxyl radical or add to molecular oxygen to form peroxy-hydroperoxyl-alkyl ($\dot{O}_2CH_2OCH_2O_2H$) radicals. At low temperatures, addition to O_2 dominates, and these radicals undergo a second isomerisation reaction leading to the formation of stable HO_2CH_2OCHO molecules and reactive hydroxyl radicals. The subsequent decompositions of HO_2CH_2OCHO molecules yield more hydroxyl radicals and $\dot{O}CH_2OCHO$ radicals.

Table 3.5 presents a list of the low-temperature oxidation pathways of CH_3OCH_3. Quantum-Rice-Ramsperger-Kassel (QRRK) theory with a modified strong-collision (MSC) model for energy transfer, was used to initially assess the pressure-dependencies of these low-temperature oxidation pathways.

Table 3.5: Low-temperature DME reactions treated as pressure dependent.

$$CH_3O\dot{C}H_2 \rightleftarrows \dot{C}H_3 + CH_2O$$
$$CH_3O\dot{C}H_2 + O_2 \rightleftarrows CH_3OCH_2\dot{O}_2$$
$$CH_3O\dot{C}H_2O_2 \rightleftharpoons \dot{C}H_2OCH_2O_2H$$
$$\dot{C}H_2OCH_2O_2H \rightarrow CH_2O + CH_2O + \dot{O}H$$
$$\dot{C}H_2OCH_2O_2H + O_2 \rightleftarrows \dot{O}_2CH_2OCH_2O_2H$$
$$\dot{O}_2CH_2OCH_2O_2H \rightleftharpoons HO_2CH_2OCHO + \dot{O}H$$

The QRRK/MSC method herein [79] requires as input, a high-pressure limiting rate constant for each reaction pathway, Lennard-Jones parameters for the reactant and bath gas (N_2), and an estimate of the average energy transferred in deactivating collisions $\langle \Delta E_d \rangle$. As part of these calculations we employed the high-pressure limiting rate constants recommended by Li *et al.* [80] for the $CH_3O\dot{C}H_2$ radical β-scission, and the CBS-q calculations of Yamada *et al.* [75] for the remaining low-temperature oxidation reactions as listed in Table 3.5. However, the high-pressure limiting rate constants for the O_2 addition reactions were taken as those estimated in the Curran/Fischer model [49, 50].

For the energy transfer model, Miller and Klippenstein [81] performed RRKM/ME computations on *n*-propyl radical decomposition reactions and found that a temperature-dependent function, $\langle \Delta E_d \rangle = 110(T/300)^{1.0}$ cm^{-1}, gave good agreement with experiment. We therefore adopt these energy transfer parameters for the structurally similar $CH_3O\dot{C}H_2$ radical. For the $R\dot{O}_2$ and $\dot{O}_2QOOH$ radical potential energy surfaces $\langle \Delta E_d \rangle = 200(T/300)^{0.85}$ cm^{-1} and $\langle \Delta E_d \rangle = 300(T/300)^{0.85}$ were estimated respectively, based on direct analogy to those used by Goldsmith *et al.* [82] for the corresponding radicals on the *n*-propyl + O_2 ($C_3H_7\dot{O}_2$) and $C_3H_7\dot{O}_2$ + O_2 potential energy surfaces.

Lennard-Jones parameters for $CH_3O\dot{C}H_2$ radical were determined empirically from the correlations of Kee *et al.* [83], where the critical constants of DME [84] were employed to calculate $\sigma = 4.71$ Å and $\varepsilon/k_B = 296.6$ K. For the $R\dot{O}_2$ and $\dot{O}_2QOOH$ radicals, the Lennard-Jones parameters used by Goldsmith *et al.* [82] were adopted. All computations were carried out in an N_2 bath gas with Lennard-Jones parameters of $\sigma = 3.681$ Å and $\varepsilon/k_B = 67.89$ K used as in the study of Jasper and Miller [85].

The initial QRRK/MSC computations were incorporated into the kinetic mechanism, and it was found that the pressure-dependency of the $CH_3O\dot{C}H_2$ radical decomposition were particularly sensitive in predicting ignition delay times. Therefore, a re-evaluation of the $k(T,p)$'s for this reaction *via* quantum chemistry and TST/RRKM/ME computations was performed. Geometry optimisation, frequency and single-point energy calculations were carried out using the CBS-QB3 [86], CBS-APNO [87] and G3 [88] compound methods. Relaxed potential energy surface scans of dihedral angles were carried out in 10 ° increments using the B3LYP method [89, 90] with a CBSB7 basis set, and the computed rotational barriers were used in 1-D hindered internal rotation treatments. Gaussian 09 [91] has been used for quantum chemical calculations with the ChemRate [92] code used for the statistical rate theory calculations. An energy grain size of 30 cm^{-1} was used for the computation of densities and sums of states of the reactant and transition state, and thus microscopic rate constants, up to a maximum energy of 100000 cm^{-1}, with a time-dependent solution of the master equation ultimately employed.

A high-pressure limiting rate constant of $8.03\times10^{12}T^{0.44}\exp(13330/T)$ s^{-1} follows based on B3LYP/CBSB7 ro-vibrational properties and a CBS-QB3 barrier of 106.9 kJ mol^{-1} (0 K). The high-pressure limiting rate constant is within $14-64\%$ of that proposed by Li *et al.* [80] from 500–2000 K, and the results of *this study* therefore corroborate their recommendation. These calculations were carried by Dr. Kieran Somers.

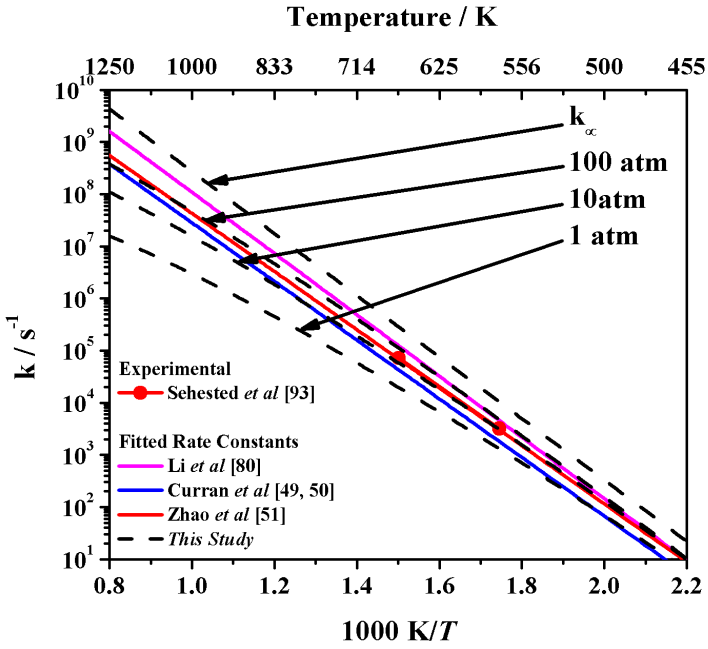

Figure 3.1: Rate constants for $CH_3O\dot{C}H_2 \rightleftharpoons \dot{C}H_3 + CH_2O$.

Figure 3.1 presents the pressure-dependent rate constants used in *this study* and compares them to the available literature rate constants for β-scission of the $CH_3O\dot{C}H_2$ radical. At 1000 K and 10 atm, the newly computed rate constant is a factor of 8.6 slower than

the high-pressure limiting one. The rate constants used for this reaction in the two studies of Curran/Fischer *et al.* [49,50] and Zhao *et al.* [51] are approximately a factor of 2.3 and 3.5 slower than the high-pressure limiting rate constant calculated by Li *et al.* [80] at this temperature respectively, and a factor of 6.3 and 9.7 lower than the high-pressure limiting rate constant recommended in *this study*. The study of Zhao *et al.* [51] found that using the rate constant of Li *et al.* [80] meant that they could not achieve accurate predictions in particular for intermediate temperatures ($800-1000$ K), for both flow reactor data and ignition delay times. It is interesting to note that the estimations of Curran/Fischer *et al.* [49, 50] and Zhao *et al.* [51] are in close agreement with the pressure-dependent rate constants used at 10 atm in this study, possibly indicating why they had to alter the high-pressure limiting rate constant recommended by Li *et al.* to achieve agreement with experiment. The measurement of Sehested *et al.* [93] was measured at 17 atm and it lies between the 10 and 100 atm computed rate constants of *this study*. A direct comparison of a computed 17 atm rate constant to the measurement of Sehested *et al.* [93] was made and the computed rate constant differed by no more than 20% of the measurement.

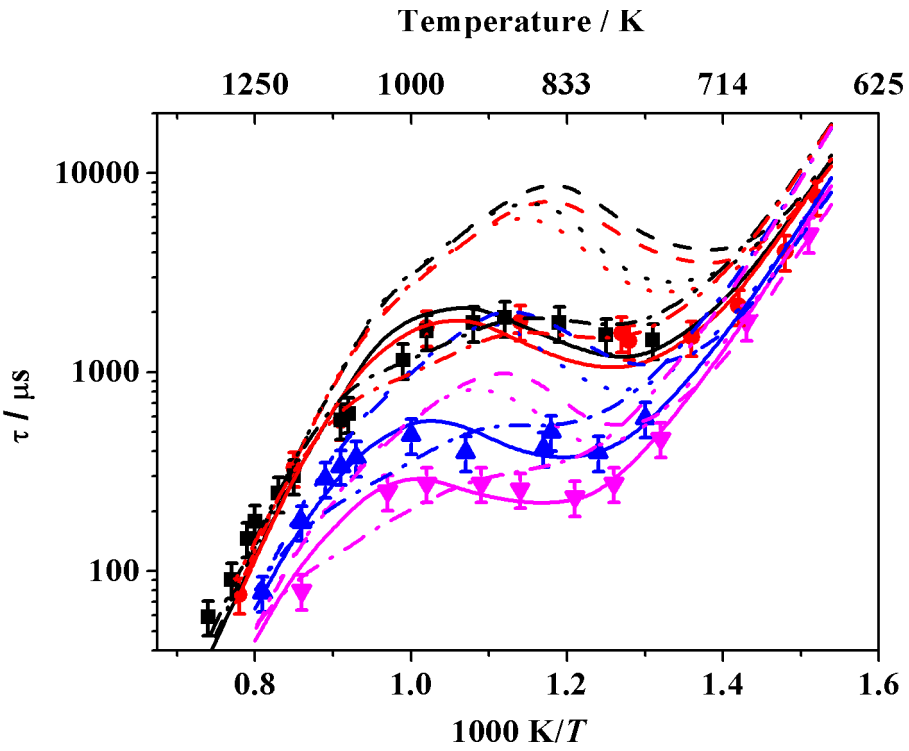

Figure 3.2: Comparison of ignition delay times over a range of pressures for DME in 'air' $\phi = 1.0$ from this study ($p_5 = 11.9$ and 25.0 atm) and Pfahl *et al.* [64] ($p_5 = 12.8$ and 39.5 atm). Symbols are experimental results; ■ – $p_5 = 11.9$ atm, ● – $p_5 = 12.8$ atm, ▲ – $p_5 = 25.0$ atm, ▼ – $p_5 = 39.5$ atm. Solid lines are predictions using the current mechanism using pressure-dependent rate constants, dashed lines represent the predictions of the current mechanism using high-pressure limiting rate constants, dotted lines represent the predictions using pressure-dependent rate constants for all reactions except methoxymethyl radical β-scission and dash -dot lines represent the predictions of the Curran/Fischer *et al.* mechanism [49, 50].

Figure 3.2 shows the difference observed when pressure-dependent rate constants were included in the mechanism. It also shows that the change in the predictions is mainly

due to the pressure-dependent treatment of $CH_3O\dot{C}H_2 \rightleftarrows \dot{C}H_3 + CH_2O$. Figure 3.2 also illustrates the improvement in the predictions compared to the previous model of Curran/Fischer *et al.* [49, 50]. Ultimately, it is the pressure-dependent treatment of the methoxymethyl radical β-scission that has the greatest effect on model predictions. The pressure-dependent treatment of the other reactions listed in Table 3.5 has a minor effect on the model predictions when compared to the effect of the methoxymethyl radical β-scission. The QRRK/MSC approach used to assess the pressure-dependency of these reactions is therefore not updated to a more sophisticated RRKM/ME treatment, as the added expense of the latter is unlikely to offer any great improvements with respect to the final model predictions.

Finally, the rate constant for the decomposition of the carbonyl-hydroperoxide species ($HO_2CH_2OCHO \rightleftarrows \dot{O}CH_2OCHO + \dot{O}H$) was adapted from the study of Sahetchian *et al.* [94]. This rate constant was increased by a factor of 5 to gain agreement with our low-temperature RCM data. The previous studies of Curran/Fischer *et al.* [49,50] and Zhao *et al.* [51] required unreasonable increases in this rate constant of factors of approximately 10 and 24, respectively, to achieve model agreement with experiment.

3.6 Results and Discussion

The shock-tube results for 80/20 and 60/40 CH_4/DME mixtures have been described in the thesis of Zinner [95], and the shock-tube results for both of the pure fuels were presented in a conference paper [96]. The shock-tube data (presented as half-filled symbols) and the RCM data are presented for the first time in the present study. This section first presents the pure CH_4 data and the chemistry which describes its oxidation under the conditions studied here. This first section is followed by the extensive set of experimental results and model analyses for 80/20 CH_4/DME and 60/40 CH_4/DME blends. Pure DME mixtures are then presented and discussed. Finally, the relative reactivities of the pure fuels and their mixtures are compared and discussed.

3.6.1 Methane Oxidation

Methane data are presented as a function of pressure in Fig. 3.3. It is observed that ignition delay times decrease with increasing temperature and pressure, as expected. Mech_56.54 captures the overall trends in the experimental data quite well but tends to under-predict reactivity at 10 atm and at the lower-temperature conditions of the RCM experiments.

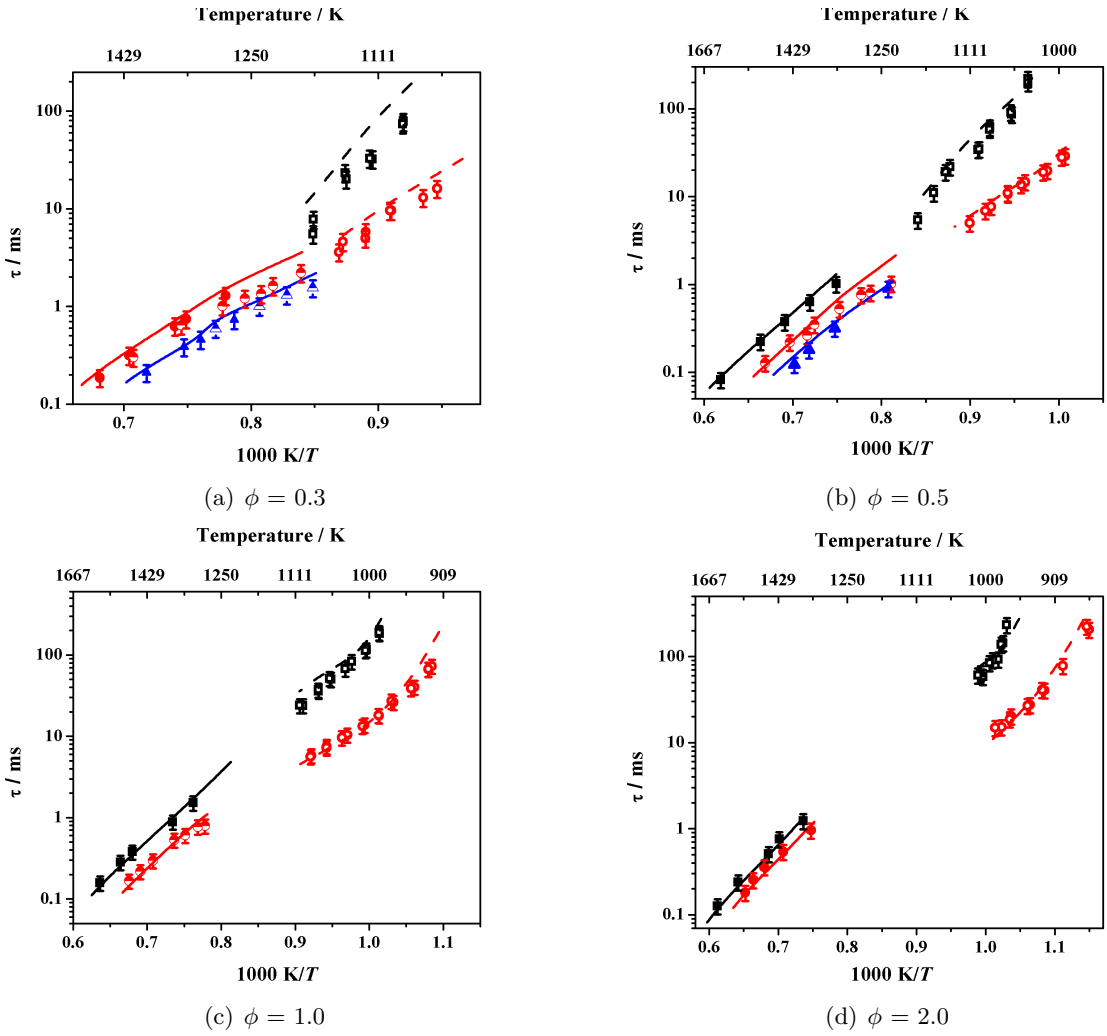

(a) $\phi = 0.3$

(b) $\phi = 0.5$

(c) $\phi = 1.0$

(d) $\phi = 2.0$

Figure 3.3: Influence of pressure on pure methane in air mixtures at ■ – ∼ 10 atm, ● – 25 atm (15 atm for Fig. 3.3(d) ST data), ▲ – 44 atm. Open symbols are RCM data, filled symbols ST data, half-filled symbols are ST data measured during *this study*. Lines are Mech_56.54 predictions, dashed lines are simulations accounting for RCM facility effects.

An intermediate temperature of 1177 K was chosen to perform brute-force sensitivity analyses as a function of pressure for data in Fig. 3.3(a). The brute-force sensitivity analyses consisted of performing ignition delay time simulations while increasing and decreasing rate constants by a factor of 2. Sensitivity coefficients (S) were determined using the equation:

$$S = \frac{\log(\tau_+/\tau_-)}{\log(k_+/k_-)} = \frac{\log(\tau_+/\tau_-)}{\log(2.0/0.5)}$$

Where τ_+ denotes the ignition delay time when a rate constant has been increased by a factor of 2, τ_- refers to the ignition delay time when a rate constant has been decreased by a factor of 2, k_+ is the rate constant increased by a factor of 2 and k_- is the rate constant decreased by a factor of 2. Negative sensitivity coefficients denote a promoting effect (decreasing ignition delay time by increasing the rate constant), while a positive coefficient points to an inhibiting effect.

Figure 3.4 shows that for all pressures the most promoting reaction is $\dot{C}H_3 + O_2 \rightleftarrows$

CH_2O + $\dot{O}H$. While the most inhibiting reaction under all conditions is methyl radical combination to form ethane. From 9.9 atm to 41.6 atm, the sensitive reactions do not change; this is an indication that it is not a change in the controlling chemistry that causes the observed decrease in ignition delay time with increasing pressure but the increased concentration of reactants (CH_4 and O_2).

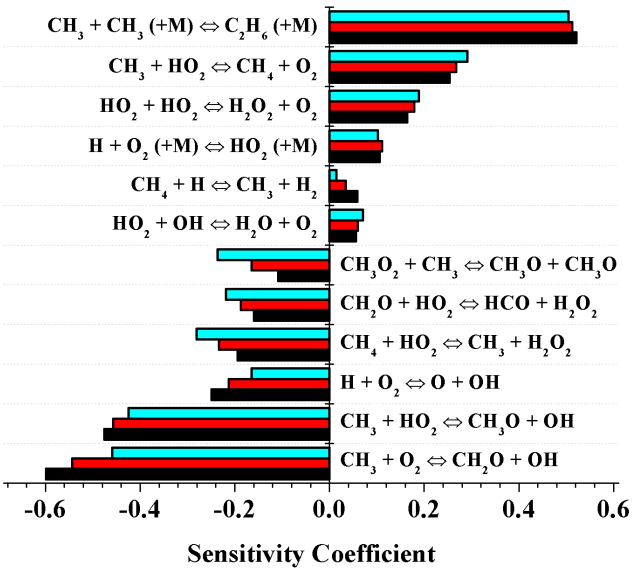

Figure 3.4: Sensitivity analyses at 1177 K and at $\phi = 0.30$, ■ – 9.9 atm, ■ – 19.7 atm, ■ – 41.6 atm.

Figure 3.5 presents ignition delay times for pure methane mixtures at equivalence ratios of $\phi = 0.3 - 2.0$ and pressures of 10 and 25 atm. Figure 3.5(a) shows that at the lowest temperatures, ignition delay times decrease with increasing equivalence ratio. However the opposite trend is true for experimental data above 1312 K. This inversion in the effect of equivalence ratio is not seen in Fig. 3.5(b) where ignition times decrease with increasing equivalence ratio. There is an overlap of ignition delay times of varying equivalence ratios at the highest reflected-shock temperatures presented; this is most evident at temperatures above 1430 K.

Figure 3.6 depicts brute-force sensitivity analyses performed for the experimental conditions presented in Fig. 3.5. Figures 3.6(a) and 3.6(b) present high and low temperature (1470 and 1056 K) sensitivity analyses at $p = 10$ atm. Figures 3.6(c) and 3.6(d) present high and low temperature (1436 and 993 K) sensitivity analyses at $p = 25$ atm. Under all of the conditions shown the most inhibiting reaction is methyl radical combination to form ethane. For both pressures the reaction $CH_3\dot{O}_2 + \dot{C}H_3 \rightleftarrows CH_3\dot{O} + CH_3\dot{O}$, promotes reactivity at low-temperature. Both reactants are fuel derived and as a result, fuel-rich mixtures have faster ignition delay times at low temperatures. At high temperature for both pressures ($p = 10$ atm and 25 atm), the reaction $\dot{H} + O_2 \rightleftarrows \ddot{O} + \dot{O}H$ becomes one of the most promoting reactions leading to the inversion in the effect of equivalence ratio at $p = 10$ atm. This inversion is observed at $p = 10$ atm but is not seen at $p = 25$ atm, and at the highest temperatures studied in Fig. 3.5(b) there is no effect of equivalence ratio. This overlap of equivalence ratios was noted at $T = 1250$ K for the 10 atm data. The inversion temperature for the 25 atm data is increased at higher pressure as the rate constant for the reaction $\dot{C}H_3 + O_2$ (+M) $\rightleftarrows CH_3\dot{O}_2$ (+M) is pressure-dependent and increases with pressure. Therefore, at higher pressure the equilibrium of this reaction favors

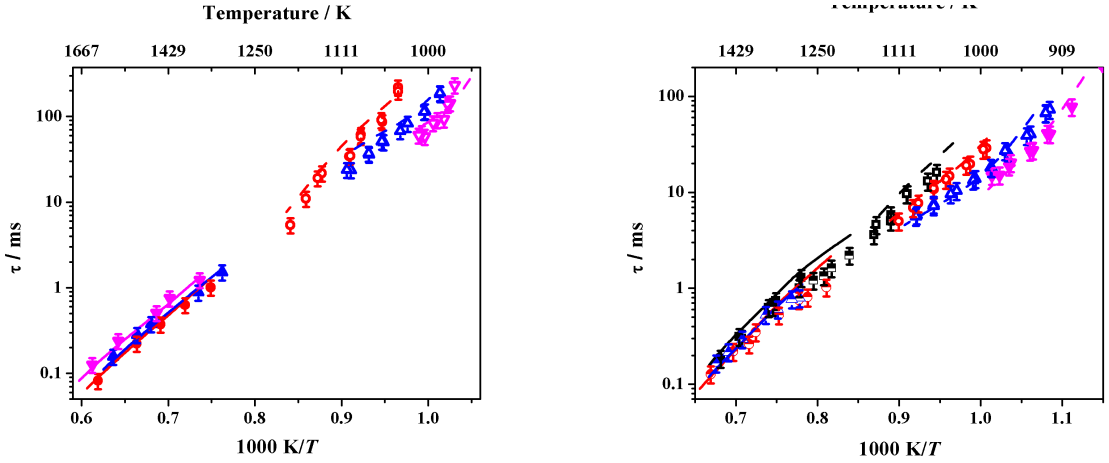

(a) 10 atm

(b) 25 atm

Figure 3.5: Influence of equivalence ratio on CH_4 mixtures at ■ – $\phi = 0.3$, ● – $\phi = 0.5$, ▲ – $\phi = 1.0$, ▼ – $\phi = 2.0$. Open symbols are RCM data, filled symbols ST data, half-filled symbols are ST data measured during *this study*. Lines are Mech_56.54 predictions, dashed lines are simulations accounting for RCM facility effects.

the formation of $CH_3\dot{O}_2$ radicals up to higher temperatures when compared to the 10 atm data.

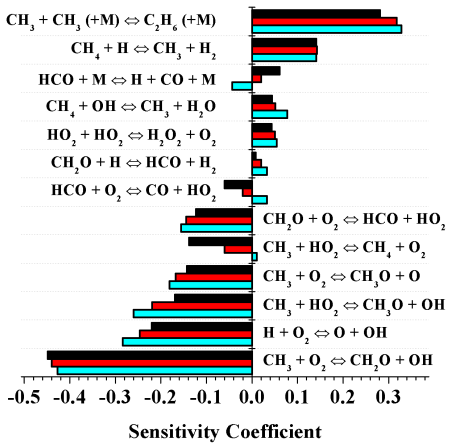

(a) 1470 K, $p = 10$ atm

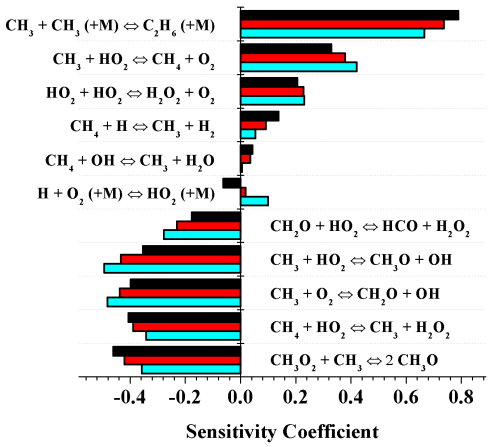

(b) 1056 K, $p = 10$ atm

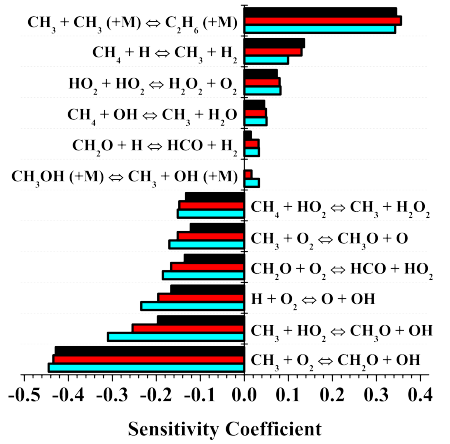

(c) 1436 K, $p = 25$ atm

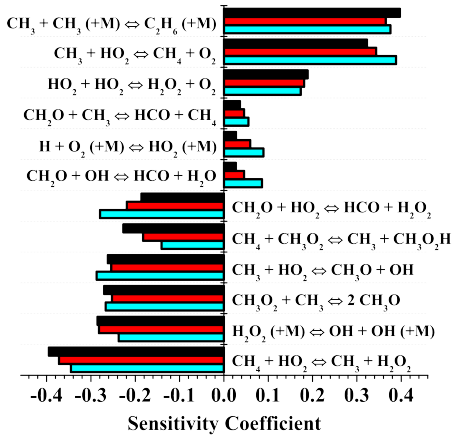

(d) 993 K, $p = 25$ atm

Figure 3.6: Sensitivity analyses CH_4/'air' mixtures, ■ – $\phi = 2.0$, ■ – $\phi = 1.0$, ■ – $\phi = 0.5$.

3.6.2 80% CH_4 / 20% DME

Ignition delay times were measured for mixtures of 80/20 CH_4/DME. The results of the experimental data and computational simulations are presented in Fig. 3.7 as a function of pressure. Similar to pure methane, the 80/20 CH_4/DME blend shows that ignition delay times globally decrease with increasing pressure.

Figure 3.8 presents brute-force sensitivity analyses adhering to the conditions presented in Fig. 3.7(d) $\phi = 2.0$ in 'air' mixtures at 706 K. What is notable is that under the conditions studied, the most-sensitive reactions are those involving DME. For example, the most-promoting reaction is $CH_3OCH_3 + \dot{O}H \rightleftarrows CH_3O\dot{C}H_2 + H_2O$, while the most-inhibiting reaction is $\dot{C}H_2OCH_2O_2H \rightarrow CH_2O + CH_2O + \dot{O}H$. This high sensitivity to DME is interesting because, despite the fact that there is four times more methane present in the blend, the reactions controlling ignition involve DME chemistry. Pure methane is unreactive at 706 K, but with the addition of a small quantity of DME its reactivity increases significantly. At approximately 1150 K and 10 atm, ignition delay time decreases by a factor of 5.1 from pure methane to 80/20 CH_4/DME. From the point of view of gas turbine operation at low temperatures, this decrease in the ignition delay time as a function of DME addition is significant as the addition of only small quantities

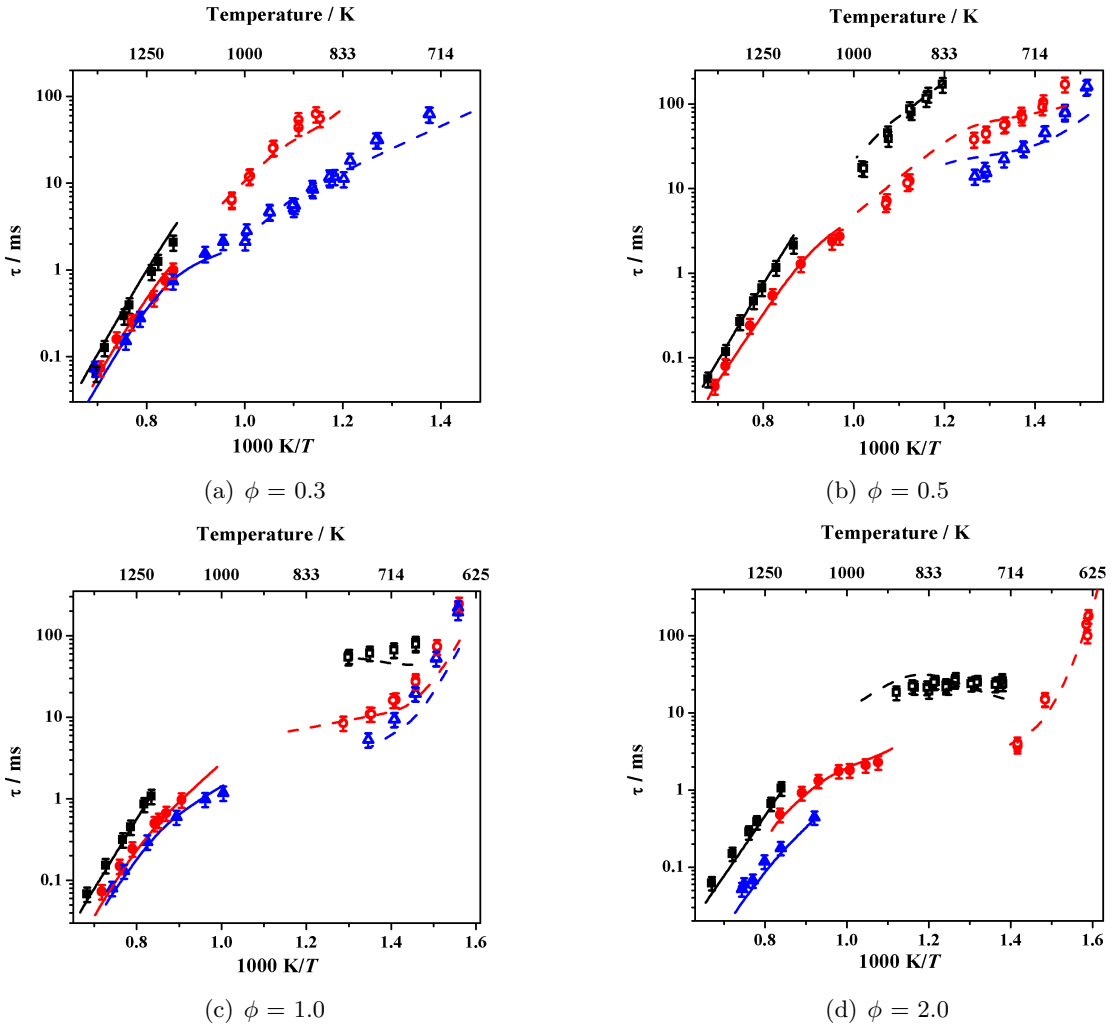

(a) $\phi = 0.3$

(b) $\phi = 0.5$

(c) $\phi = 1.0$

(d) $\phi = 2.0$

Figure 3.7: Influence of pressure on 80/20 CH_4/DME mixtures. ■ – ∼ 10 atm, ● – ∼ 20 atm, ▲ – ∼ 30 atm. Open symbols are RCM data, filled symbols ST data. Lines are Mech_56.54 predictions, dashed lines are simulations accounting for RCM facility effects.

of DME could theoretically be used to tailor the operation of the gas turbine for a given temperature and pressure.

Figure 3.9 presents ignition delay times and model simulations for the 80/20 CH_4/DME blends as a function of equivalence ratio. Figure 3.9(b) shows that ignition delay times decrease with increasing equivalence ratio at low temperatures (< 1100 K). Figure 3.9(a) shows that ignition delay time is independent of equivalence ratio in the temperature range $1200 - 1490$ K. Mech_56.54 predicts all of these trends very well.

Figure 3.10 presents the results of sensitivity analyses on mixtures shown in Fig. 3.9(b) at 1250 K and 706 K. These temperatures were chosen to show the change in the sensitive reactions from low to high temperature. As discussed above, the 80/20 blend reactivity at low temperature is controlled primarily by DME-containing reactions. All equivalence ratios show sensitivity to DME reactions, Fig. 3.10(b). The three most-promoting reactions for all three equivalence ratios are listed below.

$$CH_3OCH_3 + \dot{O}H \rightleftarrows CH_3O\dot{C}H_2 + H_2O$$
$$\dot{C}H_2OCH_2O_2H + O_2 \rightleftarrows \dot{O}_2CH_2OCH_2O_2H$$

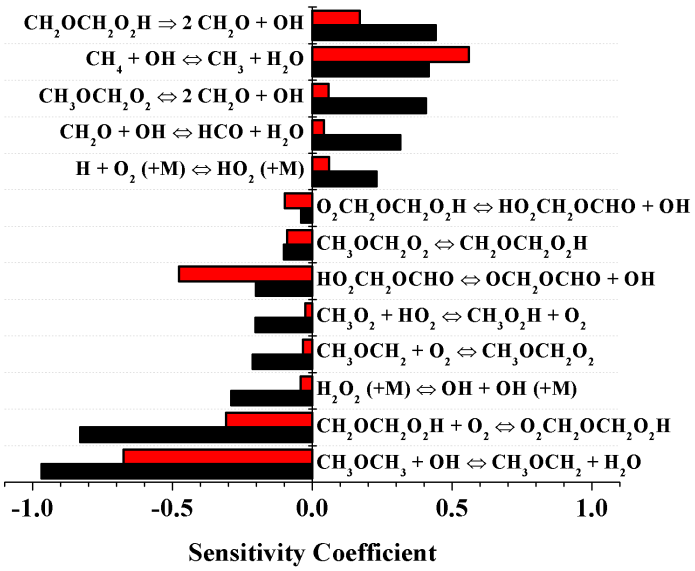

Figure 3.8: Sensitivity to ignition delay time at 706 K, $\phi = 2.0$ at ■ – 5.9 atm, ■ – 25.3 atm.

$$HO_2CH_2OCHO \rightleftarrows \dot{O}CH_2OCHO + \dot{O}H$$

Figure 3.12(a) shows sensitivity analyses at 1250 K. The most-promoting reactions are $\dot{C}H_3 + H\dot{O}_2 \rightleftarrows CH_3\dot{O} + \dot{O}H$ and $CH_3OCH_3(+M) \rightleftarrows CH_3\dot{O} + \dot{C}H_3(+M)$. The most-inhibiting reactions are $\dot{C}H_3 + H\dot{O}_2 \rightleftarrows CH_4 + O_2$ and $\dot{C}H_3 + \dot{C}H_3\ (+M) \rightleftarrows C_2H_6\ (+M)$

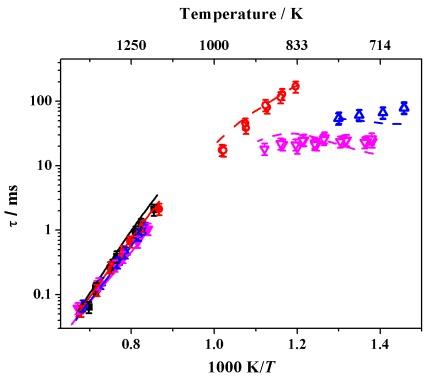

(a) 7 atm

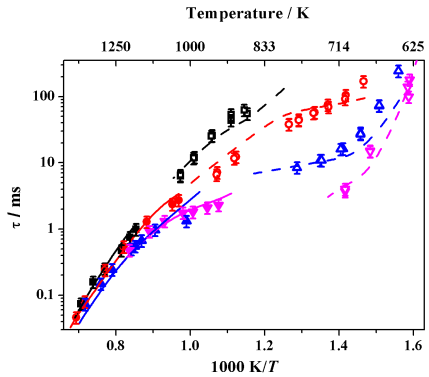

(b) 15–20 atm

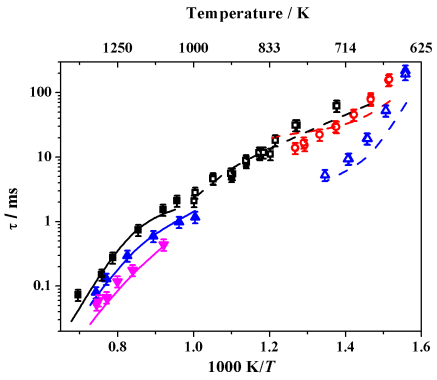

(c) 30 atm

Figure 3.9: Influence of equivalence ratio for 80/20 CH_4/DME mixtures. ■ – $\phi = 0.3$, ● – $\phi = 0.5$, ▲ – $\phi = 1.0$, ▼ – $\phi = 2.0$. Open symbols are RCM data, filled symbols ST data. Lines are Mech_56.54 predictions, dashed lines are simulations accounting for RCM facility effects.

Flux analyses were performed in order to monitor the consumption and production of species under the experimental conditions of interest. All flux analyses were taken at the point of 20% fuel consumption. These analyses provide an understanding of the reactions and associated rate constants that control the predictions of the ignition times.

Figure 3.11 shows the results of flux analyses for data shown in Fig. 3.9(b) at 1250 K. Similar to the sensitivity analyses, the flux analyses show that methyl radical chemistry is very important. Methyl radicals are produced by H-atom abstraction reactions from CH_4 and unimolecular decomposition of DME. β-scission of the methoxymethyl radical also produces methyl radicals. Unimolecular decomposition of DME is the second most-sensitive reaction over all equivalence ratios; this shows that DME is controlling ignition at high temperature as well as low temperatures.

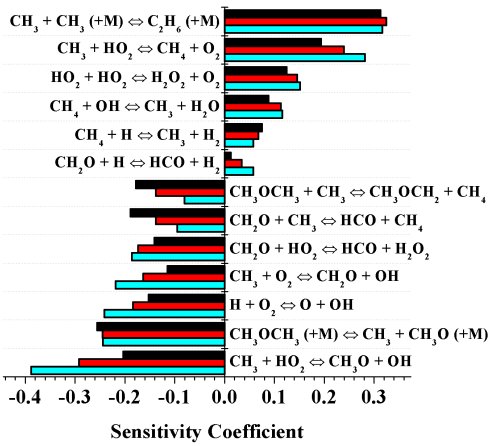

(a) 1250 K

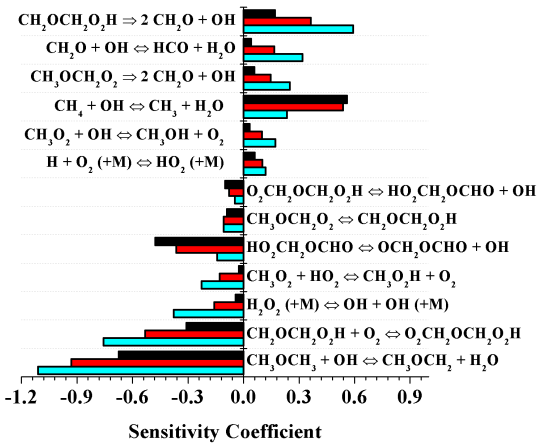

(b) 706 K

Figure 3.10: Sensitivity analyses for ignition delay times at $p = 10$ atm and at ■ – $\phi = 2.0$, ■ – $\phi = 1.0$, ■ – $\phi = 0.5$.

CH_4/DME is iso-electronic when compared to CH_4/C_3H_8, this provides an interesting comparison. Figure 3.12 shows that reactivity is increased overall in CH_4/DME blends when compared to CH_4/C_3H_8. The C–H bonds in DME are weaker than the C–H bonds in propane. This is due to the oxygen atom present in DME. This increases the overall reactivity of DME when compared to propane. Propane has an extra chain propagation $H\dot{O}_2$ elimination pathway, $C_3H_7\dot{O}_2 \rightleftarrows C_3H_6 + H\dot{O}_2$, that is not possible in the DME oxidation mechanism. Thus, there are more chain propagation pathways possible for propane compared to DME which only has the β-scission of the hydroperoxy-alkyl radical to two molecules of formaldehyde and $\dot{O}H$ radical. This also contributes to the reduced reactivity.

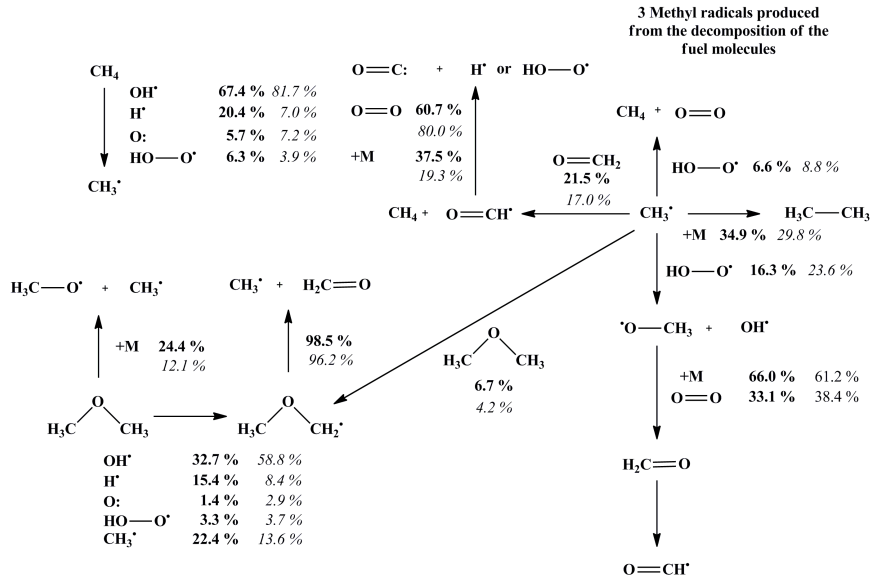

Figure 3.11: Flux analyses at 1250 K and $p = 17.0$ atm in 'air', $\phi = 2.0$ – **bold font**, $\phi = 0.5$ – *italic font*.

3.6.3 60% CH_4 / 40% DME

The same trends in experimental data are observed for the 60/40 CH_4/DME blends. The controlling chemistry is the same as that described for the 80/20 CH_4/DME blends. These similar results are not surprising since DME chemistry is controlling ignition for the 80/20 blends, so it logically follows that it is also controlling ignition for the 60/40 blends which contain even more DME.

Figure 3.7 presents ignition delay times compared as a function of pressure over four different equivalence ratios, $\phi = 0.3 - 2.0$ in 'air'. Mech_56.54 predicts the data well, with some discrepancies with the RCM data at $\phi = 0.3$ and $\phi = 2.0$.

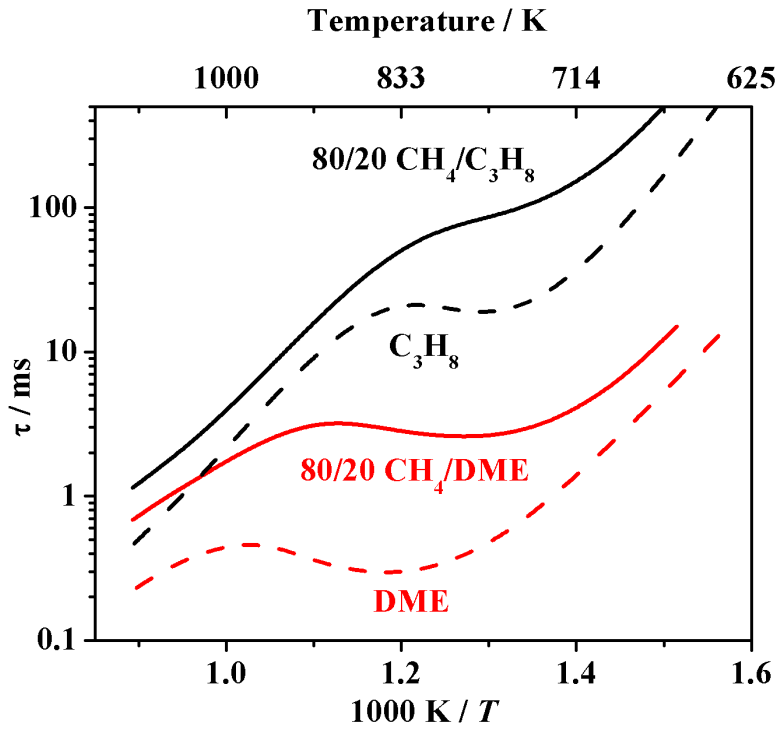

Figure 3.12: Model predictions for n-C_3H_8, DME, and 80/20 CH_4/(DME or n-C_3H_8) in 'air' mixtures at p = 30 atm. Black lines are n-C_3H_8, red lines are DME. Solid line are 80/20 mixtures, dashed lines are pure fuels.

Once again brute force sensitivity analyses were performed this time at ϕ = 1.0, T = 1135 K over the three pressures presented in Fig. 3.13(c). The results are shown in Fig. 3.14. The results are similar to those observed for the 80/20 CH_4/DME blends, methyl radicals combination forming ethane is the most inhibiting reaction for all three pressures. H-atom abstraction from DME by methyl and hydroperoxyl radicals are the most promoting reactions. Also, for p = 8.2 atm DME unimolecular decomposition is one of the most promoting reactions. These analyses serve to reinforce the point made in the previous section that it is DME chemistry that is driving the reactivity of the blends.

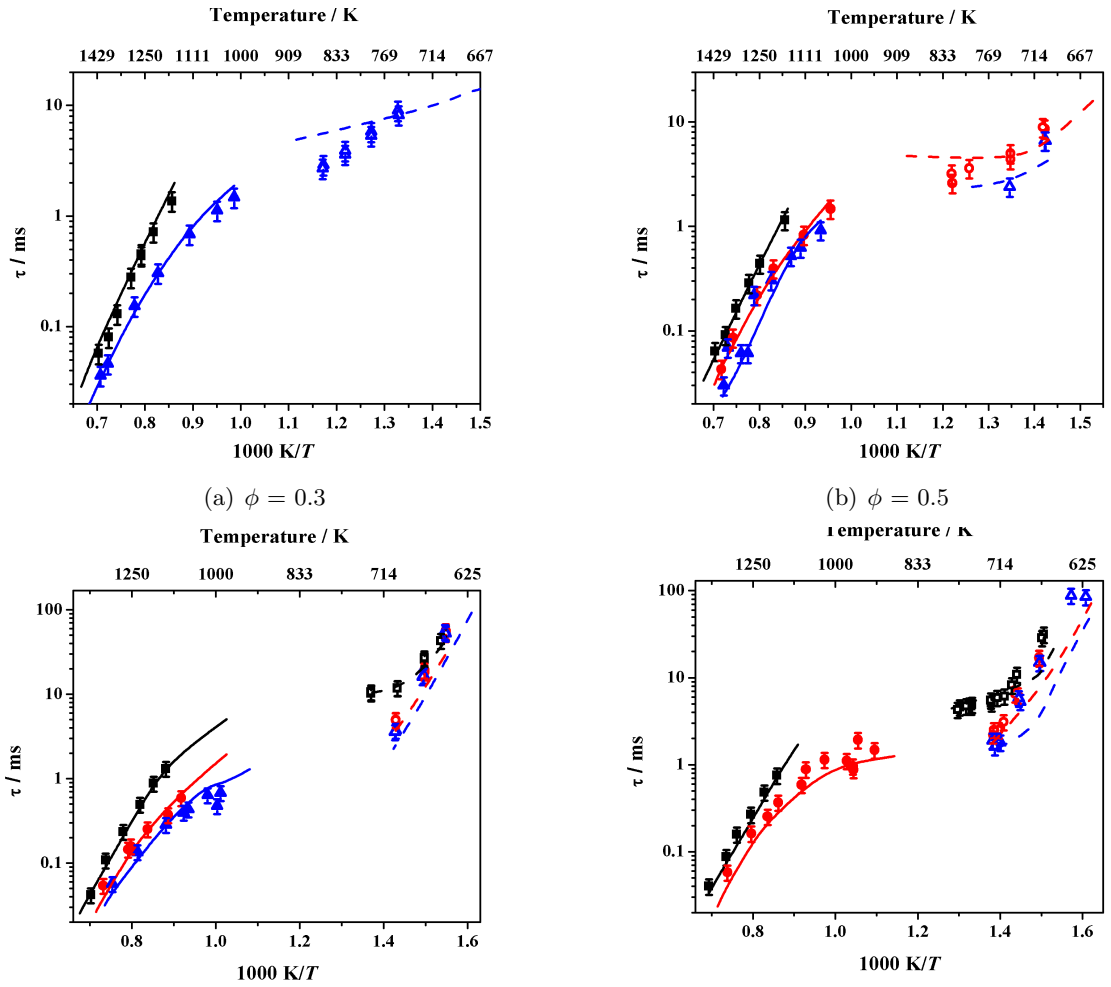

(a) $\phi = 0.3$

(b) $\phi = 0.5$

(c) $\phi = 1.0$

(d) $\phi = 2.0$

Figure 3.13: Influence of pressure on 60/40 CH_4/DME mixtures. ■ – ∼ 8 atm, ● – ∼ 20 atm, ▲ – ∼ 30 atm. Open symbols are RCM data, filled symbols ST data. Lines are Mech_56.54 predictions, dashed lines are simulations accounting for RCM facility effects.

Flux analyses for the 60/40 CH_4/DME blends were performed for $\phi = 1.0$, $T = 1135$ K at pressures of 23.2 atm and 8.2 atm. The results are presented in Fig. 3.15. The general reaction mechanism follows the same scheme as that observed and described in the previous section for the 80/20 CH_4/DME blends. The two pressures analysed show no significant difference in the mechanism of oxidation. The observed decrease in ignition delay time with increasing pressure is an artifact of the increased concentration of reactants as mentioned in the previous two sections and these results simply support this explanation.

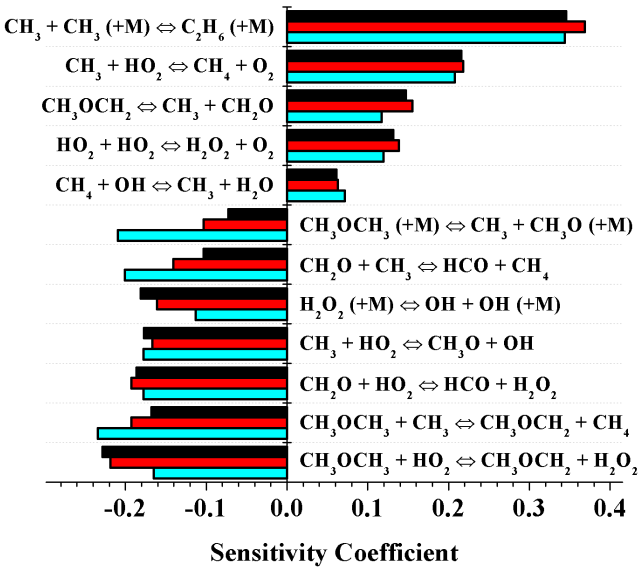

Figure 3.14: Sensitivity to ignition delay time at 1135 K, $\phi = 1.0$ at ■ – 34.1 atm, ■ – 23.2 atm, ■ – 8.2 atm.

3.6.4 Dimethyl Ether Oxidation

Ignition delay times for pure DME in 'air' mixtures are presented in Fig. 3.16 comparing the effect of pressure over four equivalence ratios. DME displays a negative temperature coefficient (NTC) region where the ignition delay times increase with increasing temperature. The temperature at which NTC behavior begins is dependent on both the mixture composition and on the pressure studied. As equivalence ratio increases, so does the temperature at which the NTC behavior begins. The same effect is noted as the pressure increases. Overall, ignition delay times decrease as the pressure increases. As in sections 3.6.1, 3.6.2 and 3.6.3, this decrease is mainly due to the increase in the concentration of reactants with pressure.

Mech_56.54 predictions together with those by the Zhao *et al.* [51] and Fischer/Curran [49, 50] mechanisms are compared to the experimental data. Mech_56.54's predictions offer an improvement over previous mechanisms for all conditions shown. Improvements in predictions are seen at high temperatures (>1000 K) when compared to the Zhao *et al.* [51] mechanism, and at low temperatures (<800 K) when compared to the mechanism of Fischer/Curran [49, 50].

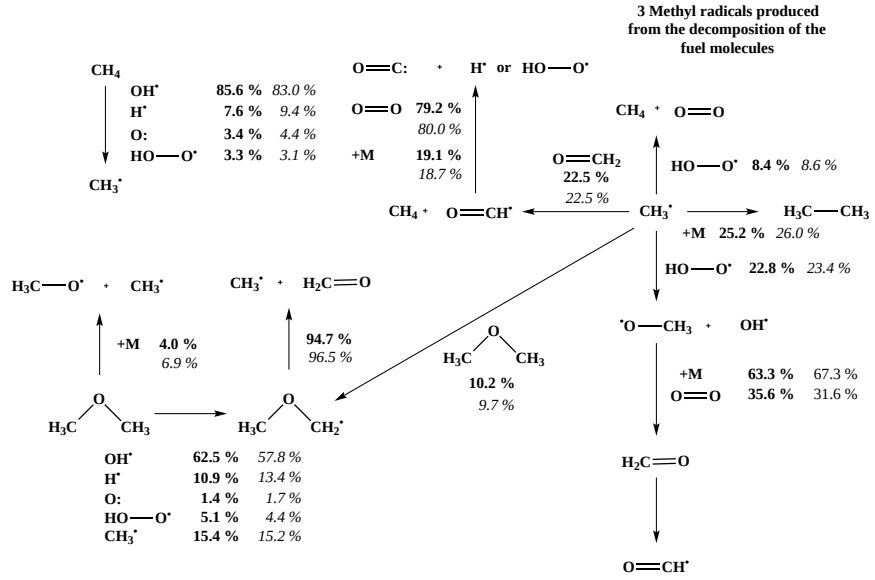

Figure 3.15: Flux analyses at 1135 K and $\phi = 1.0$ in 'air', $p = 23.2$ atm – **bold font**, $p = 8.2$ atm – *italic font*.

Brute-force sensitivity analyses were carried out under the conditions shown in Fig. 3.16(b) at $\phi = 0.5$ in 'air' and 827 K. This temperature was chosen as it showed the largest effect of pressure on ignition delay times. Similar to pure methane and the two different blends studied, the most-sensitive reactions are the same for the two pressures as shown in Fig. 3.17. This common result reinforces the idea that the decrease in ignition delay time is largely due to increased reactant concentrations at higher pressure, rather than a difference in the reactions controlling ignition. The most-inhibiting reaction for both pressures is $\dot{C}H_2OCH_2O_2H \rightarrow CH_2O + CH_2O + \dot{O}H$, while the most-promoting reaction for both pressures is $\dot{C}H_2OCH_2O_2H + O_2 \rightleftarrows \dot{O}_2CH_2OCH_2O_2H$.

Figure 3.18 shows flux analyses at a temperature of 827 K for the two pressures presented in the sensitivity analyses. Both pressures show that DME is consumed by H-atom abstraction forming methoxymethyl radical. Methoxymethyl radical is consumed through three reactions:

$$\text{(1) } CH_3O\dot{C}H_2 \rightleftarrows \dot{C}H_3 + CH_2O$$
$$\text{(2) } CH_3O\dot{C}H_2 + O_2 \rightarrow CH_2O + CH_2O + \dot{O}H$$
$$\text{(3) } CH_3O\dot{C}H_2 + O_2 \rightleftarrows CH_3OCH_2\dot{O}_2$$

At both pressures of 12.4 and 24.7 atm, the dominant reaction is R3. At 24.6 atm 11.1% more of the methoxymethyl radical is consumed via R3 compared to 12.4 atm. The methoxymethyl radical can react via the chemically activated reaction (R2) so that at lower pressure, chemically activated $CH_3OCH_2\dot{O}_2$ radicals are formed and decompose directly to products. Figure 3.18 supports this idea because at 12.4 atm, 2.4% more of the methoxymethyl radical is consumed by R2 when compared to 24.6 atm. A similar trend is observed for the consumption of $CH_3OCH_2\dot{O}_2$ radicals. In previous models [49–51] these chemically activated reactions were not considered.

The sensitivity analyses indicates that the fate of the $\dot{C}H_2OCH_2O_2H$ radical is all important as it is associated with the two most sensitive reactions, R4 and R5:

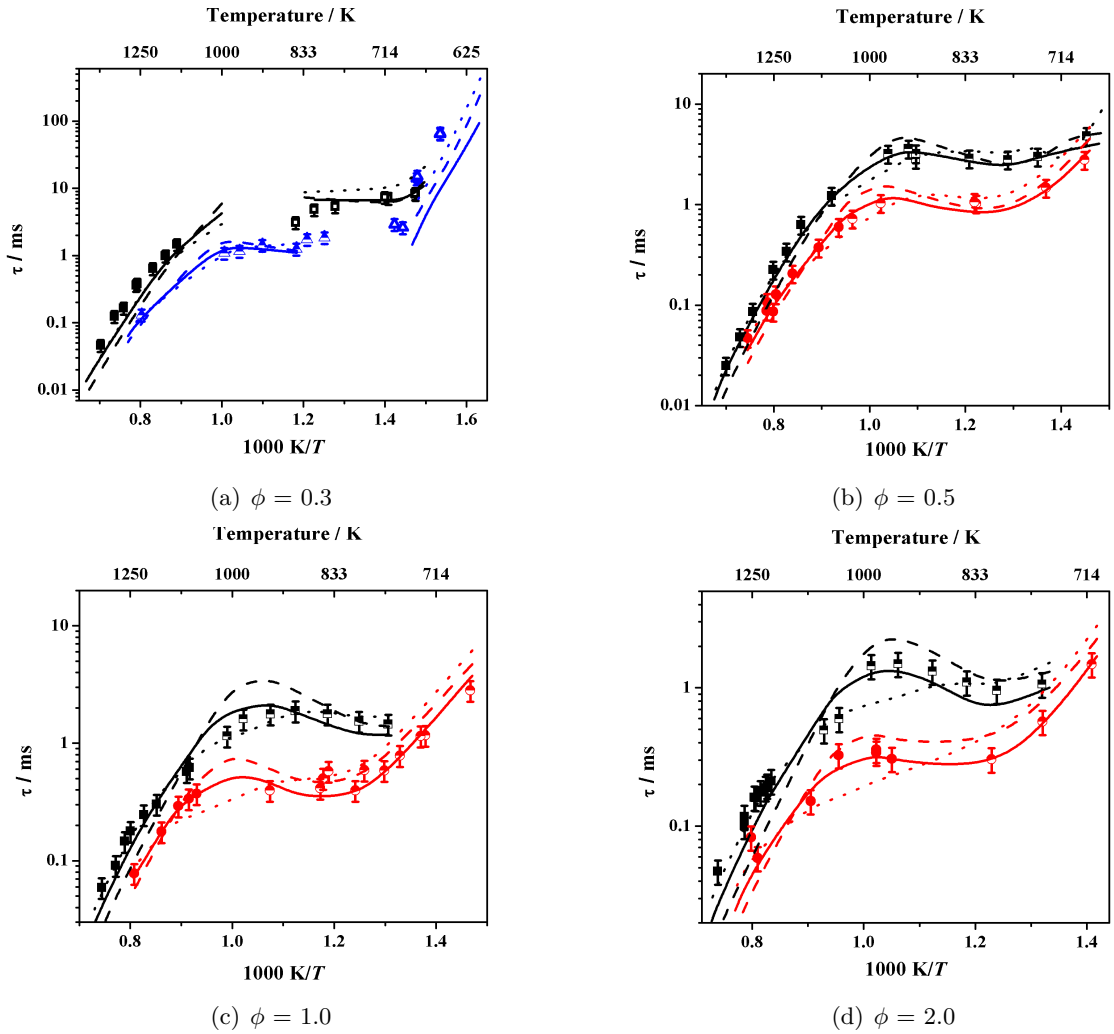

Figure 3.16: Influence of pressure on DME mixtures, ■ – ∼ 11 atm, ● – ∼ 25 atm, ▲ – ∼ 30 atm. Open symbols are RCM data, filled symbols ST data, half-filled symbols are ST data measured during *this study*. Solid lines – Mech_56.54, dashed lines – Zhao *et al.* [51], dotted lines – Fischer/Curran *et al.* [49, 50].

(4) $\dot{C}H_2OCH_2O_2H \rightarrow CH_2O + CH_2O + \dot{O}H$
(5) $\dot{C}H_2OCH_2O_2H + O_2 \rightleftarrows \dot{O}_2CH_2OCH_2O_2H$

R4 is the most-inhibiting reaction, while R5 is the most-promoting reaction. R4 inhibits reactivity as it produces two stable formaldehyde molecules and one hydroxyl radical, whereas R5 leads to the formation of $\dot{O}_2CH_2OCH_2O_2H$ radicals, which ultimately lead to chain branching, the production of two hydroxyl radicals.

Figure 3.18 shows that, under the conditions analyzed, the $\dot{C}H_2OCH_2O_2H$ radical is consumed predominantly via R4. The formaldehyde produced competes with DME for hydroxyl radicals, and this leads to decreased reactivity. In Fig. 3.19, ignition delay times for pure DME are compared as a function of equivalence ratio ($\phi = 0.3 - 2.0$ in 'air') for two pressures. Ignition delay times decrease with increasing equivalence ratio over all temperatures and pressures presented. As equivalence ratio increases, so too does the temperature at which NTC behavior begins.

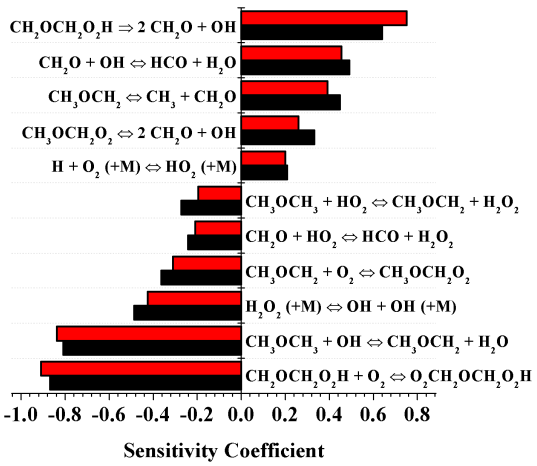

Figure 3.17: Sensitivity analysis at 827 K and $\phi = 0.50$ at ■ – 12.4 atm, ■ – 24.7 atm.

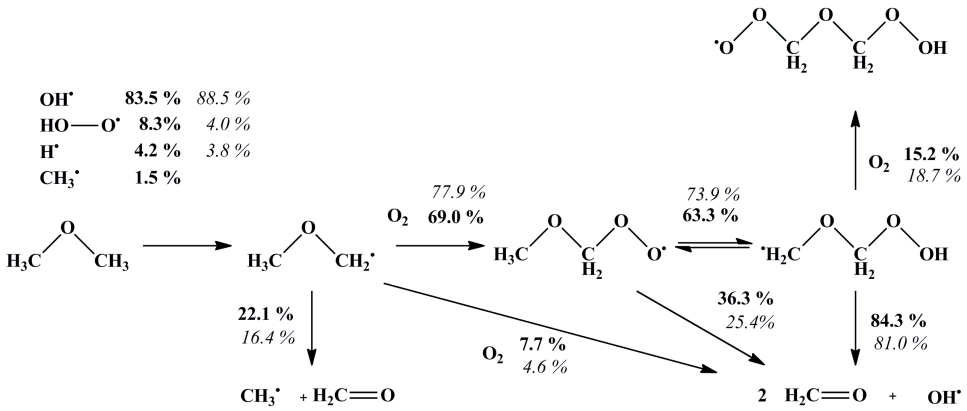

Figure 3.18: Flux analyses at 827 K and $\phi = 0.50$, 12.4 atm – bold font, 24.7 atm – italic font.

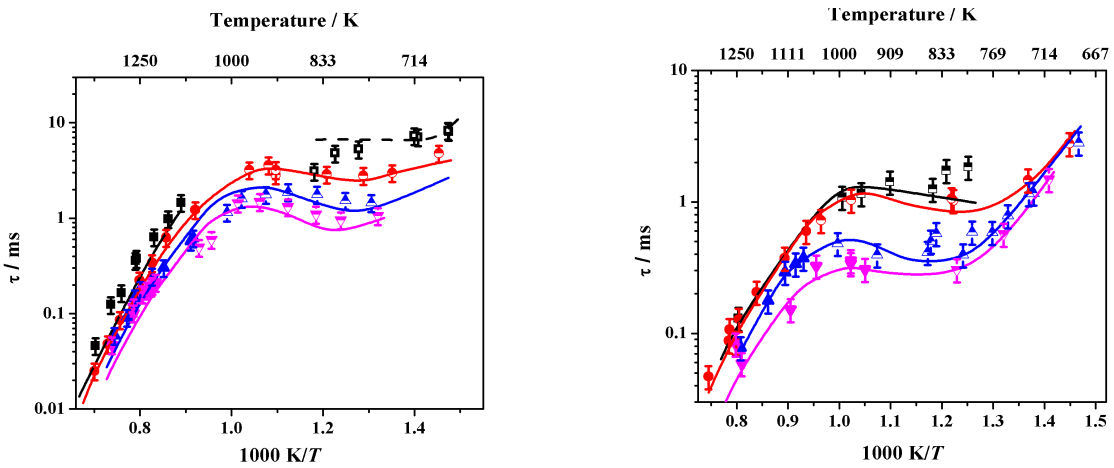

(a) 11 atm

(b) 25–30 atm

Figure 3.19: Influence of equivalence ratio for DME mixtures. ■ – $\phi = 0.3$, ● – $\phi = 0.5$, ▲ – $\phi = 1.0$, ▼ – $\phi = 2.0$. Open symbols are RCM data, filled symbols ST data, half-filled symbols are ST data measured during *this study*. Lines are Mech_56.54 predictions, dashed lines are simulations accounting for RCM facility effects.

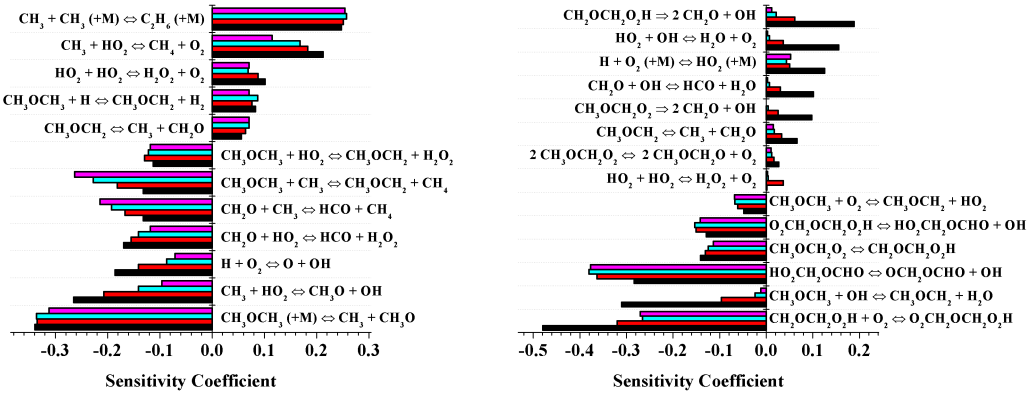

(a) 1250 K

(b) 670 K

Figure 3.20: Sensitivity analyses at $p = 10$ atm and at ■ – $\phi = 0.3$, ■ – $\phi = 0.5$, ■ – $\phi = 1.0$, ■ – $\phi = 2.0$.

Sensitivity analyses were performed at low (670 K) and high (1250 K) temperatures for mixtures corresponding to Fig. 3.19(a). In contrast to the analyses for pure methane oxidation, the reactions controlling DME ignition at the two temperatures are very different. For example, sensitivity analyses for pure methane showed that at both low and high temperatures, methyl radicals combination was the most inhibiting reaction. In contrast, DME shows methyl radicals combination is only sensitive at high temperatures. At low temperatures, the most-inhibiting reaction is $\dot{C}H_2OCH_2O_2H \rightarrow CH_2O + CH_2O + \dot{O}H$ as it competes with the $\dot{C}H_2OCH_2O_2H$ radical addition to molecular oxygen, which subsequently proceeds to chain branching. This reaction is seen to be highly promoting for all four equivalence ratios at low temperatures (600−900 K). It is the most-promoting reaction for $\phi = 0.3$ in 'air' and the second most-promoting reaction for the other three equivalence ratios. The most-promoting reaction at $\phi = 0.5$, 1.0 and 2.0 in 'air' is $HO_2CH_2OCHO \rightleftarrows \dot{O}CH_2OCHO + \dot{O}H$. This reaction produces two radical species from one stable molecule, and thus it has a promoting effect on ignition. An interesting note is that all the reactions associated with DME low-temperature chemistry (listed in Table 3.5) are highlighted as being important in the low-temperature sensitivity analyses.

The most-inhibiting reaction for pure DME at high temperatures is methyl radicals combination, similar to pure methane and the two CH_4/DME blends. The most-promoting reaction for all equivalence ratios is unimolecular decomposition, $CH_3OCH_3(+M) \rightleftarrows CH_3\dot{O} + \dot{C}H_3(+M)$. Another highly promoting reaction is $CH_3OCH_3 + \dot{C}H_3 \rightleftarrows CH_3O\dot{C}H_2 + CH_4$, highlighting the importance of methyl radical chemistry in DME oxidation at high temperatures.

In order to further evaluate the low-temperature reaction kinetics of DME oxidation the current model was compared against the first stage ignition delay time data of Sung and Mittal [65]. Comparing the model predictions against first stage ignition delay times enables the evaluation of the performance of the low-temperature reaction kinetics as the exothermic release in heat which increases the temperature after first stage ignition is omitted and therefore the kinetics controlling the first ignition delay times of DME is solely due to the low-temperature reactions of DME discussed earlier.

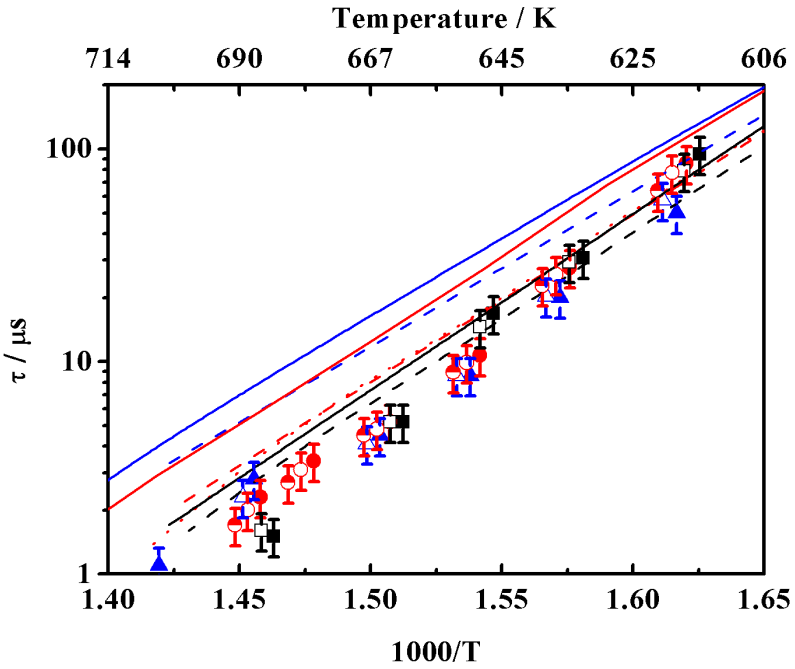

Figure 3.21: First stage ignition delay times for a range of compressed pressures and equivalence ratios. ■ – $\phi = 0.43$, ● – $\phi = 0.75$, ▲ – $\phi = 1.50$, filled symbols - 10bar, open symbols - 15 bar, half-filled symbols - 20bar. Lines are Mech_56.54 predictions, all simulations account for RCM facility effects.

The first observation to be noted from Fig. 3.21 is the fact that the experimental data show no clear effect of pressure or equivalence ratio on ignition delay time. The model however shows that first stage ignition delay time decreases with increasing pressure and that it also decreases with decreasing equivalence ratio. The simulations using Mech_56.54 show reasonable agreement with the measured first stage ignition delay times, with the exception of $\phi = 0.75$ and 1.50, $p_c = 10$bar and $\phi = 1.50$, $p_c = 15$ bar.

3.6.5 Influence of Mixture Composition

The comparison of the ignition delay times of the four mixture compositions studied is shown in Fig. 3.22 for pressures of 7 to 10 atm. This comparison shows that as DME concentration increases, ignition delay time decreases over the whole temperature range of this study. Mech_56.54 predicts all experimental data very well. The mechanism in particular predicts the decrease in ignition delay time as the mixture composition changes.

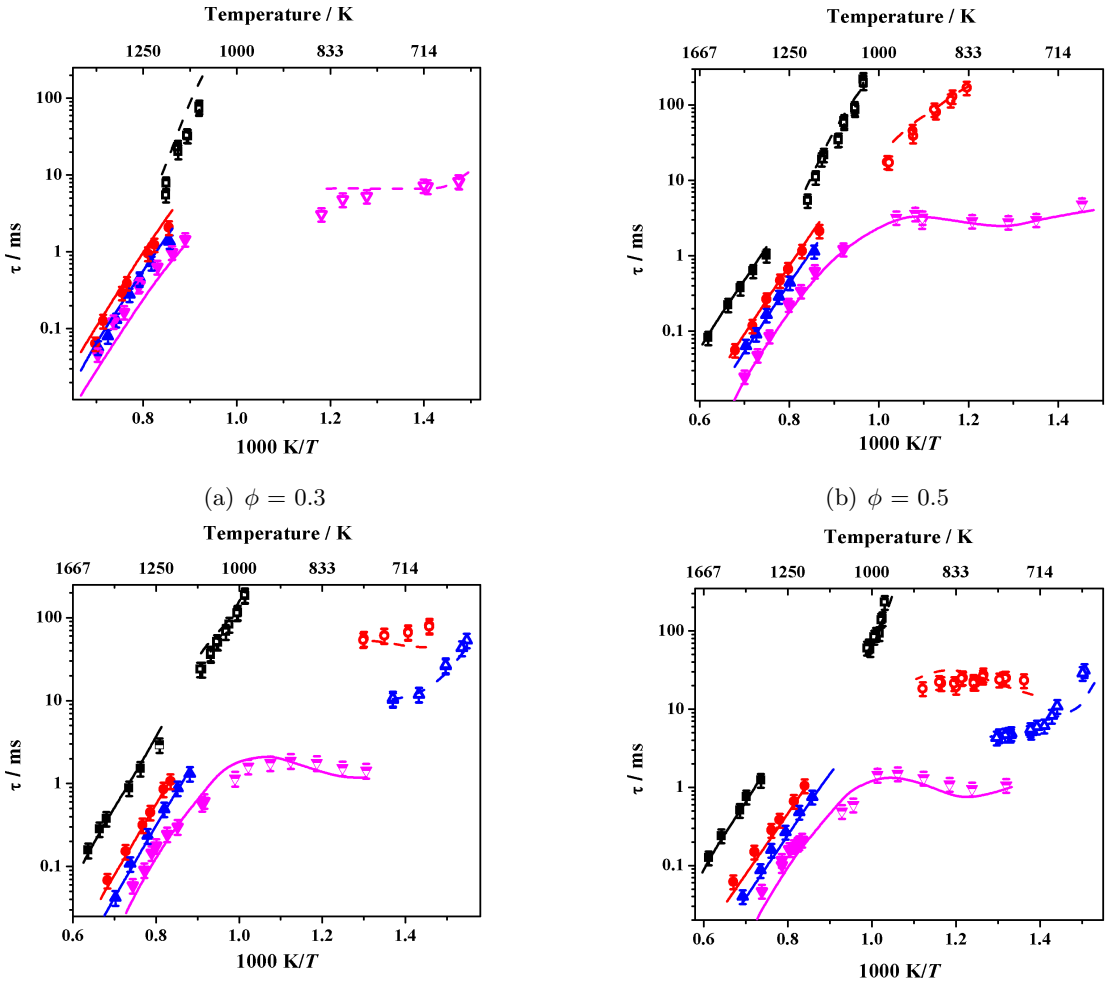

Figure 3.22: Influence of mixture composition at $p = 7 - 10$ atm, ■ – CH_4, ● – 80/20 CH_4/DME, ▲ – 60/40 CH_4/DME, ▼ – DME. Open symbols are RCM data, filled symbols ST data, half-filled symbols are ST data measured during *this study*. Lines are Mech_56.54 predictions, dashed lines are simulations accounting for RCM facility effects.

As has been stated previously, it is the reactions of DME which control the ignition of the blends even though there is a greater concentration of methane. This importance of DME concentration shows how the addition of small amounts of DME allows the radical pool to build at lower temperatures and therefore increase the rate of methane combustion. To quantify this effect, at approximately 1361 K in Fig. 3.22(c) at $\phi = 1.0$ the ignition delay time for pure methane is 884 μs; for 80/20 it is 152 μs; for 60/40 it is 108 μs; and for pure DME it is 59 μs. So ignition delay time is reduced by a factor of 5.8 when just 20% DME is added to methane.

Figure 3.23 shows sensitivity analyses for different mixture compositions presented in Fig. 3.22(c) at $\phi = 1.0$ and at 1237 K. Methyl radicals combination is again the most-inhibiting reaction over all mixture compositions, as discussed earlier. As has also been discussed previously, both blends show high sensitivity to reactions involving DME and methyl radicals.

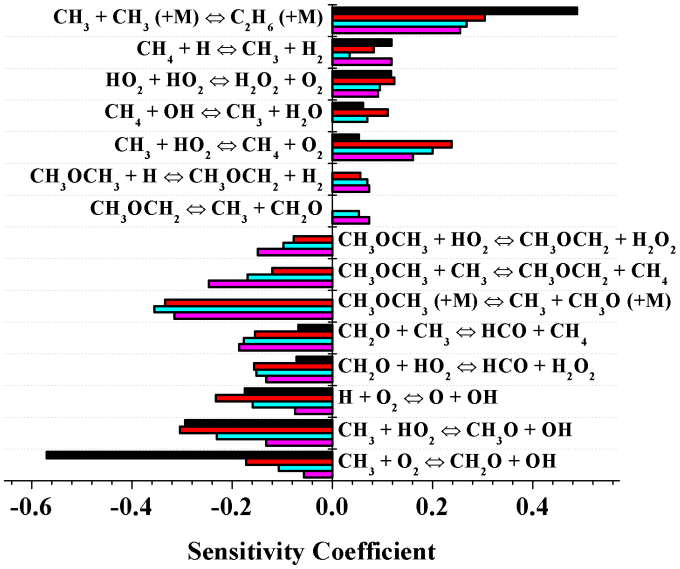

Figure 3.23: Sensitivity analyses at 1237 K and $\sim$ 10 atm. Comparing mixture composition. ■ – CH_4 (9.4 atm), ■ – 80/20 CH_4/DME (7.7 atm), ■ – 60/40 CH_4/DME (7.3 atm), ■ – DME (11.4 atm).

In summary, as the DME concentration increases, the ignition delay times decrease. The addition of DME to methane enhances the reactivity of methane by increasing radical production at low temperature through DME's chain branching pathway, and through its unimolecular decomposition and relatively fast H-atom abstraction rate constants at high temperature.

3.7 Conclusions

A wide range of new ignition delay time data for pure methane, pure DME, 80/20, and 60/40 methane/DME mixtures in 'air' are presented. Pressures from 7 to 41 atm were studied in the temperature range $600-1600$ K. These data allow for mechanism validation under conditions similar to those found in compression ignition engines and gas turbines, where methane and DME have been burned previously. A new detailed chemical kinetic model (Mech_56.54) for the combustion of DME is presented and validated with the new data and data available in literature (Flow reactor; JSR; RCM; shock-tube ignition delay time and shock-tube speciation; flame speeds and flame speciation). The new model utilises AramcoMech1.3 [76], which had been well-validated previously, and is the first model to incorporate the calculations of Li *et al.* [80] and Yamada *et al.* [75]. It is able to predict the pure methane ignition delay times measured and presented here. It was found that, to accurately predict the ignition delay times of DME, the inclusion of a QRRK pressure-dependent treatment of the low-temperature oxidation reactions was important. In particular, the β-scission of the methoxymethyl radical showed significant pressure-dependent fall-off. RRKM/ME calculations were performed to calculate the pressure-dependent rate constants for the β-scission of the methoxymethyl radical.

The rate constants for unimolecular decomposition and H-atom abstractions by a variety of radical species from DME have been adopted from high-accuracy measurements and/or calculations where possible in Mech_56.54. The use of these calculated rate constants and the application of pressure-dependent rate constants for the low-temperature reactions of DME is an important improvement to its chemical kinetic mechanism. Further investigation into these low-temperature reactions would help to remove any remaining uncertainty in this chemical kinetic model. The new data presented in *this study* comprehensively covers a wide range of engine- and combustor-relevant conditions. Validation of the detailed chemical kinetic mechanism under these wide range of conditions presents an important improvement in the understanding of the combustion chemistry of DME due to its dominance in controlling the ignition behavior of its mixtures with methane.

Chapter 4

Methanol

4.1 Abstract

Two ST's and an RCM have been used to measure ignition delay times for methanol oxidation from 2 to 50 atm and at equivalence ratios of 0.5, 1.0, and 2.0. These measurements include dilute and 'fuel in air' conditions (1.5% to 21.9% methanol), over a temperature range of $820-1650$ K. The new data is compared to published studies and provides insight into compression ignition (CI) engine relevant conditions which are previously un-studied at pressures of 10, 20 and 50 atm. The data presented is compared to model simulations, using a detailed chemical kinetic mechanism. The high-pressure data is very sensitive to the rate constant of the reaction: $CH_3OH + H\dot{O}_2 \rightleftarrows \dot{C}H_2OH + H_2O_2$. A number of rate constants for this reaction have been estimated and calculated, and these differ significantly. We have simulated our data by replacing only the rate constant of this reaction with each recommended and/or calculated value in the chemical kinetic mechanism. The effect of the rate constants on predicting ignition delay times are evaluated and the rate constant providing optimum agreement with the experimental data available for model validation is adopted. The need for a direct measurement of this important reaction rate constant is highlighted in order to further improve detailed chemical kinetic modeling efforts.

4.2 Introduction

The demand for a change in the way we consume and produce our energy has been motivated by increasing climate change due to the release of CO_2 into the atmosphere by burning fossil fuels leading to warming of the planet. Our energy demands will continue to increase into the future, and it is important that we now put systems in place that will allow us to begin to move away from our dependence on traditional fossil fuels. Methanol produced from sources such as lignocellulosic biomass, carbon capture technologies [97] and algae make methanol potentially viable as a renewable energy resource. The main production route for methanol currently is from syngas. The main drawback to methanol, when compared to gasoline, is its low energy density and corrosivity, as mentioned in the introduction of *this study*. For this reason much emphasis is now being placed in looking at longer chain alcohols. Chemical kinetic mechanisms can provide insight into which of these alcohols best lends itself to replacing gasoline in SI engines.

These mechanisms are built in a hierarchical manner, and because of this it is important to understand the simplest alcohol, methanol, if accurate mechanisms for longer chain

alcohols are to be developed. Data such as the ST and RCM ignition delay times presented in this paper are extremely useful in the validation of these mechanisms, and though there is a large quantity of previously published data on methanol there is a lack of high-pressure data, especially at low temperatures. If alcoholic compounds are to be considered as alternatives to gasoline in SI and CI engines, then data to represent these fuels at the conditions within an engine, such as high pressures ($10-50$ atm) are needed to allow for confidence in the predictive power of chemical kinetic mechanisms under these conditions.

Several existing studies, which are listed in Table 4.1, have investigated the ignition characteristics of methanol. Cooke *et al.* [98] investigated ignition delay times for stoichiometric mixtures of methanol (and ethanol) in the temperature range of $1570-1870$ K and measured the ignition delay time using both $CH^\star$ and $OH^\star$ emission. Bowman [99] studied the oxidation of methanol behind reflected shock waves in the temperature range of $1545-2180$ K and at reflected shock pressures of $1.5-4.2$ atm while ignition delay time was defined at the attainment of the maximum concentration of CO and O-atom concentrations. Tsuboi and Hashimoto [100] measured CH_3OH, H_2O, CO_2, CO and CH_2O profiles behind reflected shock waves for a variety of mixtures in Ar. All these early studies were conducted under highly dilute conditions. Fieweger *et al.* [101] studied the self-ignition characteristics of several fuels including stoichiometric methanol in 'air' mixtures at pressures of 13 and 40 bar and temperatures of approximately $800-1200$ K, the authors used CH-band emissions and the maximum rate of change of pressure to define the ignition delay time. Noorani *et al.* [102] studied the high temperature ignition of C_1-C_4 straight chain alcohols at 2, 10 and 12 atm. The authors used $CH^\star$ emissions to measure the ignition delay time. The only RCM study of methanol oxidation to date was performed by Kumar and Sung [103]. This study covered compressed pressures from $7-30$ bar over a temperature range of $850-1100$ K, for equivalence ratios of $0.25-1.0$ diluted in 'air' using Ar as the bath gas. The ignition delay definition used was the maximum rate of pressure increase.

Dayma *et al.* [104] studied the oxidation of methanol in the absence and in the presence of NO or NO_2 in a JSR at 10 atm. The authors reported species concentrations for CH_3OH, NO, NO_2, CO, CO_2 and CH_2O.

Cathonnet *et al.* [105] performed pyrolysis experiments using a static reactor. The study was conducted at pressures of $0.3-0.5$ atm over a temperature range of $875-975$ K.

Methanol oxidation has been studied several times [106–108] in flow reactors. Aronowitz *et al.* [106] performed experiments on methanol oxidation at atmospheric pressure, in the initial temperature and equivalence ratio ranges of $950-1030$ K and $0.03-3.16$, respectively. Norton and Dryer [107] performed detailed methanol oxidation experiments using a turbulent flow reactor at equivalence ratios ranging from $0.6-1.6$ and at initial temperatures from $1025-1090$ K at atmospheric pressure. Held and Dryer [108] reported species profiles for the fuel products and intermediates at 1 and 10 atm at initial temperatures of $810-1043$ K.

Other flow reactor studies include investigations by Alzueta *et al.* [109], Ing *et al.* [110], Rasmussen *et al.* [111] and Aranda *et al.* [112]. Alzueta *et al.* studied the oxidation of methanol in the absence and in the presence of NO in a flow reactor, performing the experiments at atmospheric pressure in the temperature range $700-1500$ K. Ing *et al.* [110] reported experimental data of methanol in a flow reactor under pyrolysis and oxidation conditions. Methanol pyrolysis was studied at 1073 K over a pressure range of $1-10$ atm while oxidation experiments were conducted over a temperature range of $873-1073$ K and a pressure range of $1-5$ atm. Rasmussen *et al.* [111] also studied the oxidation of methanol in a flow reactor with and without the presence of NO in a temperature range

of $650-1350$ K. Recently Aranda *et al* [112] studied methanol oxidation at high pressures ($20-100$ atm) and low temperatures ($600-900$ K).

A stirred reactor study of methanol oxidation was conducted by Aniolek and Wilk [113] in 1995. This covered a temperature range of $650-700$ K and a pressure of 0.92 atm.

A low pressure flame speciation study was reported by Akrich *et al* [114]. Measuring the species of CH_3OH, O_2, H_2O, CO_2, CO and H_2 as a function of distance from the burner.

Egolfopoulos *et al.* [115] measured laminar flame speeds for methanol at 1 atm at $298-368$ K using the counterflow twin flame technique. Liao *et al.* [116] reported laminar burning velocities using the spherical combustion bomb technique for mixtures of methanol and "air" at 358 K. Veloo *et al.* [117] experimentally determined the laminar flame speed of methanol using the counterflow configuration technique at atmospheric pressure and an unburned mixture temperature of 343 K. Vancoillie *et al.* [118] reported laminar flame speed measurements at atmospheric pressure for methanol in 'air' mixtures at unburned gas temperatures of $298-358$ K using the heat flux method.

Table 4.1: Experimental data for the pyrolysis and oxidation of methanol.

Study	Reactor Type	Temperature Range, K	Pressure Range, atm	ϕ Range	Ref.
Oxidation	Shock Tube	$1570-1870$	1.00	1.0	[98]
Oxidation	Shock Tube	$1545-2180$	$1.5-4.2$	$0.38-6.0$	[99]
Oxidation	Shock Tube	$1200-1800$	$0.02-0.71$	$0.2-2.0$	[100]
Oxidation	Shock Tube	$800-1200$	13, 40	1.0	[101]
Oxidation	Shock Tube	$1068-1776$	$2-12$	$0.5-2.0$	[102]
Oxidation	RCM	$850-1100$	$6.91-29.61$	$0.25-1.0$	[103]
Oxidation	JSR	$700-1090$	10	$0.3-1.0$	[104]
Pyrolysis	Static Reactor	$875-975$	$0.3-0.5$	–	[105]
Oxidation	Flow Reactor	$950-1030$	1.0	$0.03-3.13$	[106]
Oxidation	Flow Reactor	$1025-1090$	1.0	$0.6-1.6$	[107]
Oxidation	Flow Reactor	$810-1043$	$1-10$	$0.6-1.6$	[108]
Oxidation	Flow Reactor	$700-1500$	1.0	$0.07-2.7$	[109]
Oxidation	Flow Reactor	$873-1073$	$1-5$	$0.75-1.0$	[110]
Pyrolysis	Flow Reactor	1073	$1-10$	–	[110]
Oxidation	Flow Reactor	$650-1350$	1.0	$0.004-0.08$	[111]
Oxidation	Flow Reactor	$600-900$	$20-100$	$4.35-0.06$	[112]
Oxidation	Stirred Reactor	$650-700$	0.92	$0.5-1.5$	[113]
Flame Speciation	Flat Flame	298	0.11	$0.77-1.53$	[114]
Flame Speed	Counterflow	$298-368$	1.0	$0.5-2.0$	[115]
Flame Speed	Spherical Bomb	358	1.0	$0.7-1.4$	[116]
Flame Speed	Counterflow	343	1.0	$0.7-1.5$	[117]
Flame Speed	Heat Flux	$298-343$	1.0	$0.7-1.5$	[118]

A tabulated list of the experimental measurements is shown in Table 4.1. A selection of these studies provide the validation for the detailed chemical kinetic model presented in *this study*, Mech_56.55.

What is absent for the most part in the previous studies is validation for engine relevant conditions at pressures in the range $10-50$ atm and at temperatures of $800-1600$ K. *This study* provides a comprehensive set of data in this regime and covers low- to high-temperature chemistry, coupling both ST and RCM measurements for the first time for methanol oxidation.

The high pressure and low temperature conditions of *this study* also act as a guide towards the assignment of the rate constant for the reaction:

$$CH_3OH + H\dot{O}_2 \rightleftarrows \dot{C}H_2OH + H_2O_2$$

This rate constant has previously been calculated theoretically in 2010 by both Klippenstein *et al.* [119] and Altarawneh *et al.* [120], these two calculations differ significantly. While the recent calculation of this rate constant by Alecu *et al.* [121] provides another alternative value.

This study tests the detailed chemical kinetic model Mech_56.55 using the available calculated rate constants for this reaction and recommends the one that can best-predict our present data in addition to the other validation targets. *This study* also highlights the need for a direct measurement of this rate constant in order to improve and increase confidence in the detailed chemical kinetic models.

4.3 Experimental

Methanol was obtained from Sigma Aldrich $\geqslant$ 99.8% purity and Tokyo Chemicals Industry $\geqslant$ 99.5% purity. All other gases were supplied by BOC Ireland; nitrogen (CP Grade) $\geqslant$ 99.95%, argon (Research Grade) $\geqslant$ 99.9995%, oxygen (Medical Grade) $\geqslant$ 99.5% and all of these were used without further purification.

The test mixtures were prepared in stainless steel mixing vessels using partial pressures to determine the volumetric percentage of each constituent to within 1% of their reported value. Test mixtures were allowed to mix overnight before use to ensure homogeneity. This method has been discussed in detail in Sections 2.3.1 and 2.3.2. Sections 2.1.3 and 2.1.4 outline the method of measuring the ignition delay times in the high and low pressure shock tubes for *this study*.

Table 4.3 presents the range of mixtures studied herein. The experimental results are available in Appendix B.1.

Table 4.2: Experimental data sets studied. % Molar volumes of each constituent.

Mixture	%CH_3OH	%O_2	%N_2	%Ar	ϕ	Average p / atm
1	5.00	15.00	80.00	0.00	0.5	20.00
2	6.54	19.62	73.84	0.00	0.5	49.61
3	2.85	8.55	66.45	22.15	0.5	29.07
4	2.85	8.55	66.45	22.15	0.5	39.10
5	8.00	12.00	80.00	0.00	1.0	20.00
6	12.28	18.43	69.29	0.00	1.0	30.88
7	12.28	18.43	69.29	0.00	1.0	49.27
8	5.70	8.55	0.00	85.75	1.0	10.18
9	5.70	8.55	0.00	85.75	1.0	49.18
10	5.70	8.55	64.31	21.44	1.0	9.37
11	5.70	8.55	64.31	21.44	1.0	30.10
12	5.70	8.55	64.31	21.44	1.0	38.65
13	3.10	4.65	0.00	92.25	1.0	10.12
14	21.88	16.41	0.00	61.71	2.0	1.96
15	21.88	16.41	61.71	0.00	2.0	50.95
16	11.40	8.55	60.04	20.01	2.0	29.52
17	11.40	8.55	60.04	20.01	2.0	40.04

4.4 Results and Discussion

4.4.1 New Ignition Delay Time Measurements

Experimental ignition delay times were measured at the same condition as previously published by Noorani *et al.* [102]. These measurements served as validation for the experimental methods utilised here, Fig. 4.1. Good agreement is observed between *this data* and that of Noorani *et al.* [102]. One of the major differences between *this study* and previous methanol ignition delay time studies such as those presented by Kumar and Sung [103] and Noorani *et al.* [102] is the coupling of measurements from two experimental facilities, both RCM and ST measurements.

Figure 4.2(a) shows ignition delay times for mixtures of 5.7% CH_3OH and 8.55% O_2 at $\phi = 1.0$, and $p = 10$ atm (Mixes 8 and 10, ST and RCM respectively). The data taken in the ST and those taken in the RCM complement and agree well with one another. This coupling of data taken in both facilities allows us to study a much wider range of times and thereby temperatures than has previously been studied. We have also measured data at a wide range of pressures, 2, 10, 30, 40 and 50 atm, with varying dilution.

Figure 4.2(b) shows data taken at 5.7% CH_3OH and 8.55% O_2 at $\phi = 1.0$, and at pressures of 10 and 50 atm (Mixes 8 and 9 respectively). The observed effect of pressure is as expected, with increasing pressures leading to a reduction in ignition delay times due to the corresponding increase in reactant concentration. Mech_56.55 has been used to simulate this data with which it agrees well.

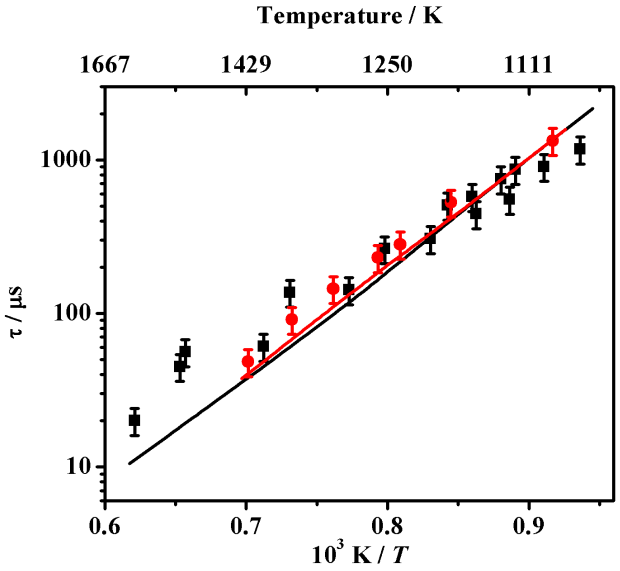

Figure 4.1: 3.10% CH_3OH, 4.65% O_2 (Mixture 13), $\phi = 1.0$ at $p = 10$ atm. ■ – Noorani *et al.* [102], ● – *This study*. Lines are Mech_56.55 predictions.

The effect of equivalence ratio was also studied. Figure 4.3(a) presents data for 2.85, 5.7 and 11.4% CH_3OH with 8.55% O_2 ($\phi = 0.5$, 1.0 and 2.0) at pressures of 30 (Mixes 3, 11 and 16) and 40 atm (Mixes 4, 12 and 17). The experimental data shows that ignition delay times decrease as the equivalence ratio and pressure increases and Mech_56.55 reproduces well the experimental data.

Figure 4.3(b) shows a comparison of the Li *et al.* [122] mechanism, Mech_56.55 and the experimental data at 40 atm. It is observed that the Li *et al.* [122] mechanism predicts ignition delay times that are slower compared to the experimental data and the Mech_56.55 predictions. Flux analyses have been performed at the point of 20% fuel consumed to compare the mechanism of oxidation predicted by these two models, shown in Fig. 4.4. Both models indicate that the fuel is consumed *via* H-atom abstraction reactions, and also that this is mainly *via* abstraction by hydroxyl radicals. However, abstraction can occur at two different sites; abstraction from the methyl site produces hydroxyl-methylene ($\dot{C}H_2OH$) radical while abstraction of the alcoholic H-atom produces methoxy ($CH_3\dot{O}$) radicals. The Li *et al.* [122] mechanism predicts that 23.3% of CH_3OH is consumed to produce $CH_3\dot{O}$ radicals whereas Mech_56.55 only predicts 4.0% consumption via this route, with the majority producing $\dot{C}H_2OH$ radicals. The Li *et al.* [122] mechanism utilizes the rate constants proposed by Bott and Cohen [123] while Mech_56.55 uses the more recent calculations by Xu and Lin [124]. H-atom abstraction by $\dot{H}$ atoms also differs between the two models with the mechanism of Li *et al.* [122] using the rate constants proposed by Warnatz *et al.* [125] and Mech_56.55 using the recent calculations of Meana-Pañeda *et al.* [126]. Once again these different rate constants change the predictions of the amount of CH_3OH consumed by the reactions shown in Fig. 4.4.

These two models differ in the sub-mechanism chemistry also. Incorporated into Mech_56.55 is the recent modeling studies of Kéromnès *et al.* [127] (H_2/CO sub-mechanism), Metcalfe *et al.* [76] (C_1-C_2 sub-mechanism) and Burke *et al.* [128] (Propene sub-mechanism). These studies are all part of the ongoing development of a comprehensive C_0−C_4 mechanism. Of particular importance to the mechanism of methanol oxidation under the conditions presented in *this study* is the H_2/CO sub-mechanism, and the recent publication

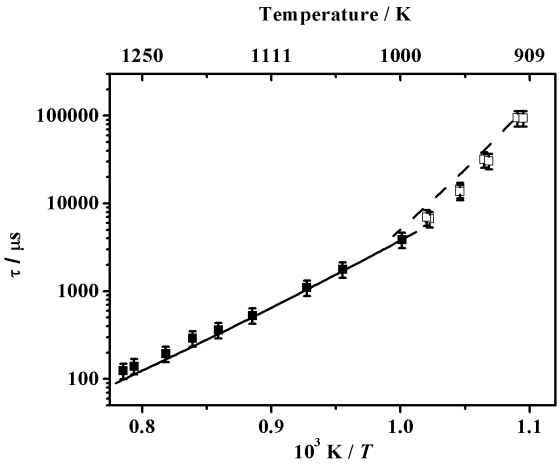

(a) ST and RCM Data

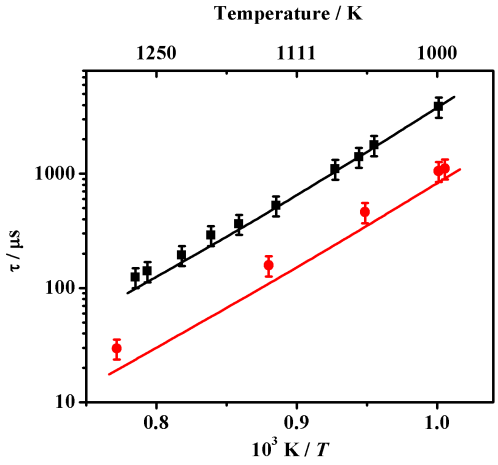

(b) Influence of Pressure

Figure 4.2: 5.70% CH_3OH, 8.55% O_2, $\phi = 1.0$. (a) $p = 10$ atm. Open symbols correspond to RCM data (Mixture 10), filled symbols correspond to ST data (Mixture 8). Lines represent Mech_56.55 predictions. (b) ■ – $p = 10$ atm (Mixture 8), ● – $p = 50$ atm (Mixture 9). Lines represent Mech_56.55 predictions.

of Olm *et al.* [129] which statistically compared a variety of H_2/CO sub-mechanisms concluded that the model of Kéromnès *et al.* [127] ranked highest. It was for these reasons that Mech_56.55 was used to carry out the subsequent model analysis in *this study*.

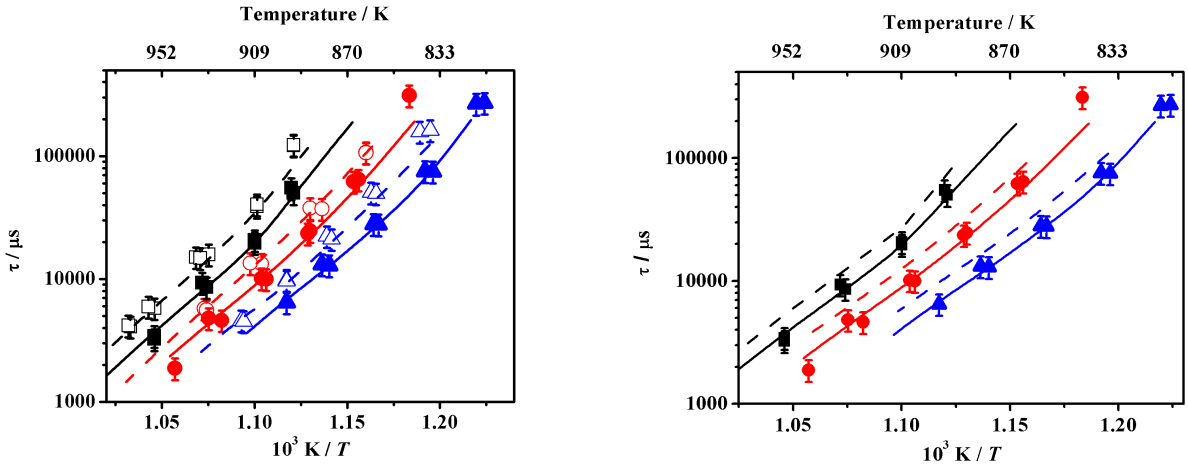

(a) Influence of ϕ and pressure.

(b) Comparison of model predictions.

Figure 4.3: (a) CH_3OH with 8.55% O_2, open symbols – $p = 30$ atm (Mixes 3, 11 and 16), solid symbols – $p = 40$ atm (Mixes 4, 12 and 17). ■ – $\phi = 0.5$, ● – $\phi = 1.0$, ▲ – $\phi = 2.0$. Lines represent Mech_56.55 predictions, dashed lines – $p = 30$ atm, solid lines – $p = 40$ atm. (b) CH_3OH with 8.55% O_2 $p = 40$ atm, solid lines – Mech_56.55, dashed lines – Li *et al.*'s [122] mechanism. ■ – $\phi = 0.5$ (Mixture 4), ● – $\phi = 1.0$ (Mixture 12), ▲ – $\phi = 2.0$ (Mixture 17).

This study when compared to Mech_56.53 [128] published recently, has updated the rate constants for:

$$\text{(1) } CH_3OH + H\dot{O}_2 \rightleftarrows \dot{C}H_2OH + H_2O_2$$
$$\text{(2) } CH_3OH + H\dot{O}_2 \rightleftarrows CH_3\dot{O} + H_2O_2$$
$$\text{(3) } CH_3OH + O_2 \rightleftarrows \dot{C}H_2OH + H\dot{O}_2$$

Reaction (1) employs the calculation of Altarawneh *et al.* [120] with an increase to the activation energy (E_a) of 500 cal mol^{-1}. The calculations of Alecu *et al.* [121] and Klippenstein *et al.* [119] have been adopted for reactions (2) and (3), respectively. The assignment of the rate constant for reaction (1) in particular, is of vital importance when predicting the experimentally measured data. This will be discussed in detail later.

The effect of dilution is compared, 3.1 (Mixture 13), 5.7 (Mixes 8 and 9) and 12.28% (Mixture 7) CH_3OH ($\phi = 1.0$) in Fig. 4.5. Good agreement between the model and the experimental data is observed. The trend shows that the more dilute the mixture the longer the ignition delay time under a given temperature and pressure.

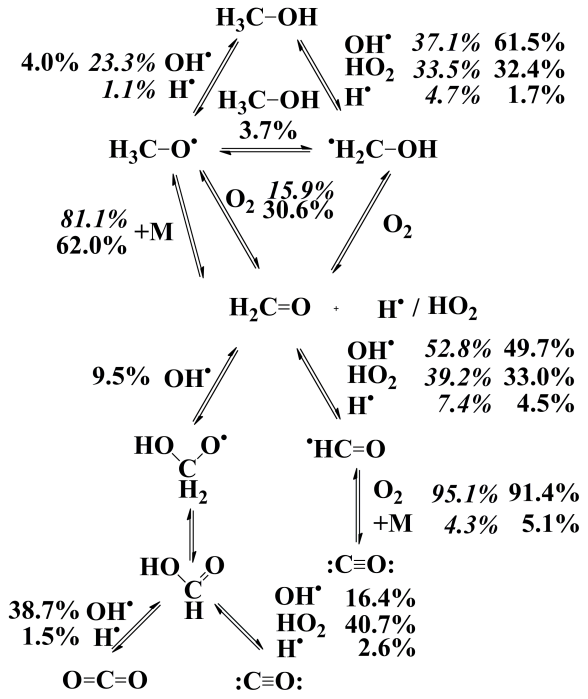

Figure 4.4: Flux analyses at 5.70% CH_3OH, 8.55% O_2, $\phi = 1.0$, $p = 38.4$ atm (Mixture 12), $T = 906$ K. Mech_56.55 – **Bold font**, Li *et al.*'s mechanism – *Italic font.*

Experimental data is compared as function of pressure, Fig. 4.6. Model predictions once again agree well with the experimental data. Note also the presence of pre-ignition in the data. This is a phenomenon which has been reported and discussed for methanol ignition studies presented previously by Fieweger *et al.* [101]. This effect causes inhomogeneous ignition and is only apparent for concentrated fuel in "air" mixtures at long residence times (> 1000 μs) in the ST as shown in Fig. 4.6. It was detected in *this study* through the presence of a noticeable yet gradual increase in pressure before the main ignition event. This pressure increase is independent of the usual ST facility effects caused by the boundary layer growth and chemical reaction.

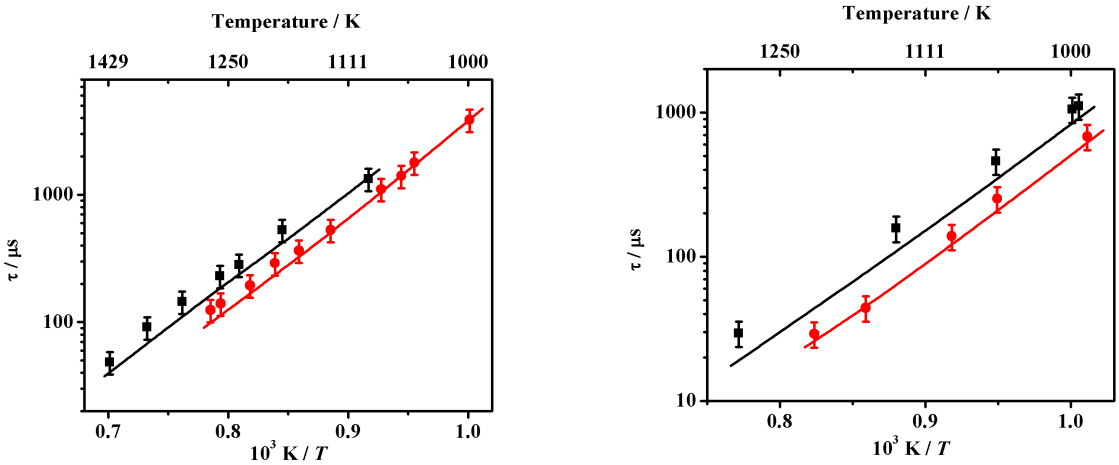

(a) $\phi = 1.0$, $p = 10$ atm

(b) $\phi = 1.0$, $p = 50$ atm

Figure 4.5: Influence of dilution. (a) ■ – 3.1% CH_3OH (Mixture 13), ● – 5.7% CH_3OH (Mixture 8). (b) ■ – 5.7% CH_3OH (Mixture 9), ● – 12.28% CH_3OH (Mixture 7). Lines are Mech_56.55 predictions.

An RCM is used to measure ignition delay times at low-temperatures, a temperature range where there is currently little or no experimental data available for model validation. Fig. 4.7(a) compares data as a function of pressure, while Fig. 4.7(b) compares data as a function of equivalence ratio. Mech_56.55 predictions can predict the data well despite being too slow for the $p = 10$ atm data in Fig. 4.7(a).

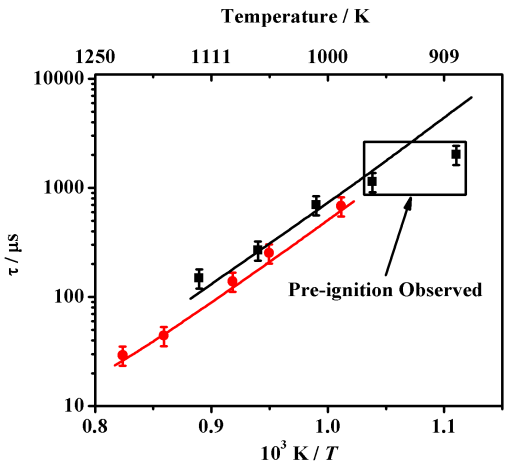

(a) $\phi = 1.0$, CH_3OH in "air"

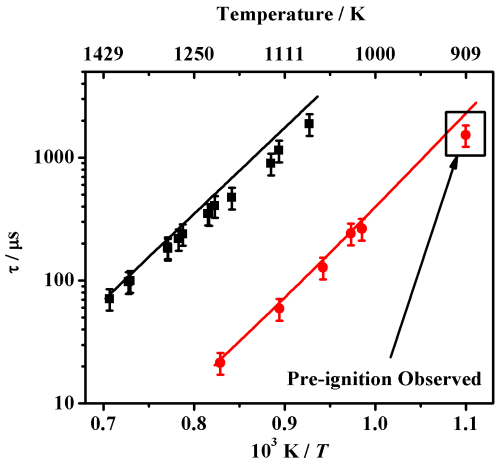

(b) $\phi = 2.0$, CH_3OH in "air"

Figure 4.6: Influence of Pressure. (a) ■ – $p = 30$ atm (Mixture 6), ● – $p = 50$ atm (Mixture 7). Lines represent Mech_56.55 predictions. (b) ■ – $p = 2$ atm (Mixture 14), ● – $p = 50$ atm (Mixture 15). Lines represent Mech_56.55 predictions.

Finally experimental ignition delay times have been measured for methanol in 'air' mixtures for $\phi = 0.5$, 1.0 and 2.0 (Mixes 2, 7 and 15 respectively) at 50 atm for the first time. These data are presented and compared to model predictions in Fig. 4.8. Mech_56.55's predictions agree well with the experimentally measured data.

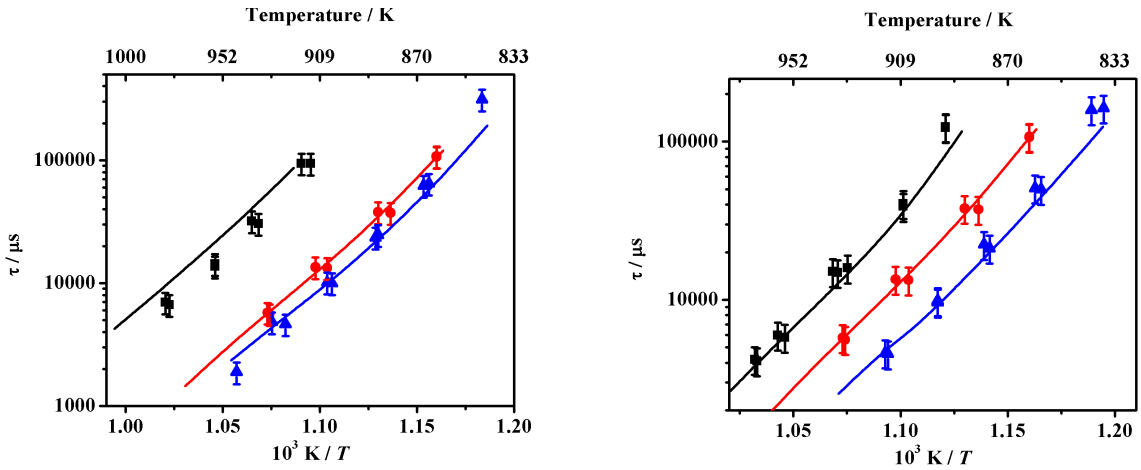

(a) 5.7% CH_3OH, 8.55% O_2, $\phi = 1.0$

(b) 8.55% O_2, $p = 30$ atm

Figure 4.7: Measured RCM ignition delay times. (a) Influence of pressures. ■ – $p = 10$ atm (Mixture 10), ● – $p = 30$ atm (Mixture 11), ▲ – $p = 40$ atm (Mixture 12). Lines represent Mech_56.55 predictions. (b) Influence of equivalence ratios. ■ – $\phi = 0.5$ (Mixture 3), ● – $\phi = 1.0$ (Mixture 11), ▲ – $\phi = 2.0$ (Mixture 16). Lines represent Mech_56.55 predictions.

4.4.2 H-Atom Abstraction by Hydroperoxyl Radical

As has been discussed earlier there is a wide range of ignition delay time studies of methanol oxidation available in the literature. There is however a dearth of experimental data when it comes to high pressures and in particular for low temperatures. Previous modeling efforts [76, 109, 122] have well characterized the oxidation mechanism of methanol. Using Mech_56.55 a sensitivity analysis was performed to identify the pertinent reactions at high-pressure and low-temperature conditions.

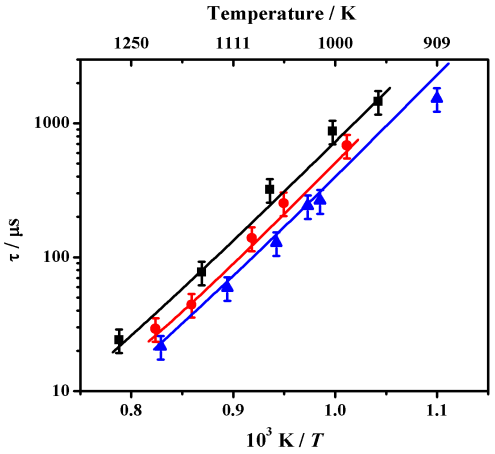

Figure 4.8: Influence of equivalence ratios, CH_3OH in "air", $p = 50$ atm. Lines represent Mech_56.55 predictions, ■ – $\phi = 0.5$ (Mixture 2), ● – $\phi = 1.0$ (Mixture 7), ▲ – $\phi = 2.0$ (Mixture 15).

The sensitivity analysis shows that the most sensitive reaction is $CH_3OH + H\dot{O}_2 \rightleftarrows \dot{C}H_2OH + H_2O_2$, Fig. 4.9(a). Figure 4.9(b) shows calculated and estimated rate constants available in the literature for this reaction. It is clear that there is still a great deal of uncertainty when it comes to the assignment of this rate constant.

The rate constants of Rasmussen *et al.* [111], Cathonnet *et al.* [105] and Metcalfe *et al.* [76] are all estimates used in detailed chemical kinetic models. While the rate constants of Alecu *et al.* [121], Altarawneh *et al.* [120] and Klippenstein *et al.* [119] are ab-initio calculations of this rate constant. The temperature range shown in Fig. 4.9(b) covers the temperature range in *this study*. At 1111 K there is a factor of 39 difference between the fastest rate constant on this plot of Rasmussen *et al.* [111] and the slowest Klippenstein *et al.* [119]. There is a difference of a factor of 3.5 between the two calculated rate constants of Alecu *et al.* [121] and Klippenstein *et al.* [119] at 1111 K. This difference between the calculations has been assigned to the different treatments of anharmonicity in the publication of Alecu *et al.* [121]. There is also a difference of a factor of 14.4 between the calculations of Klippenstein *et al.* [119] and Altarawneh *et al.* [120]. These three studies also calculated the rate constant for the reaction $CH_3OH + H\dot{O}_2 \rightleftarrows CH_3\dot{O} + H_2O_2$. While the three studies vary by over an order of magnitude for reaction (1) they are within a factor of 2.76 for the temperature range $800 - 1300$ K for reaction (2).

Mech_56.55 was the base mechanism used for all the analysis presented hereafter. The rate constant for $CH_3OH + H\dot{O}_2 \rightleftarrows \dot{C}H_2OH + H_2O_2$ was varied using the available rate constants for this reaction. The simulation results were compared to the measured experimental data. The first data used to compare to the simulation results was the $p = 40$ atm data presented in Fig. 4.3(b).

Four of the rate constants shown in Fig. 4.9(b) were used to simulate the data, the simulation results are shown in Fig. 4.10. The calculated rate constants of Alecu *et al.* [121], Klippenstein *et al.* [119] and Altarawneh *et al.* [120], and the estimation of and Cathonnet *et al.* [105]. The results show that using the two calculated rate constants of Alecu *et al.* [121] and Klippenstein *et al.* [119] results in the simulated ignition delay times being too slow compared to the experimental measurements. Reasonable agreement is observed when the estimated rate constant of Cathonnet *et al.* [105] is used to simulate the data. While the calculation of Altarawneh *et al.* [120] yields results that are too fast. These

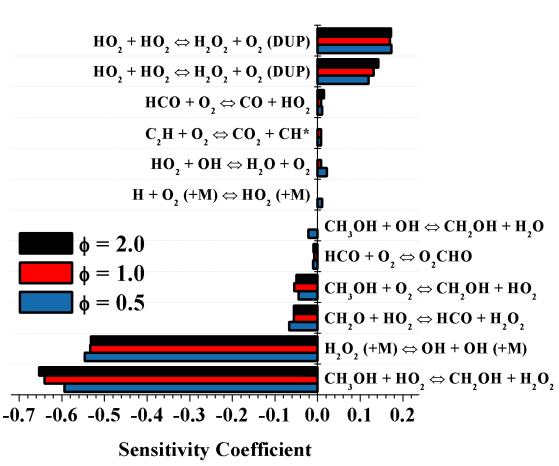

(a) Sensitivity analysis

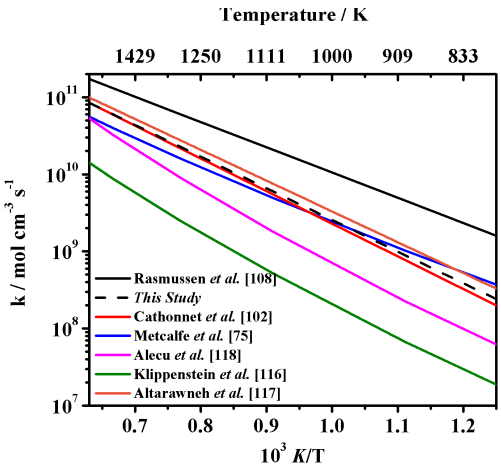

(b) Rate constants

Figure 4.9: (a) Sensitivity analyses for 8.55% O_2, $p = 40$ atm and $T = 885$ K (Mixes 4, 12 and 17). (b) Temperature dependent rate constants for the reaction $CH_3OH + H\dot{O}_2 \rightleftarrows \dot{C}H_2OH + H_2O_2$.

results could be expected considering Fig. 4.9.

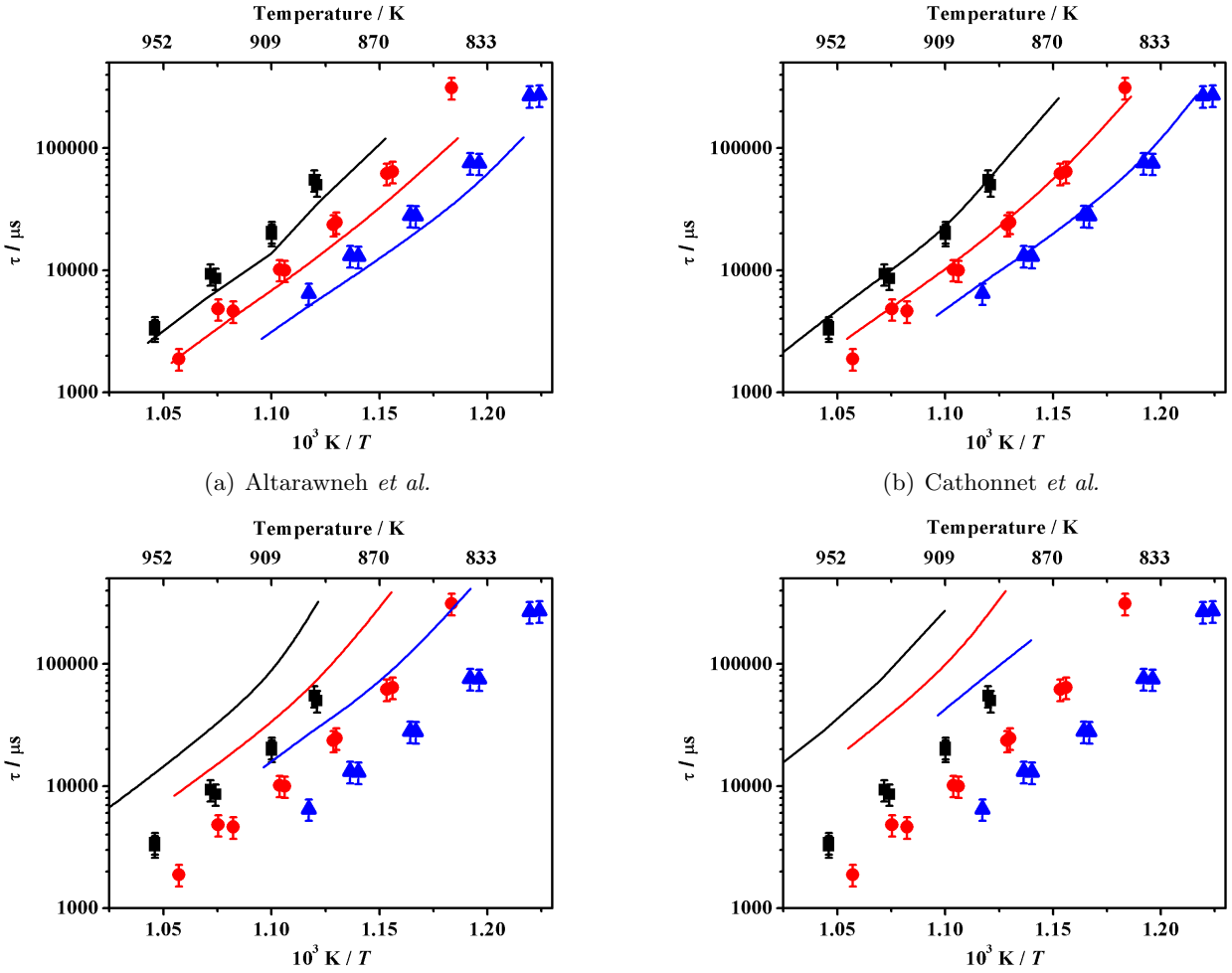

(a) Altarawneh *et al.*

(b) Cathonnet *et al.*

(c) Alecu *et al.*

(d) Klippenstein *et al.*

Figure 4.10: Constant O_2 concentration of 8.55% O_2, $p = 40$ atm. ■ – $\phi = 0.5$ (Mixture 4), ● – $\phi = 1.0$ (Mixture 12), ▲ – $\phi = 2.0$ (Mixture 17).

The flux analyses in Fig. 4.11 shows that there is no fundamental change in the mechanism through which methanol is oxidized by using the rate constant proposed by Cathonnet *et al.* [105] or Klippenstein *et al.* [119] even though there is an order of magnitude difference. Using either of these rate constants, the fuel is consumed via H-atom abstraction forming either methoxy or hydroxy-methylene radicals, both of which decompose to form formaldehyde. However using Klippenstein *et al.*'s [119] rate constant results in 92.2% of the fuel being consumed by hydroxyl radical however with the use of Cathonnet *et al.*'s [105] rate constant only 63.5% of the fuel is consumed by hydroxyl radical. More emphatic still is the the consumption of the fuel by hydroperoxyl radicals, changing from 4.9% using Klippenstein *et al.*'s [119] rate constant compared to 34.7% using Cathonnet *et al.*'s [105] rate constant. Two sensitivity analyses were carried out at the same conditions as the flux analyses, comparing the effect of the aforementioned rate constants. The results are presented in Fig. 4.12. Using the rate constant of Klippenstein *et al.* [119] we see a reduced sensitivity to $CH_3OH + H\dot{O}_2 \rightleftarrows \dot{C}H_2OH + H_2O_2$. However it is still the most promoting reaction from the methanol sub-mechanism despite the fact that it only consumes 4.9% of the fuel as shown in the flux analyses (Fig. 4.11). The main

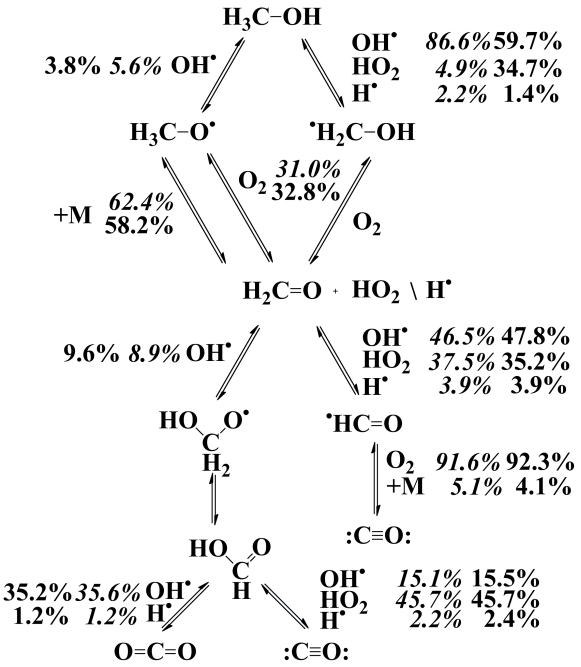

Figure 4.11: Flux analyses at CH_3OH = 5.70%, O_2 = 8.55% and N_2 = 85.75%, T = 880 K, p = 38.90 atm. Using the rate constants of Cathonnet *et al.* [105] (**Bold figures**) and Klippenstein *et al.* [119] (*Italic figures*).

reaction consuming the fuel is H-atom abstraction by hydroxyl radical. The rate constant for this reaction in Mech_56.55 is from the theoretical calculation from Xu and Lin [124], as mentioned earlier. This abstraction reaction is the fastest methanol H-atom abstraction reaction and hence is not rate limiting i.e. a reasonable increase or decrease results in this reaction remaining the main fuel consumption reaction. This explains why this reaction does not appear to be as sensitive in the brute force sensitivity analyses.

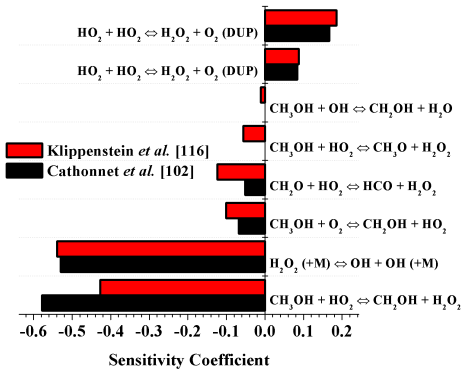

Figure 4.12: Sensitivity analyses for 5.70% CH_3OH, 8.55% O_2, $p = 10$ atm and $T = 956$ K.

To broaden the scope of conditions of *this study* and indeed the available validation data, fuel in 'air' mixtures at $\phi = 0.5$, 1.0 and 2.0 and for the first time at reflected shock pressures of 50 atm are studied. A similar analysis was applied where each of the four rate constants discussed earlier were systematically included in Mech_56.55 and the various predictions compared to the measured data, the results of these simulations are shown in Fig. 4.13. Once again it is clear that the two calculated rate constants of Alecu *et al.* [121] and Klippenstein *et al.* [119] result in predictions which are far too slow when compared to the experimental data while reasonable predictions are observed when using the estimated rate constant of Cathonnet *et al.* [105]. In this case the calculation of Altarawneh *et al.* [120] yields reasonable predictions when compared with experimental data. Sensitivity analyses are once again performed using either the rate constant of Klippenstein *et al.* [119] and that of Cathonnet *et al.* [105]. The results again show that under the conditions studied the most sensitive reaction is abstraction by hydroperoxyl radical.

The sensitivity analyses using the two rate constants (Klippenstein *et al.* [119] and Cathonnet *et al.* [105]) are presented in Fig. 4.14. The results once again show that the main reactions promoting and inhibiting reactivity do not change when the rate constant for $CH_3OH + H\dot{O}_2 \rightleftarrows \dot{C}H_2OH + H_2O_2$ changes from the calculation of Klippenstein *et al.* [119] to the estimate from the study of Cathonnet *et al.* [105]. At 1060 K there is a factor of 11 difference in the rate constants, with Klippenstein *et al.*'s [119] being slower.

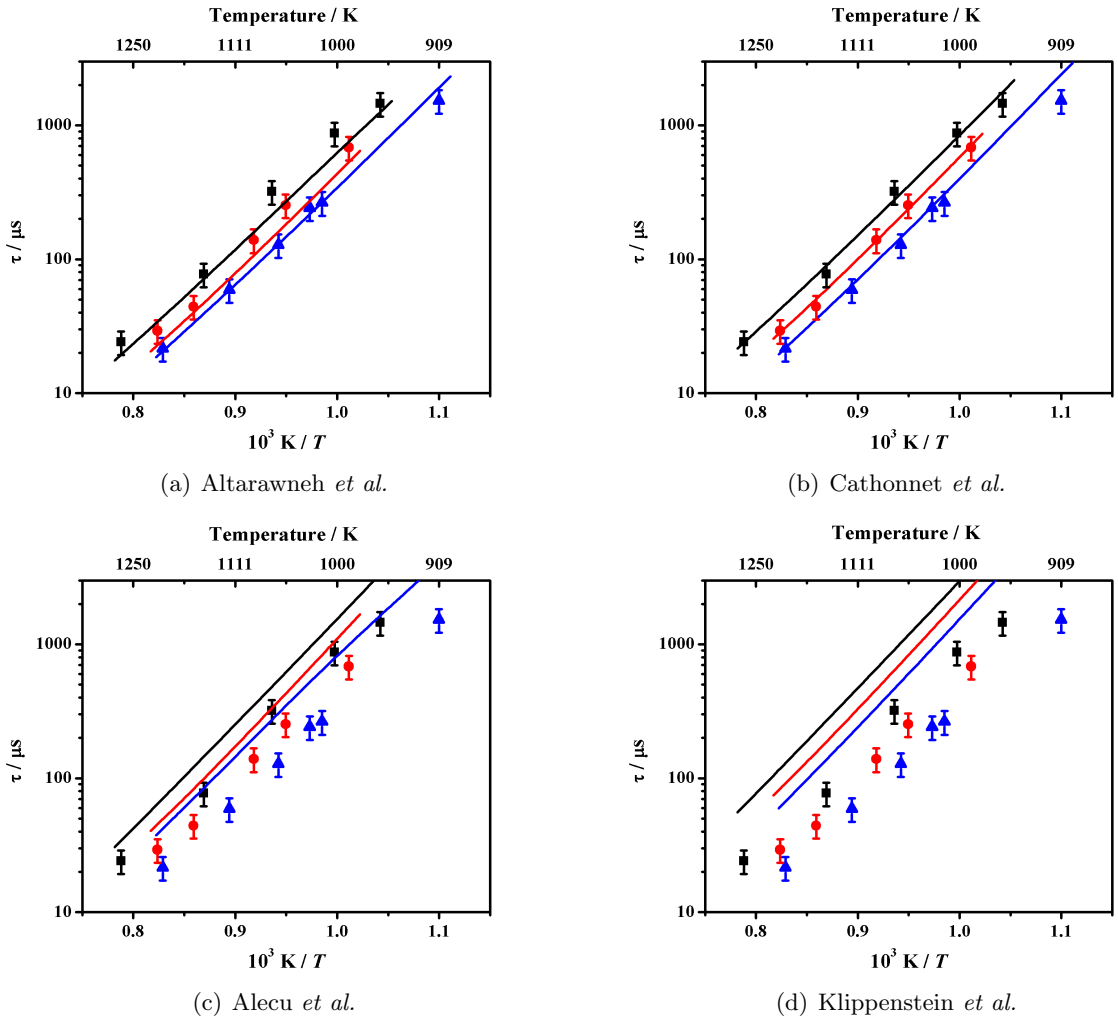

(a) Altarawneh *et al.*

(b) Cathonnet *et al.*

(c) Alecu *et al.*

(d) Klippenstein *et al.*

Figure 4.13: Fuel in "air" mixtures showing the influence of equivalence ratio, $p = 50$ atm. ■ – $\phi = 0.5$, ● – $\phi = 1.0$, ▲ – $\phi = 2.0$.

As in all detailed models the mechanism of oxidation is complex and the reason for discrepancies may be due to several reactions. Thus, further analysis of the base mechanism is important. Ignition delay time predictions are also sensitive to the reactions, $H\dot{O}_2 + H\dot{O}_2 \rightleftarrows H_2O_2 + O_2$ – [RX] and H_2O_2 (+M) $\rightleftarrows \dot{O}H + \dot{O}H$ (+M) – [RY]. The rate constants of these reactions are taken from measurements by Hippler *et al.* [130] for RX and calculations by Troe [131] for RY. A factor of two is a reasonable uncertainty for the rate constant for RX. The calculation of Klippenstein *et al.* [119], which is the slowest rate constant available, is incorporated into Mech_56.55 while applying a factor of two decrease in the rate constant for RX. The predictions remain considerably slow compared to the measured experimental data, as shown in Fig. 4.15. These results indicate a reasonable change to the rate constants of other sensitive reactions fail to yield more favorable predictions using the calculated rate constant for $CH_3OH + H\dot{O}_2 \rightleftarrows \dot{C}H_2OH + H_2O_2$, and further emphasize the importance of this reaction's rate constant. Additionally, changing a rate constant in the H_2/O_2 sub-mechanism, which has been previously robustly validated (Kéromnès *et al.* [127]), in an attempt to optimize the methanol sub-mechanism is contrary hierarchical nature of model development.

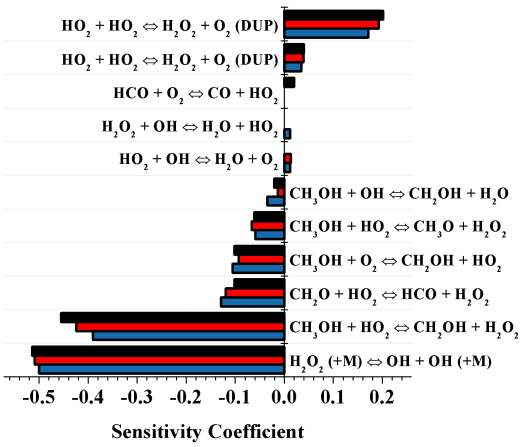

(a) Klippenstein *et al.*

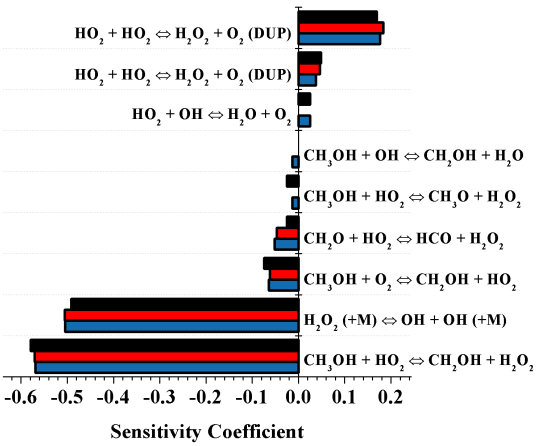

(b) Cathonnet *et al.*

Figure 4.14: Sensitivity analyses for Methanol in "air", $p = 50$ atm, $T = 1060$ K. (a) – Klippenstein *et al.*'s [119] rate constant, (b) – Cathonnet *et al.*'s [105] rate constant.

In an attempt to reconcile the model predictions using theoretical calculations of the rate constant for $CH_3OH + H\dot{O}_2 \rightleftarrows \dot{C}H_2OH + H_2O_2$ the activation energy of the calculation of Altarawneh *et al.* [120] was increased by 500 cal mol^{-1} and used to simulate the newly measured experimental data. Figures 4.1–4.8 show that simulating the newly measured ignition delay times using this rate constant yields good agreement with the new experimental data.

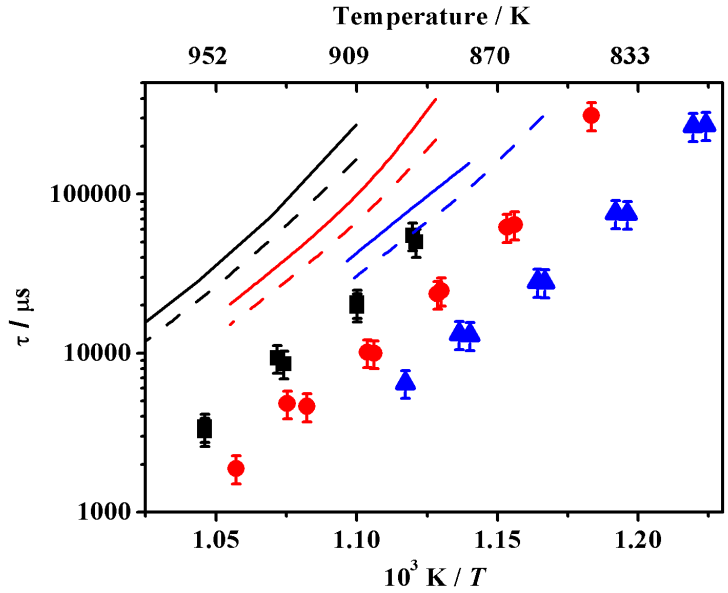

Figure 4.15: Effect of varying the rate constant for $H\dot{O}_2 + H\dot{O}_2 \rightleftarrows H_2O_2 + O_2$ using Klippenstein *et al.*'s [119] rate constant for H-atom abstraction by hydroperoxyl radical. 8.55% O_2, $p = 40$ atm. ■ – $\phi = 0.5$, ● – $\phi = 1.0$, ▲ – $\phi = 2.0$. Solid lines are predictions using [130]'s rate constant for $H\dot{O}_2 + H\dot{O}_2 \rightleftarrows H_2O_2 + O_2$, dashed lines represent predictions applying a factor of 2 decrease to this rate constant.

4.5 Conclusions

This study provides new ignition delay time data. In particular measurements at high pressure (> 10 atm) and low temperatures (800−1000 K) are provided for model validation. This data has been shown herein to be highly sensitive to the rate constant for:

$$CH_3OH + H\dot{O}_2 \rightleftarrows \dot{C}H_2OH + H_2O_2$$

The rate constant for this reaction has a number of literature values available which differ by up to a factor of 10. These rate constants were used in Mech_56.55 and tested against the measured experimental data of *this study* and other experimental data available in the literature (shown in appendix B.2).

The results showed that the calculated rate constants of Klippenstein *et al.* [119] and Alecu *et al.* [121] available in the literature (which differ by a factor of 3.42 at 1000 K) result in consistently slow ignition delay times when compared to the measured experimental data. Reasonable agreement was observed when the rate constant proposed by Cathonnet *et al.* [105] was employed. At 1000 K this rate constant was faster than the calculated rate constants of Klippenstein *et al.* [119] by a factor of 11.3 and a factor of 3.3 faster than Alecu *et al.* [121]. While the calculation of Altarawneh *et al.* [120] results in ignition delay time which are faster than experimental data.

Considering the importance of this rate constant under the engine relevant conditions in the pressure range $10 - 50$ atm, and temperature range of $800 - 1600$ K, at $\phi = 0.5$, 1.0, and 2.0 in 'air', a direct measurement of this rate constant is desirable in order to further reduce the uncertainty in the rate constant of this very important reaction. Such a measurement may be possible considering the recent hydrogen peroxide measurements by Guo *et al.* [69].

Based on the *this study* an updated version of Mech_56.53 [128] using the rate constant calculated by Altarawneh *et al.* [120], increasing the activation energy by 500 cal mol^{-1} (resulting in a rate constant less than a factor of 2 different than the original rate constant), for $CH_3OH + H\dot{O}_2 \rightleftarrows \dot{C}H_2OH + H_2O_2$ is provided in Mech_56.55. This update improves the predictive capability of the detailed kinetic model for pressures > 10 atm and temperatures below 1000 K relevant to methanol oxidation.

Chapter 5

Tri-Propylene Gylcol Mono-Methyl Ether

5.1 Abstract

Tri-propylene glycol mono-methyl ether (TPGME) is an important oxygenated fuel additive that can be used to reduce soot in diesel engines. Fundamental experimental data are needed that can be used to validate a TPGME mechanism. In *this study* shock tube ignition delay time data have been acquired for the first time. A temperature range of $980 - 1545$ K and pressures of 10 and 20 atm were studied for three equivalence ratios of 0.5, 1.0 and 2.0. The predictions from a surrogate model developed at Lawrence Livermore National Laboratory (LLNL_Mech) have been compared to experimental measurements showing good agreement.

5.2 Introduction

TPGME is an attractive oxygenated additive that is effective for reducing soot emissions in diesel engines [13, 14]. It has been used in research diesel engines to obtain non-sooting combustion [13]. To further understand the mechanism through which TPGME is oxidised, and therefore the mechanism that makes it an effective soot reducer, development of a chemical kinetic mechanism for TPGME is required. This must be capable of accurately predicting the combustion chemistry of TPGME under engine relevant conditions, at high pressures and over a wide range of temperatures. Westbrook *et al.* [132] developed a model for TPGME capable of predicting production of soot precursor species. However, a TPGME mechanism validated against fundamental experimental data is currently unavailable. The LLNL_Mech currently in development is validated against the ignition delay times measured in *this study*. There is currently no other fundamental experimental data available for the validation of a chemical kinetic mechanism for TPGME.

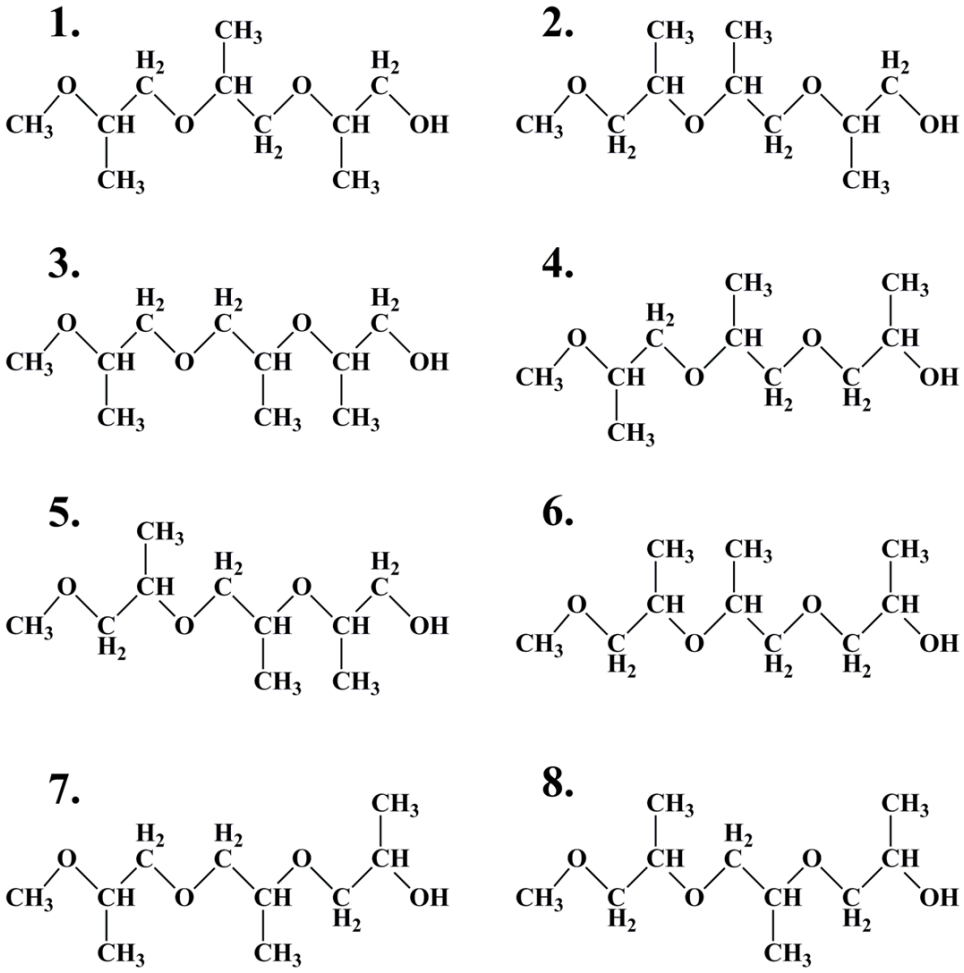

Figure 5.1: All possible TPGME structural isomers in the isomeric mixture experimentally studied.

From a molecular structure point of view, TPGME is an interesting case. It is highly branched, with four oxygen atoms distributed throughout the molecule, as shown in Fig. 5.1. Most other oxygenated fuels previously investigated are much smaller in molecular size than TPGME, and either have a low level of branching or are straight-chained in their skeletal structure. These characteristics of TPGME represent a challenge for chemical kinetic model development. The LLNL_Mech under development is a surrogate model using structural isomer number 1, as shown in Fig. 5.1, as a surrogate for the isomeric mixture studied using a ST in *this study*. The isomeric mixture studied consists of eight structural isomers, as shown in Fig. 5.1.

5.3 Experimental

Ignition delay times were measured using a heated high pressure ST described in Section 2.1.3. The full list of mixtures studied can be seen in Table 5.3.

Mixtures were prepared manometrically in a stainless steel mixing vessel following the procedure described in Section 2.3.1. TPGME was obtained from Sigma-Aldrich at a purity of $> 97.0\%$, and is a mixture containing eight isomers of TPGME as discussed

Table 5.1: Experimental data sets studied showing species concentrations on % molar volume.

Mix No.	p_5 / atm	ϕ	TPGME / Mole %	O_2 / Mole %	Ar / Mole %
1	10	0.50	0.25	6.75	93.00
2	10	1.00	0.25	3.38	96.38
3	10	2.00	0.25	1.69	98.06
4	20	0.50	0.25	6.75	93.00
5	20	1.00	0.25	3.38	96.38
6	20	2.00	0.25	1.69	98.06

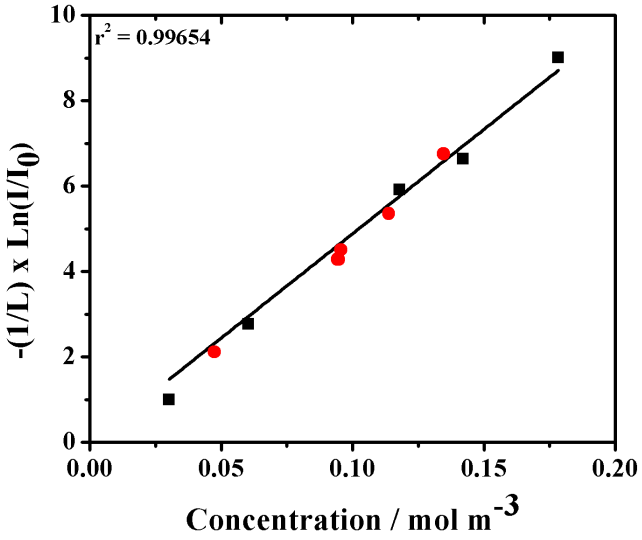

Figure 5.2: Laser absorption measurements. ■ – Test cell, ● – In-situ. Line is a linear correlation to the test measurements. Absorption measured at a wavelength of 3.39 μm, using a He-Ne laser.

above. The sample was treated to remove any peroxides by elution through alumina (80-200 mesh, Fisher Chemical A540, conditioned overnight at 673 K). This technique was performed by the funding authority Ford Motor Company Ltd. Oxygen and argon, and driver gases, helium and nitrogen, were obtained from BOC Ireland at purities of $\geq$ 99.50% for argon, and $\geq$ 99.99% for the others, and were used without further purification. TPGME has a very low vapour pressure (6x10^{-3} Torr at 298 K), therefore the ST, mixing vessel, and manifold were heated to 423 K during experiments to prevent condensation of the fuel.

Additionally, to confirm the fuel concentration during experiments, in-situ laser absorption measurements were performed, Fig. 5.2. This method has been described, and used, previously by Darcy *et al.* [133] and Mével *et al.* [134]. An infrared helium-neon laser was used to monitor the absorption at 3.39 μm for gas phase liquid hydrocarbons. 2 Thorlabs PDA20H-EC photodiode array detectors were used to measure the absorption. The first one was positioned before the test cell and the second after, this provided a reference and measured signal and the ratio between the two signals corresponded to the measured absorption at a given gas pressure. The gaseous pressure was used to calculated

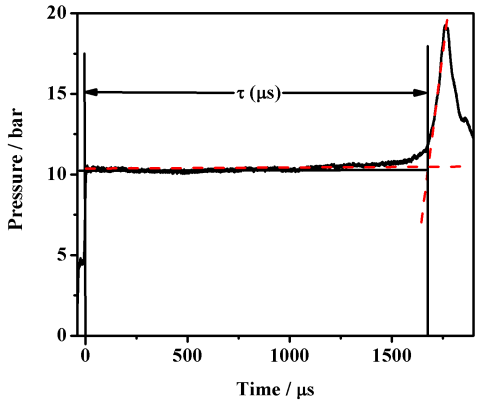

Figure 5.3: Experimental pressure trace. Reflected shock conditions: $p = 10.4$ atm, $T = 1154$ K, $\phi = 1.0$

the concentration of fuel in the test cell using the ideal gas equation. These concentrations were plotted against measured absorptions and a standard curve developed using the Beer-Lambert law. The same setup was then used to measure the absorption of the mixture prepared *in-situ* and the results finally compared to the test cell measurements. The absorption analysis confirmed that there was no condensation occurring.

Ignition delay times were defined in the same fashion as outlined in Section 2.1.3. Figure 5.3 shows an example of a typical pressure trace measured for the TPGME data.

5.4 Results and Discussion

The LLNL_Mech model was used to simulate the ignition delay times measured in *this study*. The measured ignition delay times span a range of temperatures ($980 - 1545$ K), pressures (10 and 20 atm), and equivalence ratios (0.5, 1.0 and 2.0). Figure 5.4 presents the data showing the effect of equivalence ratio for reflected shock pressures of 10 and 20 atm.

At both reflected shock pressures ignition delay times decrease with decreasing equivalence ratio. There is good agreement between model simulation results and experimental data except for the data at the lowest temperatures for $\phi = 0.5$, $p_5 = 10$ atm.

Figure 5.5 compares the data showing the effect of pressure and equivalence ratio on ignition delay time. As has been observed in the previous chapters for the other fuels studied during *this study*, as pressure increases ignition delay times decrease. A flux analysis was performed using the LLNL_Mech to garner an insight into the mechanism of oxidation of TPGME under one of the conditions studied. Figure 5.6 presents the results of a flux analysis performed at $p_5 = 18.41$ atm, $T_5 = 1187$ K and $\phi = 2.0$. The mechanism predicts that TPGME is consumed by H-atom abstraction and molecular elimination reactions. The importance of molecular elimination reactions for the consumption of branched ethers has been discussed previously by Yasunaga *et al.* [135]. It is from this that the rate constants used in the LLNL_Mech for the molecular eliminations stem. The

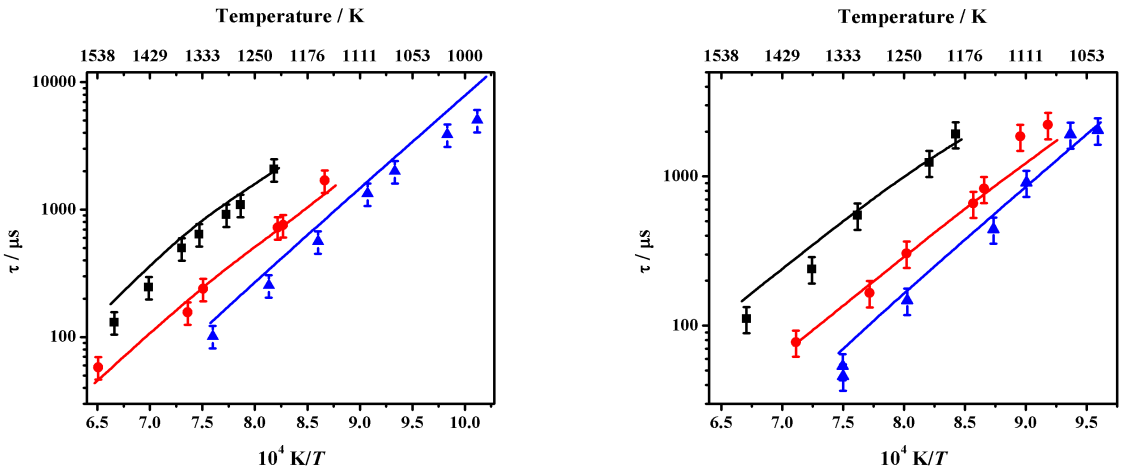

(a) $p_5 = 10$ atm (b) $p_5 = 20$ atm

Figure 5.4: Effect of equivalence ratio, 0.25% TPGME. ■ – $\phi = 2.0$, ● – $\phi = 1.0$, ▲ – $\phi = 0.5$. Lines represent LLNL_Mech simulation results.

H-atom abstraction reactions are adapted as analogies to rate constants proposed by the studies of Sarathy *et al.* [136, 137] for all abstraction sites other than the primary ether site. The H-atom abstraction reaction rate constants from the primary ether site are adopted from the DME mechanism presented by *this study*. The intermediate products produced from the decomposition of TPGME are decomposed to C_1−C_3 species. The major products predicted by the LLNL_Mech are acetaldehyde, propene and formaldehyde.

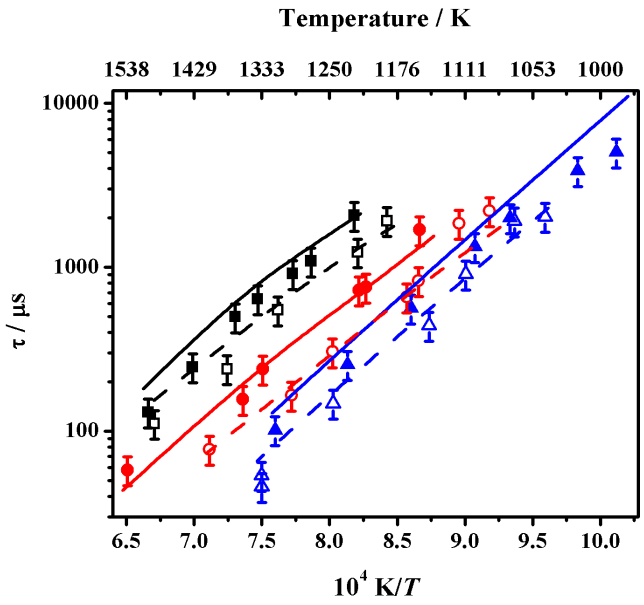

Figure 5.5: Effect of pressure and ϕ, 0.25% TPGME. Filled symbols are $p_5 = 10$ atm and open symbols are $p_5 = 20$ atm. ■ – $\phi = 2.0$, ● – $\phi = 1.0$, ▲ – $\phi = 0.5$. Lines represent LLNL_Mech simulation results. Solid lines = 10 atm data, dashed lines = 20 atm data.

5.5 Conclusion

The first fundamental experimental data have been measured for TPGME. Ignition delay times at pressures of 10 and 20 atm covering the range of temperatures, 980 – 1545 K, and equivalence ratios of 0.5, 1.0 and 2.0 have been measured and are now available for the validation of a detailed chemical mechanism. The surrogate model, LLNL_Mech, was used to simulate the measured experimental data. The model's simulations agree well with the experimental data. In order to further develop the model, more data is required to provide validation targets. In particular low-temperature (< 1000 K) data is essential, considering TPGME's application as a diesel fuel additive.

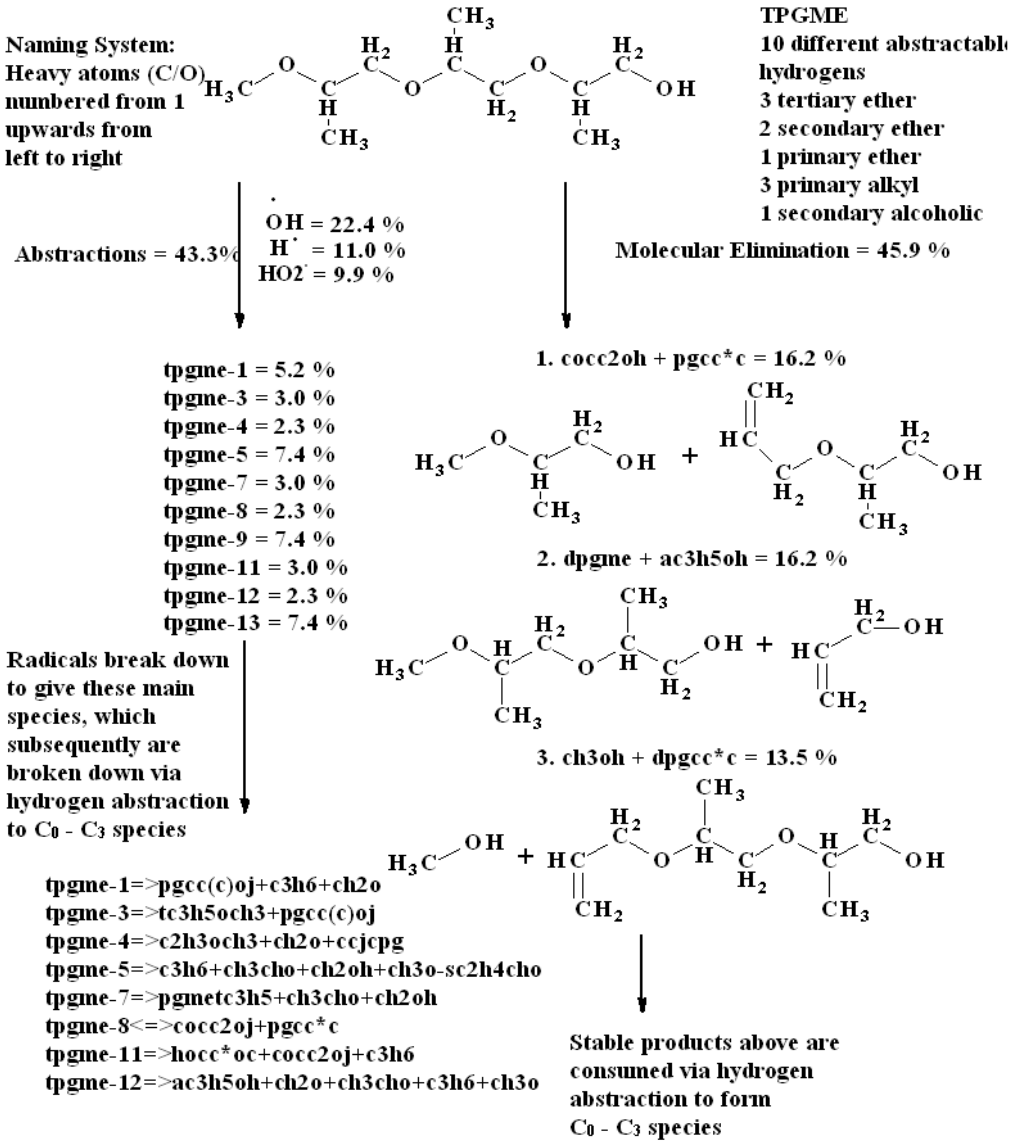

Figure 5.6: Flux analysis for 0.25% TPGME, 1.69% O_2, 98.06% Ar for $p_5 = 18.41$ atm, $T_5 = 1187$ K, $\phi = 2.00$ and at 20% fuel consumed. Percentages represent net flux of reaction from indicated species.

Chapter 6

Other Compounds

Other compounds have also been studied during the course of *this study*. Propene (C_3H_6) and 2-Methylfuran (2-MF) ignition delay times were measured. C_3H_6 data was recorded to supplement a large collaborative project providing a wide range of experimental data for the validation of C_3H_6 pyrolysis and oxidation chemistry under combustion relevant conditions. The first ignition delay times for 2-MF were measured in *this study*. These were used in the validation of a detailed mechanism and are published in [138].

6.1 Propene

A large collaborative project was udertaken in order to produce experimental data for the validation of a C_3H_6 mechanism. Figure 6.1 shows the experimental matrix including the available ignition delay time data in the literature. Flame speed measurements were also included as part of this collaboration. The collaborating groups were:

1. NUIG, ST and RCM ignition delay times.
2. Stanford University (SU), ST ignition delay times.
3. TAMU, ST ignition delay times and constant volume bomb flame speeds.
4. Rensselaer Polytechnic Institute (RPI), ST ignition delay times.
5. King Abdullah University of Science and Technology (KAUST), ST ignition delay times.
6. University of Conneticut (UConn), RCM ignition delay times.
7. Princeton University (PU), outwardly propagating spherical flame speeds.
8. Vrije Universiteit Brussel (VUB), heat-flux flame speeds.

Each institute contributed a range of experimental data. The plan of experiments for the ignition delay times was carried out by *this author*. Details of work carried out by each of the institutions is shown in Table 6.1. The plan was designed in order to cover a wide range of pressures, temperatures, dilutions and equivalence ratios in an efficient manner. The data sets were distributed as evenly as possible between the participating institutes. The plan also ensured that each facility had at least one overlapping condition with a different facility in order to directly compare ignition delay time measurements taken in

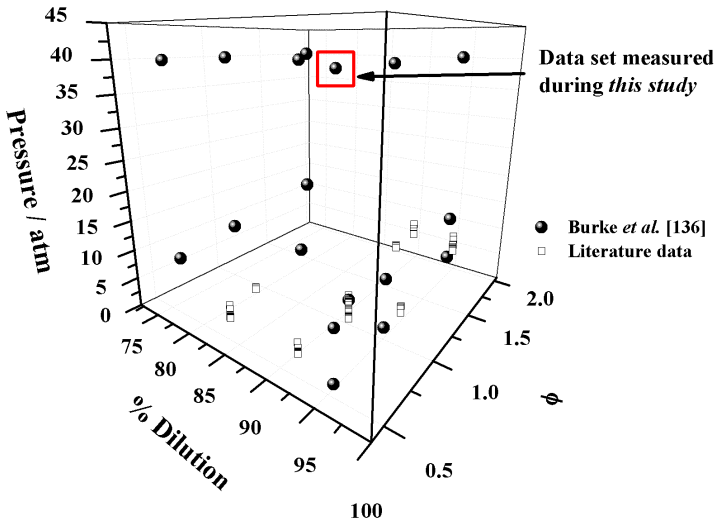

Figure 6.1: Ignition delay time data sets measured previously and in [139].

different facilities. For example, ST data taken at $p = 10$ atm, $\phi = 1.0$ in 'air' were taken in the facilities at NUIG, TAMU, RPI and KAUST. There is also an overlapping data set between NUIG and SU at 0.89% C_3H_6, 4% O_2 and $p = 40$ atm. This NUIG data set was measured during *this study*.

Figure 6.2 show the data collected in *this study*. It is compared to the same data taken in the SU facility. Both facilities use pressure to measure the ignition delay time. The ignition delay time definition for these data is the same as that outlined for data measured in the NUIG high pressure shock tube in Chapter 2.1.3. The comparison of the data taken in the two facilities agree well with one another. A linear correlation performed on all of the data collected by the two facilities results in an R^2 value of 0.998. This shows just how well the two data sets taken in the separate facilities correlate with one another.

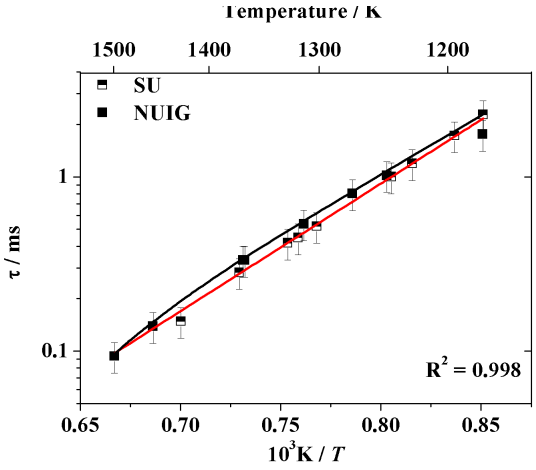

Figure 6.2: Comparison of ignition delay times measured for 0.89% C_3H_6, 4% O_2 and p = 40 atm in the STs at SU and NUIG.

A detailed chemical kinetic model (Mech_56.53) was developed and validated against all of the data collected as part of this collaboration. This model represents a important

improvement in the understanding of the combustion chemistry of this common intermediate species of n-alkane combustion. Figure 6.2 compares the predictions of Mech_56.53 with the experimental data measured in *this study* and the complimentary data set measured in the SU facility. There is excellent agreement between the model predictions and the measured experimental data.

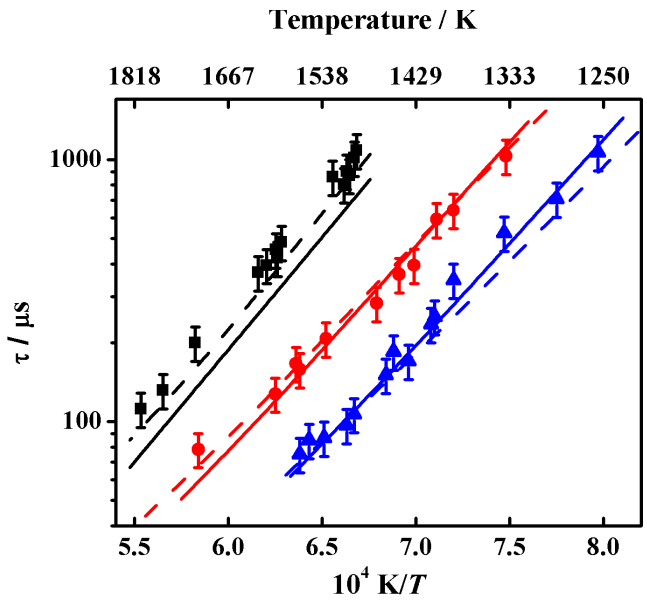

Figure 6.3: Effect of equivalence ratio, 1.00% 2-MF, p_5 = 1 atm. ■ – ϕ = 2.0, ● – ϕ = 1.0, ▲ – ϕ = 0.5. Solid lines = updated mechanism [140], dashed lines = original mechanism [138].

6.2 2-Methylfuran

Ignition delay times were measured for equivalence ratios of 0.5, 1.0 and 2.0 using 1% 2-MF and diluted in argon. The reflected shock pressure studied was 1 atm and the temperature range covered was 1200 – 1800 K. As was seen with TPGME as equivalence ratio decreases so does ignition delay times of 2-MF, as shown in Fig. 6.3. These ignition delay times were the first measured for this oxygenated biofuel. The ignition delay time definition used for these data was from derived from the maximum rate of CH^* production as outlined in Chapter 2.1.4. They provided one of the validation targets for the model developed by Somers *et al.* [138]. Figure 6.3 compares the the measured experimental data to the predictions of Somers *et al.* [138] model. The model predicts the data well.

This model was subsequently updated [140] using newly calculated pressure-dependent rate constants for the fuel radical decomposition reactions. The model was then re-validated against the original and new targets. When comparing the updated model against the ignition delay times of *this study* the model under-predicts the ignition delay times measured for ϕ = 2.0. In general the updated model predicts the rest of the data better than the original including the ϕ = 1.0 and 0.5 data collected during *this study*. Further experimental studies, incrementally increasing the concentration of 2-MF, could help in the identifying the source of the discrepancy at ϕ = 2.0.

6.3 Conclusions of these studies

The ignition delay times measured in isolation for propene and 2-MF by *this study* represent important and useful validation targets. These data were collected when there was little or no fundamental experimental data available for the validation of chemical kinetic mechanisms for these two compounds. Without these validation targets the continued development of the chemical kinetic mechanisms would not be possible.

Table 6.1: C_3H_6 ignition delay time data sets measured by each of the collaborating institutes. Species concentrations presented as % molar volume. Dataset taken by *this author* is highlighted in bold.

No.	% Propene	% O_2	% Diluent	ϕ	p / atm	Facility
			NUIG			
1	2.25	20.53	77.22	0.5	10	ST
2	4.46	20.07	75.47	1.0	10	ST
3	**0.89**	**4.00**	**95.11**	**1.0**	**40**	**ST**
4	2.25	20.53	77.22	0.5	10	RCM
5	0.45	4.00	95.55	0.5	10	RCM
6	4.46	20.07	75.47	1.0	10	RCM
7	2.67	12.00	85.33	1.0	10	RCM
8	0.89	4.00	95.11	1.0	10	RCM
9	2.25	20.53	77.22	0.5	40	RCM
10	0.45	4.00	95.55	0.5	40	RCM
11	4.46	20.07	75.47	1.0	40	RCM
12	2.67	12.00	85.33	1.0	40	RCM
13	0.89	4.00	95.11	1.0	40	RCM
			TAMU			
14	2.25	20.53	77.22	0.5	2	ST
15	2.67	12.00	85.33	1.0	2	ST
16	0.89	4.00	95.11	1.0	2	ST
17	1.78	4.00	94.22	2.0	2	ST
18	2.25	20.53	77.22	0.5	10	ST
19	4.46	20.07	75.47	1.0	10	ST
20	2.67	12.00	85.33	1.0	10	ST
21	0.89	4.00	95.11	1.0	10	ST
22	1.78	4.00	94.22	2.0	10	ST
			RPI			
23	2.25	20.53	77.22	0.5	10	ST
24	4.46	20.07	75.47	1.0	10	ST
25	2.67	12.00	85.33	1.0	10	ST
26	8.54	19.21	72.25	2.0	10	ST
27	2.25	20.53	77.22	0.5	40	ST
28	4.46	20.07	75.47	1.0	40	ST
29	2.67	12.00	85.33	1.0	40	ST
30	8.54	19.21	72.25	2.0	40	ST
			SU			
31	0.89	4.00	95.11	1.0	2	ST
32	0.45	4.00	95.55	0.5	2	ST
33	1.78	4.00	94.22	2.0	2	ST
34	0.89	4.00	95.11	1.0	4.5	ST
35	1.60	7.20	91.13	1.0	4.5	ST
36	0.89	4.00	95.11	1.0	40	ST
37	1.78	4.00	94.22	2.0	40	ST
			UConn			
38	4.46	20.07	75.47	1.0	10	RCM
39	2.67	12.00	85.33	1.0	10	RCM
40	8.54	19.21	72.25	2.0	10	RCM
41	0.89	4.00	95.11	1.0	10	RCM
42	0.89	4.00	95.11	1.0	40	RCM
43	2.67	12.00	85.33	1.0	40	RCM
44	1.78	4.00	94.22	2.0	10	RCM
45	1.78	4.00	94.22	2.0	40	RCM
			KAUST			
46	4.46	20.07	75.47	1.0	10	ST
47	2.25	20.53	77.22	0.5	40	ST
48	4.46	20.07	75.47	1.0	40	ST
49	8.54	19.21	72.25	2.0	40	ST

Chapter 7

Conclusions and Outlook

The overall goal of *this study* was to measure ignition delay times in order to provide validation targets for detailed chemical kinetic models, and also to develop robustly validated chemical kinetic mechanisms, and this has been achieved. Ignition delay times have been measured for CH_4, DME, 60/40 CH_4/DME, 80/20 CH_4/DME, CH_3OH, TPGME, C_3H_6, and 2-MF. A new detailed chemical kinetic model for DME has been developed. Re-validation and updates to an existing CH_3OH mechanism have also been carried out.

7.1 CH_4/DME

The experimental and modelling results regarding CH_4, DME, 60/40 CH_4/DME, and 80/20 CH_4/DME have been published in [141]. The range of conditions studied experimentally are $p = 7 - 44$ atm, $T = 600 - 1600$ K and equivalence ratios of $0.3 - 2.0$. The model presented in *this work* represents the first DME mechanism to apply pressure-dependent rate constants to the major low-temperature chemistry reactions governing the oxidation of DME. It was found that application of these pressure-dependent rate constants had an appreciable effect on the models predictive capabilities, improving these capabilities significantly when compared to previous chemical kinetic models developed for DME. High-level calculations or measurements have been adopted where available for the rest of the reaction rate constants. Updated thermochemical groups (C/H2/O/OO and CJOC) have been estimated based on calculations by Yamada *et al.* [75], thus improving the accuracy of the thermochemistry of DME's combustion species. *This model* was then validated using a wide range of experimental data available in the literature, flow reactor speciation, JSR speciation, flame speeds and flame speciation, RCM ignition delay times, ST ignition delay times and ST speciation. This robust validation provides users with confidence in the accuracy of the predicted results from this model.

7.2 Methanol

The methanol experiments taken covered a range of conditions of, $p = 2 - 50$ atm, $T = 850 - 1600$ K, CH_3OH concentrations of $1.5 - 21.9\%$ and equivalence ratios from $0.5 - 2.0$. The data collected represents an important expansion of the data conditions available for validation of detailed chemical kinetic models. An available model was updated using the new data and the data found in the literature as validation. An in-depth analysis surrounding the disputed value for the rate constant of $CH_3OH + H\dot{O}_2 \rightleftarrows \dot{C}H_2OH +$

H_2O_2 was performed using the updated model. The results of the analysis led to the assignment of the rate constant best able to predict all of the experimental data available for model validation. The rate constant adopted was from the calculation of Altarawneh *et al.* [120], with a 500 cal mol^{-1} increase applied to the activation energy. The validation of the model over the high-pressure conditions presented in *this study* represents an important development of the mechanism of oxidation of the simplest alcohol under engine relevant conditions.

7.3 TPGME

Previous studies [13, 14] have identified TPGME as an effective soot-reducing additive when utilised in diesel combustion. Before *this study* there was no fundamental experimental data available for the validation of chemical kinetic models. The experimental conditions studied were, 0.25% TPGME, $p = 10 - 20$ atm, $T = 980 - 1545$ K, and equivalence ratios of 0.5, 1.0 and 2.0. The ignition delay times measured are being used in the continued development of a surrogate chemical kinetic model developed to provide predictions about the mechanism of oxidation of TPGME. Under the experimental conditions studied it was found that molecular eliminations and H-atom abstractions mainly consumed TPGME. Further experimental data is required to develop the chemical kinetic model. This illustrates the importance of fundamental experimental data taken in order to provide validation targets for chemical kinetic models, such as the ignition delay times presented throughout *this study*.

7.4 Other Compounds

Other experimental data have been measured for C_3H_6 and 2-MF. C_3H_6 is an important intermediate produced during the combustion of *n*-alkanes. 2-MF is a potential alternative to petrol in SI engines. Its oxygenated structure results in cleaner emissions. The data taken during *this study* for C_3H_6 was as part of a large collaboration in an effort to develop a robustly validated chemical kinetic mechanism for C_3H_6 pyrolysis and oxidation which has been published [139]. The data taken for 2-MF oxidation has also been used in the validation of a chemical kinetic model and published [138]. The ignition delay times studied for C_3H_6 were for 0.89% C_3H_6, 4.00% O_2 at $p = 40$ atm, and over a temperature range of $T = 1175 - 1500$ K. The experimental range studied for 2-MF was, 1% 2-MF, $p = 1$ atm, $T = 1200 - 1800$ K, and equivalence ratios of 0.5, 1.0 and 2.0. These data were the first ignition delay times ever measured for 2-MF. The C_3H_6 ignition delay times were used as a cross-facility check between NUIG and Stanford University yielding good agreement between the data from the two facilities. These data were also used for validation of a chemical kinetic model.

7.5 Outlook

From the point of view of the motivation for *this study*, outlined in the introduction, the goals of providing novel ignition delay times for validation of chemical kinetic models and the further development of chemical kinetic models, in particular for oxygenated biofuels, have been acheived. *This study* provides new measurements and more accurate detailed chemical kinetic models for a selection of oxygenated species. The models developed and

updated using new ignition delay times as validation may be used as base mechanisms for reduction and implementation into CFD simulations which may be used to further improve current combustion systems. The large quantity of high-pressure ignition delay times from *this study* are extremely useful validation targets under engine relevant conditions. These high pressure validation targets will be required more and more in the future for a wider range of compounds in order to further validate chemical kinetic mechanisms at practical combustor operating conditions. In general, there is a dearth of experimental data available for model validation for many oxygenated compounds. In particular for longer chain and branched oxygenated compounds. Taking TPGME as an example, low-temperature ($<$ 1000 K) and high-pressure ($>$ 30 atm) data is completely absent and would be very important in order to further develop the chemical kinetic model. While there is a reasonable amount of data for *n*-alcohols there is not a lot at high pressures ($>$ 30 atm), or for branched alcohols. DME is one of the most widely studied oxygenated compounds, however there is only very sparse data available for larger ethers. Since the ignition delay times of 2-MF from *this thesis* were published a wide range of experimental data has been collected. Nonetheless, these cyclic ether compounds are being considered as potential biofuels derived from biomass, and more experimental data is continually being sought in order to validate chemical kinetic mechanisms for these compounds. As a general conclusion, in order to further develop models for the combustion of oxygenated compounds more high-pressure experimental data is required to validate these models at engine relevant conditions. In relation to further model development a continued effort is needed in order to incorporate the theoretical calculations, becoming more and more widely available, into the existing mechanisms and re-validate these mechanisms. This is essential in order to bridge the gap between theory and experiment and to reduce the level of uncertainty in the available computational models. The example of where theory and experiment collide is shown in *this study* through the discussion of the rate constant for $CH_3OH + H\dot{O}_2 \rightleftarrows \dot{C}H_2OH + H_2O_2$. However this case seems to be more the exception rather than the rule because theoretical rate constants have been successfully applied where available for Mech_56.54 decribing the combustion chemistry of DME. Furthermore throughout *this study* effort has been made to implement measured and calculated rate constants where available.

Bibliography

[1] T.F. Stocker, D. Qin, G.-K. Plattner, L.V. Alexander, S.K. Allen, N.L. Bindoff, F.-M. Bréon, J.A. Church, U. Cubasch, S. Emori, P. Forster, P. Friedlingstein, N. Gillett, J.M. Gregory, D.L. Hartmann, E. Jansen, B. Kirtman, R. Knutti, K. Krishna Kumar, P. Lemke, J. Marotzke, V. Masson-Delmotte, G.A. Meehl, I.I. Mokhov, S. Piao, V. Ramaswamy, D. Randall, M. Rhein, M. Rojas, C. Sabine, D. Shindell, L.D. Talley, D.G. Vaughan and S.-P. Xie, 2013: Technical Summary. In: Climate Change 2013: The Physical Science Basis. Contribution of Working Group I to the Fifth Assessment Report of the Intergovernmental Panel on Climate Change [T.F. Stocker, D. Qin, G.-K. Plattner, M. Tignor, S.K. Allen, J. Boschung, A. Nauels, Y. Xia, V. Bex and P.M. Midgley (eds.)]. Cambridge University Press, Cambridge, United Kingdom and New York, NY, USA.

[2] International Energy Agency, *Key World Energy Statistics 2013*. <http://www.iea.org/publications/freepublications/publication/KeyWorld2013.pdf>.

[3] Independent Statistics & Analysis, U. S. Energy Information Administration, *International Energy Statistics*. <http://www.eia.gov/countries/data.cfm#undefined>.

[4] M. Wang, C. Saricks, D. Santini, In: Effects of Fuel Ethanol Use on Fuel-Cycle Energy and Greenhouse Gas Emissions, Argonne National Laboratory, 9700 South Cass Avenue, Argonne, Illinois 60439, Chicago, 1999.

[5] P. Fuchs, C. Loeseken, J.K. Schubert, W. Miekisch, International Journal of Cancer, 126 (2010) 2663 – 2670.

[6] European Commission, 2011, *Energy Infrastructure Priorities for 2020 and Beyond - A Blueprint for an Integrated European Energy Network*. Available at http://ec.europa.eu/energy/infrastructure/strategy/2020_en.htm.

[7] F.M.A. Geilen, T. vom Stein, B. Engendahl, S. Winterle, M.A. Liauw, J. Klankermayer, W. Leitner, Angewandte Chemie International Edition, 50 (2011) 6831 – 6834.

[8] J. Klankermayer, M. Thewes, M. Müther, Proceedings of the 4th TMFB International Workshop of the Cluster of Excellence, "Tailor-Made Fuels form Biomass"; Aachen, Germany, 2011, 25 – 27.

[9] C. Wang, H. Xu, R. Daniel, A. Ghafourian, J.M. Herreros, S. Shuai, X. Ma, Fuel, 103 (2013) 200 – 211.

[10] Wang, C., Xu, H., and Lattimore, T., "Impacts of Low-Level 2-Methylfuran Content in Gasoline on DISI Engine Combustion Behavior and Emissions," SAE Technical Paper 2013-01-1317, 2013, doi:10.4271/2013-01-1317.

[11] M. Pan, G. Shu, J. Pan, H. Wei, D. Feng, Y. Guo, Y. Liang, Fuel, 132 (2014) 36 – 43.

[12] (OECD), in: 11 November 2003 ed.; United Nations Environmental Programme (UNEP), <http://www.chem.unep.ch/irptc/sids/OECDSIDS/PGEs.pdf>: 2003.

[13] C. J. Mueller, W. J. Pitz, L. M. Pickett, G. C. Martin, D. L. Siebers, C. K. Westbrook, in: Soc. Automotive Eng.: 2003.

[14] M.A. Gonzalez D, W. Piel, T. Asmus, W. Clark, J. Garbrak. E. Liney, M. Natarajan, D.W. Naegeli, D. Yost, E.A. Frame, J.P. Wallace, SAE Technical Paper 2001-01-3632, doi:10.4271/2001-01-3632, (2001).

[15] R.L. Belford, R.A. Strehlow, Ann. Rev. Phys. Chem., 20 (1969) 247 – 272.

[16] E.L. Petersen, Ph.D. Thesis, Department of Mechanical Engineering , Stanford University, (1998).

[17] J.M. Smith, Ph.D. Thesis, Department of Chemistry, National University of Ireland Galway, Galway, (2004).

[18] Reaction Design, CHEMKIN-PRO 15101, Theory manual, San Diego, 2010.

[19] W.J.M. Rankine, Philosophical Transactions of the Royal Society of London, 160 (1870) 277 – 288.

[20] H. Hugoniot, Journal de l'Ecole Polytechnique, (1887).

[21] D. Darcy, C.J. Tobin, K. Yasunaga, J.M. Simmie, J. Würmel, W.K. Metcalfe, T. Niass, S.S. Ahmed, C.K. Westbrook, H.J. Curran, Combust. Flame 159 (7) (2012) 2219 – 2232.

[22] D.F. Davidson, R.K. Hanson, Int. J. Chem. Kinet. 36 (9) (2004) 510 – 523

[23] H.J. Curran, P. Gaffuri, W.J. Pitz, C.K. Westbrook, Combust. Flame 114 (1–2) (1998) 149 – 177.

[24] B.M. Gauthier, D.F. Davidson, R.K. Hanson, Combust. Flame, 139 (2004) 300 – 311.

[25] K.A. Heufer, H. Olivier, Shock Waves, 20 (2010) 307 – 316.

[26] D. Davidson, D. Horning, R. Hanson, Shock tube ignition time measurements for n-heptane/O2/Ar and JP-10/O2/Ar mixtures, in: 35th Joint Prop. Conf. and Exhibit, American Inst. Aeronautics Astronautics, 1999.

[27] D. Lee, S. Hochgreb, Combust. Flame 114 (3-4) (1998) 531 – 545.

[28] D. Lee, S. Hochgreb, Int. J. Chem. Kinet., 30 (6) (1998) 385 – 406.

[29] C.-J. Sung; H.J. Curran, Prog. Energy Combust. Sci., 44 (2014) 1 – 18 <http://dx.doi.org/10.1016/j.pecs.2014.04.001>.

[30] D. Darcy, H. Nakamura, C.J. Tobin, M. Mehl, W.K. Metcalfe, W.J. Pitz, C.K. Westbrook, H.J. Curran, Combustion and Flame, 161 (2014) 65 – 74.

[31] A. Molino, F. Nanna, Y. Ding, B. Bikson, G. Braccio, Fuel, 103 (2013) 1003 – 1009.

[32] Y. Adachi, M. Komoto, I. Watanabe, Y. Ohno, K. Fujimoto, Fuel, 79 (2000) 229 – 234.

[33] T.A. Semelsberger, R.L. Borup, H.L. Greene, J. of Power Sources, 156 (2006) 497 – 511.

[34] W. Ying, L. Genbao, Z. Wei, Z. Longbao, Fuel Process. Tech., 89 (2008) 1272 – 1280.

[35] W. Ying, Z. Longbao, Energy & Fuels, 21 (2007) 1454 – 1458.

[36] S. C. Sorensen, ASME transactions, J. Eng. Gas Turbines Power, 123 (2001) 652−658.

[37] P. Kapus, H. Ofner, Development of Fuel Injection Equipment and Combustion System for DI Diesels Operated on Dimethyl Ether, SAE Technical Paper 950062, 1995.

[38] M.C. Lee, S.B. Seo, J.H. Chung, Y.J. Joo, D.H. Ahn, Fuel, 88 (2009) 657 – 662.

[39] P.A. Glaude, R. Fournet, R. Bounacceur, M. Moliere, DME as a Potential Alternative Fuel for Gas Turbines: A Numerical Approach to Combustion and Oxidation Kinetics, ASME 2011 Turbo Expo: Turbine Technical Conference and Exposition, 2011, 649 – 658.

[40] M. Konno, Z. Chen, SAE Paper 2005-01-0182, 2005, <doi:10.4271/2005-01-0182>.

[41] Y. Tsutsumi, K. Hoshina, A. Iijima, H. Shoji, SAE Paper, 2007-32-0041, 2007.

[42] C.A. Daly, J.M. Simmie, J. Würmel, N. DjebaÏli, C. Paillard, Combust. Flame, 125 (2001) 1329 – 1340.

[43] Z. Zhao, A. Kazakov, F.L. Dryer, Combust. Flame, 139 (2004) 52 – 60.

[44] X.L. Zheng, T.F. Lu, C.K. Law, C.K. Westbrook, H.J. Curran, Proc. Combust. Inst., 30 (2005) 1101 – 1109.

[45] X. Qin, Y. Ju, Proc. Combust. Inst., 30 (2005) 233 – 240.

[46] Y.L. Wang, A.T. Holley, C. Ji, F.N. Egolfopoulos, T.T. Tsotsis, H.J. Curran, Proc. Combust. Inst., 32 (2009) 1035 – 1042.

[47] J. de Vries, W.B. Lowry, Z. Serinyel, H.J. Curran, E.L. Petersen, Fuel, 90 (2011) 331 – 338.

[48] P. Dagaut, C. Daly, J.M. Simmie, M. Cathonnet, Proc. Combust. Inst., 27 (1998) 361 – 369.

[49] S.L. Fischer, F.L. Dryer, H.J. Curran, Int. J. Chem. Kinet., 32 (2000) 713 – 740.

[50] H.J. Curran, S.L. Fischer, F.L. Dryer, Int. J. Chem. Kinet., 32 (2000) 741 – 759.

[51] Z. Zhao, M. Chaos, A. Kazakov, F.L. Dryer, Int. J. Chem. Kinet., 40 (2008) 1 – 18.

[52] J. Wang, M. Chaos, B. Yang, T.A. Cool, F.L. Dryer, T. Kasper, N. Hansen,K. Kohse-Höinghaus, P.R. Westmoreland, Phys. Chem. Chem. Phys., 11 (2009) 1328 – 1339.

[53] T.A. Cool, J. Wang, N. Hansen, P.R. Westmoreland, F.L. Dryer, Z. Zhao, A. Kazakov, T. Kasper, K. Kohse-Höinghaus, Proc. Combust. Inst., 31 (2007) 285 – 293.

[54] R.D. Cook, D.F. Davidson, R.K. Hanson, J. Phys. Chem. A, 113 (2009) 9974 – 9980.

[55] S.H. Pyun, W. Ren, K.-Y. Lam, D.F. Davidson, R.K. Hanson, Combust. Flame, 160 (2013) 747 – 754.

[56] L.J. Spadaccini, M.B. Colket III., Prog. Energy Combust. Sci., 20 (1994) 431 – 460.

[57] T. Tsuboi, H.G. Wagner, Proc. Combust. Inst., 15 (1975) 883 – 890.

[58] E.L. Petersen, M. Röhrig, D.F. Davidson, R.K. Hanson, C.T. Bowman, Proc. Combust. Inst., 26 (1996) 799 – 806.

[59] E.L. Petersen, D.F. Davidson, R.K. Hanson, Combust. Flame, 117 (1999) 272 – 290.

[60] E.L. Petersen, D.F. Davidson, R.K. Hanson, J. Prop. Power 15 (1999) 82 – 91.

[61] L. Brett, J. Macnamara, P. Musch, J.M. Simmie, Combust. Flame, 124 (2001) 326 – 329.

[62] V.P. Zhukov, V.A. Sechenov, A.Y. Starikovskii, Combust. Expl. Shock Waves, 30 (2003) 487 – 495.

[63] J. Huang, P.G. Hill, W.K. Bushe, S.R. Munshi, Combust. Flame, 136 (2004) 25 – 42.

[64] U. Pfahl, K. Fieweger, G. Adomeit, Proc. Combust. Inst. 26 (1996) 781 – 789.

[65] G. Mittal, M. Chaos, C.-J. Sung, F.L. Dryer, Fuel Proc. Tech., 89 (2008) 1244 – 1254.

[66] R.D. Cook, D.F. Davidson, R.K. Hanson, Proc. Combust. Inst. 32 (2009) 189 – 196.

[67] C. Tang, L. Wei, J. Zhang, X. Man, Z. Huang, Energy Fuels, 26 (2012) 6720 – 6728.

[68] D. Liu, J. Santner, C. Togbé, D. Felsmann, J. Koppmann, A. Lackner, X. Yang, X. Shen, Y. Ju, K. Kohse-Höinghaus, Combust. Flame, 160 (2013) 2654 – 2668.

[69] H. Guo, W. Sun, F.M. Haas, T. Farouk, F.L. Dryer, Y. Ju, Proc. Combust. Inst., 34 (2013) 573 – 581.

[70] F. Herrmann, J. Beeckmann., P. Oβwald, L. Cai, H. Pitsch, K. Kohse-Höinghaus, Combust. Flame, 161 (2014) 384 – 397.

[71] CHEMKIN-PRO 15112, Reaction Design: San Diego, 2011.

[72] J. Würmel, Detailed Chemical Kinetics Combined with a Computational Fluid Dynamics Study of a Twin Piston Rapid Compression Machine, PhD Thesis, Dept. Chem., Natl. Univ. Ireland Galway, Ireland, 2004.

[73] E.R. Ritter, J.W. Bozzelli, Int. J. Chem. Kinet. 23 (1991) 767 – 778.

[74] S. M. Burke, Development of a Chemical Kinetic Mechanism for Small Hydrocarbons, PhD thesis, Dept. Chem., Natl. Univ. Ireland Galway, Ireland, 2013.

[75] T. Yamada, J.W. Bozzelli, T.H. Lay, Int. J. Chem. Kinet., 32 (2000) 435 – 452.

[76] W.K. Metcalfe, S.M. Burke, S.S. Ahmed, H.J. Curran, Int. J. Chem. Kinet., 45 (2013) 638 – 675.

[77] H.-H. Carstensen, A.M. Dean, Proc. Combust. Inst., 30 (2005) 995 – 1003.

[78] R.S. Tranter, P.T. Lynch, C.J. Annesley, J. Phys. Chem. A, 116 (2012) 7287 – 7292.

[79] A.Y. Chang, J.W. Bozzelli, A.M. Dean,, Z. Phys. Chem., 214 (2000) 1533 – 1568.

[80] Q.S. Li, Y. Zhang, S. Zhang, J. Phys. Chem. A, 108 (2004) 2014 – 2019.

[81] J.A. Miller, S.J. Klippenstein, J. Phys. Chem. A, 117 (2013) 2718 – 2727.

[82] C.F. Goldsmith, W.H. Green, S.J. Klippenstein, J. Phys. Chem. A, 116 (2012) 3325 – 3346.

[83] M.E.C. R. J. Kee, P. Glarborg, Chemically Reacting Flow Theory and Practice, 1st ed., John Wiley and Son, Inc. New Jersey, 2003.

[84] W.M. Haynes, Critical Constants of Organic Compounds, CRC Handbook of Chemistry and Physics, 91st ed., CRC Press, Boca Raton, Florida.

[85] A.W. Jasper, J.A. Miller, Combust. Flame., 2014, Volume 161, Issue 1, 101 – 110.

[86] J.A. Montgomery, M.J. Frisch, J.W. Ochterski, G.A. Petersson, J. Chem. Phys., 2000, 112, 6532 – 6542.

[87] J.W. Ochterski, G.A. Petersson, J.A. Montgomery, J. Chem. Phys., 1996, 104, 2598 – 2619.

[88] L.A. Curtiss, K. Raghavachari, P.C. Redfern, V. Rassolov, J.A. Pople, J. Chem. Phys., 1998, 109, 7764 – 7776.

[89] A.D. Becke, J. Chem. Phys., 1993, 98, 5648 – 5652.

[90] C. Lee, W. Yang, R.G. Parr, Phys. Rev. B, 1988, 37, 785 – 789.

[91] Gaussian 09, Revision C.01, M. J. Frisch, G. W. Trucks, H. B. Schlegel, G. E. Scuseria, M. A. Robb, J. R. Cheeseman, J. A. Montgomery, Jr., T. Vreven, K. N. Kudin, J. C. Burant, J. M. Millam, S. S. Iyengar, J. Tomasi, V. Barone, B. Mennucci, M. Cossi, G. Scalmani, N. Rega, G. A. Petersson, H. Nakatsuji, M. Hada, M. Ehara, K. Toyota, R. Fukuda, J. Hasegawa, M. Ishida, T. Nakajima, Y. Honda, O. Kitao, H. Nakai, M. Klene, X. Li, J. E. Knox, H. P. Hratchian, J. B. Cross, V. Bakken, C. Adamo, J. Jaramillo, R. Gomperts, R. E. Stratmann, O. Yazyev, A. J. Austin, R. Cammi, C. Pomelli, J. W. Ochterski, P. Y. Ayala, K. Morokuma, G. A. Voth, P. Salvador, J. J. Dannenberg, V. G. Zakrzewski, S. Dapprich, A. D. Daniels, M. C. Strain, O. Farkas, D. K. Malick, A. D. Rabuck, K. Raghavachari, J. B. Foresman, J. V. Ortiz, Q. Cui, A. G. Baboul, S. Clifford, J. Cioslowski, B. B. Stefanov, G. Liu, A. Liashenko, P. Piskorz, I. Komaromi, R. L. Martin, D. J. Fox, T. Keith, M. A. Al-Laham, C. Y. Peng, A. Nanayakkara, M. Challacombe, P. M. W. Gill, B. Johnson, W. Chen, M. W. Wong, C. Gonzalez, and J. A. Pople, Gaussian, Inc., Wallingford CT, 2004.

[92] Mokrushin, V.; Tsang, W. ChemRate version 1.5.8, NIST, Gaithersburg, MD 20899, <http://mokrushin.com/ChemRate/chemrate.html> (accessed June 21 2013).

[93] J. Sehested, K. Sehested, J. Platz, H. Egsgaard, O.J. Nielsen, Int. J. Chem. Kinet., 29 (1997) 627 – 636.

[94] K.A. Sahetchian, R. Rigny, J. Tardieu de Maleissye, L. Batt, M. Anwar Khan, S. Mathews, Sym. (Int.) Combust. 24 (1992) 637 – 643.

[95] C.M. Zinner, Methane and Dimethyl Ether Oxidation at Elevated Temperatures and Pressure, M.Sc. Thesis, Univ. of Central Florida, USA, 2006.

[96] J. Pemelton, N. Marquet, W. Metcalfe, H.J. Curran, E.L. Petersen, 7th US Natl. Tech. Meet. Combust. Inst., Atlanta, GA (2011).

[97] G.A. Olah, A. Goeppert, G.K.S. Prakash, J. Org. Chem. 74 (2008) 487 – 498.

[98] D.F. Cooke, M.G. Dodson, A. Williams, Combust. Flame 16 (1971) 233 – 236.

[99] C.T. Bowman, Combust. Flame 25 (1975) 343 – 354.

[100] T. Tsuboi, K. Hashimoto, Combust. Flame 42 (1981) 61 – 76.

[101] K. Fieweger, R. Blumenthal, G. Adomeit, Combust. Flame 109 (1997) 599 – 619.

[102] K.E. Noorani, B. Akih-Kumgeh, J.M. Bergthorson, Energy Fuels 24 (2010) 5834 – 5843.

[103] K. Kumar, C.J. Sung, Int. J. Chem. Kinet. 43 (2011) 175 – 184.

[104] G. Dayma, K.H. Ali, P. Dagaut, Proc. Combust. Inst. 31 (2007) 411 – 418.

[105] Cathonnet, M., Boettner, J.-C., James, H., J. Chim. Phys. 76 (1979) 183 – 189.

[106] D. Aronowitz, D.W. Naegeli, I. Glassman, J. Phys. Chem. 81 (1977) 2555 – 2559.

[107] T.S. Norton, F.L. Dryer, Combust. Sci. Technol. 63 (1989) 107 – 129.

[108] T.J. Held, F.L. Dryer, Proc. Combust. Inst. 25 (1994) 901 – 908.

[109] M.U. Alzueta, R. Bilbao, M. Finestra, Energy Fuels 15 (2001) 724 – 729.

[110] W.-C. Ing, C.Y. Sheng, J.W. Bozzelli, Fuel Proc. Technol. 83 (2003) 111 – 145.

[111] C.L. Rasmussen, K.H. Wassard, K. Dam-Johansen, P. Glarborg, Int. J. Chem. Kinet. 40 (2008) 423 – 441.

[112] V. Aranda, J.M. Christensen, M.U. Alzueta, P. Glarborg, S. Gersen, Y. Gao, P. Marshall, Int. J. Chem. Kinet. 45 (2013) 283 – 294.

[113] K.W. Aniolek, R.D. Wilk, Energy Fuels 9 (1995) 395 – 405.

[114] R. Akrich, C. Vovelle, R. Delbourgo, Combust. Flame 32 (1978) 171 – 179.

[115] F.N. Egolfopoulos, D.X. Du, C.K. Law, Combust. Sci. Tech. 83 (1992) 33 – 75.

[116] S.Y. Liao, D.M. Jiang, Z.H. Huang, W.D. Shen, C. Yuan, Q. Cheng, Energy Convers. Manag. 48 (2007) 857 – 863.

[117] P.S. Veloo, Y.L. Wang, F.N. Egolfopoulos, C.K. Westbrook, Combust. Flame 157 (2010) 1989 – 2004.

[118] J. Vancoillie, M. Christensen, E.J.K. Nilsson, S. Verhelst, A.A. Konnov, Energy Fuels 26 (2012) 1557 – 1564.

[119] S.J. Klippenstein, L.B. Harding, M.J. Davis, A.S. Tomlin, R.T. Skodje, Proc. Combust. Inst. 33 (2011) 351 – 357.

[120] M. Altarawneh, A.A.H. Al-Muhtaseb, B.Z. Dlugogorski, E.M. Kennedy, J.C. Mackie, J. Comp. Chem. 32 (2011) 1725 – 1733.

[121] I.M. Alecu, D.G. Truhlar, J. Phys. Chem. A 115 (2011) 14599 – 14611.

[122] J. Li, Z. Zhao, A. Kazakov, M. Chaos, F.L. Dryer, J.I. Scire Jr, Int. J. Chem. Kinet. 39 (2007) 109 – 136.

[123] J.F. Bott, N. Cohen, Int. J. Chem. Kinet. 23 (1991) 1075 – 1094.

[124] S. Xu, M.C. Lin, Proc. Combust. Inst. 31 (2007) 159 – 166.

[125] J. Warnatz, In Combustion Chemistry. W.C. Gardiner, Jr. (Ed.), Springer-Verlag, New York, 1984.

[126] R. Meana-Pañeda, D.G. Truhlar, A. Fernández-Ramos, J. Chem. Phys. 134 (2011) - 094302.

[127] A. Kéromnès, W.K. Metcalfe, K.A. Heufer, N. Donohoe, A.K. Das, C.-J. Sung, J. Herzler, C. Naumann, P. Griebel, O. Mathieu, M.C. Krejci, E.L. Petersen, W.J. Pitz, H.J. Curran, Combust. Flame 160 (2013) 995 – 1011.

[128] S. M. Burke, W.K. Metcalfe, O. Herbinet, F. Battin-Leclerc, F. M. Haas, J. Santner, F. L. Dryer, H. J. Curran, Combust. Flame 2014, 161 (11), 2765 – 2784.

[129] C. Olm, I.G. Zsély, R. Pálvölgyi, T. Varga, T. Nagy, H.J. Curran, T. Turányi, Combust. Flame (2014) http://dx.doi.org/10.1016/j.combustflame.2014.03.006.

[130] H. Hippler, J. Troe, J. Willner, J. Chem. Phys. 93 (1990) 1755 – 1760.

[131] J. Troe, Combust. Flame 158 (2011) 594 – 601.

[132] C.K. Westbrook, W.J. Pitz, H.J. Curran, J. Phys. Chem. A 110 (21) (2006) 6912 – 6922.

[133] D. Darcy, M. Mehl, J.M. Simmie, J. Würmel, W.K. Metcalfe, C.K. Westbrook, W.J. Pitz, H.J. Curran, Proc. Combust. Inst. 34 (1) (2013) 411 – 418.

[134] R. Mével, P.A. Boettcher, J.E. Shepherd, Chem. Phys. Lett. 531 (2012) 22 – 27.

[135] K. Yasunaga, J.M. Simmie, H.J. Curran, T. Koike, O. Takahashi, Y. Kuraguchi, Y. Hidaka, Combust. Flame, 158 (2011) 1032 – 1036.

[136] S.M. Sarathy, S. Vranckx, K. Yasunaga, M. Mehl, P. Oβwald, W.K. Metcalfe, C.K. Westbrook, W.J. Pitz, K. Kohse-Höinghaus, R.X. Fernandes, H.J. Curran, Combust. Flame, 159 (2012) 2028 – 2055.

[137] S.M. Sarathy, C.K. Westbrook, M. Mehl, W.J. Pitz, C. Togbe, P. Dagaut, H. Wang, M.A. Oehlschlaeger, U. Niemann, K. Seshadri, P.S. Veloo, C. Ji, F.N. Egolfopoulos, T. Lu, Combust. Flame, 158 (2011) 2338 – 2357.

[138] K.P. Somers, J.M. Simmie, F. Gillespie, U. Burke, J. Connolly, W.K. Metcalfe, F. Battin-Leclerc, P. Dirrenberger, O. Herbinet, P.A. Glaude, H.J. Curran, Proc. Combust. Inst., 34 (2013) 225 – 232.

[139] S.M. Burke, U. Burke, R. McDonagh, O. Mathieu, I. Osorio, C. Keesee, A. Morones, E.L. Petersen, W. Wang, M.A. Oehlschlaeger, B. Rhodes, R.K. Hanson, D. Davidson, B.W. Weber, C.J. Sung, J. Santner, Y. Ju, E.N. Volkov, A.A. Konnov, M. Alrefae, F. Khaled, A. Farooq, H.J. Curran, *accepted for publication in* Combust. Flame, <doi:10.1016/j.combustflame.2014.07.032>.

[140] K.P. Somers, J.M. Simmie, W.K. Metcalfe, H.J. Curran, Phys. Chem. Chem. Phys., 16, (2014), 5349 – 5367.

[141] U. Burke, K. P. Somers, P. O'Toole, C. M. Zinner, N. Marquet, G. Bourque, E. L. Petersen, W. K. Metcalfe, Z. Serinyel, H. J. Curran, Combust. Flame <doi:10.1016/j.combustflame.2014.08.014>.

Appendix A

Dimethyl Ether Mechanism Validation

A.1 Updated Group Values

Table A.1: Optimised Group Values Pertaining to Ether Thermochemistry.

			C_p / cal mol^{-1}						
Group	**H_f / kcal mol^{-1}**	**S / cal mol^{-1}**	**300**	**400**	**500**	**600**	**800**	**1000**	**1500**
C/H2/O/OO	-14.46	6.35	3.78	5.58	7.58	8.85	10.30	11.66	27.86
BD Group	**ΔH_r / kcal mol^{-1}**	**Δ S / cal mol^{-1}**	**ΔC_p / cal mol^{-1}**						
CJOC	95.94	1.48	-1.04	-1.12	-1.44	-1.88	-2.85	-3.61	-4.26

A.2 CH_4 Experimental Data

ϕ = 0.30 CH4 in "air" (RCM)			
Temp / K	**1000/T**	**p / atm**	**ign. delay / μs**
1087.25	0.92	9.59	78000
1087.82	0.92	9.61	73600
1116.77	0.90	9.82	32300
1119.38	0.89	9.88	32800
1143.04	0.87	9.84	20100
1144.26	0.87	9.88	23300
1177.79	0.85	10.11	7800
1178.19	0.85	10.21	5500

ϕ = 0.30 CH4 in "air"			
Temp / K	**1000/T**	**p / atm**	**ign. delay / μs**
1056.78	0.95	21.69	16100 (RCM)
1069.16	0.94	22.51	13000 (RCM)
1098.61	0.91	22.55	9600 (RCM)
1099.88	0.91	22.65	9600 (RCM)
1123.72	0.89	22.58	5000 (RCM)
1123.46	0.89	22.58	5800 (RCM)
1146.59	0.87	22.29	4600 (RCM)
1150.55	0.87	22.50	3600 (RCM)
1223.60	0.82	19.50	1623.00 (ST)
1191.70	0.84	19.66	2202.00 (ST)
1237.60	0.81	19.16	1342.00 (ST)
1342.00	0.75	19.91	642.14 (ST)
1285.90	0.78	19.76	1009.00 (ST)
1413.50	0.71	19.91	300.23 (ST)
1257.80	0.80	19.80	1208.00 (ST)
1282.00	0.78	20.00	1289.00 (ST)
1335.00	0.75	19.10	742.00 (ST)
1351.00	0.74	18.20	627.00 (ST)
1420.00	0.70	17.20	314.00 (ST)
1468.00	0.68	16.50	186.00 (ST)

ϕ = 0.30 CH4 in "air" (ST)			
Temp / K	**1000/T**	**p / atm**	**ign. delay / μs**
1239.80	0.81	42.31	1006.00
1178.50	0.85	41.57	1549.00
1207.60	0.83	41.44	1310.00
1295.10	0.77	39.88	593.03
1271.00	0.79	49.20	731.00
1315.00	0.76	47.00	458.00
1338.00	0.75	46.70	385.00
1393.00	0.72	41.80	209.00

ϕ = 0.50 CH4 in "air"			
***p* / atm**	**Temp / K**	**1000/*T***	**ign. delay / μs**
10.41	1035.97	0.97	219500 (RCM)
10.41	1035.80	0.97	196700 (RCM)
10.37	1055.83	0.95	86500 (RCM)
10.43	1057.10	0.95	91200 (RCM)
10.59	1084.15	0.92	61300 (RCM)
10.61	1084.47	0.92	58200 (RCM)
10.30	1100.13	0.91	34300 (RCM)
10.32	1098.68	0.91	34700 (RCM)
10.76	1139.71	0.88	21800 (RCM)
10.96	1146.32	0.87	19100 (RCM)
10.89	1164.00	0.86	11000 (RCM)
10.89	1164.27	0.86	11000 (RCM)
10.94	1189.20	0.84	5400 (RCM)
11.80	1335.00	0.75	1011.00 (ST)
11.10	1390.00	0.72	630.00 (ST)
11.10	1447.00	0.69	373.00 (ST)
9.90	1507.00	0.66	223.00 (ST)
9.00	1616.00	0.62	82.00 (ST)

ϕ = 0.50 CH4 in "air"			
p / atm	Temp / K	1000/T	ign. delay / μs
24.75	992.93	1.01	28900 (RCM)
25.03	996.72	1.00	28000 (RCM)
24.55	1013.06	0.99	19700 (RCM)
24.96	1017.89	0.98	19000 (RCM)
24.74	1039.43	0.96	14700 (RCM)
25.11	1044.35	0.96	13600 (RCM)
24.40	1060.92	0.94	10700 (RCM)
24.64	1061.19	0.94	11000 (RCM)
24.24	1082.59	0.92	7700 (RCM)
24.80	1090.27	0.92	6900 (RCM)
24.44	1111.49	0.90	5000 (RCM)
24.48	1111.77	0.90	5000 (RCM)
26.20	1287.10	0.78	756.61 (ST)
24.77	1328.60	0.75	525.21 (ST)
24.78	1380.40	0.72	350.10 (ST)
25.89	1269.10	0.79	807.95 (ST)
25.06	1232.90	0.81	1025.00 (ST)
25.35	1435.70	0.70	219.61 (ST)
26.01	1396.30	0.72	262.07 (ST)
25.14	1494.70	0.67	127.85 (ST)

ϕ = 0.50 CH4 in "air" (ST)			
p / atm	Temp / K	1000/T	ign. delay / μs
48.20	1238.00	0.81	894.00
43.00	1338.00	0.75	316.00
42.60	1392.00	0.72	179.00
42.00	1425.00	0.70	122.00

ϕ = 1.00 CH4 in "air"			
p / atm	Temp / K	1000/T	ign. delay / μs
10.55	986.31	1.01	183600 (RCM)
10.58	986.67	1.01	188300 (RCM)
10.52	1003.62	1.00	115800 (RCM)
10.58	1004.78	1.00	113400 (RCM)
10.45	1024.33	0.98	82900 (RCM)
10.80	1033.40	0.97	67700 (RCM)
10.79	1054.17	0.95	50200 (RCM)
10.79	1056.43	0.95	51400 (RCM)
10.70	1073.28	0.93	35900 (RCM)
10.73	1073.58	0.93	37100 (RCM)
10.92	1098.06	0.91	23800 (RCM)
11.05	1103.55	0.91	23900 (RCM)
9.38	1236.80	0.81	2914.00 (ST)
12.30	1312.00	0.76	1519.00 (ST)
11.40	1361.00	0.73	884.00 (ST)
10.20	1470.00	0.68	378.00 (ST)
9.60	1506.00	0.66	282.00 (ST)
9.20	1571.00	0.64	157.00 (ST)

ϕ = **1.00 CH4 in "air"**			
p **/ atm**	**Temp / K**	**1000/** T	**ign delay /** μ**s**
24.30	921.84	1.08	72800 (RCM)
24.68	926.02	1.08	66400 (RCM)
24.70	926.16	1.08	67300 (RCM)
24.20	942.36	1.06	40200 (RCM)
24.54	946.54	1.06	38800 (RCM)
24.35	968.13	1.03	26200 (RCM)
24.59	971.00	1.03	27100 (RCM)
24.13	986.80	1.01	17900 (RCM)
24.20	987.64	1.01	18100 (RCM)
24.00	1006.33	0.99	13800 (RCM)
24.26	1009.32	0.99	13300 (RCM)
24.08	1030.42	0.97	10400 (RCM)
24.70	1038.15	0.96	9600 (RCM)
24.65	1060.92	0.94	7500 (RCM)
24.67	1061.23	0.94	7200 (RCM)
24.70	1084.92	0.92	5800 (RCM)
24.79	1085.94	0.92	5600 (RCM)
26.16	1285.20	0.78	792.61 (ST)
24.74	1301.20	0.77	770.32 (ST)
25.11	1233.00	0.81	1130.00 (ST)
24.90	1331.20	0.75	606.74 (ST)
24.92	1357.50	0.74	530.61 (ST)
25.04	1412.50	0.71	295.73 (ST)
25.58	1181.30	0.85	1324.00 (ST)
24.99	1447.50	0.69	216.76 (ST)
24.70	1479.80	0.68	165.89 (ST)

ϕ = **2.00 CH4 in "air"**			
p **/ atm**	**Temp / K**	**1000/** T	**ign. delay /** μ**s**
10.40	970.29	1.03	232600 (RCM)
10.59	975.15	1.03	143500 (RCM)
10.72	977.83	1.02	138500 (RCM)
10.30	982.12	1.02	93100 (RCM)
10.62	989.58	1.01	91200 (RCM)
10.82	994.29	1.01	83900 (RCM)
10.36	1003.83	1.00	58100 (RCM)
10.50	1007.17	0.99	64400 (RCM)
10.66	1011.07	0.99	60400 (RCM)
10.10	1358.00	0.74	1233.00 (ST)
10.00	1425.00	0.70	756.00 (ST)
9.10	1457.00	0.69	508.00 (ST)
7.80	1557.00	0.64	240.00 (ST)
7.20	1633.00	0.61	126.00 (ST)

ϕ = 2.00 CH4 in "air"			
p / atm	Temp / K	1000/T	ign. delay / μs
23.04	869.90	1.15	206200 (RCM)
23.21	872.26	1.15	222900 (RCM)
23.76	899.45	1.11	77700 (RCM)
23.88	921.44	1.09	40500 (RCM)
24.35	924.41	1.08	41000 (RCM)
24.13	939.58	1.06	27400 (RCM)
24.43	942.89	1.06	26800 (RCM)
24.53	964.43	1.04	20300 (RCM)
24.69	966.23	1.03	18700 (RCM)
23.81	977.37	1.02	15100 (RCM)
24.76	986.41	1.01	14900 (RCM)
15.30	1338.00	0.75	959.00 (ST)
15.10	1414.00	0.71	540.00 (ST)
14.10	1471.00	0.68	359.00 (ST)
13.50	1506.00	0.66	254.00 (ST)
12.70	1533.00	0.65	181.00 (ST)

ϕ = 0.30 80/20 CH4/DME in "air" (ST)			
Temp / K	1000/T	p / atm	ign. delay / μs
1170.00	0.85	8.00	2075.00
1214.00	0.82	7.90	1244.00
1234.00	0.81	7.60	949.00
1307.00	0.77	7.60	391.00
1325.00	0.75	7.20	293.00
1400.00	0.71	7.00	126.00
1433.00	0.70	6.70	64.00

ϕ = 0.30 80/20 CH4/DME in "air"			
p / atm	Temp / K	1000/T	ign. delay / μs
14.85	867.00	1.15	55200 (RCM)
15.27	873.00	1.15	62600 (RCM)
14.50	901.00	1.11	53700 (RCM)
14.53	901.00	1.11	43800 (RCM)
14.48	944.00	1.06	25800 (RCM)
14.43	946.00	1.06	25300 (RCM)
14.44	989.00	1.01	12100 (RCM)
14.43	991.00	1.01	11800 (RCM)
14.43	1027.00	0.97	6300 (RCM)
14.39	1027.00	0.97	6500 (RCM)
24.60	1170.00	0.85	988.00 (ST)
24.30	1193.00	0.84	746.00 (ST)
22.50	1227.00	0.81	474.00 (ST)
21.70	1299.00	0.77	250.00 (ST)
19.60	1353.00	0.74	159.00 (ST)
19.00	1416.00	0.71	74.00 (ST)

ϕ = 0.30 80/20 CH4/DME in "air"			
p / atm	Temp / K	1000/T	ign. delay / μs
29.99	727.00	1.38	62700 (RCM)
29.98	726.00	1.38	62100 (RCM)
32.74	786.00	1.27	31400 (RCM)
32.95	789.00	1.27	31200 (RCM)
32.23	823.00	1.22	18200 (RCM)
31.82	852.00	1.17	11200 (RCM)
31.89	853.00	1.17	11700 (RCM)
31.24	878.00	1.14	8400 (RCM)
31.37	879.00	1.14	8900 (RCM)
31.16	907.00	1.10	5500 (RCM)
31.39	909.00	1.10	5100 (RCM)
28.73	832.00	1.20	11200 (RCM)
30.32	845.00	1.18	11800 (RCM)
30.48	911.00	1.10	5600 (RCM)
29.52	952.00	1.05	4700 (RCM)
29.75	951.00	1.05	4600 (RCM)
29.59	996.00	1.00	2800 (RCM)
29.87	999.00	1.00	2100 (RCM)
34.10	1046.00	0.96	2114.00 (ST)
32.60	1088.00	0.92	1532.00 (ST)
31.20	1171.00	0.85	740.00 (ST)
29.50	1271.00	0.79	276.00 (ST)
28.00	1320.00	0.76	151.00 (ST)
28.20	1438.00	0.70	73.00 (ST)

ϕ = 0.50 80/20 CH4/DME in "air"			
p / atm	**Temp / K**	**1000/T**	**ign delay / μs**
9.75	836.00	1.20	169200 (RCM)
9.83	859.00	1.16	129300 (RCM)
9.89	862.00	1.16	115400 (RCM)
9.65	887.00	1.13	80580 (RCM)
9.77	890.00	1.12	86950 (RCM)
9.58	929.00	1.08	38800 (RCM)
9.68	930.00	1.08	45200 (RCM)
9.58	982.00	1.02	17540 (RCM)
9.46	978.00	1.02	17230 (RCM)
8.40	1153.00	0.87	2133.00 (ST)
8.20	1207.00	0.83	1159.00 (ST)
8.10	1254.00	0.80	668.00 (ST)
7.60	1283.00	0.78	469.00 (ST)
7.50	1335.00	0.75	266.00 (ST)
7.10	1393.00	0.72	118.00 (ST)
6.50	1473.00	0.68	56.00 (ST)

ϕ = 0.50 80/20 CH4/DME in "air"			
p / atm	**Temp / K**	**1000/T**	**ign. delay / μs**
19.50	890.00	1.12	12320 (RCM)
19.89	894.00	1.12	11650 (RCM)
19.47	932.00	1.07	7148 (RCM)
19.66	934.00	1.07	6604 (RCM)
19.78	682.00	1.47	170300 (RCM)
19.57	705.00	1.42	104900 (RCM)
19.51	706.00	1.42	91920 (RCM)
19.39	730.00	1.37	75330 (RCM)
19.43	729.00	1.37	69440 (RCM)
18.89	749.00	1.34	57700 (RCM)
19.17	751.00	1.33	55960 (RCM)
19.15	774.00	1.29	44990 (RCM)
19.18	774.00	1.29	44030 (RCM)
19.30	790.00	1.27	38150 (RCM)
19.26	790.30	1.27	37960 (RCM)
21.40	1032.00	0.97	2719.00 (ST)
20.60	1050.00	0.95	2366.00 (ST)
19.50	1132.00	0.88	1283.00 (ST)
18.60	1218.00	0.82	541.00 (ST)
17.60	1297.00	0.77	240.00 (ST)
16.20	1395.00	0.72	80.00 (ST)
15.60	1442.00	0.69	46.00 (ST)

ϕ = 0.50 80/20 CH4/DME in "air" (RCM)			
p / atm	Temp / K	1000/T	ign. delay / μs
29.40	661.00	1.51	156000
29.25	660.00	1.52	161400
28.87	682.00	1.47	81770
30.11	682.00	1.47	78390
30.24	682.00	1.47	78000
29.46	704.00	1.42	45310
29.46	703.00	1.42	45380
29.58	728.00	1.37	30100
29.58	727.00	1.38	29360
29.37	751.00	1.33	22280
30.02	773.70	1.29	15310
29.92	775.50	1.29	16850
30.29	788.90	1.27	13870
30.21	789.50	1.27	13890

ϕ = 1.00 80/20 CH4/DME in "air"			
p / atm	Temp / K	1000/T	ign. delay / μs
9.85	686.00	1.46	80980 (RCM)
9.91	686.00	1.46	78320 (RCM)
9.92	711.00	1.41	67200 (RCM)
9.91	711.00	1.41	66150 (RCM)
9.68	741.00	1.35	61230 (RCM)
9.73	741.00	1.35	60690 (RCM)
9.50	769.00	1.30	55930 (RCM)
9.55	770.00	1.30	53820 (RCM)
8.10	1198.00	0.83	1074.00 (ST)
7.70	1223.00	0.82	854.00 (ST)
7.50	1272.00	0.79	450.00 (ST)
7.00	1303.00	0.77	316.00 (ST)
6.80	1376.00	0.73	152.00 (ST)
6.10	1464.00	0.68	68.00 (ST)

ϕ = 1.00 80/20 CH4/DME in "air"			
p / atm	Temp / K	1000/T	ign. delay / μs
19.78	641.00	1.56	243800 (RCM)
19.37	663.00	1.51	72530 (RCM)
19.32	663.00	1.51	73410 (RCM)
19.65	686.00	1.46	28250 (RCM)
19.66	686.00	1.46	27110 (RCM)
19.49	709.00	1.41	16310 (RCM)
19.89	712.00	1.40	16080 (RCM)
19.42	741.00	1.35	10930 (RCM)
19.47	739.00	1.35	10920 (RCM)
20.07	777.00	1.29	8461 (RCM)
20.09	777.00	1.29	8448 (RCM)
24.90	1104.00	0.91	970.00 (ST)
24.40	1150.00	0.87	667.00 (ST)
23.20	1174.00	0.85	548.00 (ST)
21.10	1188.00	0.84	499.00 (ST)
20.90	1266.00	0.79	244.00 (ST)
20.30	1316.00	0.76	149.00 (ST)
18.90	1393.00	0.72	73.00 (ST)

ϕ = 1.00 80/20 CH4/DME in "air"			
p / atm	Temp / K	1000/T	ign. delay / μs
29.75	642.00	1.56	220400 (RCM)
29.61	642.00	1.56	194500 (RCM)
28.91	664.00	1.51	52540 (RCM)
29.05	664.00	1.51	53120 (RCM)
29.36	687.00	1.46	19500 (RCM)
29.26	686.00	1.46	19330 (RCM)
29.22	710.00	1.41	9465 (RCM)
29.34	711.00	1.41	9355 (RCM)
29.28	743.00	1.35	5270 (RCM)
29.28	743.00	1.35	5284 (RCM)
35.20	996.00	1.00	1180.00 (ST)
32.50	1040.00	0.96	985.00 (ST)
31.60	1119.00	0.89	598.00 (ST)
30.00	1212.00	0.83	296.00 (ST)
27.70	1299.00	0.77	130.00 (ST)
26.00	1347.00	0.74	80.00 (ST)

ϕ = 2.00 80/20 CH4/DME in "air"			
p / atm	Temp / K	1000/T	ign. delay / μs
5.99	734.00	1.36	23200 (RCM)
5.73	758.00	1.32	25100 (RCM)
5.87	762.00	1.31	24600 (RCM)
5.78	759.00	1.32	24900 (RCM)
6.01	767.00	1.30	23700 (RCM)
5.76	790.00	1.27	27400 (RCM)
5.78	791.00	1.26	25900 (RCM)
6.06	802.00	1.25	21500 (RCM)
6.12	833.00	1.20	19100 (RCM)
6.14	836.00	1.20	21300 (RCM)
6.16	805.00	1.24	22800 (RCM)
6.17	805.00	1.24	21600 (RCM)
5.79	822.00	1.22	25200 (RCM)
5.79	824.00	1.21	24800 (RCM)
5.73	858.00	1.17	21400 (RCM)
5.88	892.00	1.12	18300 (RCM)
5.87	862.00	1.16	22100 (RCM)
7.50	1190.00	0.84	1049.00 (ST)
7.20	1227.00	0.81	662.00 (ST)
6.90	1281.00	0.78	383.00 (ST)
6.30	1314.00	0.76	283.00 (ST)
5.90	1387.00	0.72	149.00 (ST)
5.40	1491.00	0.67	62.00 (ST)

ϕ = 2.00 80/20 CH4/DME in "air"			
p / atm	Temp / K	1000/T	ign. delay / μs
25.30	631.00	1.58	139600 (RCM)
25.38	629.00	1.59	179400 (RCM)
25.52	630.00	1.59	99600 (RCM)
25.26	674.00	1.48	15100 (RCM)
25.38	674.00	1.48	14800 (RCM)
25.11	706.00	1.42	3700 (RCM)
25.17	706.00	1.42	4000 (RCM)
21.60	929.00	1.08	2287.00 (ST)
20.50	956.00	1.05	2091.00 (ST)
20.20	993.00	1.01	1809.00 (ST)
19.10	1020.00	0.98	1754.00 (ST)
18.90	1074.00	0.93	1311.00 (ST)
17.70	1123.00	0.89	915.00 (ST)
17.00	1195.00	0.84	477.00 (ST)

ϕ = 2.00 80/20 CH4/DME in "air" (ST)			
p / atm	Temp / K	1000/T	ign. delay / μs
39.70	1086.00	0.92	440.00
45.20	1192.00	0.84	177.00
46.30	1251.00	0.80	118.00
46.30	1298.00	0.77	67.00
47.70	1335.00	0.75	60.00
44.20	1344.00	0.74	52.00

ϕ = 0.30 60/40 CH4/DME in "air" (ST)			
Temp / K	**1000/*T***	***P* / atm**	**ign. delay / μs**
1168.00	0.86	8.40	1363.00
1223.00	0.82	8.20	717.00
1262.00	0.79	7.90	436.00
1262.00	0.79	7.90	453.00
1297.00	0.77	7.70	278.00
1347.00	0.74	7.40	130.00
1380.00	0.72	7.00	80.00
1422.00	0.70	6.70	57.00

ϕ = 0.30 60/40 CH4/DME in "air"			
p / atm	Temp / K	1000/T	ign. delay / μs
28.90	753.00	1.33	9000 (RCM)
28.92	752.00	1.33	8200 (RCM)
27.74	786.00	1.27	5800 (RCM)
28.01	786.00	1.27	5300 (RCM)
27.76	821.00	1.22	3600 (RCM)
27.79	821.00	1.22	3900 (RCM)
27.09	853.00	1.17	2900 (RCM)
27.06	854.00	1.17	2700 (RCM)
35.70	1014.00	0.99	1476.00 (ST)
34.50	1052.00	0.95	1120.00 (ST)
33.80	1120.00	0.89	683.00 (ST)
33.10	1209.00	0.83	304.00 (ST)
30.00	1285.00	0.78	153.00 (ST)
27.60	1384.00	0.72	46.00 (ST)
26.80	1414.00	0.71	36.00 (ST)

ϕ = 0.50 60/40 CH4/DME in "air" (ST)			
p / atm	Temp / K	1000/T	ign. delay / μs
8.50	1169.00	0.86	1145.00
8.30	1248.00	0.80	439.00
7.80	1287.00	0.78	287.00
7.70	1335.00	0.75	164.00
7.10	1377.00	0.73	91.00
6.80	1422.00	0.70	64.00

ϕ = 0.50 60/40 CH4/DME in "air"			
p / atm	Temp / K	1000/T	ign. delay / μs
19.05	703.00	1.42	8600 (RCM)
19.25	705.00	1.42	8900 (RCM)
18.85	742.00	1.35	4400 (RCM)
18.87	742.00	1.35	5000 (RCM)
18.48	795.00	1.26	3600 (RCM)
22.02	819.00	1.22	2600 (RCM)
20.66	820.00	1.22	3200 (RCM)
21.00	1047.00	0.96	1474.00 (ST)
20.30	1115.00	0.90	828.00 (ST)
20.00	1204.00	0.83	396.00 (ST)
18.50	1258.00	0.79	219.00 (ST)
17.10	1347.00	0.74	86.00 (ST)
16.00	1395.00	0.72	43.00 (ST)

ϕ = 0.50 60/40 CH4/DME in "air"			
p / atm	Temp / K	1000/T	ign. delay / μs
28.46	702.00	1.42	6600 (RCM)
28.62	703.00	1.42	6600 (RCM)
28.50	743.00	1.35	2400 (RCM)
25.70	1071.00	0.93	915.00 (ST)
25.60	1124.00	0.89	624.00 (ST)
24.20	1151.00	0.87	522.00 (ST)
23.60	1211.00	0.83	305.00 (ST)
22.80	1268.00	0.79	220.00 (ST)
60.90	1291.00	0.77	61.00 (ST)
52.20	1316.00	0.76	61.00 (ST)
21.60	1368.00	0.73	69.00 (ST)
45.10	1385.00	0.72	30.00 (ST)

ϕ = 1.00 60/40 CH4/DME in "air"			
p / atm	Temp / K	1000/T	ign. delay / μs
10.22	651.00	1.54	42990 (RCM)
9.92	646.00	1.55	53390 (RCM)
9.70	668.00	1.50	26020 (RCM)
9.64	668.00	1.50	26820 (RCM)
9.50	698.00	1.43	11910 (RCM)
9.49	698.00	1.43	11790 (RCM)
9.52	730.00	1.37	10280 (RCM)
9.43	730.00	1.37	10620 (RCM)
8.20	1135.00	0.88	1314.00 (ST)
8.20	1174.00	0.85	882.00 (ST)
8.10	1220.00	0.82	493.00 (ST)
7.30	1283.00	0.78	235.00 (ST)
7.00	1356.00	0.74	108.00 (ST)
6.50	1424.00	0.70	42.00 (ST)

ϕ = 1.00 60/40 CH4/DME in "air"			
p / atm	Temp / K	1000/T	ign. delay / μs
19.71	646.00	1.55	56030 (RCM)
19.76	646.00	1.55	52100 (RCM)
19.33	668.00	1.50	19240 (RCM)
19.27	668.00	1.50	18320 (RCM)
19.18	700.00	1.43	5005 (RCM)
19.24	700.00	1.43	4955 (RCM)
24.20	1090.00	0.92	592.00 (ST)
23.20	1128.00	0.89	373.00 (ST)
24.00	1194.00	0.84	253.00 (ST)
24.30	1254.00	0.80	159.00 (ST)
20.80	1264.00	0.79	145.00 (ST)
19.10	1366.00	0.73	54.00 (ST)

ϕ = 1.00 60/40 CH4/DME in "air"			
p / atm	Temp / K	1000/T	ign. delay / μs
29.87	623.00	1.61	287700 (RCM)
29.93	624.00	1.60	219600 (RCM)
29.66	647.00	1.55	55150 (RCM)
29.58	646.00	1.55	52410 (RCM)
29.21	669.00	1.49	16760 (RCM)
29.29	670.00	1.49	16010 (RCM)
28.87	700.00	1.43	3718 (RCM)
29.05	701.00	1.43	3588 (RCM)
34.40	989.00	1.01	679.00 (ST)
30.50	997.00	1.00	477.00 (ST)
29.90	1020.00	0.98	641.00 (ST)
34.90	1070.00	0.93	435.00 (ST)
33.90	1083.00	0.92	397.00 (ST)
34.10	1135.00	0.88	285.00 (ST)
32.20	1229.00	0.81	135.00 (ST)
28.00	1327.00	0.75	57.00 (ST)

ϕ = 2.00 60/40 CH4/DME in "air"			
p / atm	Temp / K	1000/T	ign. delay / μs
6.58	664.00	1.51	31400 (RCM)
6.67	666.00	1.50	28700 (RCM)
6.67	694.00	1.44	10900 (RCM)
6.92	700.00	1.43	8200 (RCM)
6.34	709.00	1.41	6100 (RCM)
6.83	718.00	1.39	5900 (RCM)
6.67	725.00	1.38	5100 (RCM)
6.75	726.00	1.38	5500 (RCM)
7.12	751.00	1.33	4900 (RCM)
7.23	752.00	1.33	4700 (RCM)
6.29	755.00	1.32	4800 (RCM)
6.41	759.00	1.32	4700 (RCM)
6.75	768.00	1.30	4600 (RCM)
6.83	771.00	1.30	4300 (RCM)
7.70	1165.00	0.86	753.00 (ST)
7.40	1208.00	0.83	483.00 (ST)
7.30	1258.00	0.79	267.00 (ST)
6.70	1314.00	0.76	158.00 (ST)
6.00	1360.00	0.74	87.00 (ST)
5.80	1443.00	0.69	40.00 (ST)

ϕ = 2.00 60/40 CH4/DME in "air"			
p / atm	Temp / K	1000/T	ign. delay / μs
19.71	669.00	1.49	16800 (RCM)
19.73	669.00	1.49	17100 (RCM)
19.03	693.00	1.44	6300 (RCM)
19.39	696.00	1.44	6500 (RCM)
18.33	710.00	1.41	3100 (RCM)
19.04	716.00	1.40	2500 (RCM)
18.89	722.00	1.39	2500 (RCM)
18.81	723.00	1.38	2200 (RCM)
22.00	913.00	1.10	1474.00 (ST)
21.70	948.00	1.05	1928.00 (ST)
19.70	958.00	1.04	875.00 (ST)
20.60	959.00	1.04	959.00 (ST)
20.30	973.00	1.03	1108.00 (ST)
20.60	1027.00	0.97	1142.00 (ST)
20.30	1077.00	0.93	885.00 (ST)
17.90	1089.00	0.92	589.00 (ST)
18.80	1161.00	0.86	367.00 (ST)
18.30	1197.00	0.84	254.00 (ST)
16.20	1256.00	0.80	162.00 (ST)
14.20	1355.00	0.74	58.00 (ST)

ϕ = **2.00 60/40 CH4/DME in "air" (RCM)**			
p **/ atm**	**Temp / K**	**1000/** T	**ign. delay /** μ**s**
26.03	622.00	1.61	84900
28.82	636.00	1.57	88000
29.28	668.00	1.50	14900
29.26	669.00	1.49	14800
27.92	690.00	1.45	5300
28.36	692.00	1.45	5800
26.70	714.00	1.40	1800
29.03	718.00	1.39	1900
29.16	721.00	1.39	1600
28.30	724.00	1.38	1900

ϕ = 0.30 DME in "air"			
Temp / K	**1000/T**	**p / atm**	**ign. delay / μs**
677.95	1.48	10.98	8100 (RCM)
678.65	1.47	11.04	8300 (RCM)
710.29	1.41	10.41	7100 (RCM)
714.62	1.40	10.55	7300 (RCM)
782.67	1.28	13.01	5300 (RCM)
782.56	1.28	13.01	5300 (RCM)
815.19	1.23	12.56	4800 (RCM)
815.59	1.23	12.57	4800 (RCM)
846.85	1.18	12.38	3100 (RCM)
846.76	1.18	12.38	3100 (RCM)
1124.00	0.89	12.70	1458.00 (ST)
1160.00	0.86	12.70	985.00 (ST)
1161.00	0.86	12.20	981.00 (ST)
1204.00	0.83	12.00	636.00 (ST)
1262.00	0.79	11.90	377.00 (ST)
1266.00	0.79	11.90	359.00 (ST)
1317.00	0.76	11.40	165.00 (ST)
1358.00	0.74	11.00	124.00 (ST)
1423.00	0.70	10.40	46.00 (ST)

ϕ = 0.30 DME in "air"			
p / atm	Temp / K	1000/T	ign. delay / μs
29.68	651.22	1.54	66400 (RCM)
29.78	651.51	1.53	64200 (RCM)
29.84	676.89	1.48	13900 (RCM)
29.80	676.09	1.48	15100 (RCM)
26.16	692.75	1.44	2600 (RCM)
27.68	702.70	1.42	2900 (RCM)
32.65	845.70	1.18	1252.00 (ST)
31.39	958.73	1.04	1156.00 (ST)
34.04	799.00	1.25	1843.00 (ST)
31.45	827.30	1.21	1735.00 (ST)
31.69	910.00	1.10	1421.00 (ST)
30.62	994.20	1.01	1084.00 (ST)
30.95	1245.00	0.80	130.13 (ST)

ϕ = 0.50 DME in "air" (ST)			
p / atm	Temp / K	1000/T	ign. delay / μs
11.85	688.20	1.45	4802.00
12.45	740.20	1.35	2991.00
12.71	776.10	1.29	2795.00
12.42	827.80	1.21	2882.00
12.92	911.90	1.10	2850.00
12.36	911.70	1.10	3221.00
11.63	925.00	1.08	3600.00
11.51	962.72	1.04	3205.00
12.50	1086.00	0.92	1224.00
12.50	1167.00	0.86	628.00
12.50	1210.00	0.83	341.00
12.50	1252.00	0.80	225.00
12.50	1323.00	0.76	86.00
12.50	1371.00	0.73	48.00
12.50	1428.00	0.70	25.00

ϕ = 0.50 DME in "air" (ST)			
p / atm	Temp / K	1000/T	ign. delay / μs
26.75	690.20	1.45	2782.00
24.83	730.80	1.37	1469.00
24.52	817.90	1.22	1023.00
24.70	820.40	1.22	1059.00
23.76	977.20	1.02	1034.00
24.60	1037.00	0.96	722.92
24.40	1069.00	0.94	599.00
25.70	1119.00	0.89	374.00
27.70	1192.00	0.84	206.00
26.90	1243.00	0.80	128.00
28.20	1252.00	0.80	86.00
23.50	1272.00	0.79	107.00
25.10	1274.00	0.78	88.00
21.80	1342.00	0.75	47.00

ϕ = 1.00 DME in "air" (ST)			
p / atm	Temp / K	1000/T	ign. delay / μs
11.98	765.77	1.31	1451.00
11.76	800.70	1.25	1537.00
11.44	842.40	1.19	1774.00
11.67	889.70	1.12	1885.00
11.66	930.20	1.08	1771.00
11.88	978.50	1.02	1609.00
11.62	1010.00	0.99	1150.00
13.20	1091.00	0.92	618.00
12.20	1098.00	0.91	574.00
12.50	1174.00	0.85	302.00
11.50	1210.00	0.83	246.00
11.40	1249.00	0.80	178.00
10.90	1267.00	0.79	146.00
10.50	1296.00	0.77	91.00
10.70	1344.00	0.74	59.00

ϕ = 1.00 DME in "air" (ST)			
p / atm	Temp / K	1000/T	ign. delay / μs
20.87	681.70	1.47	2819.00
21.13	725.30	1.38	1168.00
19.33	730.10	1.37	1155.00
20.48	752.60	1.33	787.05
21.14	794.20	1.26	591.17
21.71	840.90	1.19	576.66
22.32	885.10	1.13	626.68
22.10	911.80	1.10	690.93
24.83	770.20	1.30	586.73
26.26	805.60	1.24	395.97
26.79	852.80	1.17	414.92
23.67	848.50	1.18	503.13
28.00	931.20	1.07	395.61
27.08	1003.00	1.00	483.41
26.30	1075.00	0.93	373.00
25.90	1093.00	0.91	337.00
24.90	1118.00	0.89	292.00
26.10	1161.00	0.86	177.00
26.40	1238.00	0.81	78.00

ϕ = 1.00 DME in "air" (ST)			
p / atm	Temp / K	1000/T	ign. delay / μs
24.83	770.20	1.30	586.73
26.26	805.60	1.24	395.97
26.79	852.80	1.17	414.92
23.67	848.50	1.18	503.13
28.00	931.20	1.07	395.61
27.08	1003.00	1.00	483.41
26.30	1075.00	0.93	373.00
25.90	1093.00	0.91	337.00
24.90	1118.00	0.89	292.00
26.10	1161.00	0.86	177.00
26.40	1238.00	0.81	78.00

ϕ = **2.00 DME in "air" (ST)**			
***p* / atm**	**Temp / K**	**1000/*T***	**ign. delay / μs**
11.70	757.70	1.32	1061.00
11.65	807.30	1.24	955.72
11.51	844.00	1.18	1097.00
11.37	890.30	1.12	1314.00
11.42	941.90	1.06	1491.00
11.27	986.50	1.01	1440.00
11.52	1045.90	0.96	596.96
11.92	1076.60	0.93	493.94
11.60	1199.00	0.83	212.00
11.30	1209.00	0.83	197.00
13.00	1213.00	0.82	189.00
11.10	1227.00	0.81	176.00
10.90	1241.00	0.81	160.00
10.80	1244.00	0.80	161.00
9.20	1272.00	0.79	117.00
10.20	1272.00	0.79	101.00
9.60	1354.00	0.74	47.00

ϕ = **2.00 DME in "air" (ST)**			
***p* / atm**	**Temp / K**	**1000/*T***	**ign. delay / μs**
25.91	709.80	1.41	1483.00
25.44	757.20	1.32	569.32
26.00	813.50	1.23	304.48
28.00	952.00	1.05	307.00
26.50	978.00	1.02	358.00
26.70	978.00	1.02	340.00
27.30	1047.00	0.96	326.00
26.50	1105.00	0.90	152.00
28.20	1235.00	0.81	59.00
23.50	1253.00	0.80	83.00

A.3 Validation of the DME Model

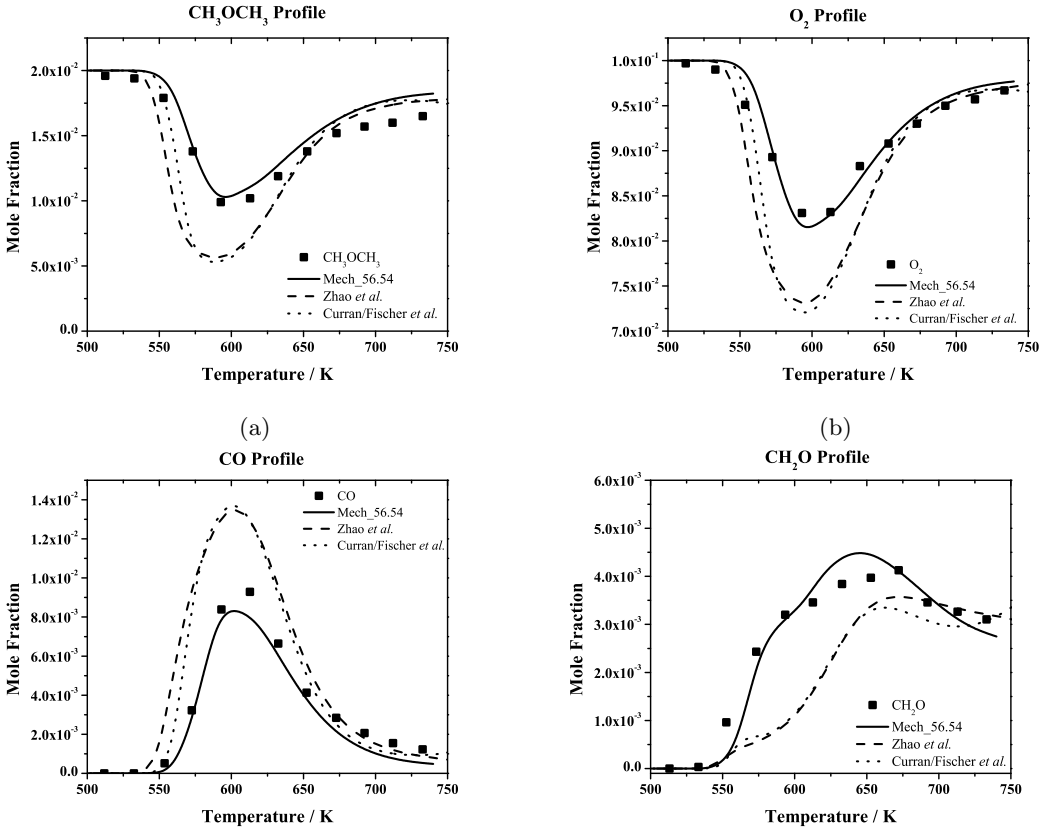

Figure A.1: Atmospheric Flow Reactor Data: H. Guo, W. Sun, F. M. Haas, T. Farouk, F. L. Dryer, Y. Ju, Proceedings of the Combustion Institute, 34, (2013), 573–581.

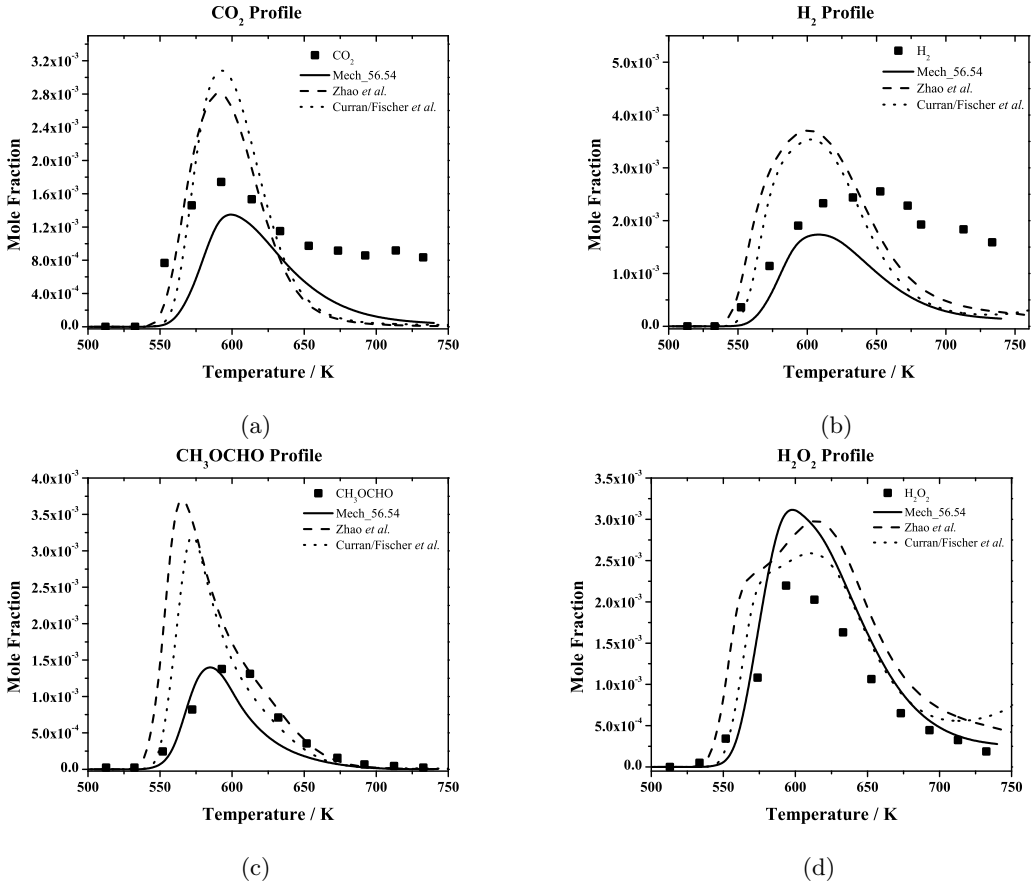

Figure A.2: Atmospheric Flow Reactor Data: H. Guo, W. Sun, F. M. Haas, T. Farouk, F. L. Dryer, Y. Ju, Proceedings of the Combustion Institute, 34, (2013), 573–581.

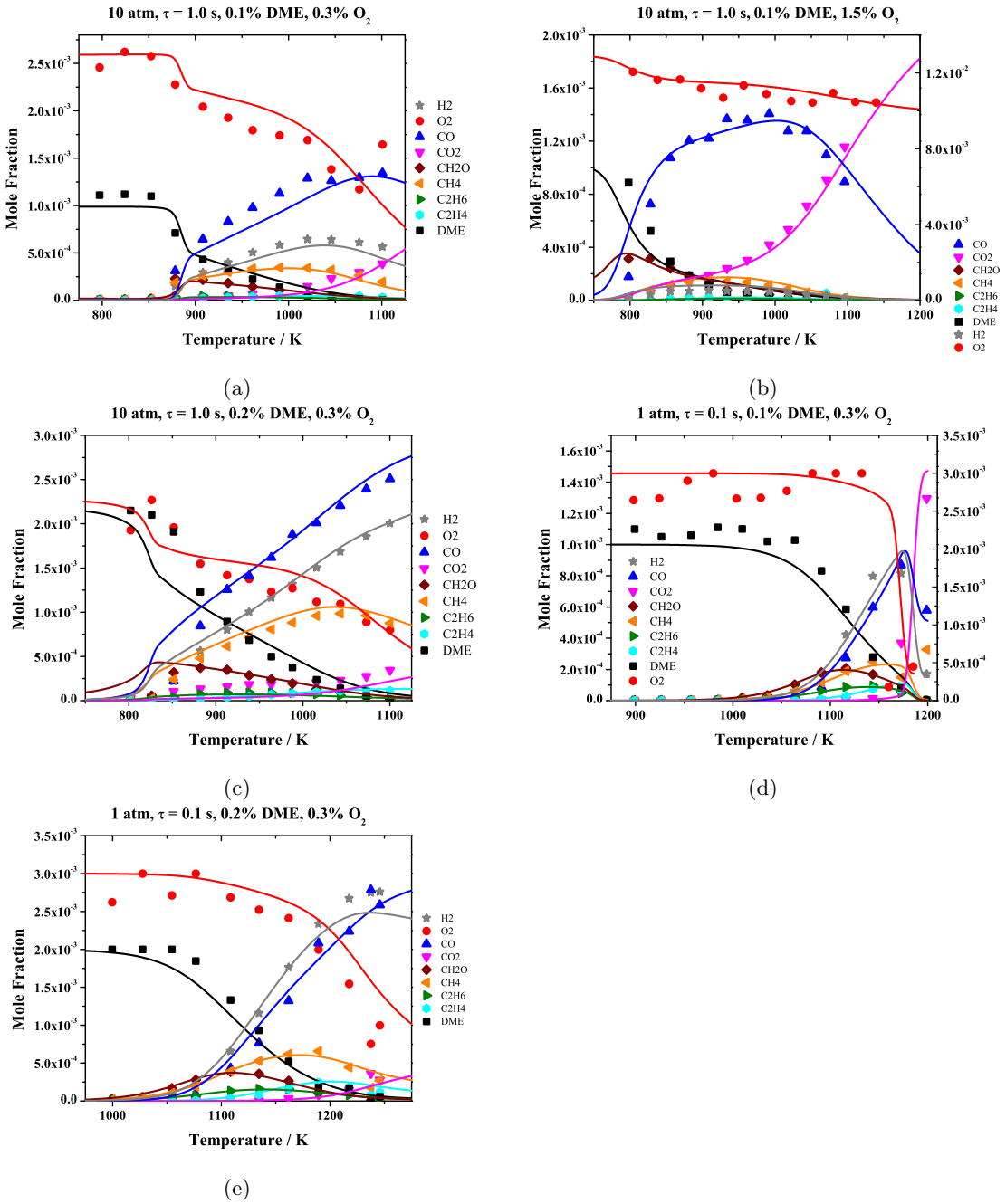

Figure A.3: Jet Stirred Reactor: P. Dagaut, C. Daly, J. M. Simmie, M. Cathonnet, Symposium (International) on Combustion, 27, (1998) 361–369.

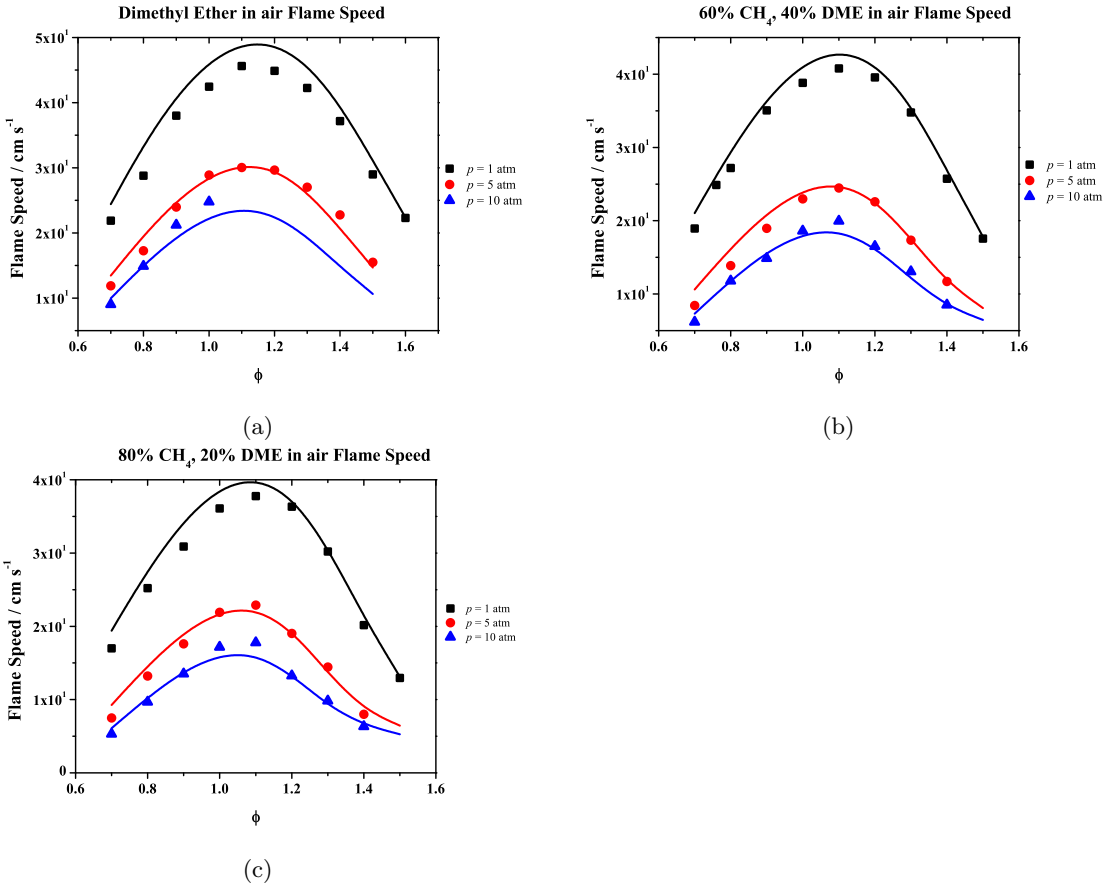

Figure A.4: Flame Speed: J. de Vries, W. B. Lowry, Z. Serinyel, H. J. Curran, E. L. Petersen, Fuel, 90 (2011) 331–338.

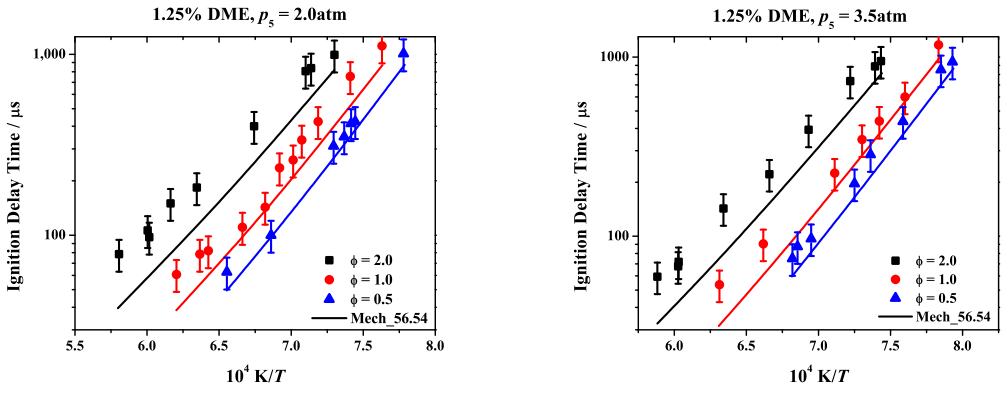

Figure A.5: Ignition Delay Times: An Experimental and Modelling Study of the Combustion of Oxygenated Hydrocarbons, Ph.D. Thesis, Fiona R. Gillespie, Department of Chemistry, National University of Ireland Galway, Ireland, 2014.

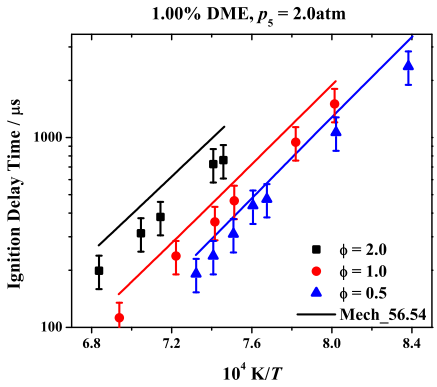

Figure A.6: Ignition Delay Times: R. D. Cook, D. F. Davidson, R. K. Hanson, Proceedings of the Combustion Institute, 32, (2009), 189–196.

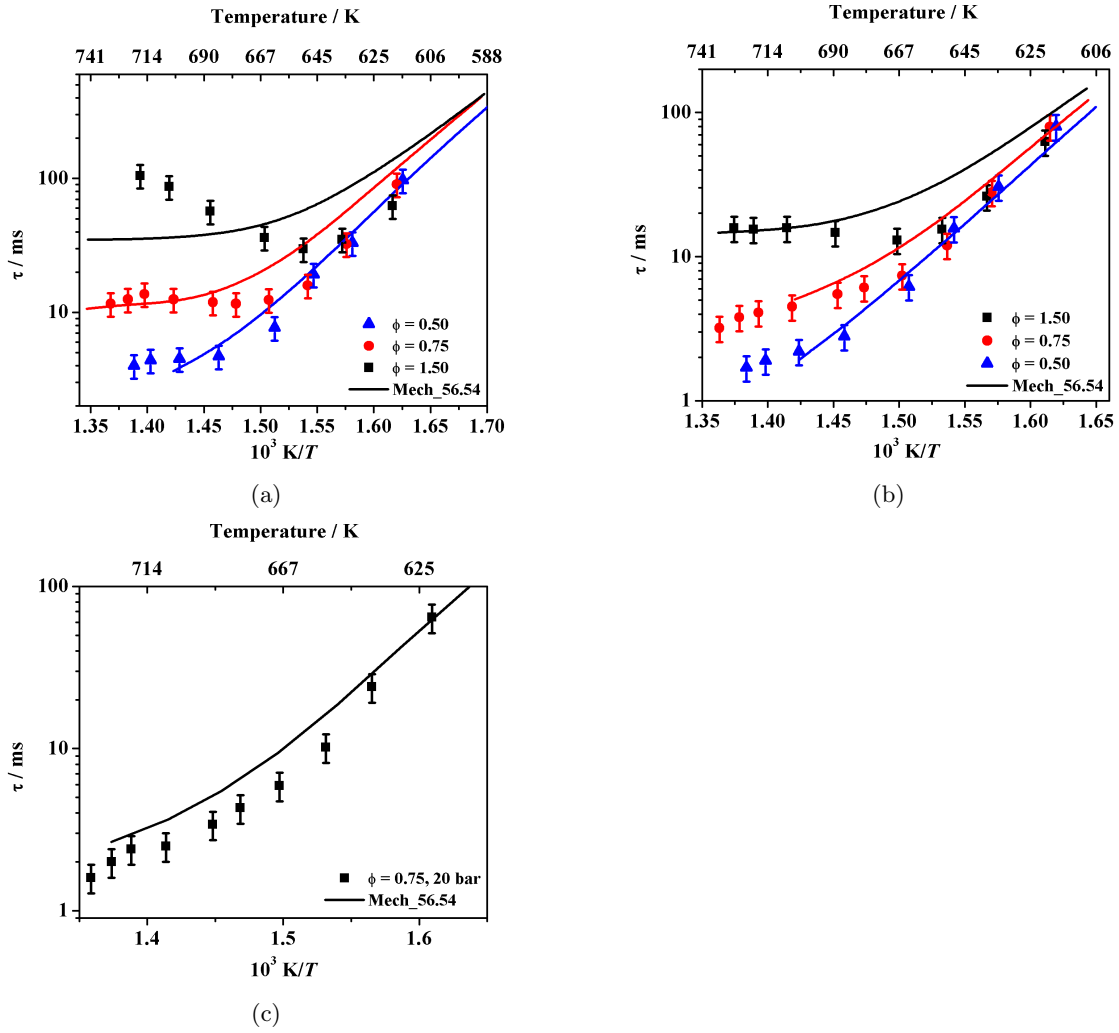

Figure A.7: Ignition Delay Times: G. Mittal. M. Chaos, C. -J. Sung, F. L. Dryer, Fuel Processing Technology, 89, (2008), 1244–1254.

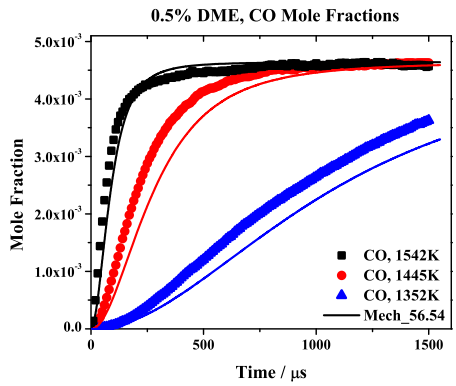

(a)

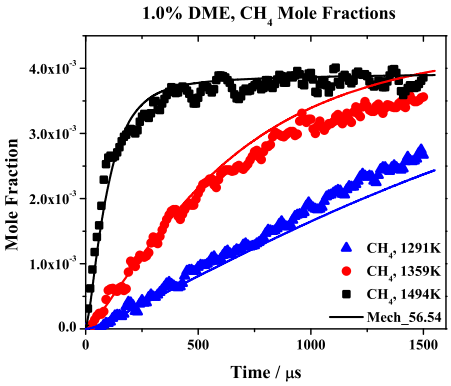

(b)

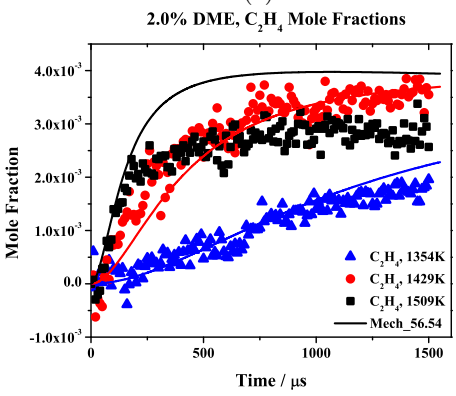

(c)

Figure A.8: ST Speciation: S. H. Pyun, W. Ren, K. -Y. Lam, D. F. Davidson, R. K. Hanson, Combustion and Flame, 160, (2013), 747-754.

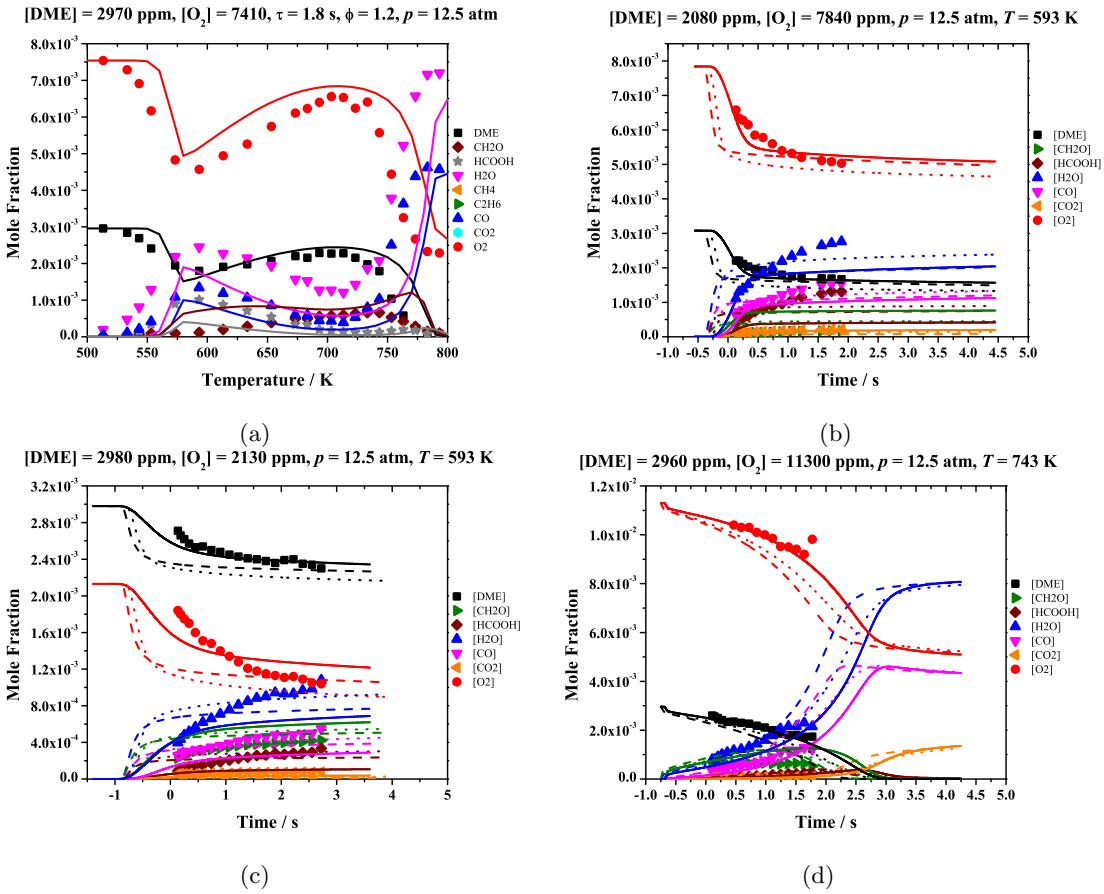

Figure A.9: Variable Pressure Flow Reactor Data: H. J. Curran, S. L. Fischer, F. L. Dryer, International Journal of Chemical Kinetics, 32, (2000), 741–759. S. L. Fischer, F. L. Dryer, H. J. Curran, International Journal of Chemical Kinetics, 32, (2000), 713–740.

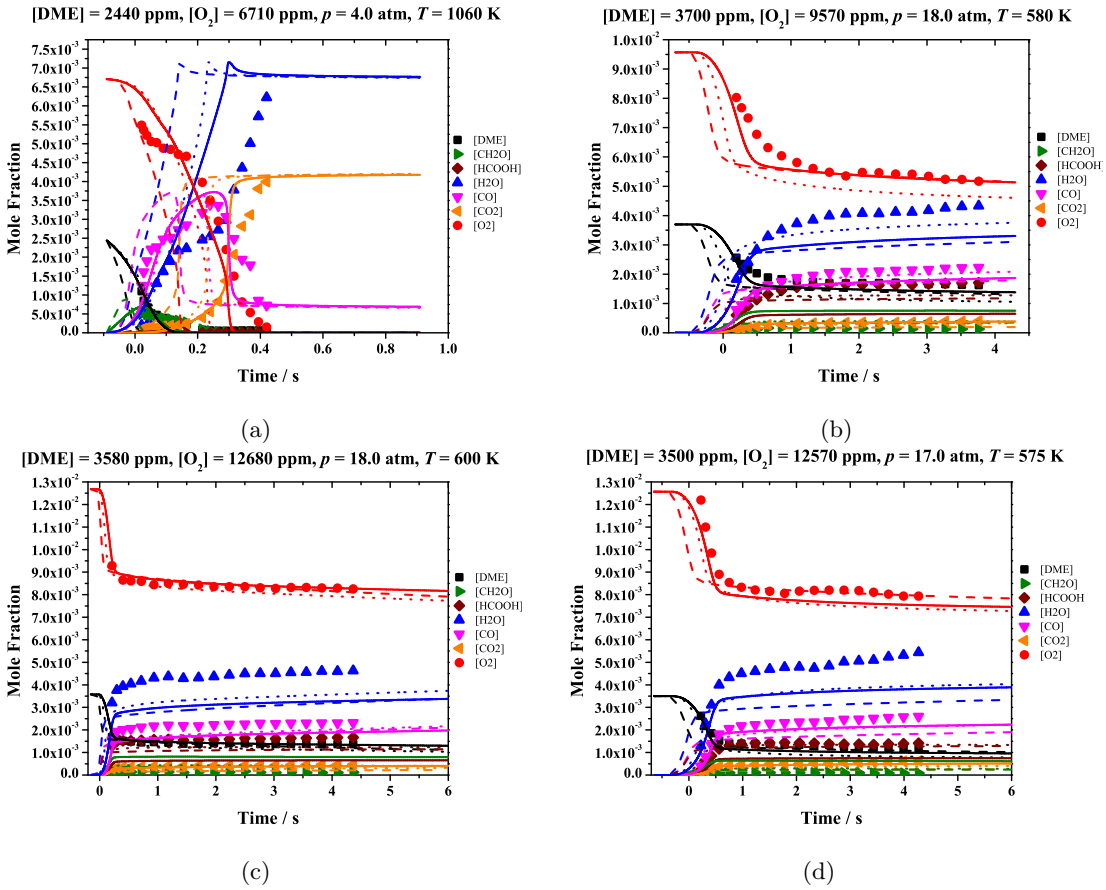

Figure A.10: Variable Pressure Flow Reactor Data: H. J. Curran, S. L. Fischer, F. L. Dryer, International Journal of Chemical Kinetics, 32, (2000), 741–759. S. L. Fischer, F. L. Dryer, H. J. Curran, International Journal of Chemical Kinetics, 32, (2000), 713–740.

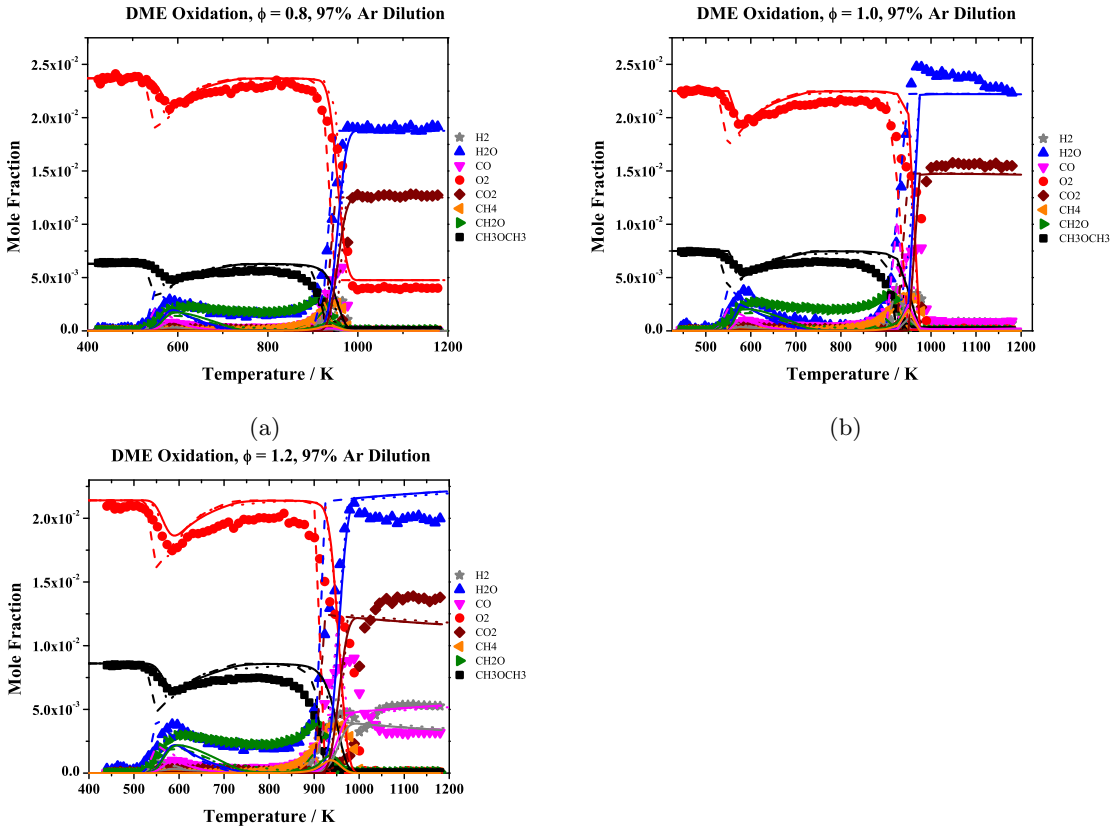

Figure A.11: Atmospheric Flow Reactor Data: F. Herrmann, B. Jochim, P. Oβwald, L. Cai, H. Pitsch, K. Kohse-Höinghaus, Combustion and Flame, 161, (2014), 384-397.

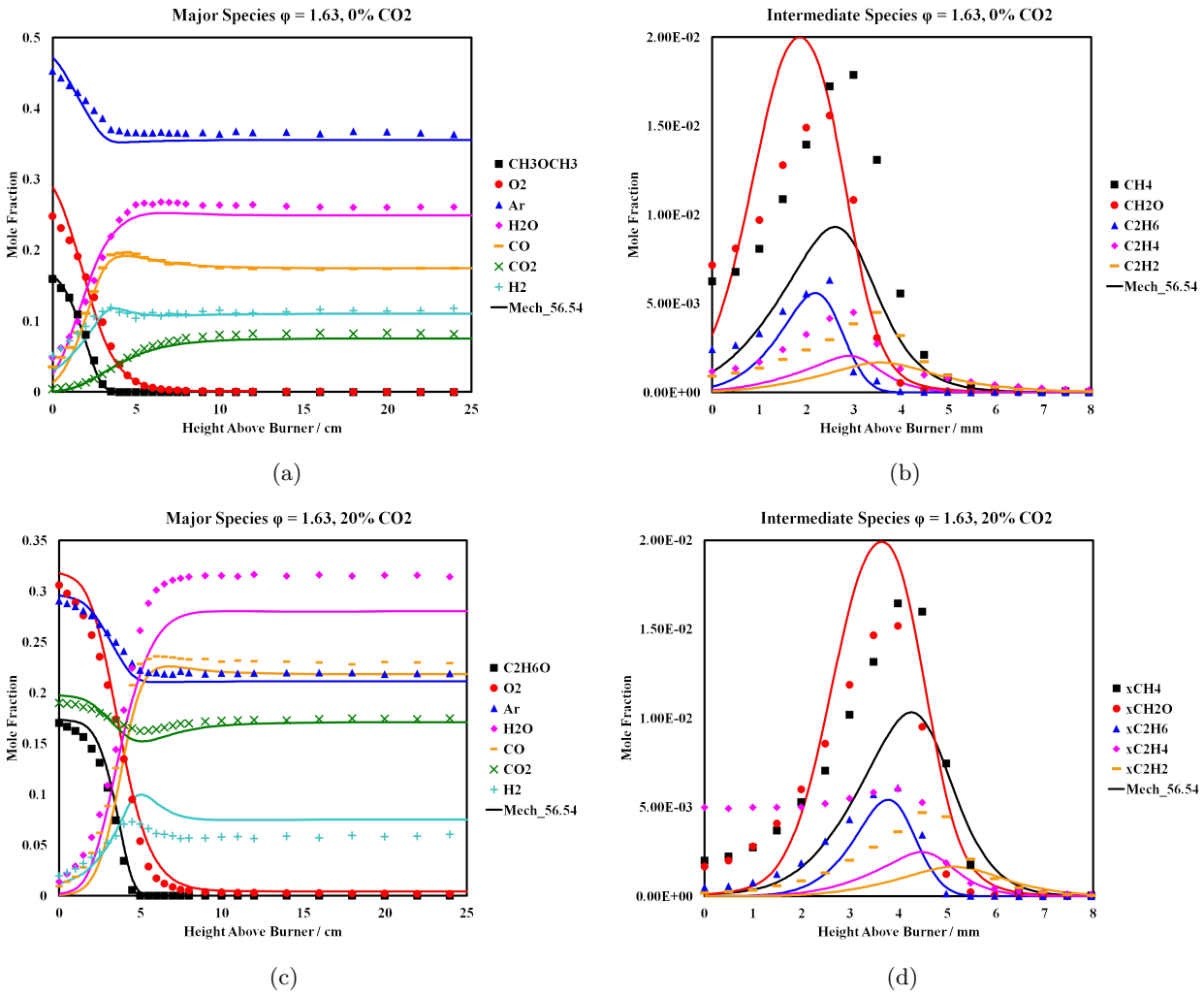

Figure A.12: Flame Speciation Data: D. Liu, J. Santner, C. Togbé, D. Felsmann, J. Koppmann, A. Lackner, X. Yang, X. Shen, Y. Ju, K. Kohse-Höinghaus, Combustion and Flame, 160, (2013), 2654-2668.

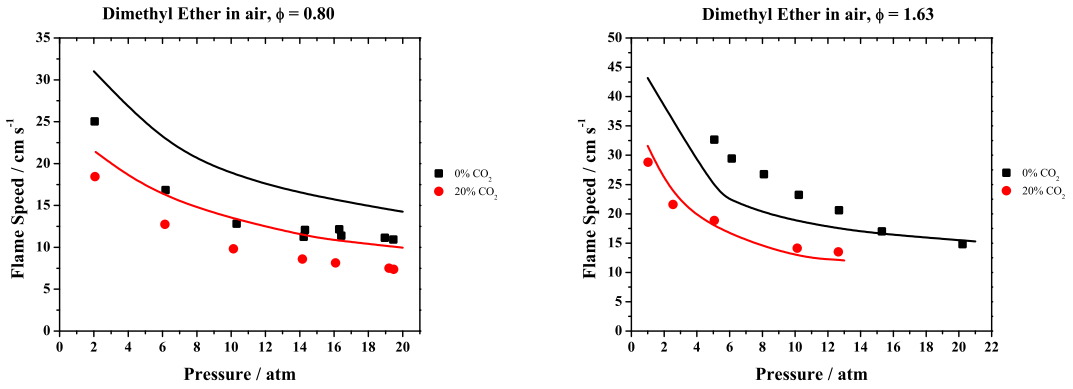

Figure A.13: Flame Speed Data: D. Liu, J. Santner, C. Togbé, D. Felsmann, J. Koppmann, A. Lackner, X. Yang, X. Shen, Y. Ju, K. Kohse-Höinghaus, Combustion and Flame, 160, (2013), 2654-2668.

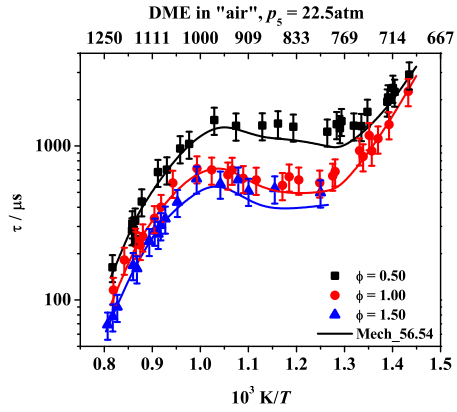

(a)

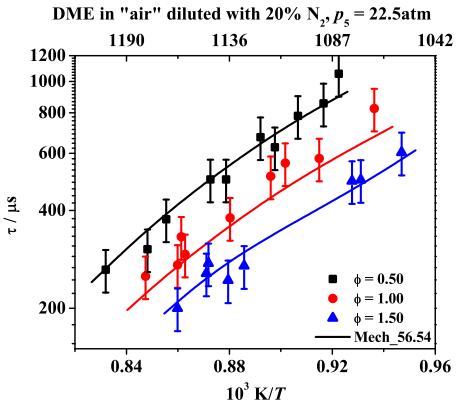

(b)

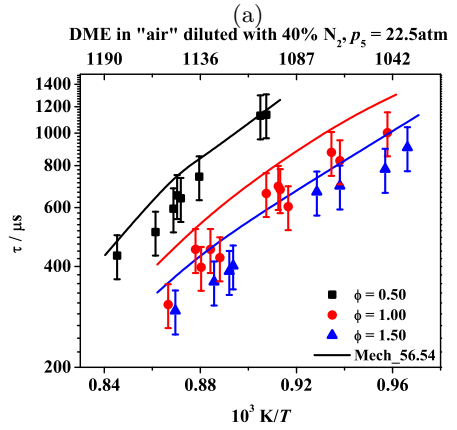

(c)

Figure A.14: Ignition Delay Time Data: Z. Li, W. Wang, Z. Huang, M. A. Oehlschlaeger, Energy & Fuels, 27, (2013), 2811–2817.

Appendix B

Methanol

B.1 Methanol Experimental Data

Dataset 1 (ST)								
% CH3OH	**% O2**	**% N2**	**% Ar**	ϕ	$\boldsymbol{p}$	**Temp / K**	**1000/$\boldsymbol{T}$**	τ / μ**s**
5	15	80	0	0.5	20.358	998	1.002004	1430.4
5	15	80	0	0.5	20.154	1038.7	0.962742	738.4
5	15	80	0	0.5	20.487	1096.8	0.911743	298.4
5	15	80	0	0.5	20.061	1117.8	0.894614	244.4
5	15	80	0	0.5	20.188	1155.5	0.865426	154.4
5	15	80	0	0.5	19.978	1184.9	0.843953	112.4
5	15	80	0	0.5	19.632	1214	0.823723	84.4
5	15	80	0	0.5	19.877	1061.5	0.942063	608.4
5	15	80	0	0.5	19.988	1068.8	0.935629	440
5	15	80	0	0.5	19.269	1240.4	0.806192	66
Dataset 2 (ST)								
% CH3OH	**% O2**	**% N2**	**% Ar**	ϕ	$\boldsymbol{p}$	**Temp / K**	**1000/$\boldsymbol{T}$**	τ / μ**s**
6.544	19.634	73.822	0	0.5	49.82	1002.6	0.997407	869.136
6.544	19.634	73.822	0	0.5	48.099	1068.5	0.935891	318.922
6.544	19.634	73.822	0	0.5	49.891	1269	0.788022	24.088
6.544	19.634	73.822	0	0.5	50.699	959.5	1.042209	1452
6.544	19.634	73.822	0	0.5	49.564	1150.7	0.869036	77.255
Dataset 3 (RCM)								
% CH3OH	**% O2**	**% N2**	**% Ar**	ϕ	$\boldsymbol{p}$	**Temp / K**	**1000/$\boldsymbol{T}$**	τ / μ**s**
2.85	8.55	66.45	22.15	0.5	29.54	892	1.121076	122500
2.85	8.55	66.45	22.15	0.5	29.58	892	1.121076	123800
2.85	8.55	66.45	22.15	0.5	28.79	908	1.101322	38920
2.85	8.55	66.45	22.15	0.5	28.84	908	1.101322	40540
2.85	8.55	66.45	22.15	0.5	28.7	930	1.075269	15870
2.85	8.55	66.45	22.15	0.5	29.42	936	1.068376	15070
2.85	8.55	66.45	22.15	0.5	29.19	934	1.070664	14840
2.85	8.55	66.45	22.15	0.5	28.69	956	1.046025	5784
2.85	8.55	66.45	22.15	0.5	29.06	959	1.042753	5963
2.85	8.55	66.45	22.15	0.5	29	968	1.033058	4108
2.85	8.55	66.45	22.15	0.5	28.98	969	1.031992	4185
Dataset 4 (RCM)								
% CH3OH	**% O2**	**% N2**	**% Ar**	ϕ	$\boldsymbol{p}$	**Temp / K**	**1000/$\boldsymbol{T}$**	τ / μ**s**
2.85	8.55	66.45	22.15	0.5	40.03	893	1.119821	54980
2.85	8.55	66.45	22.15	0.5	39.75	892	1.121076	50020
2.85	8.55	66.45	22.15	0.5	38.92	909	1.10011	20720
2.85	8.55	66.45	22.15	0.5	38.49	909	1.10011	19680
2.85	8.55	66.45	22.15	0.5	38.75	931	1.074114	8578
2.85	8.55	66.45	22.15	0.5	39.12	933	1.071811	9331
2.85	8.55	66.45	22.15	0.5	38.92	956	1.046025	3435
2.85	8.55	66.45	22.15	0.5	38.83	956	1.046025	3242

Dataset 5 (ST)								
% CH3OH	**% O2**	**% N2**	**% Ar**	ϕ	p	**Temp / K**	**1000/T**	τ / μs
8	12	80	0	1	19.458	1207.2	0.828363	68
8	12	80	0	1	20.484	1154.6	0.866101	120
8	12	80	0	1	21.071	1096.2	0.912242	258
8	12	80	0	1	19.064	1010.2	0.989903	830
8	12	80	0	1	19.828	1007.6	0.992457	904
8	12	80	0	1	20.184	1067.9	0.936417	352
8	12	80	0	1	19.79	1111.4	0.899766	202
8	12	80	0	1	19.549	1172.5	0.852878	94
8	12	80	0	1	20.537	1056.8	0.946253	452
Dataset 6 (ST)								
% CH3OH	**% O2**	**% N2**	**% Ar**	ϕ	p	**Temp / K**	**1000/T**	τ / μs
12.28	18.43	69.29	0	1	31.54	1124.23	0.889498	149.422
12.28	18.43	69.29	0	1	30.79	1010	0.990099	698.146
12.28	18.43	69.29	0	1	30.03	900.58	1.110396	2028
12.28	18.43	69.29	0	1	31.04	962.95	1.038476	1139
12.28	18.43	69.29	0	1	30.98	1063.89	0.939947	269
Dataset 7 (ST)								
% CH3OH	**% O2**	**% N2**	**% Ar**	ϕ	p	**Temp / K**	**1000/T**	τ / μs
12.28	18.43	69.29	0	1	48.139	988.7	1.011429	683.777
12.28	18.43	69.29	0	1	48.344	1089.1	0.918189	138.979
12.28	18.43	69.29	0	1	48.979	1214	0.823723	29.219
12.28	18.43	69.29	0	1	49.93	1053.2	0.949487	253.049
12.28	18.43	69.29	0	1	50.962	1164	0.859107	44.255
Dataset 8 (ST)								
% CH3OH	**% O2**	**% N2**	**% Ar**	ϕ	p	**Temp / K**	**1000/T**	τ / μs
5.7	8.55	0	85.75	1	8.918	998.9	1.001101	3867
5.7	8.55	0	85.75	1	10.428	1129.5	0.885347	529.395
5.7	8.55	0	85.75	1	10.619	1192	0.838926	290.295
5.7	8.55	0	85.75	1	10.861	1260	0.793651	140.231
5.7	8.55	0	85.75	1	10.66	1273.6	0.785176	124.525
5.7	8.55	0	85.75	1	10.698	1222.3	0.81813	194.187
5.7	8.55	0	85.75	1	10.581	1164.3	0.858885	363.707
5.7	8.55	0	85.75	1	9.944	1078.2	0.927472	1105
5.7	8.55	0	85.75	1	10.026	1047	0.95511	1785
5.7	8.55	85.75	0	1	9.084	1059	0.944287	1406

Dataset 9 (ST)								
% CH3OH	**% O2**	**% N2**	**% Ar**	ϕ	p	**Temp / K**	**1000/T**	τ / μs
5.7	8.55	0	85.75	1	49.362	998.9	1.001101	1057
5.7	8.55	0	85.75	1	49.93	1054.1	0.948677	461.85
5.7	8.55	0	85.75	1	51.149	1295.6	0.771843	29.567
5.7	8.55	0	85.75	1	50.023	994.5	1.00553	1113
5.7	8.55	0	85.75	1	45.436	1136.3	0.880049	158.021
Dataset 10 (RCM)								
% CH3OH	**% O2**	**% N2**	**% Ar**	ϕ	p	**Temp / K**	**1000/T**	τ / μs
5.7	8.55	64.3125	21.4375	1	9.48	917	1.090513	94160
5.7	8.55	64.3125	21.4375	1	9.33	913	1.09529	93880
5.7	8.55	64.3125	21.4375	1	9.47	939	1.064963	31840
5.7	8.55	64.3125	21.4375	1	9.34	936	1.068376	30430
5.7	8.55	64.3125	21.4375	1	9.27	956	1.046025	14340
5.7	8.55	64.3125	21.4375	1	9.3	956	1.046025	13640
5.7	8.55	64.3125	21.4375	1	9.34	978	1.022495	6649
5.7	8.55	64.3125	21.4375	1	9.4	980	1.020408	6956
Dataset 11 (RCM)								
% CH3OH	**% O2**	**% N2**	**% Ar**	ϕ	p	**Temp / K**	**1000/T**	τ / μs
5.7	8.55	64.3125	21.4375	1	29.89	862	1.160093	107400
5.7	8.55	64.3125	21.4375	1	29.92	862	1.160093	106400
5.7	8.55	64.3125	21.4375	1	30.17	885	1.129944	37750
5.7	8.55	64.3125	21.4375	1	29.63	880	1.136364	37320
5.7	8.55	64.3125	21.4375	1	29.91	906	1.103753	13310
5.7	8.55	64.3125	21.4375	1	30.55	911	1.097695	13470
5.7	8.55	64.3125	21.4375	1	30.38	932	1.072961	5751
5.7	8.55	64.3125	21.4375	1	30.38	931	1.074114	5595
Dataset 12 (RCM)								
% CH3OH	**% O2**	**% N2**	**% Ar**	ϕ	p	**Temp / K**	**1000/T**	τ / μs
5.7	8.55	64.3125	21.4375	1	38.92	845	1.183432	312100
5.7	8.55	64.3125	21.4375	1	39.31	865	1.156069	64450
5.7	8.55	64.3125	21.4375	1	39.49	867	1.153403	62000
5.7	8.55	64.3125	21.4375	1	38.94	886	1.128668	23540
5.7	8.55	64.3125	21.4375	1	38.89	885	1.129944	24660
5.7	8.55	64.3125	21.4375	1	38.17	904	1.106195	9971
5.7	8.55	64.3125	21.4375	1	38.4	906	1.103753	10110
5.7	8.55	64.3125	21.4375	1	37.84	924	1.082251	4625
5.7	8.55	64.3125	21.4375	1	38.71	930	1.075269	4813
5.7	8.55	64.3125	21.4375	1	37.78	946	1.057082	1885

Dataset 13 (ST)								
% CH3OH	**% O2**	**% N2**	**% Ar**	ϕ	p	**Temp / K**	**1000/T**	τ / μs
3.1	4.65	0	92.25	1	9.74	1090.6	0.916926	1333.3
3.1	4.65	0	92.25	1	10.383	1183.5	0.844951	529.215
3.1	4.65	0	92.25	1	10.4	1236	0.809061	281.716
3.1	4.65	0	92.25	1	10.031	1260.7	0.79321	230.851
3.1	4.65	0	92.25	1	10.047	1312.9	0.761673	144.571
3.1	4.65	0	92.25	1	10.063	1365.3	0.73244	91.238
3.1	4.65	0	92.25	1	10.178	1425.8	0.701361	48.46
Dataset 14 (ST)								
% CH3OH	**% O2**	**% N2**	**% Ar**	ϕ	p	**Temp / K**	**1000/T**	τ / μs
21.882	16.411	0	61.707	2	1.99	1414.8	0.706814	71.06
21.882	16.411	0	61.707	2	2.061	1373.8	0.727908	97.37
21.882	16.411	0	61.707	2	2.05	1370.5	0.729661	99.39
21.882	16.411	0	61.707	2	1.912	1297	0.77101	186.83
21.882	16.411	0	61.707	2	1.911	1296.7	0.771188	182.1
21.882	16.411	0	61.707	2	2.012	1277.2	0.782963	217.83
21.882	16.411	0	61.707	2	1.829	1269.8	0.787526	239.39
21.882	16.411	0	61.707	2	1.988	1224.5	0.81666	348.64
21.882	16.411	0	61.707	2	2.069	1187.9	0.841822	474.73
21.882	16.411	0	61.707	2	1.815	1118.8	0.893815	1145.89
21.882	16.411	0	61.707	2	1.93	1078.3	0.927386	1883.38
21.882	16.411	0	61.707	2	2.068	1226.4	0.815395	350
21.882	16.411	0	61.707	2	2.027	1215	0.823045	404.615
21.882	16.411	0	61.707	2	1.793	1129.9	0.885034	895.425
Dataset 15 (ST)								
% CH3OH	**% O2**	**% N2**	**% Ar**	ϕ	p	**Temp / K**	**1000/T**	τ / μs
21.882	16.411	61.707	0	2	51.641	1015.1	0.985125	263.98
21.882	16.411	61.707	0	2	50.994	1061.2	0.942329	127.778
21.882	16.411	61.707	0	2	51.712	1118.3	0.894214	59.085
21.882	16.411	61.707	0	2	51.088	909.3	1.099747	1527
21.882	16.411	61.707	0	2	50.005	1027.7	0.973047	241.831
21.882	16.411	61.707	0	2	50.283	1206.4	0.828912	21.476

Dataset 16 (RCM)								
% CH3OH	**% O2**	**% N2**	**% Ar**	ϕ	p	**Temp / K**	**1000/T**	τ / μs
11.4	8.55	60.0375	20.0125	2	30.12	841	1.189061	158500
11.4	8.55	60.0375	20.0125	2	29.55	837	1.194743	162700
11.4	8.55	60.0375	20.0125	2	29.94	860	1.162791	50750
11.4	8.55	60.0375	20.0125	2	29.6	858	1.165501	49760
11.4	8.55	60.0375	20.0125	2	29.62	878	1.138952	22330
11.4	8.55	60.0375	20.0125	2	29.39	876	1.141553	21170
11.4	8.55	60.0375	20.0125	2	29.33	895	1.117318	9851
11.4	8.55	60.0375	20.0125	2	29.27	895	1.117318	9638
11.4	8.55	60.0375	20.0125	2	29.19	915	1.092896	4607
11.4	8.55	60.0375	20.0125	2	29.21	914	1.094092	4539
Dataset 17 (RCM)								
% CH3OH	**% O2**	**% N2**	**% Ar**	ϕ	p	**Temp / K**	**1000/T**	τ / μs
11.4	8.55	60.0375	20.0125	2	40.04	817	1.22399	271900
11.4	8.55	60.0375	20.0125	2	40.47	820	1.219512	267600
11.4	8.55	60.0375	20.0125	2	40.3	839	1.191895	75670
11.4	8.55	60.0375	20.0125	2	39.96	836	1.196172	75010
11.4	8.55	60.0375	20.0125	2	39.86	857	1.166861	27820
11.4	8.55	60.0375	20.0125	2	40.37	859	1.164144	28080
11.4	8.55	60.0375	20.0125	2	40.03	877	1.140251	12950
11.4	8.55	60.0375	20.0125	2	40.64	880	1.136364	13190
11.4	8.55	60.0375	20.0125	2	38.67	895	1.117318	6473

B.2 Methanol Validation

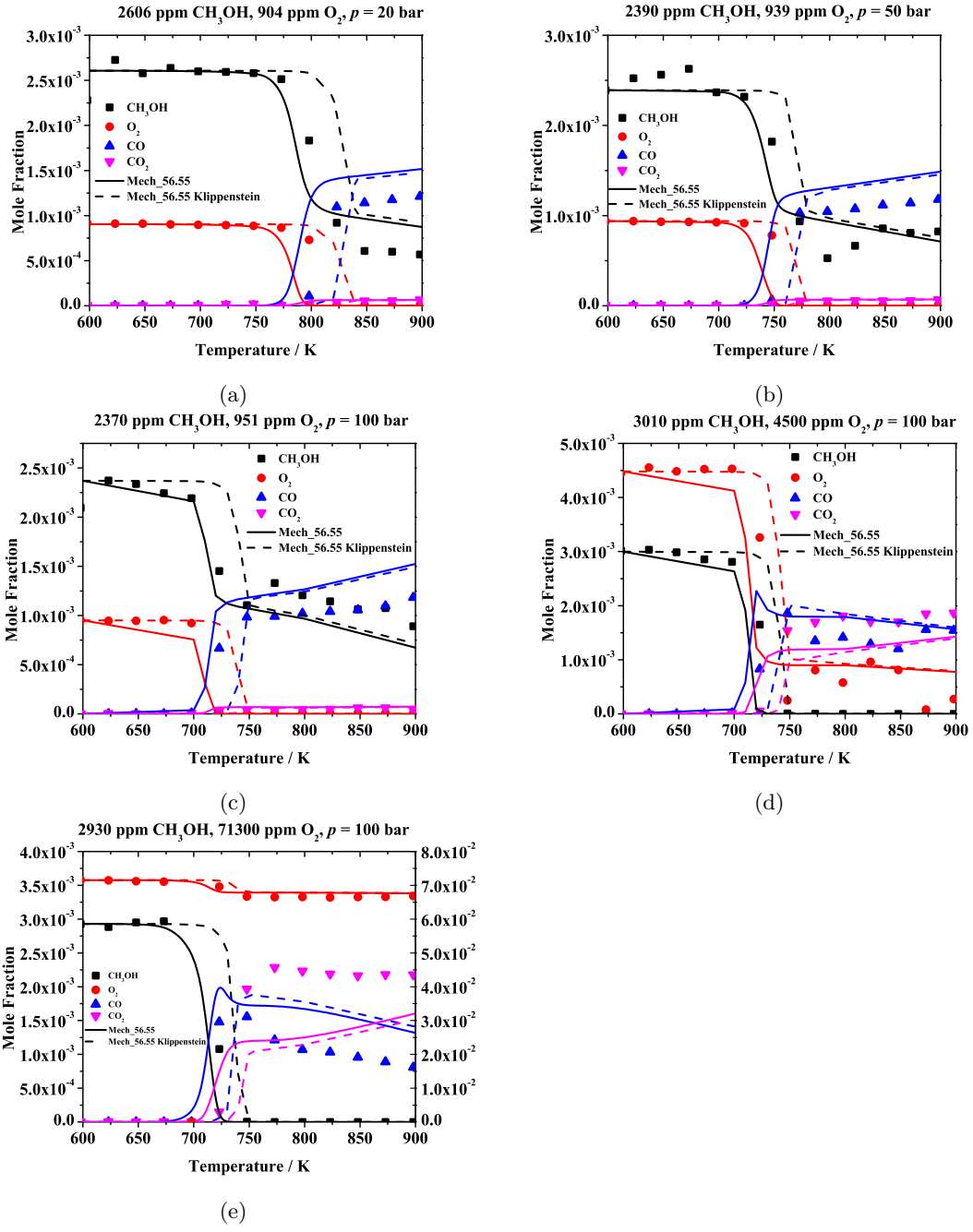

Figure B.1: Flow Reactor Data: V. Aranda, J. M. Christensen, M. U. Alzueta, P. Glarborg, S. Gersen, Y. Gao, P. Marshall, International Journal of Chemical Kinetics, 45, (2013), 283–294.

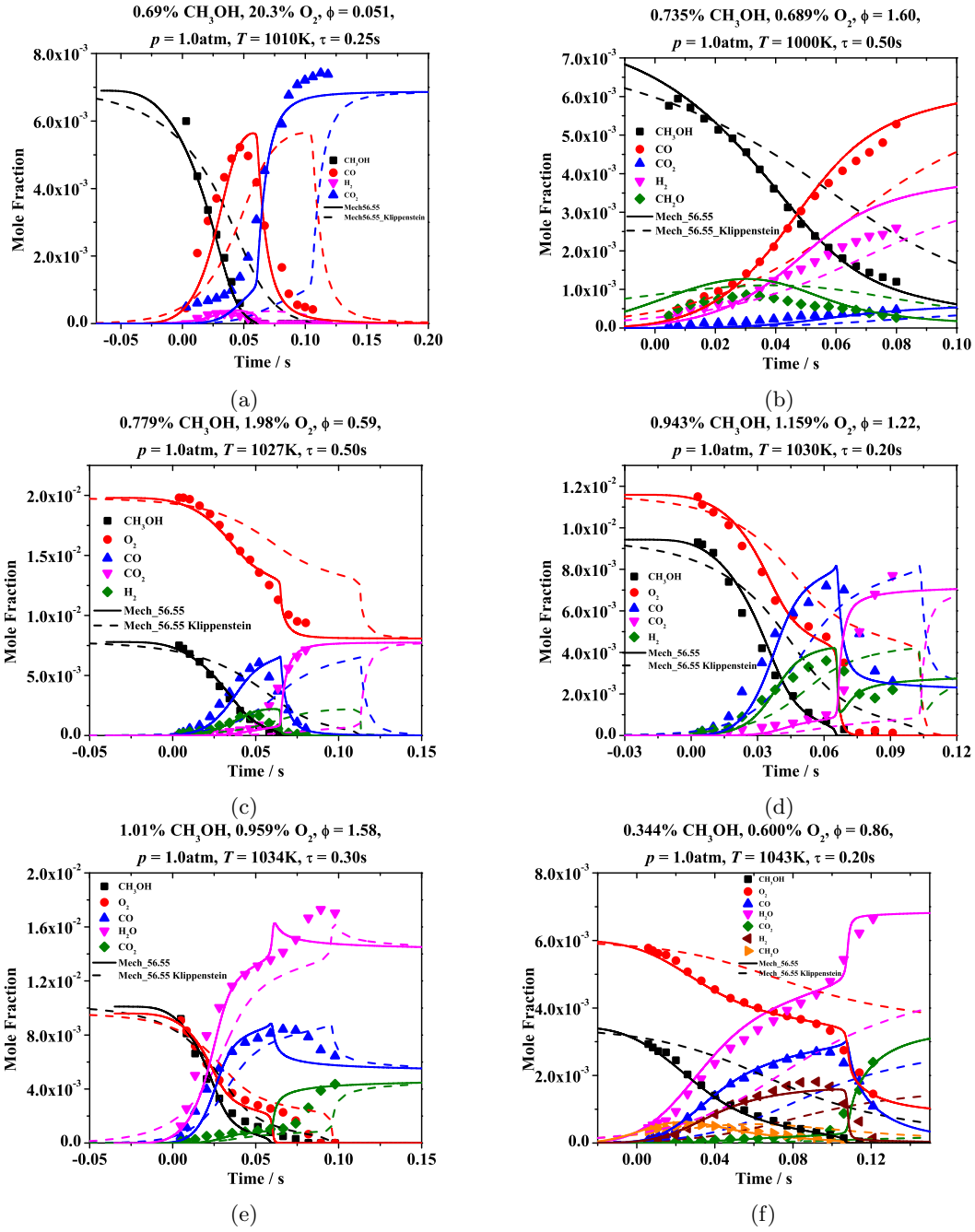

Figure B.2: Flow Reactor Data: T. J. Held, F. L. Dryer, International Journal of Chemical Kinetics, 30, (1998), 805–830.

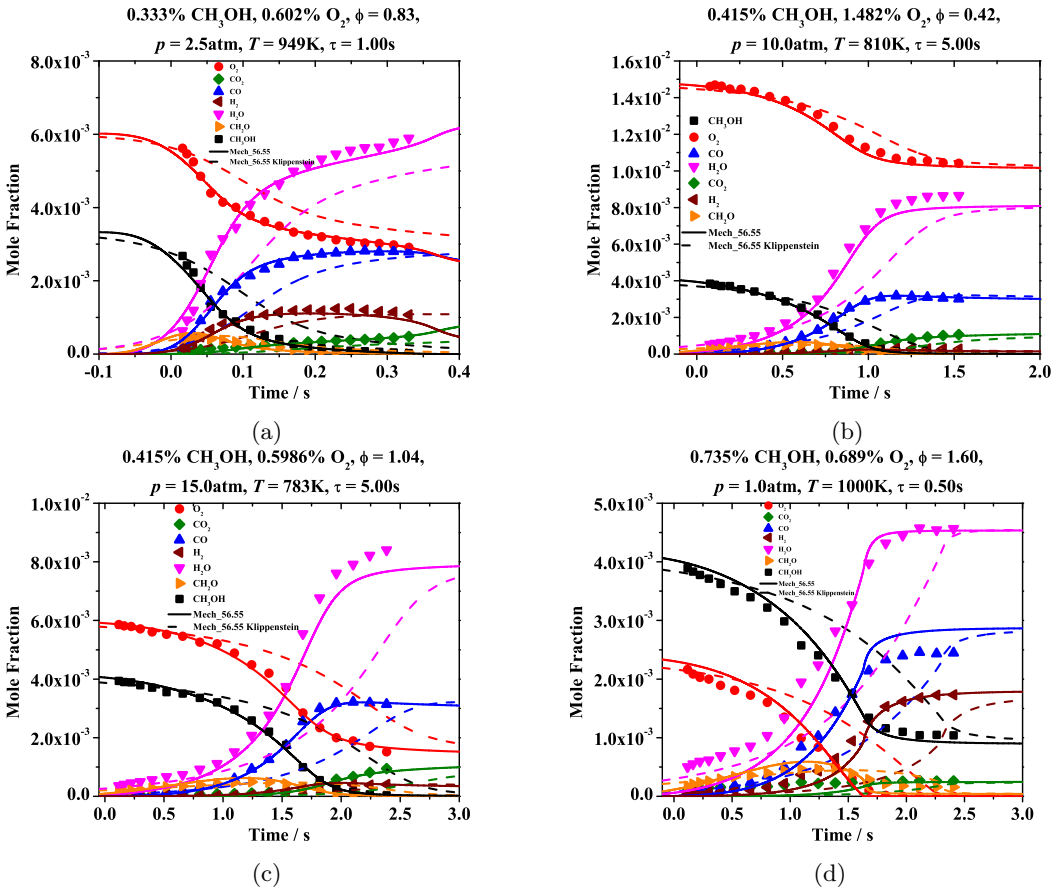

Figure B.3: Flow Reactor Data: T. J. Held, F. L. Dryer, International Journal of Chemical Kinetics, 30, (1998), 805–830.

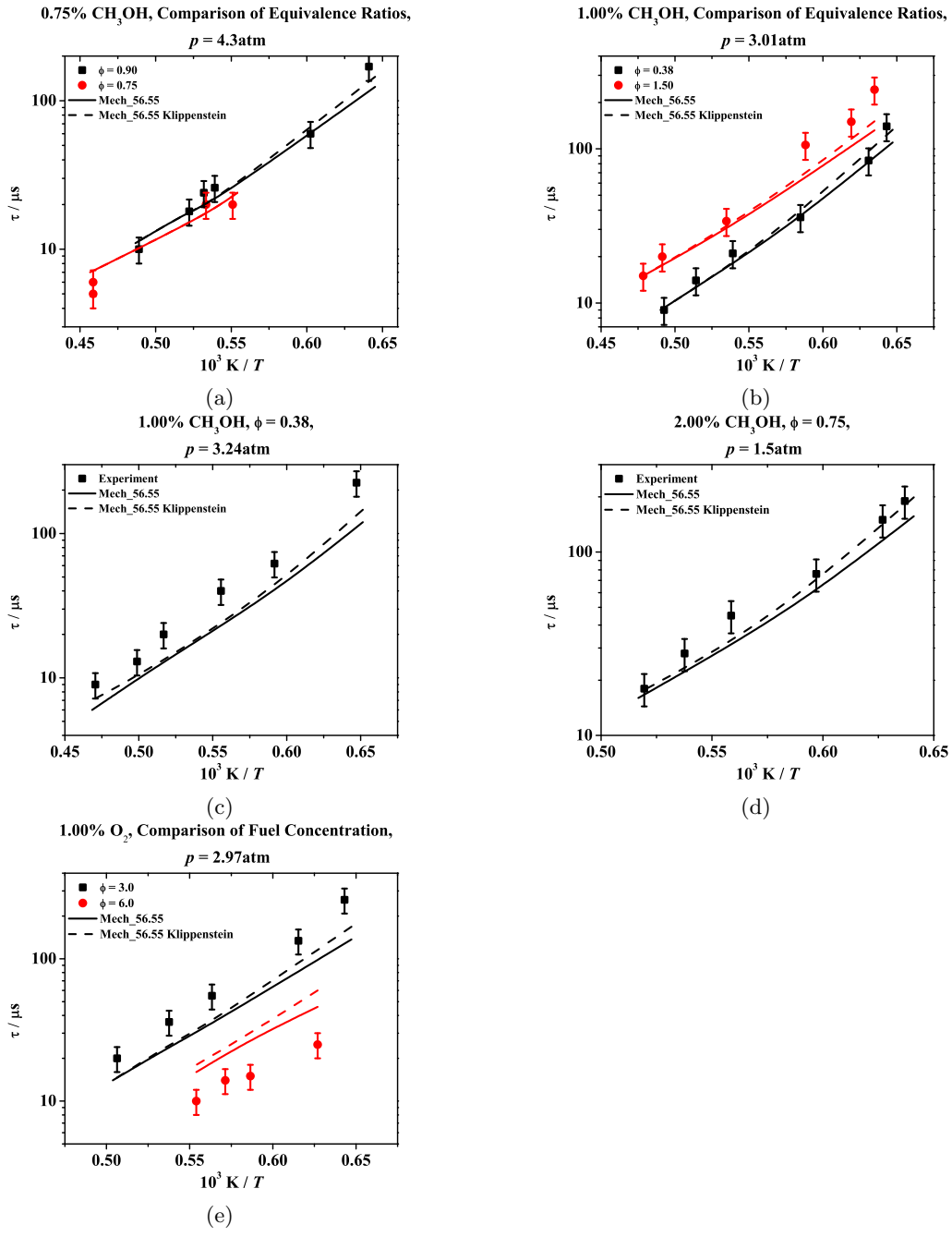

Figure B.4: Ignition Delay Time Data: C. T. Bowman, Combustion and Flame, 25, (1975), 343–354.

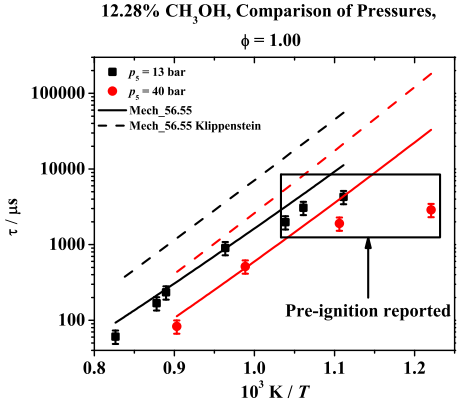

Figure B.5: Ignition Delay Time Data: K. Fieweger, R. Blumenthal, G. Adomeit, Combustion and Flame, 109, (1997), 599–619.

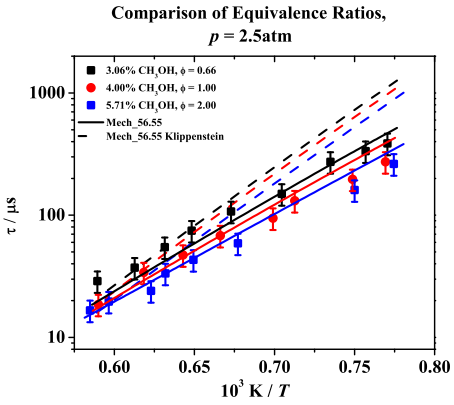

Figure B.6: Ignition Delay Time Data: K. Natarajan, K. A. Bhaskaran, Combustion and Flame, 43, (1981), 35–49.

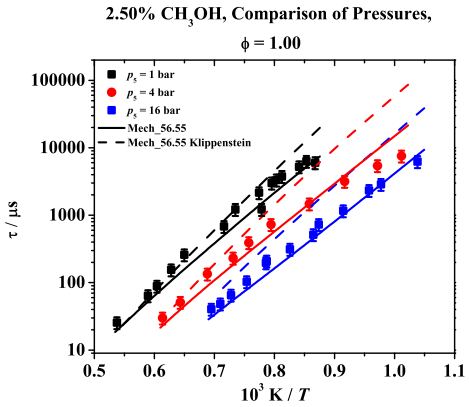

Figure B.7: Ignition Delay Time Data: J. Herzler, C. Naumann, Work in Progress Presentation (P3-8), In: *European Combustion Meeting 2013*, Lund, Sweden.

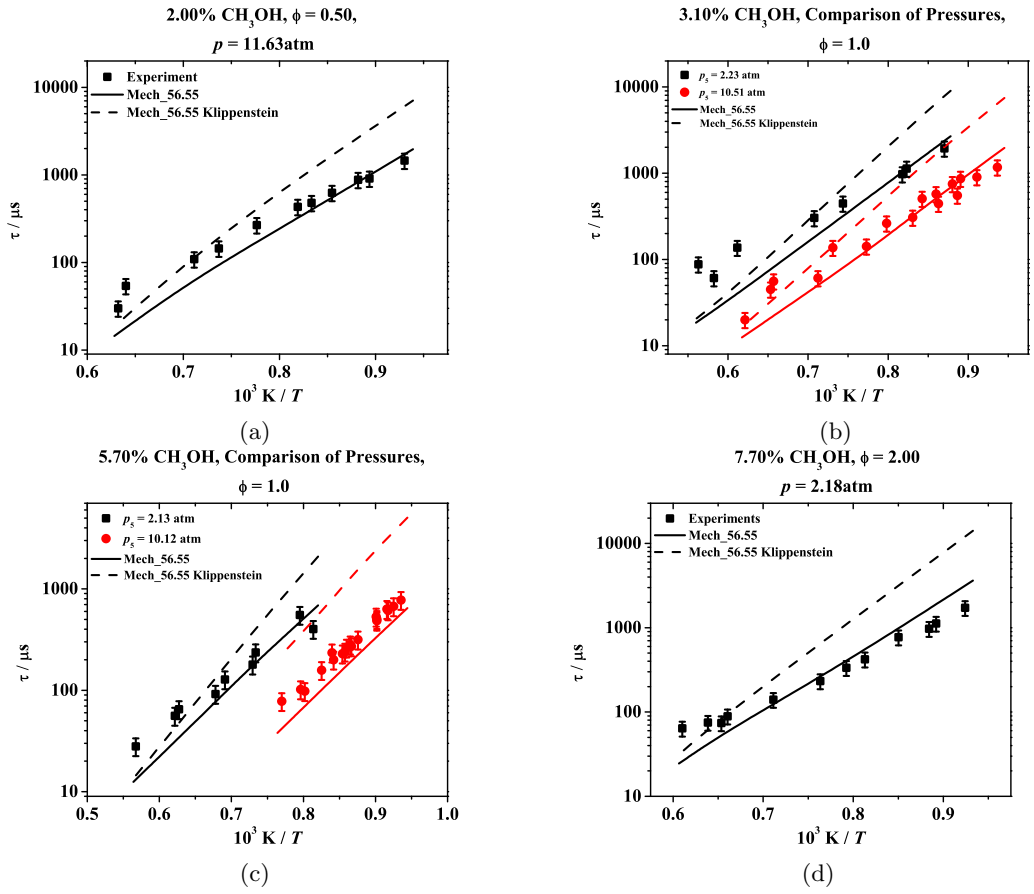

Figure B.8: Ignition Delay Time Data: K. E. Noorani, B. Akih-Kumgeh, J. M. Bergthorsen, Energy & Fuels, 24, (2010), 5834–5843.

Appendix C

TPGME

0.25 % TPGME, ϕ = 0.5, p_5 = 10 atm (ST)		
T_5 **/ K**	p_5 **/ atm**	τ**(dP/dt=MAX) / [**μ**s]**
988.40	9.35	5048.0
1017.10	9.71	3890.0
1102.30	10.54	1338.0
1162.70	10.57	563.1
1071.40	10.45	2003.0
1229.60	10.48	254.5
1316.10	10.16	101.6

0.25 % TPGME, ϕ = 0.5, p_5 = 20 atm (ST)		
T_5 **/ K**	p_5 **/ atm**	τ**(dP/dt=MAX) / [**μ**s]**
1333.50	22.82	45.9
1042.60	18.71	2043.0
1245.90	19.20	147.6
1067.70	19.13	1914.0
1110.40	19.43	910.4
1144.90	19.20	442.5
1333.80	18.89	53.7

0.25 % TPGME, ϕ = 1.0, p_5 = 10 atm (ST)		
T_5 / **K**	p_5 / **atm**	τ(**dP/dt=MAX**) / [μ**s**]
1358.70	10.36	155.8
1154.20	10.41	1692.0
1209.40	10.64	756.4
1217.20	10.08	725.9
1332.20	9.30	239.2
1536.70	8.57	57.9

0.25 % TPGME, ϕ = 1.0, p_5 = 20 atm (ST)		
T_5 / **K**	p_5 / **atm**	τ(**dP/dt=MAX**) / [μ**s**]
1089.10	19.52	2217.0
1155.10	20.53	826.8
1166.90	19.38	657.4
1405.80	19.80	77.3
1116.70	19.86	1850.0
1246.70	20.46	305.1
1295.60	20.20	165.8

0.25 % TPGME, ϕ = 2.0, p_5 = 10 atm (ST)		
T_5 / **K**	p_5 / **atm**	τ(**dP/dt=MAX**) / [μ**s**]
1222.10	11.05	2068.0
1271.70	10.71	1089.0
1294.00	10.35	913.0
1338.70	10.27	639.9
1369.20	10.21	498.3
1430.70	10.10	246.0
1501.20	10.07	130.3

0.25 % TPGME, ϕ = 2.0, p_5 = 20 atm (ST)		
T_5 **/ K**	p_5 **/ atm**	τ**(dP/dt=MAX) / [**μ**s]**
1187.10	18.41	1923.0
1380.50	21.76	239.6
1218.40	18.58	1239.0
1312.60	20.50	549.3
1491.00	18.35	111.3

Appendix D

Other Compounds

1% 2-MF ϕ = 0.50 (ST)			
p / atm	Temp. / K	10000/T	τ (d[CH*]/dt=MAX) / μs
0.95	1254.00	7.97	1066.67
0.92	1290.00	7.75	708.33
0.99	1338.50	7.47	525.00
1.01	1388.80	7.20	346.67
0.99	1408.50	7.10	251.67
0.99	1453.30	6.88	185.00
0.90	1413.30	7.08	235.00
1.01	1509.00	6.63	96.67
1.00	1556.00	6.43	85.00
1.02	1566.60	6.38	75.00
1.19	1535.00	6.51	86.67
1.07	1437.50	6.96	170.00
1.19	1461.20	6.84	150.60
1.19	1500.00	6.67	106.55

1% 2-MF ϕ = 1.00 (ST)			
p / atm	Temp. / K	10000/T	τ (d[CH*]/dt=MAX) / μs
1.03	1389.00	7.20	641.67
0.99	1430.40	6.99	395.77
0.98	1601.00	6.25	127.54
1.02	1534.90	6.52	207.38
0.90	1571.20	6.36	166.67
0.81	1472.80	6.79	283.33
1.00	1336.60	7.48	1033.33
1.00	1566.40	6.38	158.33
1.05	1407.00	7.11	591.67
0.98	1712.00	5.84	78.33
1.02	1448.00	6.91	364.74

1% 2-MF ϕ = 2.00 (ST)			
p / atm	Temp. / K	10000/T	τ (d[CH*]/dt=MAX) / μs
0.94	1496.10	6.68	1083.33
1.08	1498.80	6.67	1015.87
1.06	1504.90	6.64	870.83
1.02	1508.30	6.63	904.17
1.00	1511.30	6.62	804.17
1.06	1525.30	6.56	858.33
1.11	1591.60	6.28	483.33
1.00	1597.30	6.26	420.83
0.95	1599.20	6.25	453.33
1.11	1611.80	6.20	395.00
1.13	1623.50	6.16	370.83
1.01	1717.10	5.82	200.00
0.99	1769.40	5.65	131.67
0.97	1807.40	5.53	111.67

0.89% C3H6, 4.00% O2, in Ar, ϕ = 1.0 (ST)			
p / atm	Temp. / K	1000/T	τ / μs
44.41	1175.30	0.85	1754.00
39.73	1313.00	0.76	535.77
40.84	1367.50	0.73	332.71
38.70	1366.00	0.73	331.60
38.00	1457.10	0.69	138.71
39.84	1272.40	0.79	800.23
40.42	1245.30	0.80	1018.00
39.01	1499.10	0.67	93.37